



Norwegian University of Life Sciences
Faculty of Science and Technology

Philosophiae Doctor (PhD)
Thesis 2019:90

Design and Control of Intelligent Robotic Systems for Applications in Life Sciences: Biological Sample Preparation and Strawberry Harvesting

Design og styring av smarte robotsystemer
for applikasjoner innen biovitenskap:
biologisk prøvetaking og jordbærhøsting

Ya Xiong

Design and Control of Intelligent Robotic Systems for Applications in Life Sciences: Biological Sample Preparation and Strawberry Harvesting

Design og styring av smarte robotsystemer for applikasjoner innen biovitenskap:
biologisk prøvetaking og jordbærhøsting

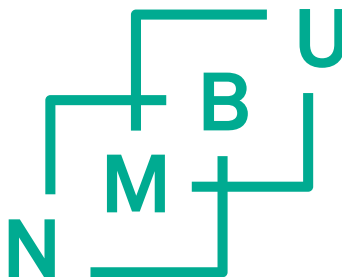
Philosophiae Doctor (PhD) Thesis

Ya Xiong

Norwegian University of Life Sciences

Faculty of Science and Technology

Ås 2019



Supervisory team

Professor **Pål Johan From** (main supervisor)

Faculty of Science and Technology, Norwegian University of Life Sciences, Ås, Norway

Associate Professor **Volha Shapaval** (co-supervisor)

Faculty of Science and Technology, Norwegian University of Life Sciences, Ås, Norway

Professor **Achim Kohler** (co-supervisor)

Faculty of Science and Technology, Norwegian University of Life Sciences, Ås, Norway

Summary

This thesis aims to contribute knowledge to support fully automation in life-science applications, which includes design, development, control and integration of robotic systems for sample preparation and strawberry harvesting, and is divided into two parts.

Part I shows the development of robotic systems for the preparation of fungal samples for Fourier transform infrared (FTIR) spectroscopy. The first step in this part developed a fully automated robot for homogenization of fungal samples using ultrasonication. The platform was constructed with a modified inexpensive 3D printer, equipped with a camera to distinguish sample wells and blank wells. Machine vision was also used to quantify the fungi homogenization process using model fitting, suggesting that homogeneity level to ultrasonication time can be well fitted with exponential decay equations. Moreover, a feedback control strategy was proposed that used the standard deviation of local homogeneity values to determine the ultrasonication termination time. The second step extended the first step to develop a fully automated robot for the whole process preparation of fungal samples for FTIR spectroscopy by adding a newly designed centrifuge and liquid-handling module for sample washing, concentration and spotting. The new system used machine vision with deep learning to identify the labware settings, which frees the users from inputting the labware information manually.

Part II of the thesis deals with robotic strawberry harvesting. This part can be further divided into three stages. i) The first stage designed a novel cable-driven gripper with sensing capabilities, which has high tolerance to positional errors and can reduce picking time with a storage container. The gripper uses fingers to form a closed space that can open to capture a fruit and close to push the stem to the cutting area. Equipped with internal sensors, the gripper is able to control a robotic arm to correct for positional errors introduced by the vision system, improving the robustness. The gripper and a detection method based on color thresholding were integrated into a complete system for strawberry harvesting. ii) The second stage introduced the improvements and updates to the first stage where the main focus was to address the challenges in unstructured environment by introducing a light-adaptive color thresholding method for vision and a novel obstacle-separation algorithm for manipulation. At this stage, the new fully integrated strawberry-harvesting system with dual-manipulator was capable of picking strawberries continuously in polytunnels. The main scientific contribution of this stage

is the novel obstacle-separation path-planning algorithm, which is fundamentally different from traditional path planning where obstacles are typically avoided. The algorithm uses the gripper to push aside surrounding obstacles from an entrance, thus clearing the way for it to swallow the target strawberry. Improvements were also made to the gripper, the arm, and the control. iii) The third stage improved the obstacle-separation method by introducing a zig-zag push for both horizontal and upward directions and a novel dragging operation to separate upper obstacles from the target. The zig-zag push can help the gripper capture a target since the generated shaking motion can break the static contact force between the target and obstacles. The dragging operation is able to address the issue of mis-capturing obstacles located above the target, in which the gripper drags the target to a place with fewer obstacles and then pushes back to move the obstacles aside for further detachment. The separation paths are determined by the number and distribution of obstacles based on the downsampled point cloud in the region of interest.

Sammendrag

Denne avhandlingen tar sikte på å bidra med kunnskap om automatisering og robotisering av applikasjoner innen livsvitenskap. Avhandlingen er todelt, og tar for seg design, utvikling, styring og integrering av robotsystemer for prøvetaking og jordbærhøsting.

Del I omhandler utvikling av robotsystemer til bruk under forberedelse av sopprøver for Fourier-transform infrarød (FTIR) spektroskopi. I første stadium av denne delen ble det utviklet en helautomatisert robot for homogenisering av sopprøver ved bruk av ultralyd-sonikering. Plattformen ble konstruert ved å modifisere en billig 3D-printer og utstyre den med et kamera for å kunne skille prøvebrønner fra kontrollbrønner. Maskinsyn ble også tatt i bruk for å estimere soppens homogeniseringsprosess ved hjelp av matematisk modellering, noe som viste at homogenitetsnivået faller eksponentielt med tiden. Videre ble det foreslått en strategi for regulering i lukker sløyfe som brukte standardavviket for lokale homogenitetsverdier til å bestemme avslutningstidspunkt for sonikeringen. I neste stadium ble den første plattformen videreutviklet til en helautomatisert robot for hele prosessen som forbereder prøver av sopprøver for FTIR-spektroskopi. Dette ble gjort ved å legge til en nyutviklet sentrifuge- og væskehåndteringsmodul for vasking, konsentrering og spotting av prøver. Det nye systemet brukte maskinsyn med dyp læring for å identifisere innstillingene for laboratorieutstyr, noe som gjør at brukerne slipper å registrere innstillingene manuelt.

Del II av avhandlingen tar for seg robotisert høsting av jordbær. Denne delen kan videre deles inn i tre stadier. i) I det første stadiet ble det designet en ny kabeldrevet griper med sensorer som gir den høy toleranse for posisjonsfeil, og som kan redusere plukketiden ved å oppbevare bærene i en beholder. Griperens fingre danner et lukket rom som kan åpnes for å omslutte et bær og deretter lukkes for å kutte av stilken. Griperen er utstyrt med interne sensorer, og er i stand til å kontrollere en robotarm slik at den korrigerer for posisjonsfeil som skyldes unøyaktigheter i maskinsynet, noe som forbedrer robustheten. Sammen med den integrerte fargebaserte deteksjonsmetoden utgjør griperen et komplett system for jordbærhøsting. ii) I andre stadium ble det introdusert forbedringer og oppdateringer av det første stadiet, der hovedfokuset var å møte utfordringene i ustrukturerte omgivelser ved å introdusere en metode for maskinsyn som kunne tilpasse seg lysforholdene, og å innføre en ny algoritme for manipulasjon. På dette stadiet var det nye helintegrerte jordbærhøstingssystemet med dobbeltmanipulator i stand til å plukke jordbær kontinuerlig i polytunneler. Det viktigste

vitenskapelige bidraget her er den nye algoritmen for baneplanlegging som dytter vekk hindringer, som er grunnleggende forskjellig fra tradisjonell baneplanlegging der hindringer vanligvis unngås. Algoritmen bruker griperen til å skyve de omkringliggende hindringene til side, slik at griperen får fri tilgang til målet, altså jordbæret som skal plukkes. Det ble også gjort forbedringer av griperen, armen og kontrollsystemet. iii) I tredje stadium ble metoden forbedret ved å introdusere et horisontalt og vertikalt sikksakk-dytt samt en ny trekkebevegelse for å skille ovenforliggende hindringer fra målet. Sikksakk-dyttet kan hjelpe griperen med å nå fram til målet, siden vibrasjonene som genereres kan skille bæret fra hindringene. Trekkoperasjonen kan løse problemet med at griperen feilaktig treffer hindringer som er plassert over målet, ved at griperen trekker målet til et sted med færre hindringer og deretter skyver det tilbake for å flytte hindringene til side. Separasjonsveiene bestemmes av antall og posisjonen til hindringer basert på den nedskalerte punktskyen i det aktuelle området.

Preface

This thesis is submitted in partial fulfilment of the requirements for the degree of Philosophy Doctor (PhD) at the Norwegian University of Life Sciences. The research presented in this thesis is the result of my doctoral studies in the period August 2016 through September 2019.

During these years I was fortunate enough to spend time at several different places. The first year I stayed 3 months at the RSN lab at University of Minnesota (USA) with Prof. Volkan Isler. I visited the L-CAS lab at University of Lincoln (UK) twice to attend the workshop in the last two years. I also participated two robotic conferences in my PhD study, the European robotics forum 2017 in Edinburg, UK and the ICRA 2018 in Brisbane, Australia. Moreover, I spent a few months in the strawberry farm to conduct my field tests. In 2017, I spent two weeks in the Myhre farm, Norway, for the field test of the first version of strawberry harvester, where I started to learn about strawberries. In 2018, I stayed in the Boxford farm, UK, for more than a month to perform my tests on the second version robot, where I learned a lot about strawberry characteristics and growing method. I subsequently visited the Boxford farm in 2019 to test the improved obstacle-separation method.

My thesis consists of two parts as I have been working on two different research projects in my PhD study. They are different, but both relate to the robotics and automation for applications in life sciences. Most importantly, these works have all contributed to science.

Acknowledgements

This work was carried out at the Faculty of Science and Technology, Norwegian University of Life Sciences. I would like to thank the university for the financial support.

I am very grateful to my main supervisor, Prof. Pål Johan From, who took me here to work on the interesting projects and supervised my PhD work. Through these years, he has guided me and helped me explore the world of robotics, and he has always found time for idea discussions and paper revisions. He also gave me with a lot of support for international exchanges.

I also would like to thank my co-supervisors Dr. Volha Shapaval and Prof. Achim Kohler who always attend my progress update presentations, giving me many suggestions on the sampling robot project. Dr. Shapaval also helped me a lot on the experiment design and preparation, and paper revisions. Prof. Kohler taught two courses with special syllabuses that helped me complete my course work.

I also want to thank Prof. Volkan Isler from the University of Minnesota for giving me the opportunity to stay in the RSN lab for three months, where I learned a lot about robotic vision from them. Also, many thanks go to Mr. Simen Myhre from the Myhre farm, and Mr. Robert England and Mr. Mihail Marita from the Boxford Suffolk Farms for providing the strawberry greenhouse and accommodation to conduct field experiments.

I also appreciate the friendship, help, support and companion from the wonderful people in the NMBU Robotics group and BioSpec group, Noronn, Saga and Chinese community in Ås.

Last but not least, I would like to thank my girlfriend for her companion, support and love, and my family, especially my parents, for their support and love.

Table of Contents

Summary	i
Sammendrag.....	iii
Preface.....	v
Acknowledgements	vii
Table of Contents	ix
List of Papers.....	xi
List of abbreviations.....	xiii
1. Introduction	1
1.1 Robotics in life sciences	1
1.2 Part I – Robotics in life-science laboratories.....	1
1.2.1 Robotic systems for sample preparation	2
1.2.2 Sample preparation systems for FTIR spectroscopy.....	3
1.3 Part II – Agricultural robotics.....	6
1.3.1 Autonomous vehicles	8
1.3.2 Robots for seeding, planting, pruning and weeding.....	9
1.3.3 Selective fruit-harvesting robots	10
2. Contributions and thesis overview	19
3. Results and discussions	21
3.1 Part I – Sample preparation robots for FTIR spectroscopy	21
3.1.1 Paper I – Ultrasonication robot for filamentous fungi homogenization.....	21
3.1.2 Paper II – A robot for the full process preparation of fungal samples for FTIR spectroscopy	22
3.2 Part II – Strawberry-harvesting robots	24
3.2.1 Paper III and VI – Gripper design, control and the first version of strawberry-harvesting robot.....	24

3.2.2	Paper IV – Adaptive color thresholding, obstacle separation and the second version of strawberry-harvesting robot	25
3.2.3	Paper V – Improvements to the novel obstacle separation method	27
4.	Conclusions	29
	References	31
	Appended papers	41

List of Papers

The material presented in this thesis is based on the papers listed below. The conference paper (vi) is not included in the thesis, since the content is partially covered by the journal version (paper iii). The published papers are appended with permissions from the publishers.

Part I – Sample preparation robots for FTIR spectroscopy

- I. **Xiong, Y.**, Shapaval, V., Kohler, A. and From, P.J., 2019. A Laboratory-Built Fully Automated Ultrasonication Robot for Filamentous Fungi Homogenization. *SLAS TECHNOLOGY: Translating Life Sciences Innovation*, 24, pp.1-13. DOI: <https://doi.org/10.1177/2472630319861361>
- II. **Xiong, Y.**, Shapaval, V., Kohler, A., Li J. and From, P.J., 2019. A Fully Automated Robot for the Preparation of Fungal Samples for FTIR Spectroscopy Using Deep Learning. *IEEE ACCESS*, 7, pp.1-12. DOI: <https://10.1109/ACCESS.2019.2941704>

Part II – Strawberry-harvesting robots

- III. **Xiong, Y.**, Peng, C., Grimstad, L., From, P.J. and Isler, V., 2019. Development and Field Evaluation of a Strawberry Harvesting Robot with a Cable-driven Gripper. *Computers and Electronics in Agriculture*, 157, pp.392-402. DOI: <https://doi.org/10.1016/j.compag.2019.01.009>
- IV. **Xiong, Y.**, Ge, Y., Grimstad, L. and From, P.J., 2019. An Autonomous Strawberry-Harvesting Robot: Design, Development, Integration, and Field evaluation. *Journal of Field Robotics*, 36, pp.1-23. DOI: <https://doi.org/10.1002/rob.21889>
- V. **Xiong, Y.**, Ge, Y. and From, P.J.. An Obstacle-separation Method for Robotic Picking of Fruits in Clusters. (Submitted to *IEEE Robotics and Automation Letters (RA-L)*).
- VI. **Xiong, Y.**, From, P.J. and Isler, V., 2018, May. Design and Evaluation of a Novel Cable-Driven Gripper with Perception Capabilities for Strawberry Picking Robots. In *2018 IEEE International Conference on Robotics and Automation (ICRA)* (pp.7384-7391). IEEE. DOI: <https://doi.org/10.1109/ICRA.2018.8460705>

List of abbreviations

3D	Three-dimensional
ANOVA	Analysis of variance
CAN	Controller area network
CiA	CAN in automation
CNN	Convolutional neural network
DC	Direct current
DOF	Degrees-of-freedom
EMSC	Extended multiplicative signal correction
FTIR	Fourier Transform Infrared (FTIR)
GNSS	Global navigation satellite system
GPU	Graphics processing unit
HSV	Hue, saturation and value
IMU	Inertial measurement unit
IR	Infrared
LED	Light-emitting diode
LfD	Learning from demonstration
LiDAR	Light detection and ranging
MALDI	Matrix-Assisted Laser Desorption/Ionization
MTP plates	Microtiter plates
PCL	Point Cloud Library
PID	Proportional-integral-derivative
PLA	Polylactic acid
RCNN	Regional CNN
RGB-D	Red, green, blue - depth

ROI	Region of interest
ROS	Robot operating system
RTK-GPS	Real-time kinematic global positioning system
s	Second
SCARA	Selective compliance assembly robot arm
SLAM	Simultaneous localization and mapping
TCP/IP	Transmission control protocol/Internet protocol
TOF	Time-off-Flight
USB	Universal serial bus
V	Voltage
W	Watts
YOLOv3	You only look once (YOLO) version 3

1. Introduction

1.1 Robotics in life sciences

Life science or biological science is regarded as one of the two main branches of natural science, the other being physical science (Rosenberg, 2011). Life sciences involve the studies that are relevant to living beings, such as microorganisms, plants, animals and human beings. Research in life sciences is helpful in improving the quality and standard of life.

Fundamental biological science includes many disciplines, such as microbiology, anatomy, physiology, botany, zoology, etc. Applied biology involves multiple disciplines, two of which - agriculture and biotechnology are tightly connected to technological sciences as for example robotics. Robotics in applied biology requires the collaboration between life sciences and physical sciences. For example, research of strawberry-harvesting robots (Yamamoto et al., 2014) may need to understand the biological characteristics of strawberry plants. Development of a surgical robot (Tanaka et al., 2008) should know the basic surgical techniques and operation sequences. In addition to the above agricultural robots and medical robots, life-science robots also include laboratory robots (Liu et al., 2013) and even the bio-inspired robots (Peyer et al., 2013). This thesis addresses some of the challenges in laboratory robotics and agricultural robotics, with special attention to the common challenges: non-uniform objects and diverse environment, presenting the design, development, integration and evaluation of sample preparation robots and strawberry-harvesting robots.

1.2 Part I – Robotics in life-science laboratories

Experimental work performed in life-science labs requires the operators to handle and monitor samples, where many of the tasks are repetitive, time-consuming and may be harmful to human beings. An automated system in life-science labs could greatly reduce the repetitive labor work and increase the throughput (Chapman, 2003), making it suitable for screening studies. The laboratory robots can further be divided into two main branches based on the experiment stages: experiment-assistant robots (Brown, 2011) and sample preparation robots (Reed et al., 2018), as the examples shown in **Fig. 1**.

Experiment-assistant robots work with the human operators to help conduct the experiments and analyze the results, which are able to increase the efficiency, accuracy and reduce the contamination. For example, as shown in **Fig. 1(a)**, a colony-picking robot uses digital-imaging

system with a robotic arm to select and pick individual colonies (Brown, 2011). A blood-typing robot is able to handle and analyze the blood samples using a robotic manipulator and imaging system (Chang et al., 2018). In addition, robotic systems for microinjection of cells were also developed, which use cameras to observe the process and robotic arms to hold the injection pipette (Ammi and Ferreira, 2005; Liu et al., 2011; Wang et al., 2007). Robotic technology overcomes the problems inherent in manual operation, such as unstable or low accuracy of operator hands and large variations in technical experiences.

Sample preparation robots are used to prepare the samples before sample analysis. As the example shown in **Fig. 1(b)**, a robotic arm is programmed to aspirate or dispense sample liquids between different well plates (Reed et al., 2018). A robot can also perform both the sample preparation and experiment-assistant (analysis) procedures, such as the one presented by Balter *et al.* capable of conducting blood sample collection, handling and analysis (Balter et al., 2018).

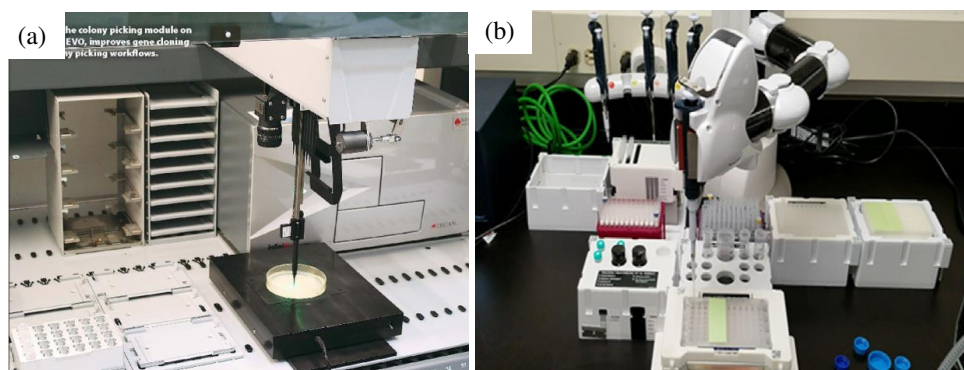


Fig. 1. Robotics in life-science laboratories: (a) a colony-picking robot (Brown, 2011); (b) a sample preparation robot (Reed et al., 2018).

1.2.1 Robotic systems for sample preparation

A number of platforms have been developed to automate the sample preparation procedures for different analyses. Meier *et al.* presented an automatic sampling spotting method using a commercially available synthetic robot to prepare samples for Matrix-Assisted Laser Desorption/Ionization Time-of-Flight (MALDI-TOF) spectrometry (MS) (Meier et al., 2003). Nejatimoharrami *et al.* developed a liquid-handling robot based on a 3D printer for placing droplets (spotting) (Nejatimoharrami et al., 2017). The system used a camera to monitor the droplet size and position. Kwee *et al.* described a robotic platform that used a vision system to identify cells and control a robotic arm to pick and place the selected cells for cell-based assays

(Kwee et al., 2017). As shown in **Fig. 2(a)**, Cherezov *et al.* showed a dual-arm system that used one arm for picking and placing of precipitant solutions while the other arm was equipped with a microsyringe for sample dispensing (Cherezov et al., 2004). **Fig. 2(b)** shows a robot to isolate lymphocytes for further blood analysis by using a centrifuge and a liquid-handling system, where a robotic arm is used to move the sample well plates (Chen et al., 2010).

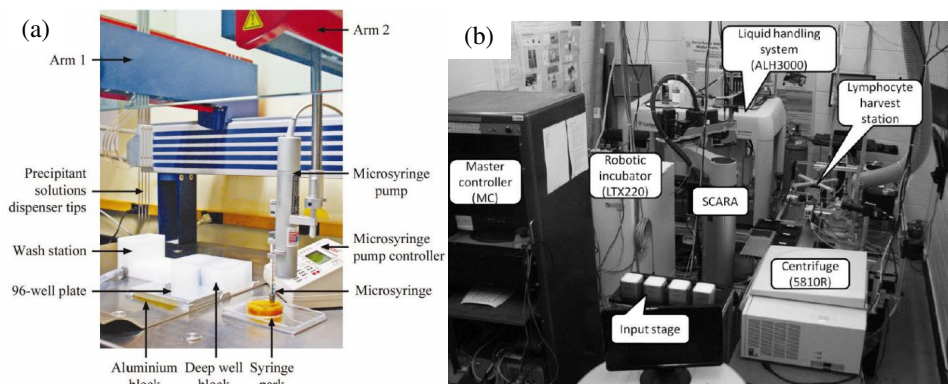


Fig. 2. Robotic system for sample preparation: (a) a liquid-handling robot (Cherezov et al., 2004); (b) a robot for isolating of cells (Chen et al., 2010).

Generally, the tasks of the sample preparation robots involve sample washing, liquid handling (aspiration, dispensing or spotting), centrifuge or sample homogenization, depending on the specific objective. The sample preparation robots generally consist of existing laboratory devices, such as centrifuge, pipette, sonicator, and labware, and add-on robotic systems, such as a robotic arm with a gripper, sensors with signal processing system or other custom-designed modules. To complete these tasks, a robotic arm with a gripper is normally used to perform the physical movements that move the samples between different devices or handling liquids. A vision system or other sensors may be used to monitor or track the experimental procedures to guarantee the output quality, although quite a lot of the traditional laboratory robots did not incorporate it.

1.2.2 Sample preparation systems for FTIR spectroscopy

Part I of this thesis focuses on the development of sample preparation robots for homogenization of fungal samples and further integrating the homogenization module with other liquid-handling modules for the full process of sample preparation for the analysis by Fourier Transform Infrared (FTIR) spectroscopy.

1.2.2.1 Manual sample preparation: background, protocol and problems

Characterization, identification and classification of microorganisms (bacteria, yeast, filamentous fungi and algae) has a high importance in the field of environmental, industrial, medical and agriculture microbiology, and microbial ecology (Fakruddin et al., 2013). There are two principle ways to characterize, identify and classify microorganisms - by using Genotyping and/or Phenotyping technologies. While genotyping technologies have been advancing rapidly and, through the integration of robotics, phenotyping technologies have been for a long time represented by the conventional microbiological techniques providing morphological, physiological and cultural characteristics. Commonly employed phenotypic methods are protein-based methods including serotyping, bacteriocin typing, phage typing, antimicrobial susceptibility patterns, etc. These phenotypic methods are associated with several problems related to reproducibility, discriminatory power, high variability, etc. Such shortcomings of phenotypically based methods have therefore led to the development of novel so called Next Generation Phenotyping (NGP) technologies, represented by two biophysical non-invasive techniques - Fourier Transform Infrared (FTIR) spectroscopy (Shapaval et al., 2013) and Matrix-Assisted Laser Desorption/Ionization MALDI-TOF MS (Bryson et al., 2019). Both techniques provide, with a high level of precision, a cellular biochemical phenotype of microbial cells - MALDI-TOF MS provides protein profile while FTIR provides total biochemical profile (proteins, lipids, polysaccharides). In addition, it has to be noted that FTIR provides not only cellular phenotype in the form of intracellular metabolites, but also extracellular phenotype in the form of extracellular metabolites. Both techniques are based on the high-throughput platform with the potential for analyzing up to 159 - 384 samples in a single analytical run.

Among different types of microorganisms, filamentous fungi are the most challenging to prepare for MALDI-TOF and FTIR analysis. The first step in the preparation of filamentous fungal samples for MALDI-TOF and FTIR analysis is the cultivation of fungi in multi-well 96-well microtiter plates (MTP). After cultivation, manual preparation of multi-well fungal samples for FTIR includes sample washing to remove culture medium, sample homogenization, up concentration for FTIR and spotting on the multi-well infrared (IR) plates. In case of high-throughput, set-up fungi are cultivated in 96-well MTP plates and the whole process for manual preparation of a 96 fungal samples may take more than 10 hours depending on the type of fungi and operator experiences. The whole process also requires highly skilled operator to perform and oversee the process, especially for sample homogenization and spotting on the IR plates.

In addition, manual operation may introduce variation to the samples due to the subjective nature of visual inspection (Kwee et al., 2017). In order to explore the high-throughput potential of the FTIR techniques, there is a strong need for the implementation of liquid-handling robotics for the sample preparation procedures.

Cell homogenization is the most time-consuming and labor-intensive procedure in FTIR sample preparation. Generally, it is possible to achieve cell homogenization by using chemical or mechanical/physical methods (Burden, 2012) and recently the development of a variety of cell homogenization procedures facilitated the efficient, low-cost and effective release of intracellular products (Klimek-Ochab et al., 2011). The effectiveness of these different homogenization techniques depends on the properties of the microbial cells, such as the physical strength of the cell wall and the location of the desired intracellular product (Klimek-Ochab et al., 2011). Ultrasound disintegration - ultrasonication - is a common mechanical cell homogenization method based on the high shear force created by a high-frequency ultrasound (above 16 kHz) (Klimek-Ochab et al., 2011), which can achieve complete disruption of the microbial cell (Borthwick et al., 2005; Gogate and Kabadi, 2009; Klimek-Ochab et al., 2011). The preparation of filamentous fungal samples for the FTIR analysis involves the application of ultrasonic homogenization (Shapaval et al., 2010). One of the benefits of ultrasonication is that it reduces cell disruption processing time and energy consumption (Tiwari et al., 2009). Unfortunately, however, the process also presents three main disadvantages. First is the manual use of the ultrasonication system requires highly skilled technicians to hold, mix, identify and monitor during processing (Li et al., 2016). Second, the process requires lengthy and repetitive operations, making it unsuitable for screening studies in which a large number of samples need to be sonicated within a short period of time. Finally, high sound intensity has negative effects on human health, causing headaches, discomfort and irritation (Smagowska and Pawlaczyk-Łuszczynska, 2013). It is, therefore, important that a platform be developed for the automation of manual ultrasonication operations.

1.2.2.2 Existing systems and challenges for automated ultrasonication and FTIR sample preparation

There are some existing robots developed for ultrasonication treatment. Mancia *et al.* presented a robotic ultrasound disintegrator with an electronically controlled sonicator probe mounted on a 5-axis industrial robotic arm (Mancia and Love, 2010). Similarly, Almo *et al.* developed an ultrasonication robot equipped with an EPSON robotic arm (Almo et al., 2013). In addition,

previous work by Li *et al.* used an ultrasonic module with a FESTO 3-axis arm to prepare samples for analysis by FTIR spectroscopy (Li et al., 2016). These systems simply used industrial robotic arms for ultrasonication manipulation without closed-loop control strategies for monitoring or automated control. The open-loop feature might, however, result in insufficient or excessive ultrasonication and, more importantly, might not always provide well-homogenized samples. Previous studies have provided neither automatic measurement methods for determining the degree of fungi homogeneity nor any mathematical models to quantify the phenomena of filamentous fungi homogenization by ultrasonication. Without appropriate sensing abilities, these machines continue to rely on the manual input of sample locations and technicians to monitor the process, adjust ultrasonication time and so on.

To the author's best knowledge, there are no other robotic systems for the whole process of sample preparation for FTIR spectroscopy, except for the first prototype developed by Li *et al.* (Li et al., 2016). This system consists of an industrial arm for pick-place of MTP plates, a linear axis with up and down motion for performing ultrasonication, an industrial centrifuge and a linear motion unit with a 96-pin dispensing head for sample washing and spotting. However, this system did not incorporate sensors for monitoring the experimental process (Li et al., 2016). The open-loop feature might not always provide well-homogenized samples. Also, due to the low accuracy of the dispensing unit, the spotting process did not provide reliable sample spots on the IR plates. In addition, the dispensing unit was often blocked by fungal mycelia during the sample washing procedure due to the straightway approach of liquid aspiration. Moreover, the washing and spotting used the same sample dispensing unit that may introduce cross-contamination issues. Furthermore, the old system required the operator to record and perform manual input of the labware information, such as the number and locations MTP plates, IR plates and sample wells, which limits the full automation of the robot. As a result of these limitations, it is necessary to develop a fully automated robot for sample preparation of FTIR spectroscopy with high precision of liquid-handling capabilities and the ability to monitor and control the experiment processes in closed loop using sensors.

1.3 Part II – Agricultural robotics

Imagine we are in 2050, and a robot manager is organising other robots working on a farm, moving back and forth for weeding, seeding, planting, spraying and harvesting, while the farmer is monitoring them using a mobile phone. In addition to plants, robots are also working on meat production. On a ranch, robots are managing grazing animals, bringing them to some

fertile grasslands and taking them back home in the evening. On a pig farm, robots are caring for each pig, monitoring their health status and feeding them with the optimal amount of fodder at the most suitable time. Will these scenarios become reality? Why do we need robots for farming and what are the current status and challenges of agricultural robotics?

According to a study conducted by the Food and Agriculture Organization of the United Nations, the world will need 70% to 100% more food to feed 9 billion people by 2050. This requires the farmers to use the same land to produce food more accurately and efficiently, and to reduce environmental impacts to achieve sustainability. For example, traditional agricultural machineries could not provide each plant with the best amount of fertilizer, water and pesticide at the best time, thus affecting the yield. Also, most of the resources are wasted on the outside area of plants. Another shortage is that traditional machines are usually very heavy and result in serious soil compaction problem, which makes it difficult for the plants to grow and also kill other beneficial organisms. Equipped with advanced sensing devices, agricultural robots are able to treat each plant with chemical and water precisely based on their needs or even replace chemical solutions with physical methods (Blackmore et al., 2005), such as laser weeding (Xiong et al., 2017). Agricultural robots are usually small in size and powered by electricity, so they are lightweight and therefore reduce soil compaction (Pedersen et al., 2008). Moreover, farming still highly relies on human labour, for example, selective fruit harvesting, weeding, machine operation and livestock caring. However, labour shortages and the high costs are increasingly serious in developed countries, such as Western Europe and the United States, which increases the demand for robotics and automation (Bechar and Vigneault, 2016).

From pastures, crop farmland to modern greenhouses, agricultural robots will be capable to work in all kinds of farming activities. Generally, an agricultural robot consists of ‘eyes’ for perception, for example, a camera, a LiDAR or other sensors, a robotic ‘arm’ for manipulation and a ‘hand’ for grasping, for example, a gripper for picking fruit, and ‘feet’ for moving the robot. The ‘eyes’ are essential for all kinds of agriculture robots, which is a significant difference from the traditional agricultural machineries, while the ‘arm’ and ‘hand’ are important for robots that need complex physical operations, such as fruit picking. The ‘eyes’ together with advanced machine learning can tell the robot what the status of the plants is, where the ripe fruit is and whether the animals feel happy. **Fig. 3** displays two robots for livestock farming, where **(a)** shows a robot rancher equipped with a camera to monitor animals (Klein, 2016) and **(b)** is a robot used for collecting eggs in poultry house using a vision system

together with a spring-like collector (Vroegindeweij et al., 2018). In this thesis, I will introduce more robotic systems related to crops.

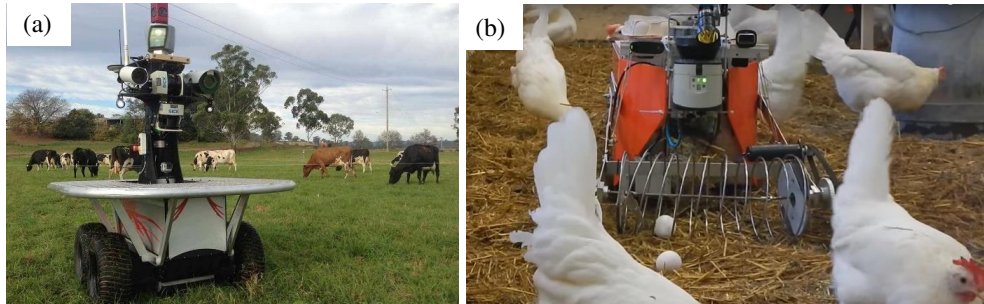


Fig. 3. Robotic system for sample preparation: (a) a robot rancher is monitoring animals on an Australian farm (Klein, 2016); (b) a robot for egg collection (Vroegindeweij et al., 2018).

1.3.1 Autonomous vehicles

Autonomous vehicles for agriculture attract much attention in research and development and might be the closest one to the market among many other types of agricultural robots. Autonomous vehicles may include traditional tractors with add-on navigation system (Carballido et al., 2014) and modern electric mobile platforms (Grimstad and From, 2017; Kachenko, 2016). Traditional tractor-based autonomous or semi-autonomous vehicles are increasingly common among commercial farming operations (Carballido et al., 2014). As shown in **Fig. 4(a)**, an autonomous tractor may have automatic steering system and localization sensors, such as Global Navigation Satellite System (GNSS) receivers or laser scanners, and obstacle avoidance sensors, such as cameras, ultrasonic sensors or laser scanners. Similar systems can also be added to traditional harvesters to achieve self driving. However, these systems still have serious environmental impacts, such as soil compaction and air pollution. Also, traditional tractors lack flexibility and are hard to use as a mobile platform for precision farming, such as weeding and selective harvesting, where in-situ steering operations are normally required. It is therefore, recently, many electric light-weight mobile platforms have been developed for precision farming, as shown in **Fig. 4(b)** and **(c)**. Thorvald robotic platform developed in our group provides four-wheel driving and four-wheel steering, giving high flexibility in applications (Grimstad and From, 2017), which was used in my second project – strawberry-harvesting robots. Without manipulator for physical interactions, autonomous

vehicles with additional sensors can be used for plant phenotyping (Grimstad et al., 2017), animal herding and etc.

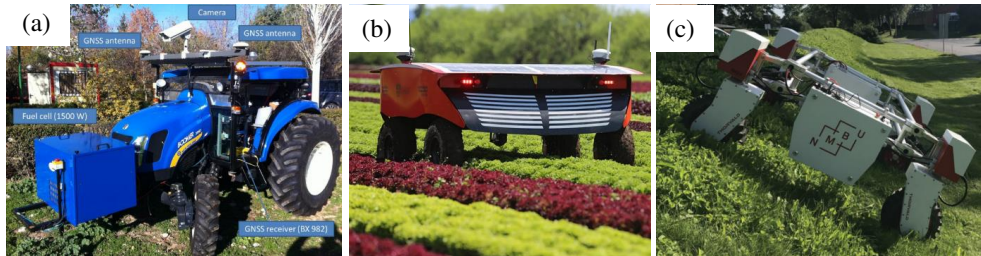


Fig. 4. Robotic system for sample preparation: (a) autonomous tractor (Carballido et al., 2014); (b) a mobile robot, named RIPPA, was developed by University of Sydney (Kachenko, 2016); (c) Thorvald robotic platform (Grimstad and From, 2017).

1.3.2 Robots for seeding, planting, pruning and weeding

Prior to harvesting, agricultural robots could be used for pruning, seeding, planting and weeding. The development of agricultural robotic systems has long appeared in Japan. In 2004, Nagasaka *et al.* developed an automated rice-transplanting robot (**Fig. 5(a)**), which employed a real-time kinematic global positioning system (RTK-GPS) for precise positioning, gyroscope sensors to determine direction and a computer to control the electric actuators, where their main challenge was the low accuracy of positioning (Nagasaka et al., 2004). They improved the system with more advanced communication devices and using an additional Inertial Measurement Unit (IMU) for better localization (Nagasaka et al., 2009). Also, researchers developed a desktop robotic system for vegetable transplanting (Kang et al., 2012). A similar application is robotic seeding (**Fig. 5(b)**), where a promising result was achieved (Haibo et al., 2015). The relatively good performance of seeding and planting might be because the system does not need to detect or manipulate the plants. A more complex robotic system was presented for pruning grape vines (**Fig. 5(c)**), which used a stereo camera to sense and build the 3D model of the vines then controlled a robotic arm to cut the canes (Botterill et al., 2017). In this system, the main challenges were inaccurate 3D modelling, slow execution speed and low reliability (Botterill et al., 2017).

My master's study explored the feasibility of laser weeding robot that used a laser pointer to target detected weeds using color thresholding, where we found the main limitation was weed detection (Xiong et al., 2017). Researchers in University of Sydney also showed a robot for weeding that used a mechanical hoe for weed removal (Underwood et al., 2015). Recently, due

to the emerging technology deep learning technique showing promising capabilities in weed detection, robotic weeding has received an increased attention. A popular weeding robot is the one developed by ecoRobotix (<https://www.ecorobotix.com>) that uses two fast delta arms to deliver herbicide, which in turn is mounted on an extra lightweight mobile platform, powered by solar. It is claimed that the robot is able to detect more than 85% of the weeds and reduce the use of herbicide by 90% (<https://www.ecorobotix.com>).

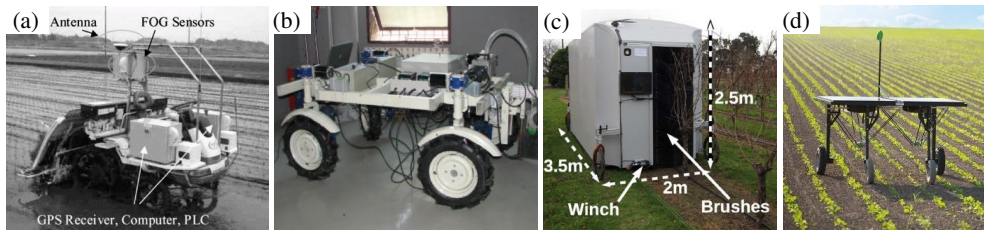


Fig. 5. Robotic system for sample preparation: (a) a rice-transplanting robot (Nagasaka et al., 2004); (b) a wheat seeding robot (Haibo et al., 2015); (c) a robot for pruning grape vines (Botterill et al., 2017); (d) ecoRobotix weeding robot (<https://www.ecorobotix.com>).

1.3.3 Selective fruit-harvesting robots

1.3.3.1 Main challenges

Fruit production that requires selective harvesting is heavily reliant on human labor. This is applicable to crops such as strawberries, sweet peppers, tomatoes, cucumbers, etc. Selective fruit harvesting involves the concept of only harvesting those fruits that meet certain quantity or quality thresholds in farm settings (Pedersen et al., 2008). Developing a robotic fruit harvester is considered to be particularly challenging (Bac et al., 2014; Lehnert et al., 2018a) and might be the most challenging one among many other agricultural robotic systems. The main reason is believed to be the cluttered and unstructured environment where both perception and manipulation struggles to cope with (Bac et al., 2014; Lehnert et al., 2018a; Silwal et al., 2017; Xiong et al., 2019a). The unstructured environment includes 1) unconstrained outdoor environmental conditions, such as changing sunlight and wind, 2) natural and complex plant structures, such as, fruit clusters, crossed branches and occluded leaves, and 3) crop variations with a variety of features, such as fruit shape, size and ripeness (Silwal et al., 2017; Xiong et al., 2019b). A harvesting robot is generally a tightly integrated system, incorporating advanced features and functionalities from numerous fields, including navigation, perception, motion planning and manipulation (Lehnert et al., 2016, 2018a; Xiong et al., 2019a). These robots are

also required to operate at high speed, with high accuracy and robustness and at a low cost, all features that are especially challenging in unstructured environments, such as the strawberry farm utilized for testing in this thesis.

1.3.3.2 Strawberry harvesting: motivations and related works

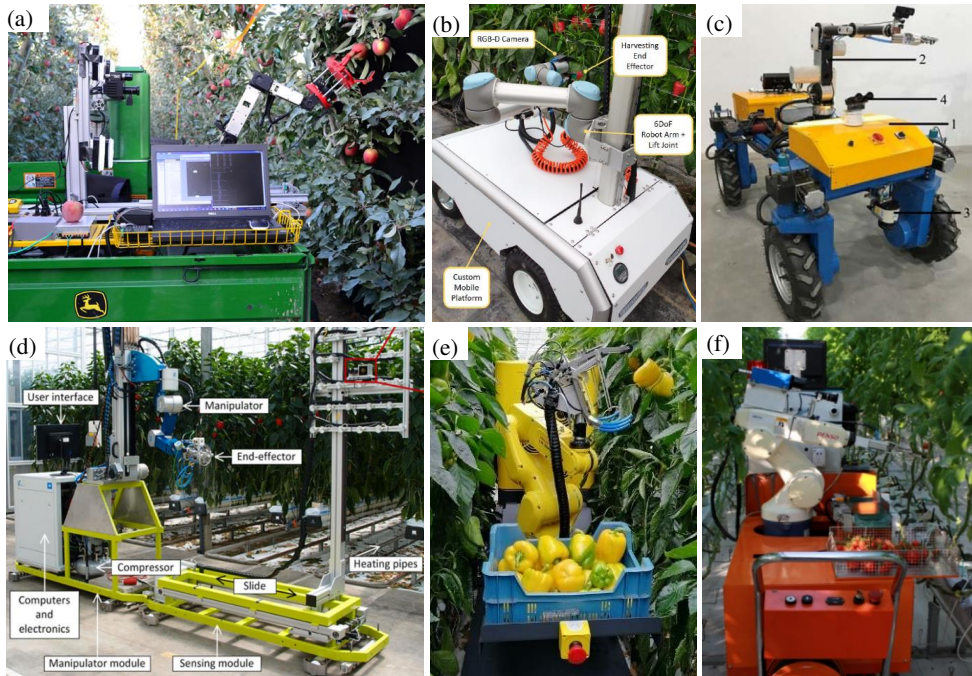


Fig. 6. Robotic systems for selective fruit harvesting: (a) an apple robotic harvester (Silwal et al., 2017); (b) ‘Harvey’ sweet pepper harvesting robot (Lehnert et al., 2017); (c) a tomato-harvesting robot: 1 – platform, 2 – manipulator, 3 – laser scanner, 4 - camera (Wang et al., 2017); (d) old version “SWEEPER” sweet pepper harvesting (Bac et al., 2017); (e) new version “SWEEPER” sweet pepper harvesting (<http://www.sweeper-robot.eu>); (f) a cherry tomato harvesting robot (Feng et al., 2018).

Strawberries (*Fragaria × ananassa* Duch.) are farmed extensively in most parts of the world, growing either outdoors in open fields or in controlled environments, like greenhouses or polytunnels. In 2016, according to market research company IndexBox, the global strawberry market amounted to 9.2 million tons, increasing by 5% against the previous year. Strawberry production is heavily reliant on human labor, especially for harvesting. It was reported that 25% of all working hours in Japan are consumed by harvesting operations (Yamamoto et al., 2014). Strawberry producers in the Western world, particularly the United Kingdom (UK) and United

States (US), are similarly concerned about the future availability of labor for picking, as well as about inflation in the cost of labor. In the UK, for example, the need is especially significant in the soft fruit sector, which uses 29,000 seasonal pickers to generate over 160,000 tons of fruit every year (British summer fruits seasonal labor report, 2017). In California, the cost of manual harvesting cost could be as much as 60% of production costs for fresh market strawberries (Anjom et al., 2017). These dual labor challenges of shortages and high costs are, therefore, advancing developments in the automation of fruit harvesting operations.

Despite several attempts to develop a robotic solution for harvesting strawberries and many other crops, a fully viable commercial system has yet to be established (Silwal et al., 2017). Fruit harvesting offers significant opportunities for the field of agricultural robotics and has, thus, gained much attention in recent decades. Several robots have been developed for harvesting fruits and vegetables, including those for apples, sweet peppers, cucumbers, tomatoes, litchis and strawberries. As shown in **Fig. 6(a)**, an apple robotic harvester was designed and evaluated with an overall success rate of 84% and an average picking time of 6.0 s per fruit, however, they encountered challenges, such as obstacle detection and avoidance (Silwal et al., 2017). **Fig. 6(d)** shows a sweet pepper harvesting robot achieved success rates of between 26% to 33% in a modified environment and a cycle time of 94 s for a full harvesting operation (Bac et al., 2017). This team subsequently presented an improved version robot using a gripper that moves along the stem to detach the fruit (**Fig. 6(d)**, <http://www.sweeper-robot.eu>). Similarly, another sweet pepper harvesting robot, named ‘Harvey’, as shown in **Fig. 6(b)**, achieved a 46% success rate for unmodified crops and 58% for modified crops, with average picking times of 35-40 s (Lehnert et al., 2017). They reported that the most common detachment failure was that of the cutter missing either side of the peduncle. This team subsequently presented an improved version of ‘Harvey’, with a higher success rate of 76.5% in a modified scenario (Lehnert et al., 2018a). A harvesting robot was developed for greenhouse tomatoes (**Fig. 6(c)**), with a success rate of 86% and a picking speed of approximately 15 s per tomato (Wang et al., 2017), however, the literature provides no in-depth analysis of their failure cases. A study of cherry tomato harvesting robot reported a success rate of 83% (**Fig. 6(f)**), with an average 1.4 attempts for each successful picking and a time cost of 8 s for a single successful harvesting excluding the time cost of moving between targets (Feng et al., 2018). The main failure found in the tests was collisions between the end-effector and the plant stems (Feng et al., 2018).

An increasing number of robots for autonomous strawberry picking have also been developed in recent few years. Japanese researchers developed and evaluated a strawberry-harvesting robot with a scissor-like cutter, as shown in **Fig. 7(a)**, which had a success rate of 34.9% and 41.3% when picking with suction and without suction, respectively (Hayashi et al., 2010). Their harvesting time for single fruit was 11.5 s. They concluded that a suction end-effector did not greatly contribute to picking performance and further reported that their failures were incorrect peduncle detection (Hayashi et al., 2010). The group also presented another version of strawberry-harvesting robot that used a serial arm with a scissor-like cutter (**Fig. 7(b)**) (Yamamoto et al., 2014). Their tests showed the rail-based moving platform has a good performance, but the robot inevitably chose wrong peduncles for cutting. Another strawberry-harvesting robot (**Fig. 7(c)**) using a 3D Cartesian type arm was tested by its detection of the peduncle before picking target strawberries laid out on a laboratory surface (Cui et al., 2013). The system achieved a successful detection rate of 70.8% with a successful picking cycle time of 16.6 s per fruit, and the authors reported the main challenge for their work as peduncle detection (Cui et al., 2013).

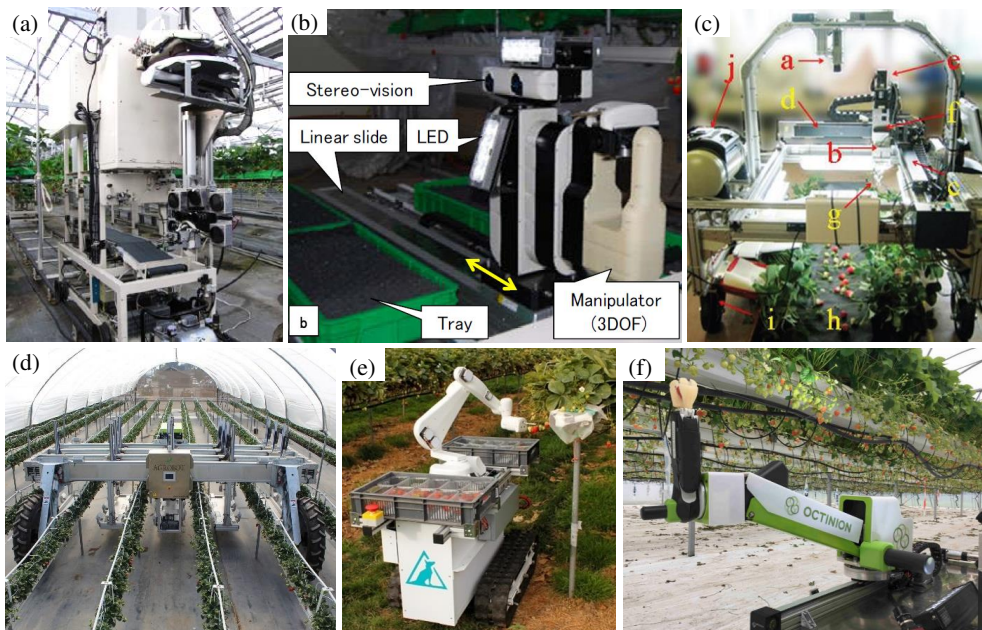


Fig. 7. Strawberry-harvesting robots: (a) a robot moving on fixed rails (Hayashi et al., 2010); (b) a robot picking from below (Yamamoto et al., 2014); (c) a robot for picking ground strawberries (Cui et al., 2013); (d) Agrobot robot (<http://agrobot.com>); (e) Dogtooth robot (<https://dogtooth.tech>); (f) Octinion robot (<http://octinion.com>).

Aside from research in academia, a number of start-up companies have also recently developed several strawberry-harvesting robots, none of which have successfully commercialized. These include AGROBOT (**Fig. 7(d)**, <http://agrobot.com>), who used 24 independent picking systems mounted on a mobile base to increase efficiency, Dogtooth (**Fig. 7(e)**, <https://dogtooth.tech>), who used a serial arm with a hook to pick and cut the target peduncle, OCTINION (**Fig. 7(f)**, <http://octinion.com>), who designed a force-limit soft gripper in an attempt to avoid damage while grasping, and Harvest CROO (<https://harvestcroo.com>) who designed a rotation apparatus that includes several grippers for picking strawberries on the ground. Unfortunately, due to the insufficient academic documents, it is hard to compare the performance data of these non-academic robots and to learn the challenges and lessons.

Generally, strawberry harvesting in cropping environment is very challenging. First, ripe strawberries are easily damaged and bruised (Dimeas et al., 2015; Hayashi et al., 2014). This feature requires gentle handling during manipulation procedures. Non-contact picking might be an acceptable solution to avoid damage. Second, strawberries are small in size and tend to grow in clusters, which makes it difficult to identify and pick individual strawberries (Yamamoto et al., 2014). Picking in clusters with dense obstacles is one of the main challenges for strawberry harvesting (Yamamoto et al., 2014) as well as for many other crop harvesting systems, such as tomato harvesting (Yaguchi et al., 2016) and sweet pepper robot (Bac et al., 2016). In this thesis, we address some of the challenges of working in unstructured farming environment. The main focuses are the manipulator design and manipulation path planning, aiming at improving the robustness of the system for working in unstructured environment.

Strawberry harvesters generally consist of four subsystems: (i) vision for detection of strawberries, (ii) a gripper for picking the strawberries, (iii) an arm for moving the gripper to the berries, and finally (iv) a platform to increase the work space of the robot and provide mobility.

1.3.3.3 Machine vision

Machine vision is an essential component for agricultural robots, enabling them to detect and localize the target crop. When the 3D position of a target is obtained, its coordinates can be further utilized to instruct the movements of the manipulation. For strawberry detection, image processing based on color thresholding is a frequently applied method in research papers (Hayashi et al., 2014; Yamamoto et al., 2014), primarily due to the significant differences of color among ripe strawberries, green strawberries and green plants. Peduncle detection is

another widely researched harvesting step (Cui et al., 2013; Hayashi et al., 2010; Huang et al., 2017; Shiigi et al., 2008). Color-based image processing methods were used to detect the strawberry first and then set a certain region above the strawberry for peduncle detection, with the accuracy influenced by the results of pre-processing and complexity of the environment. Other researchers have explored feature learning methods to analyze strawberry fruit shapes (Ishikawa et al., 2018). Recently, extensive work used deep learning as an approach for fruit detection. Deep learning, which can autonomously extract fruit features, has shown results in strawberry detection (Habaragamuwa et al., 2018). In addition to strawberries, deep learning, especially the Faster RCNN network, has been widely used for detection of many other fruits, including sweet pepper, mango, apple, almond and kiwifruit (Fu et al., 2018; Mai et al., 2018; Sa et al., 2016; Zhang et al., 2019). All these systems used detection networks to generate bounding boxes around the target fruits.

Unstructured growing conditions, including variable clustering, occlusions and varying lighting conditions, have been considered as the common challenges for fruit detection in farm environments (Silwal et al., 2017). Consequently, the focus of much ongoing research is novel ways to resolve these situations. One study proposed a color-based adaptive thresholding method for sweet pepper detection that can deal with changing illumination conditions (Vitzrabin and Edan, 2016), for example, while another proposed a visual servoing-based method accurately localize sweet peppers in occlusion situations (Lehnert et al., 2018b). Deep learning is a promising method to deal with the lighting variations and the general idea is to capture and train images under different lighting conditions (Bargoti and Underwood, 2017; Fu et al., 2018). However, this method may require additional hardware (GPU) and a large dataset as well as intensive work on image annotations, thus increasing the cost and power consumption.

1.3.3.4 Gripper design

The end-effector or gripper is a critical component in robotic systems as it could simplify requirements from other subsystems (Eizicovits et al., 2016) as well as enhance operation stability and efficiency substantially (Chiu et al., 2013). Various end-effectors have been developed for strawberry-harvesting robots. The most widely used is the scissor-like end-effector (**Fig. 8(a)**) for fruit detachment purpose only (Cui et al., 2013; Hayashi et al., 2014; Yamamoto et al., 2010). A similar one is clamp-like end-effector that combines cutting and clamping for holding peduncle after picking (AGROBOT, <http://agrobot.com>), as the one is shown in **Fig. 8(f)**. Also, with an additional suction device (**Fig. 8(b)**), the scissor-like end-

effector might be able to aspirate fruit from the plant (Arima and Kondo, 2004; Feng et al., 2012; Hayashi et al., 2010), but this may increase the damage. The scissor-like or clamp-like end-effectors are easy to make and inexpensive. However, as the individual strawberry peduncle (picking point) is difficult to detect (Huang et al., 2017), especially in a cluster where locating the correct stem is much harder than find a strawberry body, these end-effectors thus require a relatively advanced vision system to be developed. It is also easy to cut more than one stem at the time and unintentionally pick green strawberries.

Another important type of end-effector is contact-grasping gripper, as shown in **Fig. 8(c), (d)** and **(e)**. These grasping grippers are also common to see, such as the three-finger clamps with force-limit function (Dimeas et al., 2015) and two or more fingers with rotational motion to break peduncles (Yamamoto et al., 2014), (OCTINION, <http://octinion.com>; Harvest CROO, <https://harvestcroo.com>). Grasping and holding the fruit with additional motion to break the peduncle might easily bruise fragile strawberries (Hayashi et al., 2010), which might be a significant disadvantage of the grasping grippers.

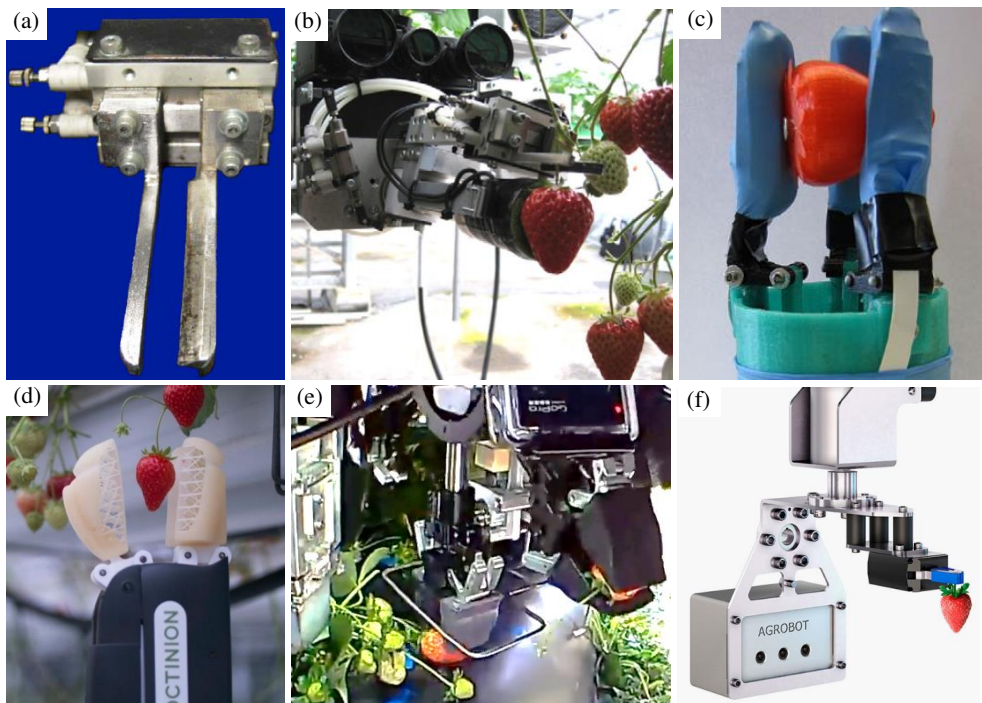


Fig. 8. Grippers for strawberry-harvesting robots: (a) a scissor-like cutter (Hayashi et al., 2010); (b) a cutters with suction device (Hayashi et al., 2010); (c) a force-limit grasping gripper: hard fingers with sensors (Dimeas et al., 2015); (d) a force-limit grasping gripper:

soft fingers (<http://octinion.com>); (e) two fingers grasp ([http:// harvestcroo.com](http://harvestcroo.com)); (f) a clamp-like gripper ([http:// agrobot.com](http://agrobot.com)).

Fruit localization is much easier than stem recognition (Yaguchi et al., 2016), because ripe fruits have large size and red color (strawberry) that is clearly different from leaves. Therefore, in this thesis, the gripper is designed to target the fruit and not the stem, which means it just needs the fruit location for picking rather than stem location. Compared to other strawberry picking robots that use stem as picking point (Hayashi et al., 2010; Huang et al., 2017), this system becomes more robust to positional errors of localization and requires less vision localization capacities.

1.3.3.5 Manipulation path planning

Several harvesters that can cope with isolated fruits have been developed. However, as mentioned above, some fruits, such as strawberries and tomatoes, tend to grow in clusters. This makes it difficult to identify and pick individual ripe fruit without damaging or accidentally picking unripe fruit (Xiong et al., 2019a; Yamamoto et al., 2014). Harvesting fruits that grow in clusters or are surrounded by obstacles, such as branches and/or leaves, while leaving the other fruits to remain undamaged on the plant, is one of the primary challenges for fruit harvesting systems (Xiong et al., 2019a; Yaguchi et al., 2016). Due to the uncertain environment, manipulation is considered one of the main challenges in getting harvesting robots to become a reality (Silwal et al., 2017). Cluster picking is difficult since the surrounding fruits, leaves, stems and other obstacles are difficult to separate from the target, both in detection and in manipulation.

Many picking systems used a point-to-point path planning method to move the arm from a start point to a point close the target (Cui et al., 2013; Hayashi et al., 2014). However, with this method, it was difficult for the gripper to avoid surrounding berries, leaves or stems along with its target berry. To avoid occlusions, a “3D-move-to-see” method was proposed to find the best view with less occlusions (Lehnert et al., 2018b). To avoid obstacles, a method for cucumber picking was developed that uses a search algorithm to explore the search space for a feasible trajectory, in which each step of the trajectory is checked by a collision detector (Van Henten et al., 2002). Another work used a randomized path planner to generate a random path tree and then tested each path with a local path planner to determine the collision-free one for pruning grape vines (Botterill et al., 2017). Furthermore, to avoid the arm’s self-collision or collision with obstacles, they incorporated a collision detector based on geometric primitives. Most of the methods found in the literature are passive obstacle avoidance methods, in which the aim is

to avoid existing obstacles without changing the environment. However, obstacles are not always avoidable, especially when picking small-size fruits in clusters, where the obstacles may be extremely close to the targets.

Without moving the obstacles out of the way, obstacles may prevent the gripper from capturing the target and may also be captured or damaged if they are located close to the target. Furthermore, when the obstacles connect to the target, the gripper may not be able to separate the target due to the static contact force between the target and obstacles.

In the field of robotic manipulation, most studies focus on obstacle avoidance. Nevertheless, we found some research working on obstacle separation for simple situations. For a warehouse picking application on desk environment, two linear pushing policies were proposed to separate rigid obstacles during the way of the gripper to reach a target bin (Danielczuk et al., 2018). Another work used Learning from Demonstration (LfD) algorithm for the same application that involves a pushing action (Laskey et al., 2016). For a similar situation, researchers proposed to use physical engine to calculate the dynamics to predict the object locations for motion planning, which also involves pushing motions (Dogar et al., 2013; Kitaev et al., 2015; Moll et al., 2017). Reinforcement learning was also used to train a robot to rearrange objects on a desk using pushing method to make them sparse for individual grasping (Zeng et al., 2018). However, all these methods were tested at simple environment where some rigid objects were placed on a 2D desk surface. In the agricultural environment, for example strawberry plants, fruits are located in 3D within diverse and unconstrained environments. The flexible peduncles, deformable fruits and many other crop variations make the dynamics difficult to calculate and predict. Moreover, the operation speed of these methods seems very slow, which may not be suitable for fruit harvesting.

This thesis provides a novel obstacle-separation method to enable the harvesting system to pick strawberries that are located in clusters. The algorithm uses the gripper to push aside surrounding leaves, strawberries, and other obstacles. It also controls the gripper to drag the target to a place with less obstacles and then push back to move the obstacles out of the way for further detachment. The proposed method might be also applicable to harvest other fruits, such as tomatoes and cucumbers.

2. Contributions and thesis overview

The main goal of this thesis is to contribute knowledge to support fully automation in life-science applications, which includes design, development, control and integration of robotic systems for sample preparation and strawberry harvesting. In addition to the system development, some scientific problems have been proposed and studied. For sample preparation robots, model fitting based on the developed robot was used to quantify and reveal the process of fungi homogenization and a control method was proposed based on the model. For strawberry harvesting, a novel obstacle-separation method was proposed and implemented to address one of the two main challenges in robotic fruit harvesting, which is fundamentally different from traditional path planning where obstacles are typically avoided.

The specific work and contributions are as follows:

Part I – Sample preparation robots for FTIR spectroscopy

- **Paper I:** (a) Developed a fully automated ultrasonication robot for the homogenization of fungal cells using machine vision to distinguish sample wells and blank wells; (b) quantified the fungi homogenization process using model fitting, suggesting that homogeneity level to ultrasonication time can be well fitted with exponential decay equations; (c) proposed a feedback control strategy that used the standard deviation of local homogeneity values to determine the ultrasonication termination time.
- **Paper II:** Developed a fully automated robot for the preparation of fungal samples for FTIR spectroscopy using deep learning to identify the labware settings.

Part II – Strawberry-harvesting robots

- **Paper III and paper VI:** (a) Designed a novel cable-driven gripper with sensing capabilities, which has high tolerance to positional errors and can reduce picking time with a storage container; (b) integrated all these subsystems into a complete and working system for strawberry harvesting, where the performance of the individual system was evaluated.
- **Paper IV:** (a) Proposed and implemented a novel active obstacle-separation path-planning algorithm for cluster picking; (b) improvements to the vision system, the gripper, the arm, and the control: an adaptive color thresholding for adaption of ambient changing light was proposed; (c) integrated a new version of the strawberry-harvesting

robot using dual-manipulator, which is able to pick strawberries continuously in polytunnels; (d) field evaluation reveals the failure reasons and provides directions for the improvements.

- **Paper V:** Improvements to the obstacle-separation method: (a) added a zig-zag push for both horizontal and upward directions; (b) proposed a novel dragging operation to separate upper obstacles from the target; (c) developed an image processing protocol to implement the method in a harvesting robot.

Fig. 9 shows a diagram that concludes the main work and contributions of this thesis, where rectangles represent the individual papers and hexagons indicate the highlights of contributions in the corresponding paper except for the system development.

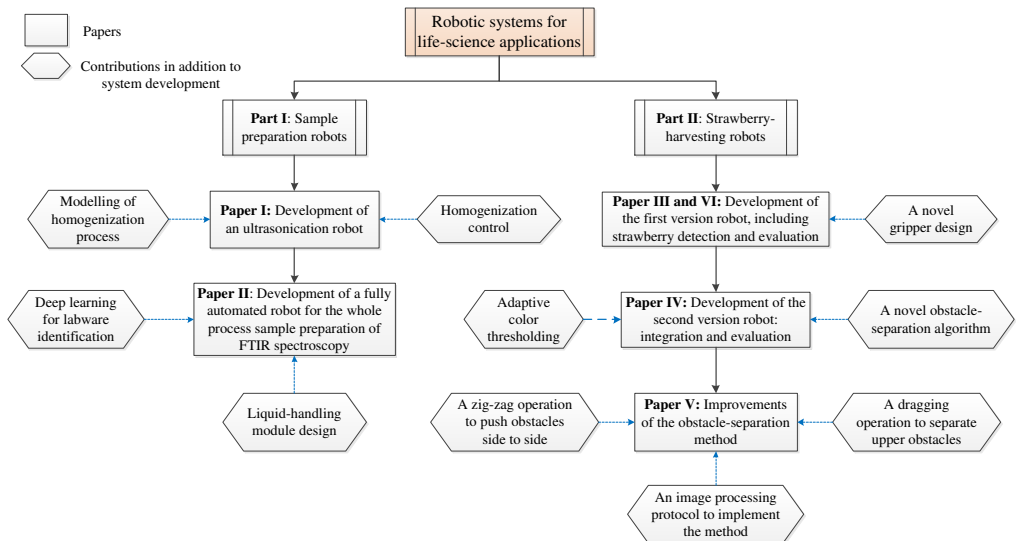


Fig. 9. Overview of the thesis: main work and contributions.

3. Results and discussions

3.1 Part I – Sample preparation robots for FTIR spectroscopy

3.1.1 Paper I – Ultrasonication robot for filamentous fungi homogenization.

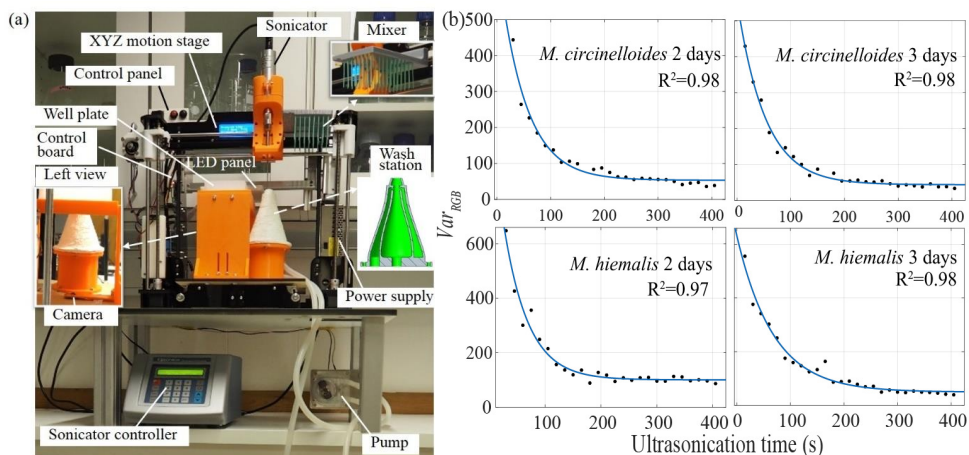


Fig. 10. Results of paper I: (a) the newly developed ultrasonication robot; (b) quantify the ultrasonication process using model fitting based on the vision system of the robot.

As shown in **Fig. 10(a)**, **paper I** presents the design and development of a new hands-free ultrasonication robot for filamentous fungi homogenization. The platform was constructed with a modified inexpensive 3D printer, equipped with an upward-facing camera, a custom-designed wash station, and an add-on sonicator. While machine vision distinguished between “sample wells” and “blank wells” based on image subtraction and color thresholding, it also measured the level of fungi homogeneity using color variance. The utilization of model fitting indicated that all the tested fungal homogenization using ultrasonication caused significant exponential decay (**Fig. 10(b)**). This process allowed for the rapid homogenization of fungal samples during the initial stages of ultrasonication treatment followed by gradual homogenization. Additionally, one-way ANOVA analysis denoted that higher ultrasound sonicator power and temperature accelerated the homogenization process, while the cultivation time exhibited no effect on homogenization. Moreover, the model parameters varied between the wells, even when subjected to the same settings, meaning that the system cannot use the same asymptote of the homogeneity level to establish the termination time for different wells. Therefore, we used the standard deviation of the four closest homogeneity level values to determine the termination

time. This method allowed for feedback control, forming a fully automated robot that did not require manual intervention during the experiment. A validation test on filamentous fungi demonstrated that the system was efficient and able to provide target quality of samples.

Since the homogeneity measurement method depended on an upward-facing camera, the bottom mycelia primarily determined the color variance calculation. Therefore, the system was not sensitive to the mycelia that remained suspended in the well. On some occasions, the mycelia did not fall to the bottom before the images were captured, which resulted in the acquisition of a smaller Var_{RGB} . We tested the system with filamentous fungi and found that filamentous fungi homogenization by ultrasonication might be an exponential decay process. However, this theory has not been verified by testing various fungi. Further work should include testing of other types of fungi or even other microorganisms.

3.1.2 Paper II – A robot for the full process preparation of fungal samples for FTIR spectroscopy

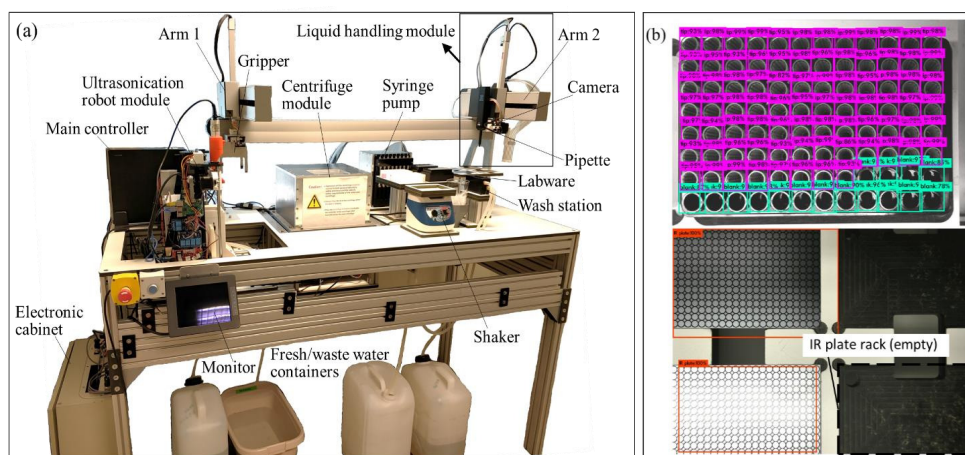


Fig. 11. Results of paper II: (a) the developed sample preparation robot; (b) the machine vision module identifies labware settings using deep learning, including IR tips and well plates.

Manual preparation of fungal samples for Fourier Transform Infrared (FTIR) spectroscopy involves sample washing, homogenization, concentration and spotting, which requires time-consuming and repetitive operations, making it unsuitable for screening studies. **Paper II** shows the design and development of a laboratory robot that fully automates the preparation of fungal samples for FTIR spectroscopy (**Fig. 11(a)**). We extended the previously developed

ultrasonication robot (**paper I**) module to the new system by adding a newly designed centrifuge module, a newly developed liquid-handling module and additional electronics. The liquid-handling module uses a high accuracy electric pipette for spotting and a low accuracy syringe pump for sample washing and concentration. A dual robotic arm system with a gripper is able to pick and place the 96-well MTP plates, which connects all of the hardware components. Furthermore, as shown in **Fig. 11(b)**, a camera on the liquid-handling module uses deep learning to identify the labware settings, which includes the number and positions of the well plates and pipette tips. The deep learning module has been integrated into the control system to avoid manual input of the labware information. Specifically, the labware identification node listens to the master node to capture images when Arm 2 arrives at the target position and outputs the bounding boxes together with class IDs of the detected objects. The master node determines the existing labware using IoU calculation. In addition, machine vision in the ultrasonication robot module can detect the sample wells and return the locations to the liquid-handling module, which makes the system hand-free for users.

We also present the development of the software under ROS architecture in low level for controlling each components and in high level for integration of all modules. The software was modular designed, so the robot is capable of performing each procedure of the operation independently, such as sample washing and spotting. The robot is able to process up to two 96-well MTP plates of samples simultaneously. Vision system evaluation indicates that the labware identification using deep learning can achieve high average precision due to the simple environment. Tests of all procedures show that the obtained sample spots have high positional accuracy (mean 0.36 mm) and can cover most of the desired region (mean 97%). The FTIR measurement indicates that all the obtained spots of one IR plate could be used for FTIR analysis, but future work is required to control the concentration of the spotted droplets to provide higher quality of spectra.

The proposed system was validated by the preparation for filamentous fungi but might also be applicable to other types of microorganisms, such as yeasts, bacteria, and algae.

3.2 Part II – Strawberry-harvesting robots

3.2.1 Paper III and VI – Gripper design, control and the first version of strawberry-harvesting robot

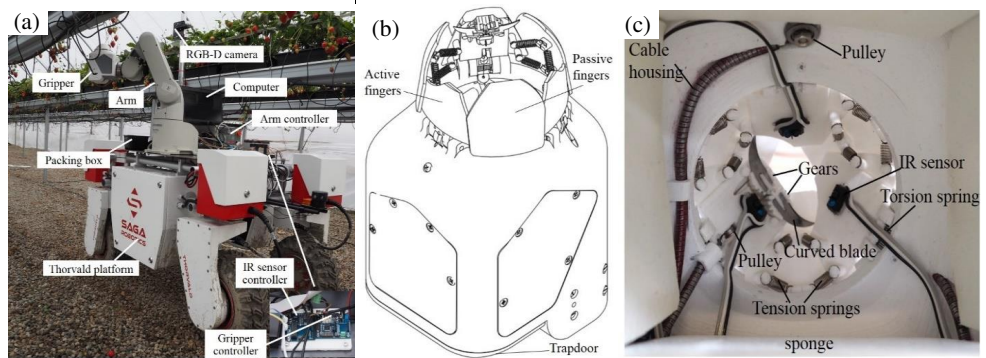


Fig. 12. Results of paper III and VI: (a) the first version of strawberry-harvesting robot; (b) the cable-driven gripper; (c) inside bottom view of the gripper, showing the mechanism, sensors and cutter.

This paper presents the development and evaluation of a robot for harvesting strawberries grown on table-tops in polytunnels. As shown in **Fig. 12(a)**, the robot is comprised of a newly designed gripper (**Fig. 12(b)** and **(c)**) mounted on an industrial arm which in turn is mounted on a mobile base along with an RGB-D camera.

The novel cable-driven gripper can open fingers to “swallow” a target. Since it is designed to target the fruit and not the stem, it just requires the fruit location for picking. The gripper consists of four functional parts for sensing, picking, transmission, and storing. The picking mechanism consists of three active fingers, three passive cover fingers and a cutter mechanism. The gripper opens the fingers to swallow a strawberry, then closes the fingers, and finally the cutter inside of the fingers rotates quickly to cut the stem. Thus, the cutter is hidden inside of the fingers to avoid damage to the target strawberry as well as the surrounding ones. While closing the fingers, the fingers can push the stem to the cutting area. If in a cluster, the fingers can open based on the strawberry size and push other surrounding strawberries away so that only one strawberry is swallowed into the container. Equipped with three IR sensors, the gripper controls a manipulator arm to correct for positional error, and can thus pick strawberries that are not exactly localized by the vision algorithm, improving the robustness. By including internal perception, we get high positional error tolerance, and avoid using slow, high-level

closed-loop control. Another important feature of the gripper is the internal container that is used to collect berries during picking. Since the manipulator does not need to go back and forth between each berry and a separate punnet, picking time is reduced significantly.

The vision system used color thresholding combined with screening of the object area and the depth range to select ripe and reachable strawberries, which is fast for processing. These components were integrated into a complete system whose performance was analyzed starting with the four main failure cases of the vision system: undetected, duplicate detections, inaccurate localization and segmentation failure. The integration enabled the robot to harvest continuously by moving the platform with a joystick. Field experiments showed the average cycle time of continuous single strawberry picking was 7.5 s and 10.6 s when including all procedures. Furthermore, the robot was able to pick isolated strawberries with a close-to-perfect success rate (96.8%). However, in the field, the success rate drops considerably due to the occlusion or other failure cases. In the natural situation, the average picking success rate for a single attempt is 53.6% without causing damage to the berries, and 59.0% when including “success with damage”, testing on the strawberry cultivar of “FAVORI”. The failure cases were analyzed and most failures were found when picking strawberries in clusters, in which both the detection algorithm and the gripper struggled to separate the berries.

3.2.2 Paper IV – Adaptive color thresholding, obstacle separation and the second version of strawberry-harvesting robot

Paper IV introduces the improvements and updates to **paper III** where the main focus is to address the challenges in unstructured environment by introducing a light-adaptive color thresholding method for vision and a novel obstacle-separation algorithm for manipulation.

This paper presents a fully integrated strawberry-harvesting system capable of picking strawberries continuously in polytunnels, as shown in **Fig. 13(a)**. While several harvesters that can cope with isolated strawberries have been developed, those growing in complex clusters remain a challenge. The main scientific contribution of this paper is the novel obstacle-separation path-planning algorithm, which allows the successful harvest of strawberries that are surrounded by other strawberries, as well as by leaves and other obstacles. The algorithm uses the gripper to push surrounding obstacles from an entrance, thus clearing the way for it to swallow the target strawberry. We present the theoretical method to generate pushing paths based on the surrounding obstacles. Specifically, the separation actions consist of pushing aside the bottom obstacles before swallowing and pushing aside the top obstacles during swallowing.

The pushing vectors are derived based on the surrounding obstacles that are calculated using downsampled blocks of 3D point cloud (**Fig. 13(b)** and (c)). This technique might be applicable to other fruit harvesting systems.

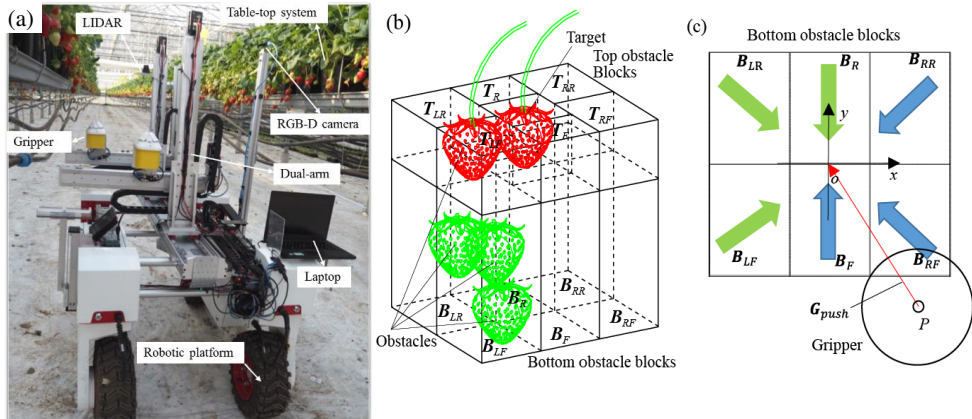


Fig. 13. Results of paper IV: (a) the second version of strawberry-harvesting robot in a greenhouse: dual-arm manipulators; active obstacle-separation algorithm: (b) schematic of ROI obstacle blocks, (c) top view of bottom obstacle blocks, showing the pushing vector.

In addition to obstacle separation, improvements were made to the gripper, the vision system, and the control. For adaptation to the field environment, a vision system that could automatically change color thresholds was developed based modeling of color against sunlight intensity, making it robust to variations in lighting. Furthermore, a low-cost single-rail two Cartesian arm system was developed, which makes it suitable for agricultural robot application. The harvesting sequence for the dual-arm was studied to optimize harvesting efficiency and avoid collision. This study also presents an improved gripper design that enables the robot to pick a market punnet and harvest berries directly into the punnet, thus eliminating the cost and time for repacking.

Finally, we show the full integration and control algorithm of the whole system, which enables the robot to harvest continuously along the polytunnels. The system was tested on the “Lusa” variety strawberries in a strawberry greenhouse. Results revealed that the robot was capable of picking partially surrounded strawberries, with success rates ranging from 50.0% to 97.1% on the first attempt, depending on the different type settings. This rate rose to between 75.0% and 100.0% on the second attempt. However, the system was not able to pick a target that was fully surrounded by obstacles, recording a first-attempt success rate of just 5.0%. The picking speed

in the one-arm mode increased to 6.1 s, including both picking and the arm's travel time to the next target, while, for the dual-arm mode, the average picking time was recorded as 4.6 s per strawberry.

However, it was still unable to pick targets that were fully surrounded by obstacles (leaving no entrance). It was also still not robust and revealed some limitations, especially from the vision side. The first limitation is the insufficient view and point cloud. In the current system, only a single view was used to get the 3D scenario. However, because of occlusions and the straight projection of the camera, the rear obstacles were not easily detected. Therefore, future work should make use of multi-view images and reconstruct more accurate scenes. The second vision problem is that of inaccurate localization. As the obstacle block size is dependent on the target bounding box, inaccurate localization of ripe strawberries might result in the gripper pushing the target when separating surrounding obstacles. In addition to the vision system limitations, closed-loop control between perception and manipulation may be able to improve the performance of obstacle separation.

3.2.3 Paper V – Improvements to the novel obstacle separation method

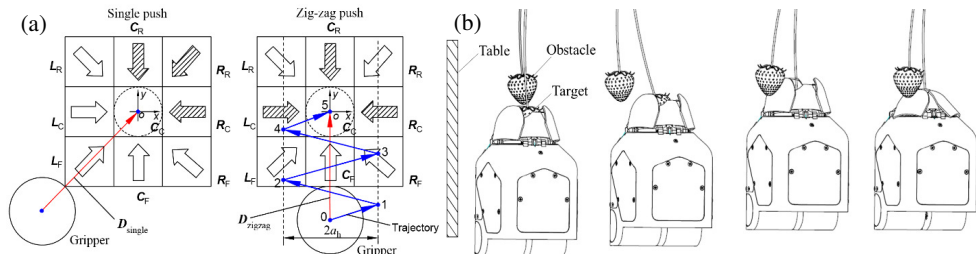


Fig. 14. Results of paper V: (a) diagram of the calculation of horizontal push: left is the single push and right is zig-zag push, where the red arrow shows the overall direction and the blue arrows are the zig-zag paths; (b) dragging operation to avoid capture the upper obstacles: an upward dragging step moves the target to an area that contains fewer obstacles and an upward push-back step pushes the upper obstacles aside.

Paper V provides the improvements to the obstacle-separation method in **paper IV**. Selectively picking a target fruit surrounded by obstacles is one of the major challenges for fruit harvesting robots. **Paper III** presented a gripper for strawberry-harvesting that can open fingers to enclose a target from below. Without moving the obstacles out of the way, obstacles may prevent the gripper from capturing the target and may also be swallowed with the target if they are located close to the target. Similar problems occur when approaching the fruit from other angles. To

solve this issue, **paper IV** proposed to use a single linear push operation to push aside the obstacles below the target based on the obstacle sensing from a 3D camera. We found that pushing obstacles aside, rather than simply avoiding them makes it possible to pick fruit that would otherwise be inaccessible to the robot. However, a single linear push may be insufficient for dense obstacles from multi-direction with respect to the target, since the linear push moves towards only one direction. Moreover, the obstacles may be adjacent together that cannot be separated during the push. Furthermore, when the obstacles connect to the target at the same height, the gripper may not be able to swallow the whole target but push it up due to the static contact force between the target and obstacles. In addition to that, one frequent failure is the gripper may capture obstacles above the target when it moves up to detach the fruit, which has not been addressed in the previous work.

This paper presents a method for actively separating obstacles from the target by using a combination of push and drag motions. A linear push was used to clear the obstacles from the area below the target, while a zig-zag push was used to push aside more dense obstacles (**Fig. 14(a)**). The zig-zag push can help the gripper capture a target since the generated shaking motion can break the static contact force between the target and obstacles. Furthermore, we proposed a novel dragging operation to address the issue of mis-capturing obstacles located above the target, in which the gripper drags the target to a place with fewer obstacles and then push back to move the obstacles aside for further detachment (**Fig. 14(b)**). We presented the theoretical calculation method of the pushing and dragging operations, which is determined by the number and distribution of obstacles based on the downsampled ROI point cloud. In addition, an image processing protocol was developed for the application in a harvesting robot. The image processing contains three steps: 1) 3D color filtering to remove noise points from the background, 2) object detection and localization using deep learning and 3) obstacle calculation.

Field tests showed that the proposed method could improve the picking performance substantially. This method helps to enable complex clusters of fruits to be harvested with a higher success rate than conventional methods. Analyses of the failure cases suggested that a closed-loop vision guided manipulation system may improve the performance of the obstacle-separation method considerably, in which the positions of the obstacles and the target are updated continuously.

4. Conclusions

This thesis provides the design, development, control and integration of robotic systems for FTIR sample preparation and strawberry harvesting, and is divided into two parts.

Part I presents the robotic systems for the preparation of fungal samples for FTIR spectroscopy. The first stage constructed an ultrasonication robot module for sample homogenization based on a modified inexpensive 3D printer, equipped with a camera to distinguish sample wells and blank wells. The main contribution in the first stage is that we proposed a vision-based method to quantify the fungi homogenization process and found that fungi homogenization using ultrasonication is an exponential decay process. Moreover, a feedback control strategy was proposed that used the standard deviation of local homogeneity values to determine the ultrasonication termination time. The second stage extended the ultrasonication robot to develop a fully automated robot for the whole process preparation of fungal samples for FTIR spectroscopy by adding a newly designed centrifuge and liquid-handling module for sample washing, concentration and spotting. The new system used machine vision with deep learning to identify the labware settings, which frees the users from inputting the labware information manually. The results indicated that all the obtained spots on the IR plate could be used for FTIR analysis, but for the future work the droplet concentration should be controlled more precisely to provide higher quality of spectra.

Part II of the thesis deals with robotic strawberry harvesting, where the main focus is gripper design and manipulation control. This part can be further divided into three stages. The first stage designed a novel cable-driven gripper with sensing capabilities for strawberry harvesting. The gripper uses fingers to form a closed space that can open to capture a fruit and close to push the stem to the cutting area. If in a cluster, the fingers can open based on the strawberry size and push other surrounding strawberries away so that only the target is swallowed into the container. The mechanical design and the internal sensors with control method make the gripper highly tolerant to positional errors and can reduce picking time with a storage container. The gripper and a detection method based on color thresholding were integrated into a complete and working system for strawberry harvesting. The second stage introduced the improvements and updates to the first stage where the main focus was to address the challenges in unstructured environment by introducing a light-adaptive color thresholding method for vision and a novel obstacle-separation algorithm for manipulation. At this stage, the new fully integrated strawberry-harvesting system with dual-manipulator was capable of picking strawberries

continuously in polytunnels. The main scientific contribution of this stage is the novel obstacle-separation path-planning algorithm, which is fundamentally different from traditional path planning where obstacles are typically avoided. The algorithm allows the successful harvest of strawberries that are surrounded by other strawberries, as well as by leaves and other obstacles. The algorithm uses the gripper to push aside surrounding obstacles from an entrance, thus clearing the way for it to swallow the target strawberry. We presented the theoretical method to generate pushing paths based on the surrounding obstacles. The third stage improved the obstacle-separation method by introducing a zig-zag push for both horizontal and upward directions and a novel dragging operation to separate upper obstacles from the target. The zig-zag push can help the gripper capture a target since the generated shaking motion can break the static contact force between the target and obstacles. The dragging operation is able to address the issue of mis-capturing obstacles located above the target, in which the gripper drags the target to a place with fewer obstacles and then push back to move the obstacles aside for further detachment. Analyses of the failure cases suggested that a closed-loop vision guided manipulation system may improve the performance of the obstacle-separation method considerably, in which the positions of the obstacles and the target are updated continuously.

References

- Almo, S.C., Garforth, S.J., Hillerich, B.S., Love, J.D., Seidel, R.D., Burley, S.K., 2013. Protein production from the structural genomics perspective: achievements and future needs. *Curr. Opin. Struct. Biol.* 23, 335–344. <https://doi.org/10.1016/j.sbi.2013.02.014>
- Ammi, M., Ferreira, A., 2005. Realistic visual and haptic rendering for biological-cell injection, in: *Proceedings of the 2005 IEEE International Conference on Robotics and Automation*. pp. 918–923.
- Anjom, F.K., Vougioukas, S.G., Slaughter, D.C., 2017. ScienceDirect Development of a linear mixed model to predict the picking time in strawberry harvesting processes. *Biosyst. Eng.* 166, 76–89. <https://doi.org/10.1016/j.biosystemseng.2017.10.006>
- Arima, S., Kondo, N., 2004. Strawberry Harvesting Robot on Table-top Culture Mitsuji Monta, Associate Professor 0300.
- Bac, C.W., Hemming, J., Barth, R., Wais, E., Henten, E.J. Van, 2017. Performance Evaluation of a Harvesting Robot for Sweet Pepper. *J. F. Robot.* 34, 1123–1139. <https://doi.org/10.1002/rob.21709>
- Bac, C.W., Roorda, T., Reshef, R., Berman, S., Hemming, J., van Henten, E.J., 2016. Analysis of a motion planning problem for sweet-pepper harvesting in a dense obstacle environment. *Biosyst. Eng.* 146, 85–97.
- Bac, C.W., van Henten, E.J., Hemming, J., Edan, Y., 2014. Harvesting robots for high-value crops: State-of-the-art review and challenges ahead. *J. F. Robot.* 31, 888–911.
- Balter, M.L., Leipheimer, J.M., Chen, A.I., Shrirao, A., Maguire, T.J., Yarmush, M.L., 2018. Automated end-to-end blood testing at the point-of-care: Integration of robotic phlebotomy with downstream sample processing. *Technology* 6, 59–66.
- Bargoti, S., Underwood, J.P., 2017. Image segmentation for fruit detection and yield estimation in apple orchards. *J. F. Robot.* 34, 1039–1060.
- Bechar, A., Vigneault, C., 2016. Agricultural robots for field operations: Concepts and components. *Biosyst. Eng.* 149, 94–111.
- Blackmore, S., Stout, B., Wang, M., Runov, B., 2005. Robotic agriculture--the future of

- agricultural mechanisation, in: Proceedings of the 5th European Conference on Precision Agriculture. pp. 621–628.
- Borthwick, K.A.J., Coakley, W.T., McDonnell, M.B., Nowotny, H., Benes, E., Gröschl, M., 2005. Development of a novel compact sonicator for cell disruption. *J. Microbiol. Methods* 60, 207–216. <https://doi.org/10.1016/j.mimet.2004.09.012>
- Botterill, T., Paulin, S., Green, R., Williams, S., Lin, J., Saxton, V., Mills, S., Chen, X., Corbett-Davies, S., 2017. A robot system for pruning grape vines. *J. F. Robot.* 34, 1100–1122.
- Brown, T., 2011. Gene Cloning and Colony Picking: Integration of Picker on Liquid-Handling Platform Increases Production of Clones. *Genet. Eng. Biotechnol. News* 31, 22–23.
- Bryson, A.L., Hill, E.M., Doern, C.D., 2019. Matrix-Assisted Laser Desorption/Ionization Time-of-Flight: The Revolution in Progress. *Clin. Lab. Med.* 39, 391–404. <https://doi.org/https://doi.org/10.1016/j.cll.2019.05.010>
- Burden, D., 2012. Guide to the Disruption of Biological Samples. *Random Prim.* 25, 1–25. <https://doi.org/10.1111/j.1474-9726.2006.00237.x>
- Carballido, J., Perez-Ruiz, M., Emmi, L., Ag'era, J., 2014. Comparison of Positional Accuracy between RTK and RTX GNSS Based on the Autonomous Agricultural Vehicles under Field Conditions. *Appl. Eng. Agric.*
- Chang, Y.-J., Fan, Y.-H., Chen, S.-C., Lee, K.-H., Lou, L.-Y., 2018. An Automatic Lab-on-Disc System for Blood Typing. *SLAS Technol. Transl. Life Sci. Innov.* 23, 172–178.
- Chapman, T., 2003. Lab automation and robotics: Automation on the move. *Nature* 421, 661–663. <https://doi.org/10.1038/421661a>
- Chen, Y., Zhang, J., Wang, H., Simaan, N., Yao, Y., Garty, G., Xu, Y., Lyulko, O., Turner, H., Randers-Pehrson, G., others, 2010. Development of a robotically-based automated biosimetry tool for high-throughput radiological triage. *Int. J. Biomechatronics Biomed. Robot.* 1, 115–125.
- Cherezov, V., Peddi, A., Muthusubramaniam, L., Zheng, Y.F., Caffrey, M., 2004. A robotic system for crystallizing membrane and soluble proteins in lipidic mesophases. *Acta Crystallogr. Sect. D Biol. Crystallogr.* 60, 1795–1807.
- Chiu, Y.C., Yang, P.Y., Chen, S., 2013. Development of the end-effector of a picking robot for

- greenhouse-grown tomatoes. *Appl. Eng. Agric.* 29, 1001–1009.
<https://doi.org/10.13031/aea.29.9913>
- Cui, Y., Gejima, Y., Kobayashi, T., Hiyoshi, K., Nagata, M., 2013. Study on cartesian-type strawberry-harvesting robot. *Sens. Lett.* 11, 1223–1228.
- Danielczuk, M., Mahler, J., Correa, C., Goldberg, K., 2018. Linear push policies to increase grasp access for robot bin picking, in: 2018 IEEE 14th International Conference on Automation Science and Engineering (CASE). pp. 1249–1256.
- Dimeas, F., Sako, D. V., Moulitanitis, V.C., Aspragathos, N.A., 2015. Design and fuzzy control of a robotic gripper for efficient strawberry harvesting. *Robotica* 33, 1085–1098.
<https://doi.org/10.1017/S0263574714001155>
- Dogar, M.R., Hsiao, K., Ciocarlie, M., Srinivasa, S.S., 2013. Physics-Based Grasp Planning Through Clutter. *Robot. Sci. Syst.* VIII 57.
- Eizicovits, D., van Tuijl, B., Berman, S., Edan, Y., 2016. Integration of perception capabilities in gripper design using graspability maps. *Biosyst. Eng.* 146, 98–113.
<https://doi.org/10.1016/j.biosystemseng.2015.12.016>
- Fakruddin, M., Mannan, B., Shahnewaj, K., Mazumdar, R.M., Chowdhury, A., Hossain, N., 2013. Identification and characterization of microorganisms: DNA-fingerprinting methods. *Songklanakarin J. Sci. Technol.* 35.
- Feng, Q., Wang, X., Zheng, W., Qiu, Q., Jiang, K., 2012. New strawberry harvesting robot for elevated-trough culture. *Int. J. Agric. Biol. Eng.* 5, 1–8.
- Feng, Q., Zou, W., Fan, P., Zhang, C., Wang, X., 2018. Design and test of robotic harvesting system for cherry tomato. *Int. J. Agric. Biol. Eng.* 11, 96–100.
<https://doi.org/10.25165/j.ijabe.20181101.2853>
- Fu, L., Feng, Y., Majeed, Y., Zhang, X., Zhang, J., Karkee, M., Zhang, Q., 2018. Kiwifruit detection in field images using Faster R-CNN with ZFNet. *IFAC-PapersOnLine* 51, 45–50.
- Gogate, P.R., Kabadi, A.M., 2009. A review of applications of cavitation in biochemical engineering/biotechnology. *Biochem. Eng. J.* 44, 60–72.
<https://doi.org/10.1016/j.bej.2008.10.006>

- Grimstad, L., From, P., 2017. The Thorvald II Agricultural Robotic System. *Robotics* 6, 24. <https://doi.org/10.3390/robotics6040024>
- Grimstad, L., Skattum, K., Solberg, E., Loureiro, G., From, P.J., 2017. Thorvald II configuration for wheat phenotyping, in: *Proceedings of the IROS Workshop on Agri-Food Robotics: Learning from Industry*.
- Habaragamuwa, H., Ogawa, Y., Suzuki, T., Shiigi, T., Ono, M., Kondo, N., 2018. Detecting greenhouse strawberries (mature and immature), using deep convolutional neural network. *Eng. Agric. Environ. Food* 11, 127–138.
- Haibo, L., Shuliang, D., Zunmin, L., Chuijie, Y., 2015. Study and experiment on a wheat precision seeding robot. *J. Robot.* 2015, 12.
- Hayashi, S., Shigematsu, K., Yamamoto, S., Kobayashi, K., Kohno, Y., Kamata, J., Kurita, M., 2010. Evaluation of a strawberry-harvesting robot in a field test. *Biosyst. Eng.* 105, 160–171. <https://doi.org/10.1016/j.biosystemseng.2009.09.011>
- Hayashi, S., Yamamoto, S., Saito, S., Ochiai, Y., Kamata, J., Kurita, M., Yamamoto, K., 2014. Field operation of a movable strawberry-harvesting robot using a travel platform. *Japan Agric. Res. Q.* 48, 307–316. <https://doi.org/10.6090/jarq.48.307>
- Huang, Z., Wane, S., Parsons, S., 2017. Towards automated strawberry harvesting: Identifying the picking point. *Lect. Notes Comput. Sci. (including Subser. Lect. Notes Artif. Intell. Lect. Notes Bioinformatics)* 10454 LNAI, 222–236. https://doi.org/10.1007/978-3-319-64107-2_18
- Ishikawa, T., Hayashi, A., Nagamatsu, S., Kyutoku, Y., Dan, I., Wada, T., Oku, K., Saeki, Y., Uto, T., Tanabata, T., others, 2018. CLASSIFICATION OF STRAWBERRY FRUIT SHAPE BY MACHINE LEARNING. *Int. Arch. Photogramm. Remote Sens. Spat. Inf. Sci.* 42.
- Kachenko, A., 2016. Robot that Detects Weeds? What a RIPPA.
- Kang, D.-H., Kim, D.-E., Lee, G.-I., Kim, Y.-H., Lee, H.-J., Min, Y.-B., 2012. Development of a vegetable transplanting robot. *J. Biosyst. Eng.* 37, 201–208.
- Kitaev, N., Mordatch, I., Patil, S., Abbeel, P., 2015. Physics-based trajectory optimization for grasping in cluttered environments, in: *2015 IEEE International Conference on Robotics and Automation (ICRA)*. pp. 3102–3109.

- Klein, A., 2016. Robot ranchers monitor animals on giant Australian farms. *New Sci.* May 20.
- Klimek-Ochab, M., Brzezińska-Rodak, M., Zymańczyk-Duda, E., Lejczak, B., Kafarski, P., 2011. Comparative study of fungal cell disruption-scope and limitations of the methods. *Folia Microbiol. (Praha)*. 56, 469–475. <https://doi.org/10.1007/s12223-011-0069-2>
- Kwee, E., Herderick, E.E., Adams, T., Dunn, J., Germanowski, R., Krakosh, F., Boehm, C., Monnich, J., Powell, K., Muschler, G., 2017. Integrated colony imaging, analysis, and selection device for regenerative medicine. *SLAS Technol. Transl. Life Sci. Innov.* 22, 217–223.
- Laskey, M., Lee, J., Chuck, C., Gealy, D., Hsieh, W., Pokorny, F.T., Dragan, A.D., Goldberg, K., 2016. Robot grasping in clutter: Using a hierarchy of supervisors for learning from demonstrations, in: 2016 IEEE International Conference on Automation Science and Engineering (CASE). pp. 827–834.
- Lehnert, C., English, A., McCool, C., Tow, A.W., Perez, T., 2017. Autonomous Sweet Pepper Harvesting for Protected Cropping Systems. *IEEE Robot. Autom. Lett.* 2, 872–879. <https://doi.org/10.1109/LRA.2017.2655622>
- Lehnert, C., McCool, C., Sa, I., Perez, T., 2018a. A Sweet Pepper Harvesting Robot for Protected Cropping Environments. *arXiv Prepr. arXiv1810.11920*.
- Lehnert, C., Sa, I., McCool, C., Upcroft, B., Perez, T., 2016. Sweet pepper pose detection and grasping for automated crop harvesting. *Proc. - IEEE Int. Conf. Robot. Autom.* 2016-June, 2428–2434. <https://doi.org/10.1109/ICRA.2016.7487394>
- Lehnert, C., Tsai, D., Eriksson, A., McCool, C., 2018b. 3D Move to See: Multi-perspective visual servoing for improving object views with semantic segmentation. *arXiv Prepr. arXiv1809.07896*.
- Li, J., Shapaval, V., Kohler, A., Talintyre, R., Schmitt, J., Stone, R., Gallant, A.J., Zeze, D.A., 2016. A modular liquid sample handling robot for high-throughput Fourier transform infrared spectroscopy, in: *Advances in Reconfigurable Mechanisms and Robots II*. Springer, pp. 769–778. <https://doi.org/10.1007/978-3-319-23327-7>
- Liu, H., Stoll, N., Junginger, S., Thurow, K., 2013. A fast method for mobile robot transportation in life science automation, in: 2013 IEEE International Instrumentation and Measurement Technology Conference (I2MTC). pp. 238–242.

<https://doi.org/10.1109/I2MTC.2013.6555416>

- Liu, X., Fernandes, R., Gertsenstein, M., Perumalsamy, A., Lai, I., Chi, M., Moley, K.H., Greenblatt, E., Jurisica, I., Casper, R.F., others, 2011. Automated microinjection of recombinant BCL-X into mouse zygotes enhances embryo development. *PLoS One* 6, e21687.
- Mai, X., Zhang, H., Meng, M.Q.-H., 2018. Faster R-CNN with Classifier Fusion for Small Fruit Detection, in: 2018 IEEE International Conference on Robotics and Automation (ICRA). pp. 7166–7172.
- Mancia, F., Love, J., 2010. High-throughput expression and purification of membrane proteins. *J. Struct. Biol.* 172, 85–93. <https://doi.org/10.1016/j.jsb.2010.03.021>
- Meier, M.A.R., Hoogenboom, R., Fijten, M.W.M., Schneider, M., Schubert, U.S., 2003. Automated MALDI-TOF-MS sample preparation in combinatorial polymer research. *J. Comb. Chem.* 5, 369–374.
- Moll, M., Kavraki, L., Rosell, J., others, 2017. Randomized physics-based motion planning for grasping in cluttered and uncertain environments. *IEEE Robot. Autom. Lett.* 3, 712–719.
- Nagasaka, Y., Saito, H., Tamaki, K., Seki, M., Kobayashi, K., Taniwaki, K., 2009. An autonomous rice transplanter guided by global positioning system and inertial measurement unit. *J. F. Robot.* 26, 537–548.
- Nagasaka, Y., Umeda, N., Kanetai, Y., Taniwaki, K., Sasaki, Y., 2004. Autonomous guidance for rice transplanting using global positioning and gyroscopes. *Comput. Electron. Agric.* 43, 223–234.
- Nejatimoharrami, F., Faina, A., Stoy, K., 2017. New Capabilities of EvoBot: A Modular, Open-Source Liquid-Handling Robot. *SLAS Technol.* 22, 500–506. <https://doi.org/10.1177/2472630316689285>
- Pedersen, S.M., Fountas, S., Blackmore, S., 2008. Agricultural robots—Applications and economic perspectives, in: *Service Robot Applications*. IntechOpen.
- Peyer, K.E., Zhang, L., Nelson, B.J., 2013. Bio-inspired magnetic swimming microrobots for biomedical applications. *Nanoscale* 5, 1259–1272.
- Reed, C.E., Fournier, J., Vamvoukas, N., Koza, S.M., 2018. Automated Preparation of MS-

- Sensitive Fluorescently Labeled N-Glycans with a Commercial Pipetting Robot. *SLAS Technol. Transl. Life Sci. Innov.* 23, 550–559.
- Rosenberg, A., 2011. *Philosophy of science: A contemporary introduction*. Routledge.
- Sa, I., Ge, Z., Dayoub, F., Upcroft, B., Perez, T., McCool, C., 2016. Deepfruits: A fruit detection system using deep neural networks. *Sensors* 16, 1222.
- Shapaval, V., Mørretrø, T., Suso, H.P., Wold Åsli, A., Schmitt, J., Lillehaug, D., Martens, H., Boeke, r U., Kohler, A., 2010. A high-throughput microcultivation protocol for FTIR spectroscopic characterization and identification of filamentous fungi. *J. Biophotonics* 3, 512–521. <https://doi.org/10.1002/jbio.201000014>
- Shapaval, V., Schmitt, J., Mørretrø, T., Suso, H.P., Skaar, I., 2013. Characterization of food spoilage fungi by FTIR spectroscopy. *J. Appl. Microbiol.* 114, 778–796. <https://doi.org/10.1111/jam.12092>
- Shiigi, T., Kondo, N., Kurita, M., Ninomiya, K., Rajendra, P., Kamata, J., Hayashi, S., Kobayashi, K., Shigematsu, K., Kohno, Y., 2008. Strawberry harvesting robot for fruits grown on table top culture. *Am. Soc. Agric. Biol. Eng. Annu. Int. Meet.* 2008 5, 3139–3148. <https://doi.org/10.13031/2013.24754>
- Silwal, A., Davidson, J.R., Karkee, M., Mo, C., Zhang, Q., Lewis, K., 2017. Design, integration, and field evaluation of a robotic apple harvester. *J. F. Robot.* 34, 1140–1159. <https://doi.org/10.1002/rob.21715>
- Smagowska, B., Pawlaczyk-Łuszczynska, M., 2013. Effects of ultrasonic noise on the human body—a bibliographic review. *Int. J. Occup. Saf. Ergon.* 19, 195–202. <https://doi.org/10.1080/10803548.2013.11076978>
- Tanaka, H., Ohnishi, K., Nishi, H., Kawai, T., Morikawa, Y., Ozawa, S., Furukawa, T., 2008. Implementation of bilateral control system based on acceleration control using FPGA for multi-DOF haptic endoscopic surgery robot. *IEEE Trans. Ind. Electron.* 56, 618–627.
- Tiwari, B.K., O'Donnell, C.P., Cullen, P.J., 2009. Effect of sonication on retention of anthocyanins in blackberry juice. *J. Food Eng.* 93, 166–171. <https://doi.org/10.1016/j.jfoodeng.2009.01.027>
- Underwood, J.P., Calleija, M., Taylor, Z., Hung, C., Nieto, J., Fitch, R., Sukkariéh, S., 2015. Real-time target detection and steerable spray for vegetable crops, in: *Proceedings of the*

- International Conference on Robotics and Automation: Robotics in Agriculture Workshop, Seattle, WA, USA. pp. 26–30.
- Van Henten, E.J., Hemming, J., Van Tuijl, B.A.J., Kornet, J.G., Meuleman, J., Bontsema, J., Van Os, E.A., 2002. An autonomous robot for harvesting cucumbers in greenhouses. *Auton. Robots* 13, 241–258. <https://doi.org/10.1023/A:1020568125418>
- Vitzrabin, E., Edan, Y., 2016. Changing task objectives for improved sweet pepper detection for robotic harvesting. *IEEE Robot. Autom. Lett.* 1, 578–584.
- Vroegindeweij, B.A., Blaauw, S.K., IJsselmuiden, J.M.M., van Henten, E.J., 2018. Evaluation of the performance of PoultryBot, an autonomous mobile robotic platform for poultry houses. *Biosyst. Eng.* 174, 295–315.
- Wang, L.L., Zhao, B., Fan, J.W., Hu, X.A., Wei, S., Li, Y.S., Zhou, Q.B., Wei, C.F., 2017. Development of a tomato harvesting robot used in greenhouse. *Int. J. Agric. Biol. Eng.* 10, 140–149. <https://doi.org/10.25165/j.ijabe.20171004.3204>
- Wang, W., Liu, X., Gelinis, D., Ciruna, B., Sun, Y., 2007. A fully automated robotic system for microinjection of zebrafish embryos. *PLoS One* 2, e862.
- Xiong, Y., Ge, Y., Grimstad, L., From, P.J., 2019a. An autonomous strawberry-harvesting robot: Design, development, integration, and field evaluation. *J. F. Robot.* rob.21889. <https://doi.org/10.1002/rob.21889>
- Xiong, Y., Ge, Y., Liang, Y., Blackmore, S., 2017. Development of a prototype robot and fast path-planning algorithm for static laser weeding. *Comput. Electron. Agric.* 142, 494–503. <https://doi.org/10.1016/j.compag.2017.11.023>
- Xiong, Y., Peng, C., Grimstad, L., From, P.J., Isler, V., 2019b. Development and field evaluation of a strawberry harvesting robot with a cable-driven gripper. *Comput. Electron. Agric.* 157, 392–402. <https://doi.org/10.1016/j.compag.2019.01.009>
- Yaguchi, H., Nagahama, K., Hasegawa, T., Inaba, M., 2016. Development of an autonomous tomato harvesting robot with rotational plucking gripper. *IEEE Int. Conf. Intell. Robot. Syst.* 2016-Novem, 652–657. <https://doi.org/10.1109/IROS.2016.7759122>
- Yamamoto, S., Hayashi, S., Saito, S., Ochiai, Y., Yamashita, T., Sugano, S., 2010. Development of robotic strawberry harvester to approach target fruit from hanging bench side. *IFAC Proc. Vol. 3.* <https://doi.org/10.3182/20101206-3-JP-3009.00016>

- Yamamoto, S., Hayashi, S., Yoshida, H., Kobayashi, K., 2014. Development of a Stationary Robotic Strawberry Harvester with Picking Mechanism that Approaches Target Fruit from Below. *Japan Agric. Res. Q. JARQ* 48, 261–269. <https://doi.org/10.6090/jarq.48.261>
- Zeng, A., Song, S., Welker, S., Lee, J., Rodriguez, A., Funkhouser, T., 2018. Learning synergies between pushing and grasping with self-supervised deep reinforcement learning, in: 2018 IEEE/RSJ International Conference on Intelligent Robots and Systems (IROS). pp. 4238–4245.
- Zhang, L., Gui, G., Khattak, A.M., Wang, M., Gao, W., Jia, J., 2019. Multi-Task Cascaded Convolutional Networks Based Intelligent Fruit Detection for Designing Automated Robot. *IEEE Access* 7, 56028–56038.


Appended papers

Part I – Sample preparation robots for FTIR spectroscopy

Paper I

Xiong, Y., Shapaval, V., Kohler, A. and From, P.J., 2019. A Laboratory-Built Fully Automated Ultrasonication Robot for Filamentous Fungi Homogenization. *SLAS TECHNOLOGY: Translating Life Sciences Innovation*, 24, pp.1-13. DOI: <https://doi.org/10.1177/2472630319861361>

A Laboratory-Built Fully Automated Ultrasonication Robot for Filamentous Fungi Homogenization

SLAS Technology
1–13
© 2019 Society for Laboratory
Automation and Screening
DOI: 10.1177/104272630319861361
journals.sagepub.com/home/jla


Ya Xiong¹ , Volha Shapaval¹, Achim Kohler¹, and Pål Johan From¹

Abstract

This article presents the design and development of a new hands-free ultrasonication robot for filamentous fungi homogenization. The platform was constructed with a modified inexpensive 3D printer, equipped with an upward-facing camera, a custom-designed wash station, and an add-on sonicator. While machine vision accomplished sample well screening based on image subtraction and color thresholding, it also determined the level of fungi homogeneity using color variance. Model fitting reveals that the process of filamentous fungi homogenization using ultrasonication included a period of significant exponential decay. Therefore, this procedure allowed for the rapid homogenization of the fungal samples during the initial stages of ultrasonication treatment followed by a deceleration in homogenization. Furthermore, a factorial experiment showed that higher sonicator power and temperature accelerated the homogenization process, while the cultivation time exhibited no effect on homogenization. In addition, the model parameters were varied between the wells, even when subjected to the same settings, meaning that the system cannot use the same asymptote of the homogeneity level to establish the termination time for different wells. Therefore, we used the standard deviation of the four most recent homogeneity level values to determine the termination time. This method was used for feedback control, forming a fully automated robot that did not require manual intervention during the experiment. A validation test on filamentous fungi demonstrated that the system was able to provide target quality of samples efficiently.

Keywords

laboratory automation, robotics, ultrasonication, fungi homogenization measurement, fungi homogenization modeling

Introduction

Microorganisms broadly serve as cell factories for the production of a variety of important high- and low-value products, such as lipids, biosurfactants, antibiotics, enzymes, therapeutic agents, exopolysaccharides, and bioplastics. It is possible to easily isolate some of these products following extracellular storage and excretion into the cultivation medium. However, others, such as lipids and polyhydroxyalkanoates, depend on intracellular production, necessitating their extraction for analysis via a process usually initialized by cell homogenization.¹ In addition, biochemical fingerprinting of microorganisms by high-throughput Fourier transform infrared (FTIR) spectroscopy, particularly in the case of filamentous fungi,^{2,3} uses homogeneous cell suspensions that require the application of ultrasonic homogenization.

Generally, it is possible to achieve cell homogenization by using chemical or mechanical/physical methods,⁴ and recently, the development of a variety of cell homogenization procedures facilitated the efficient, low-cost, and effective release of intracellular products.⁵ The effectiveness of

these different homogenization techniques depends on the properties of the microbial cell, such as the physical strength of the cell wall and the location of the desired intracellular product.⁵ Ultrasound disintegration—ultrasonication—is a common mechanical cell homogenization method based on the high shear force created by a high-frequency ultrasound (above 16 kHz),⁵ which can achieve complete disruption of the microbial cell.^{5–7} Additional benefits of ultrasonication are that it reduces cell disruption processing time and energy consumption.⁸ Unfortunately, however, the process also

¹Faculty of Science and Technology, Norwegian University of Life Sciences, Ås, Norway

Received Nov 8, 2018, and in revised form May 29, 2019. Accepted for publication Jun 13, 2019.

Supplemental material is available online with this article.

Corresponding Author:

Ya Xiong, Faculty of Science and Technology, Norwegian University of Life Sciences, Drøbakveien 31, Ås 1432, Norway.
Email: yaxio@nmbu.no

presents three main disadvantages. First, manual use of the ultrasonication system requires highly skilled technicians to hold, mix, identify, and monitor during processing.⁹ Second, the process requires lengthy and repetitive operations, making it unsuitable for screening studies in which a large number of samples need to be sonicated within a short period of time. Finally, high-sound intensity has negative effects on human health, causing headaches, discomfort, and irritation.¹⁰ It is, therefore, important that a platform be developed for the automation of manual ultrasonication operations.

Mancia and Love¹¹ presented a robotic ultrasound disintegrator with an electronically controlled sonicator probe mounted on a five-axis industrial robotic arm. Similarly, Almo et al.¹² developed an ultrasonication robot equipped with an EPSON robotic arm. In addition, previous work by Li et al.⁹ used an ultrasonic module with a FESTO three-axis arm to prepare samples for analysis by FTIR spectroscopy. These systems simply used industrial robotic arms for ultrasonication manipulation without closed-loop control strategies for monitoring or automated control. The open-loop feature might, however, result in insufficient or excessive ultrasonication and, more important, might not always provide well-homogenized samples. Previous studies have provided neither automatic measurement methods for determining the degree of fungi homogeneity nor any mathematical models to quantify the phenomena of filamentous fungi homogenization by ultrasonication. Without appropriate sensing abilities, these machines continue to rely on the manual input of sample locations and technicians to monitor the process, adjust ultrasonication time, and so on.

In the laboratory automation field, many platforms with sensing systems have been developed to automate experiments and tests ranging from robotic sample preparation systems¹³ to a machine vision-based system for sorting zebrafish embryos¹⁴ and an automated system to test irrigation sprinklers.¹⁵ Recently, the well-developed, open-source software for 3D printing technology allowed for rapid and low-cost prototyping. Based on a 3D printer, Nejatimoharrami et al.¹⁶ presented a liquid-handling robot named EvoBot while also developing a 3D printer-based platform together with an imaging system for screening microscopy.¹⁷

The main contributions presented in this article are the following:

1. We developed a novel, fully automated ultrasonication robot for the homogenization of fungal cells. The robot used machine vision to distinguish sample wells and blank wells.
2. We quantified the fungi homogenization process using model fitting, suggesting that homogeneity level to ultrasonication time of all the tested sample wells can be well fitted with exponential decay equations. A further factorial experiment showed temperature, sonicator power, fungal varieties, and well replicates have a significant influence on homogeneity level.
3. We developed a feedback control strategy that used the standard deviation of local homogeneity values to determine the ultrasonication termination time.

The proposed system was validated by the homogenization of filamentous fungi but might also be applicable to other types of microorganisms, such as yeasts, bacteria, and algae. The developed ultrasonication robot could be of particular use in processes that prepare filamentous fungi samples for biochemical phenotyping by FTIR spectroscopy, extraction of intracellular metabolites, and DNA from microbial cells.

Materials and Methods

System Design and Hardware Description

Figure 1 shows the hardware assembly of the developed platform. It comprises five functional modules: (1) an XYZ motion stage; (2) a control and vision module, including a controller and an upward-facing camera; (3) a washing module consisting of a pump and a newly designed wash station; (4) a sonicator module; and (5) the power supply. The overall size of the ultrasonication platform, excluding the water bottles, is 59 × 45 × 80 cm (length × breadth × height).

XYZ motion stage. **Figure 1a** shows that the modification of a low-cost 3D printer formed the basis for the robot actuation module (Anet A8, Anet, China). This provided three degrees of motion for the sonicator, with an original working space of 220 × 220 × 240 mm. A 3D-printed sonicator holder with which to mount the sonicator on the robot arm replaced the extruder module used for 3D printing (**Suppl. Fig. S1**). Furthermore, a custom-designed mixer with 96 pins was mounted on the same slider next to the holder. Before taking pictures, the mixer decreases sediment formation that might affect image processing. When removing mixer pins from the well, the robot moves the pins into contact with the well wall to remove droplets. After processing a microtiter plate of samples, the mixer can be washed in either a well plate with fresh water or a general container.

A laser-cut wooden board attached to a 3D-printed plate holder replaced the hotbed of the printer. Modifications to the original 3D printer controller facilitated motion control while being flashed with open-source firmware (0.92.5; Repetier, Willich, Germany) with a robust motion control algorithm that promoted external control through the G-code protocol. One disadvantage of the firmware is that it does not provide feedback upon completion of motion. However, this feedback is important in minimizing cycle

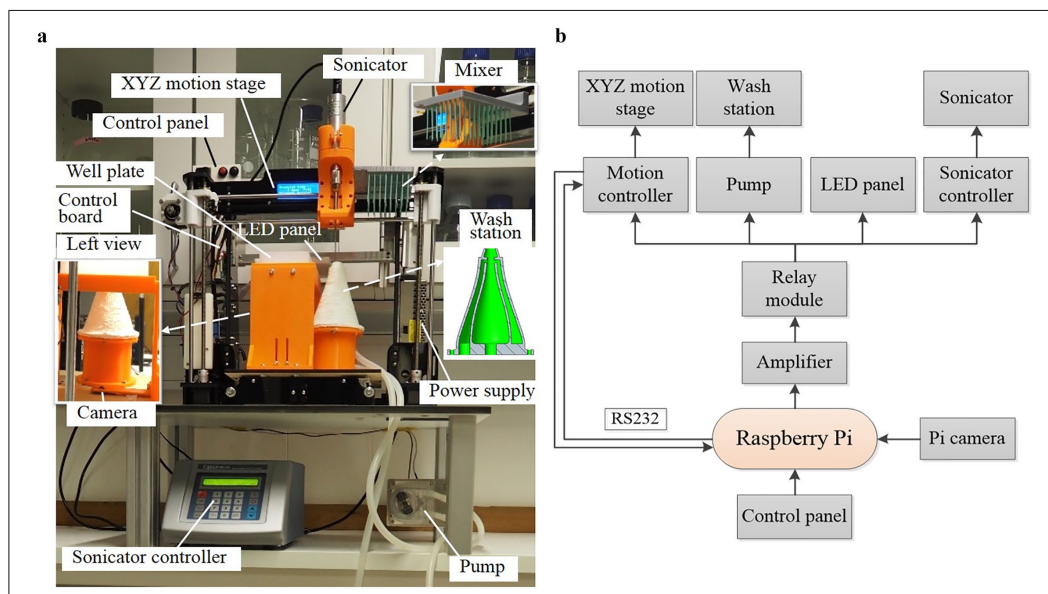


Figure 1. The ultrasonication robot: (a) robot setup and (b) schematic diagram of components and their connections.

time, since its utilization can trigger precisely sequential motions between the motion stage, pump, and sonicator. Therefore, we added a new function to the firmware to monitor when motions are complete and update the information to the upper controller. Since the robot arm is open-loop controlled, it requires calibration after each restart of the robot, as it is in 3D printing.

Control and vision module. The control board can be found on the left side of the platform. Selecting a Raspberry Pi 3 (Model B, Raspberry Pi Foundation, Cambridge, UK) as the main controller was due to its suitability for both image processing and electronics control. As shown in **Figure 1b**, the Pi controller has a serial port to communicate with the original 3D printer controller using G-code protocol for motion control. A centrally mounted, upward-facing camera (Raspberry Pi V2; Raspberry Pi Foundation) located underneath the plate holder provided a view of sample plates for image processing. The camera has a maximum resolution of 3280×2464 pixels; however, a lower resolution setting of 544×640 pixels facilitated fast processing. An LED panel consisting of several RGB LED units (5050; Golden Sun, Shenzhen, China), fixed on the center of the platform provided, a homogeneous light source for image processing. Customization of the LED panel shell allowed for easy attachment to the robot, and the lighting area (132×125 mm) was, therefore, large enough to pass light

through the 96-well microtiter plate (128×86 mm) (CR1496; EnzyScreen, Heemstede, Netherlands).

On the top-left corner of the platform is a user-friendly control panel with one power switch and two buttons (start and pause), which connected directly to the GPIO pins of the Pi controller. An intentionally positioned low-cost four-channel relay module (SainSmart, Lenexa, KS) together with a transistor array (ULN2003A; Texas Instruments, Dallas, TX), segregated the Pi controller from the 3D printer main board. As shown in **Figure 1b**, the relay module is used to control the 3D printer controller, pump, LED panel, and sonicator controller for on/off operations. The Pi controller commands the relay module with current amplification through the transistor.

Sonicator module, washing module, and power supply. A sonicator (Q125; Qsonica, Newtown, CT) combined with a standard probe facilitated the sonication of fungal cells. The washing module consists of a peristaltic pump (WPL 810; Williamson, Southwick, UK), a newly designed wash station (middle right of **Fig. 1a** and **Suppl. Fig. S2**), a fresh water bottle, a waste water bottle, and several silicone tubes. To avoid contamination during washing, the design of the wash station allows for the rinsing of the sonicator probe tip rather than bathing it, as was the case in the previous platform.⁹ The input voltage is 5V DC for the Pi controller, 12V DC for the motion stage, and 24V DC for both the pump and the LED

panel. Hence, in addition to the 12V DC power supply module of the printer, a dual-output embedded power (RD-65B; Mouser, Shanghai, China) supplies all other voltages.

Image Processing

Measurement of fungi homogeneity level. Accurate measurement of the fungi homogeneity level is essential to close the loop of ultrasonication control. Since the level of fungi homogenization in a well plate varies from well to well, analysis transpired via single-well-based image processing. This necessitated the segmentation of the wells and the identification of their centroid locations in the image pixel coordinates. One simple method was first to calculate the real-world coordinates (X, Y, Z) of the well centroids using geometry, which were then transferred into pixel coordinates (u, v) by means of camera calibration. Using the MATLAB camera calibrator toolbox and based on the classic Zhengyou Zhang calibration theory,¹⁸ the camera position changed 15 times, capturing images of a standard calibration chessboard from each position to obtain the camera's intrinsic parameters as well as its distortion coefficients. These results allowed for the identification of the relationship between the pixel coordinates and the camera coordinates (x_c, y_c, z_c). Attaching the calibration chessboard to the plate holder with its rows or columns parallel to the holder edges for camera calibration permitted the acquisition of the extrinsic coordinate transformation from the camera coordinates to the real-world coordinates. With additional geometry dimensions, the well centroids in the real world were translated to the pixel coordinate system. **Supplemental Figure S3** shows the region of interest (ROI) pixels for image processing in a camera view. The enlarged figure (lower right) illustrates the location of the ROI pixels in the center of the well and that they are smaller than the well to avoid edge effects. To reduce computation resources in the Pi controller, the transformation was conducted offline in MATLAB, and the pixel coordinates of the well centroids were imported directly into the Pi controller for real-time processing. A few months of laboratory tests indicated that the continuous use of the calibration results was possible until the camera or the plate holder position changed.

Filamentous fungi have a multicellular structure, where hyphae cells form a complex structure called mycelium. When filamentous fungi were homogenized by ultrasound sonication, we observed disruption of mycelium structure, and fungal cells were homogenized. With time, the ultrasonication treatment reduced the size of single or several large pieces of fungal mycelia in each well. Hence, the first measurement method attempted to calculate the fungal area for each well based on color thresholding. However, because of differences in the fungal biomass quality, amount, and possible fungal varieties in each well, the thresholds varied

from well to well. Furthermore, during the ultrasonication, in some cases, the whole pieces of fungal biomass split into several small pieces, making area calculation difficult. Homogenization of the filamentous fungal mycelia disrupted the mycelia into smaller pieces, causing the sample suspension to become more homogeneous. Homogeneity level, on the opposite side, also means variance level. Therefore, this study proposed a robust method based on the color variance within each single well, which calculated and combined all of the three basic color channels, R (red), G (green), and B (blue), ranging from 0 to 255. The total variance Var_{RGB} in a well can be expressed as

$$Var_{RGB} = \left[\frac{\sum_{i=1}^N (R_i - \mu_R)^2 + \sum_{i=1}^N (G_i - \mu_G)^2 + \sum_{i=1}^N (B_i - \mu_B)^2}{N} \right], \quad (1)$$

where $\mu_{R/G/B} = (\sum_{i=1}^N R_i / G_i / B_i) / N$. Generally, within a well, the smaller the Var_{RGB} , the more homogeneous the samples.

Sample screening. The purpose of sample screening was to extract the sample wells (filled with filamentous fungal mycelia) from the well plate so that the treatment could skip the blank wells (empty wells) without any preinput information, a feature that is essential for hands-free operation. **Figure 2a** shows the original picture of a well plate where a few sample wells are randomly located. To identify the sample wells, hue, saturation, and value (HSV) color thresholding was considered, since it is widely used for object segmentation.¹⁹ As mentioned above, due to the different angles at which the camera photographs the wells, the light saturation detected by the camera is uneven, and there are also shadows caused by the wells. This means that fixed global color thresholds cannot work well on different wells in the original picture, as verified by these tests. In addition, different fungal species of samples have different colors and thus require different color thresholds. To make the vision system robust to different wells and types of samples, we used a picture $B(i, j)$ that captured from a blank well plate to subtract the corresponding pixel values from the target original picture $O(i, j)$ (e.g., **Fig. 2a**), thereby obtaining a subtracted picture $S(i, j)$:

$$S(i, j) = B(i, j) - O(i, j), \quad (2)$$

where i and j represent the row and column pixel values, respectively. After this operation, as is shown in **Figure 2b**, the subtracted image $S(i, j)$ clearly shows the changes between the target picture $O(i, j)$ and the blank well plate picture $B(i, j)$, thus indicating that the fungal mycelia in the sample wells already underwent segmentation. **Figure 2c** shows that employing color thresholding to extract the

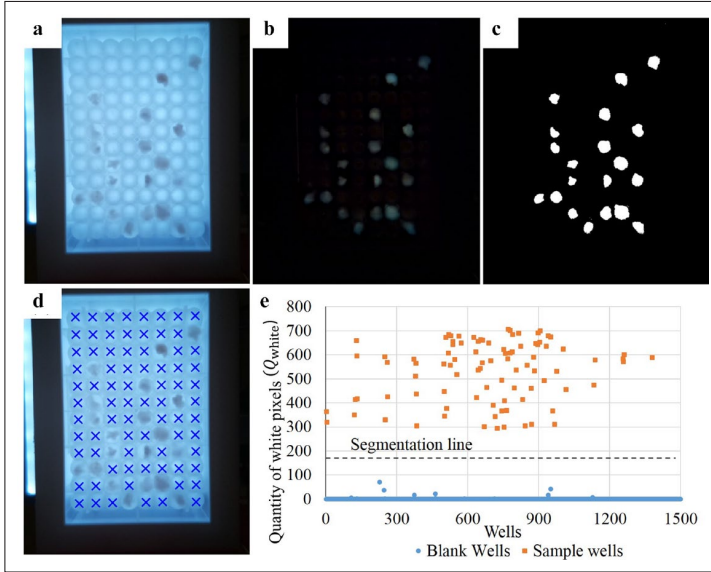


Figure 2. Sample screening approach: (a) original picture; (b) a subtracted image that was obtained by image subtraction operation between a blank well plate picture and the original picture (a), in which wells with samples were extracted; (c) a binary picture shows the samples in white pixels obtained by use of color thresholding; (d) as a result, the blank wells were skipped correctly; (e) experiment results for determining the extraction threshold of Q_{white} : generally, sample wells (orange) and blank wells (blue) show a significant difference of Q_{white} .

sample wells and converting the color image into a binary image successfully removed noise. During this process, pixels that were within the fine-tuned threshold range ($Thre_{HSV}$) were set as white pixels (value 1), while pixels out of $Thre_{HSV}$ were set as black pixels (value 0). Since the white pixels could have been disconnected within a well, rather than an area calculation, the quantity of white pixels (Q_{white}) served as the indicator to quantify the likelihood that a well either contained a sample or was empty. This can be expressed as

$$Q_{white} = \sum Pixel_{true}, Pixel_{true} = \begin{cases} 0, & Pixel_{HSV} \notin Thre_{HSV} \\ 1, & Pixel_{HSV} \in Thre_{HSV} \end{cases}, \quad (3)$$

where $Thre_{HSV}$ denotes whether or not the pixel color $Thre_{HSV}$ is within the threshold range $Thre_{HSV}$. After thresholding, the blank wells were skipped, as illustrated in **Figure 2d**.

Furthermore, an experiment performed on fourteen 96-well plates (1344 wells) with different sample well distribution and different types of filamentous fungi determined the extraction threshold of Q_{white} for regular plates. As shown in **Figure 2e**, the orange square points represent Q_{white} of sample wells while the blue circular points represent Q_{white} of blank wells. Generally, the Q_{white} values of sample wells and blank wells were significantly different. As a result, a segmentation line of 183 pixels (centerline

between the minimum point of sample well and the maximum point of blank well) separated blank wells and sample wells with a perfect classification result (100%).

Filamentous Fungi Samples for the Ultrasonication Experiment

The modeling and control tests involved two varieties of filamentous fungi—namely, *Mucor circinelloides* VI 04473 (Norwegian School of Veterinary Science, Norway) and *Mucor hiemalis* UBOCC-A-101359 (Université de Bretagne Occidentale Culture Collection, France). The selection of these two varieties was due to the well-known fact that *Mucor* fungi have a thick cell wall containing different polymers (chitin/chitosan/polyphosphate) that make the homogenization process difficult.

Fungi were cultivated in 800- μ L liquid medium malt extract broth (Oxoid, Basingstoke, UK) in 96-square polypropylene deep-well plates using the Duetz-MTPS (EnzyScreen) microtiter plate system for 2 to 3 days at 25 °C. After cultivation, the filamentous fungal mycelia were washed with distilled water in three centrifugation steps. After each centrifugation step, the mycelia formed a pellet at the bottom of wells of the microtiter plate, and supernatant above the mycelia was removed. Thereafter, the mycelia were transferred into new 96-square polypropylene deep-well plates filled with 2 mL of deionized water to homogenize fungi. We used distilled water according to the microbiology protocol

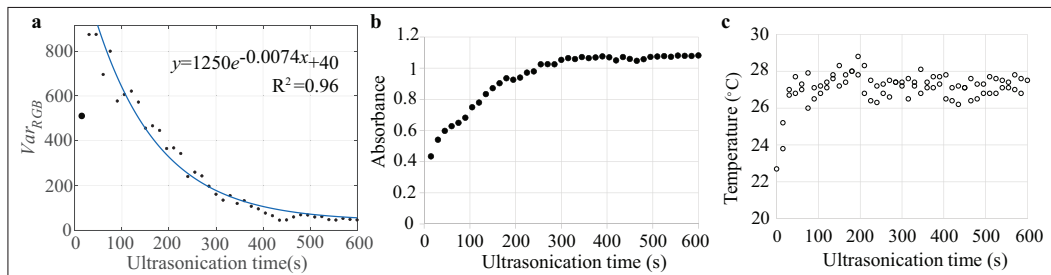


Figure 3. Var_{RGB} , sample density, and temperature changes during ultrasonication of a *Mucor circinelloides* well: (a) Var_{RGB} —ultrasonication time curve; (b) absorbance—ultrasonication time curve, showing the density of the sample liquid increased gradually; (c) temperature—ultrasonication time curve.

for washing mycelia from the growth medium. Cells of mycelia already appeared in swallowed form before washing, since the fungi grew in a liquid medium.

Modeling and Control

Modeling of the Filamentous Fungi Homogenization Process

The method used to measure the fungi homogeneity level was also the technique employed to investigate fungi homogenization changes during ultrasonication treatment. Knowledge of the exact relationship between the fungi homogeneity level and the ultrasonication treatment time could reveal the characteristics behind ultrasonication homogenization of filamentous fungi, which denoted a possible approach to precisely control ultrasonication procedures.

The first experiment intended to observe the Var_{RGB} changes against ultrasonication time by monitoring sample temperatures and liquid density. Four *M. circinelloides* wells with 2 days' cultivation were processed at room temperature (22.7 °C) with an ultrasonication duration of 15 s for each well in each interval. Each well was treated 40 times for a total of 600 s. During the experiment, the homogeneity level was measured after each 15-s treatment. We used a rapid noncontact infrared thermometer (IRT260; Biltema, Drøbak, Norway) to measure the temperature of the well bottom before and after each ultrasonication treatment. To track the sample density changes, this study used an optical density spectrophotometer (UV-T500PRO; GENESYS, Waltham, MA) to measure the sample liquid, excluding the undisrupted mycelium.

Figure 3 displays the three parameter changes during ultrasonication of a *M. circinelloides* well, and **Supplemental Figure S4** shows the corresponding visual variation of this well captured by the robot camera. As shown in **Figure 3a**, generally, except for the first point (big black point at 15 s), the Var_{RGB} decreased rapidly at the

beginning of the treatment and then steadily approached an asymptotic value. The same trend is evident in **Supplemental Figure S4**, in which the size of the black mycelium in the well became smaller and smaller and the decreasing speed seemed faster at the beginning yet slower at the end. In **Figure 3a**, the Var_{RGB} value of the first point is lower than those of the second and third points, because the mycelium at 15 s occupies most of the ROI region (**Suppl. Fig. S4**), thus reducing the color variance of the ROI region. The same phenomenon can also be found in the original picture of the well (**Suppl. Fig. S4**). This means that the Var_{RGB} may increase at the beginning of the ultrasonication due to the inherent properties of the measurement method. Without considering the original Var_{RGB} and also removing the first point, the remaining points in **Figure 3a** tend to be smooth. They can be modeled well by an exponential decay equation, as follows:

$$Var_{RGB} = f(x) = ae^{-bx} + c, \quad (4)$$

where a , b , and c are the free model parameters. As can be seen in **Figure 3a**, the fitted model has a high R^2 value. This model indicates that homogenization of the filamentous fungal samples occurs rapidly using ultrasonication at the beginning of the treatment, after which the homogenization becomes slow. The decreased size of the mycelium might play an important role in this phenomenon as there was less material to be disrupted. Also, **Figure 3b** shows that the density of the sample liquid grew gradually. This might be a second reason for the exponential decay phenomenon since the higher the density, the higher the viscosity. Higher viscosity can reduce the mycelium movement during ultrasonication so that the mycelium has less chance to be moved to the high disruption effect area around the sonicator probe. The temperature of the sample rapidly increased at the beginning, fluctuating thereafter by around 27 °C (**Fig. 3c**). The well cools naturally while the

sonicator probe processes other wells or during the washing procedures.

To identify whether factors such as temperature, sonicator power, fungi varieties, cultivation time, or even the well positions affect changes in the Var_{RGB} , a factorial experiment was performed to assess these influences. In the first subtest, the temperature was set to either 26 °C or 50 °C. The well plate was preheated to the target degree before each treatment using a heating circulator (TC120; Grant Instrument, Shepreth, UK). The ultrasonication was performed with 50% or 60% of the sonicator's rating power (effective power 62.5 or 75 watts [W]) in a pulse-regime (pause or power on, can be externally controlled) mode. For each setting, there were at least three replicates of wells. **Supplemental Figure S5** shows the results of some wells in different settings, and **Supplemental Figure S6** displays the corresponding pictures of these wells. Generally, all of them fit well with equation (4), but the model parameters (a , b , and c) vary in the different settings, as well as in the same setting with different well replicates. Two varieties of filamentous fungi (*M. hiemalis* and *M. circinelloides*) were tested with different cultivation times—2 days and 3 days. As shown in **Supplemental Figure S7**, although the settings were different, the Var_{RGB} changes in these wells still followed equation (4). This led us to conclude that filamentous fungi homogenization by ultrasonication might be an exponential decay process and is similar to many other natural decay phenomena, such as radioactive decay and temperature decrease.

This study used a statistical software (JMP 13, SAS, Medmenham, UK) to perform factor effect analysis on all the data using one-way analysis of variance (ANOVA). In this analysis, the response was Var_{RGB} , while all other settings were the factors. As shown in **Supplemental Table S1**, with the exception of the cultivation time, all the factors had a statistically significant influence on Var_{RGB} , using $\alpha = 0.05$. Particularly, the p -value of wells verified the view that even when all the settings are the same, the well replicates affect the response Var_{RGB} . It may be due to the variation, related to biomass quality and chemical composition obtained, in cultivation procedure. The ANOVA also provided a linear model using these factors, as shown in **Supplemental Figure S8**. In addition to ultrasonication time, both sonicator power and temperature are predicted to have negative influences on Var_{RGB} , indicating that the higher sonicator power and temperature would accelerate the homogenization process. Furthermore, the prediction indicates that *M. circinelloides* is more difficult to homogenize than *M. hiemalis*, which supports the point that it normally occurs in biology. The cell wall of *M. circinelloides* is richer in polymers chitin/chitosan than that of *M. hiemalis*, and because of that, theoretically it should be more difficult to homogenize it. Also, as shown in **Supplemental Figure S7b**, these curves were consolidated to pass through the same point (52, 700) by using

x -axis translation for better comparison. It is evident that the Var_{RGB} decreasing speed of *M. hiemalis* (solid and dashed lines) tends to be faster than for *M. circinelloides* (dash-dotted and dotted lines).

System Control

Termination time. Since the timeous termination of ultrasonication ensures efficiency, it is essential to be familiar with the target homogeneity level regardless of the control method employed. However, according to the results shown in **Supplemental Table S1**, the parameters of equation (4) vary for different well replicates even when the other factors remained the same. Therefore, it is challenging to subject all the wells to the same cutoff value (asymptote). Although the wells display different asymptotes for Var_{RGB} , the derivative Var_{RGB} has the same asymptote, 0. Therefore, Var_{RGB} was considered to determine whether proper homogenization of the wells has occurred. **Supplemental Figure S5** and **Supplemental Figure S6** represent the four wells at 26 °C and 75 W. The four circled points/wells (termination points) in these images indicate the required homogeneity levels based on the manual estimation. Therefore, it is evident that the Var_{RGB} changes were minimal when closing the target points. To calculate Var_{RGB} at each point, four local points (three former closest points and the current point) were used to fit a linear model and obtain the slope, $Slope_{local}$. **Supplemental Figure S9** shows the $Slope_{local}$ —ultrasonication time curves for the four wells in **Supplemental Figure S5** (26°C and 75 W). In all the wells, the $Slope_{local}$ increased rapidly during the initial stages, while decelerating when approaching 0. Similarly, the circled points represent the time that the wells reached full homogenization. Except for C4, employing a fixed value for the determination of proper homogenization points in the other three wells remained a challenge, since the slopes fluctuated around 0 before the termination points.

Then we used the standard deviation Std_{local} of the four local points (three former closest points and the current point) to determine the termination time, and it can be expressed as

$$Std_{local} = \sqrt{\sum_{i=1}^4 (Var_{RGBi} - \overline{Var_{RGB}})^2} / 4. \quad (5)$$

Figure 4 shows the Std_{local} —ultrasonication time curves for the four wells in **Supplemental Figure S5** (26°C and 75 W), where the circled points indicate the termination time. Generally, the curves in **Figure 4** appear smoother than those in **Supplemental Figure S9**. Most important, the Std_{local} values exhibited a gradual decrease before the termination points, and their Std_{local} values at termination time were 5.7, 4.9, 3.8, and 4.3, respectively. To eliminate fluctuations, the Std_{local} value was reviewed three times before

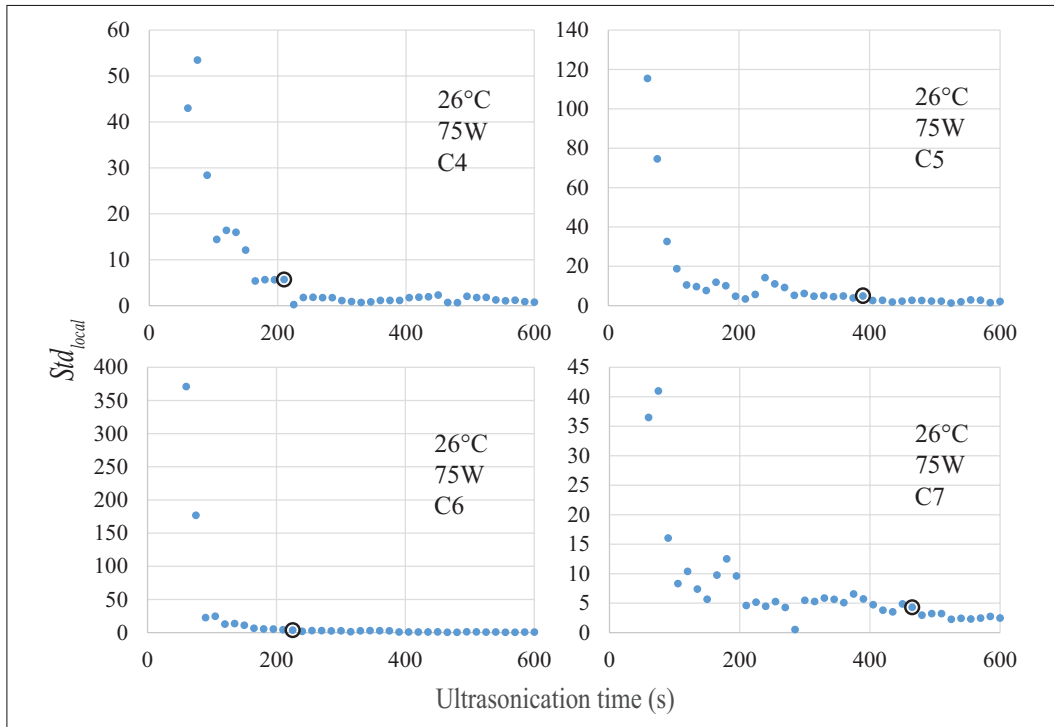


Figure 4. Std_{local} —ultrasonication time curves for the four wells in **Supplemental Figure S5** (26 °C and 75 W): the circled points (termination points) represent the time that the wells were fully homogenized; these curves show more significant changes before the termination points than those in **Supplemental Figure S5** and **Supplemental Figure S9**.

reaching a final decision. Hence, the system only terminates the treatment when the three most recent Std_{local} values are smaller than the required value. The three points following the termination point for each curve in **Figure 4** were all smaller than 3.3. Therefore, 3.3 represented the termination value during the automation process.

Sequential control. Equation (4) shows promise in model-based control for the ultrasonication process. The idea is that, after an initial period of ultrasonication (e.g., 30 s), the system uses a model from equation (4) to estimate the remaining treatment time based on the difference between the target and current Var_{RGB} values. Theoretically, the model-based control method is the fastest way to achieve fungi homogenization as it processes wells continuously within the estimated remaining time. Moreover, the sonicator tip requires only one washing per well. However, continuous ultrasonication will heat up the samples, thus damaging the sample proteins and other chemical structures. Thus, laboratory experiments usually use 15- to 30-s ultrasonication duration for 62.5-W sonicator power, with a

cool-down period for the samples between each treatment. In addition, according to the manual, the sonicator cannot be powered continuously for more than 60 s. Therefore, model-based control is not suitable for filamentous fungi as used in this article, but it might be applicable for samples requiring only short periods of ultrasonication, such as bacteria.

Due to the limitations of ultrasonication, this system used a screening-based control method for the automation. Similar to the modeling process, the robot treated each well with 15 s of ultrasonication at each interval and monitored the termination time for all wells. When reaching the termination time, the well was passed. **Figure 5** shows the entire control sequence of the robot. The codes in the Pi controller were written in Python 2.7, and the image processing was based on the *Picamera* and *OpenCV* libraries. Three main steps were evident in the ultrasonication sequence following placement of the sample well plate on the robot:

1. **Robot initialization:** The Pi controller ran a server script automatically after booting. The server

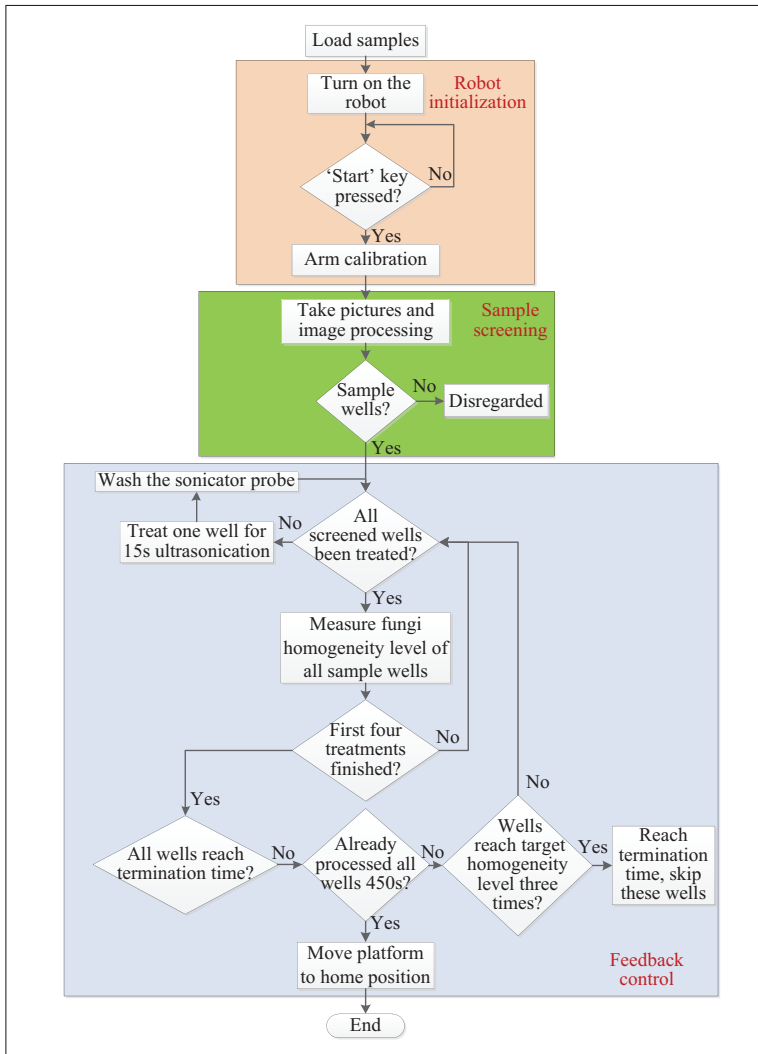


Figure 5. Workflow of the robot control sequence: the ultrasonication sequence can be divided into three main steps: robot initialization, sample screening, and feedback control. The system measured the fungi homogeneity levels of all sample wells after each 15-s ultrasonication and screened them again for a new cycle of ultrasonication until the termination requirements were satisfied or the wells had completed a 450-s processing cycle.

program ran in a loop waiting for the activation of a key followed by the initialization of the XYZ motion stage. The main program initialized once the operator pressed the start button.

2. *Sample screening:* After calibration of the arm, the vision system distinguished between blank wells and sample wells. The locations of the sample wells were recorded for ultrasonication, while the blank wells were disregarded.

3. *Feedback control:* Once the sample wells had been screened out, the feedback control step was initiated, starting with ultrasonication treatment for a duration of 15 s. During ultrasonication, the sonicator tip in the well moved in a compound manner (circling and up-down) to encourage more homogeneous fungi homogenization, which resembled the way human operators would apply the device. Furthermore, between processing any two wells, the

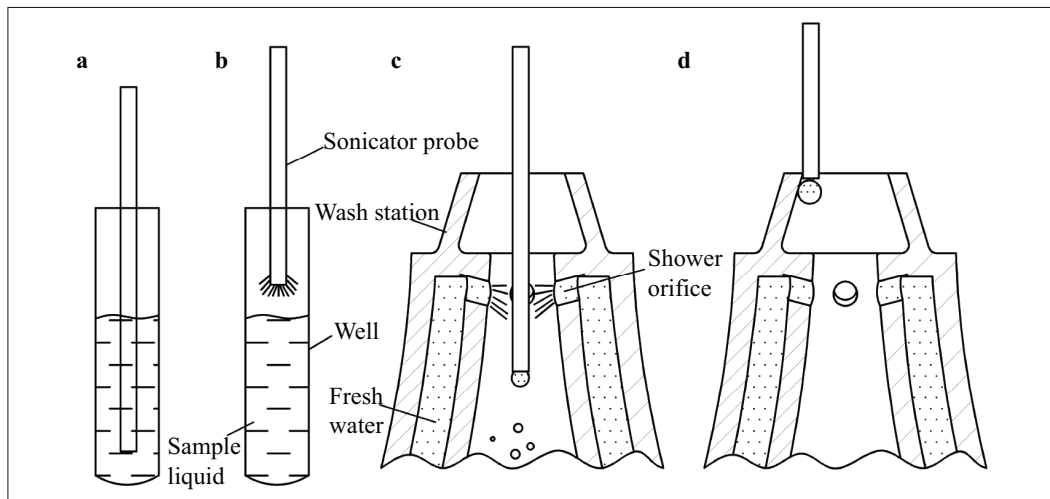


Figure 6. Schematic of ultrasonication and washing steps: (a) ultrasonication of the fungal sample; (b) the sonicator is powered on for 1 s to remove the droplet when the probe is taken out from the well; (c) washing the sonicator probe in the wash station; (d) the sonicator probe is touching the inner top of the wash station to remove the droplet.

sonicator tip was cleaned thoroughly in the wash station to avoid contamination. As shown in **Figure 6c**, fresh water passes through the outer hollow space of the wash station to clean the sonicator tip and then flows through the hollow inner space into the waste bottle. To avoid droplets from contaminating other wells, the sonicator was powered on for 1 s to remove the droplet from the tip of the sonicator probe after withdrawing it from the well (**Fig. 6b**). In addition, when extracting the sonicator probe following the washing process, the robot touched the inner top of the wash station to remove the droplet (**Fig. 6d**). The top of the wash station has a conical surface for better scraping of the droplets. Subsequently, measurement of the fungi homogeneity levels of all sample wells occurred online using the image-processing system. After completion of the first four treatments, the system began to calculate the Std_{local} value for determining the termination time. Wells that did not meet the termination requirements (reaching target homogeneity level three times continuously) were subjected to the ultrasonication process again. Once a well reached the proper termination time, no further treatment was required. Contrary to the open-loop control approach subjecting all wells to the same ultrasonication treatment time,⁹ the feedback control method reduced the ultrasonication time for an entire well plate since disregarding the homogenized wells. The maximum ultrasonication time was set to 450 s,

which could be readily changed depending on fungi species and target homogeneity level.

This screening-based control is simple, is robust, and ensures high homogenization quality. Consequently, the vision-based feedback control system allowed for the full automation of the machine without requiring manual intervention during the experiment.

Results and Discussion

Measurement Precision and Accuracy

To evaluate the precision of the fungi homogenization measurement, 11 wells with different homogeneity levels were measured continuously without any treatment and repeated 25 times. The results, illustrated in **Supplemental Figure S10a**, show horizontal lines of Var_{RGB} that were relatively stable, suggesting the acceptable repetition precision of the proposed measurement method. An average percentage deviation of 2.29%, obtained from $100\% * \sum_{i=1}^N s_i / (\bar{s} * N)$, was evident, where s_i was the standard deviation of each line in **Suppl. Fig. S10a**.

To evaluate the measurement accuracy, this study utilized fully homogenized samples to fill the well plate. As shown in **Supplemental Figure S10b**, wells located at the edges of the microtiter plate (low or high row number) presented higher Var_{RGB} , while the wells in the middle row exhibited relatively low Var_{RGB} . This could be attributed to the changes in the camera angle when observing each well.

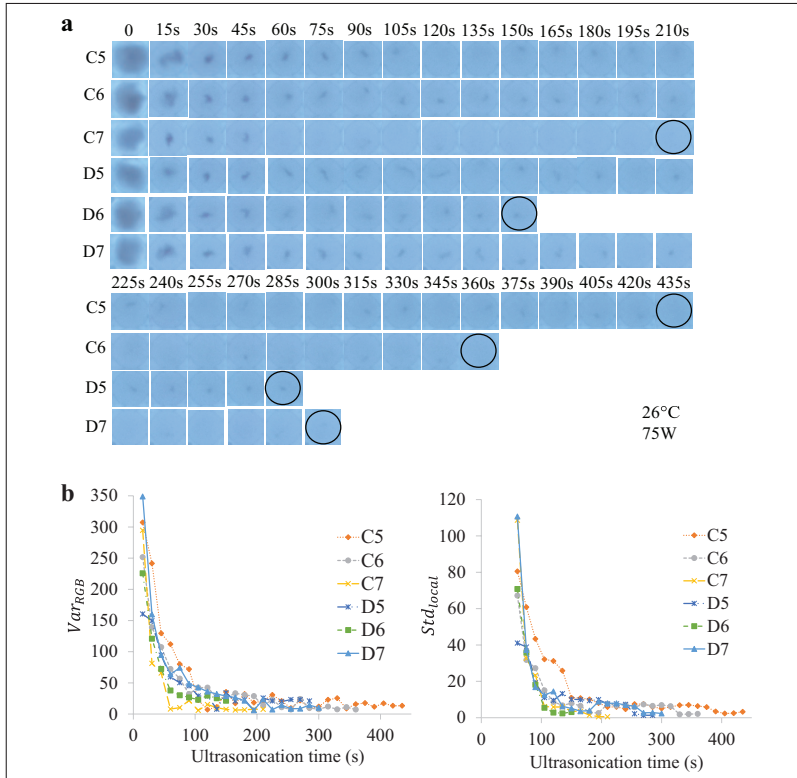


Figure 7. Validation test results: (a) images of six wells during all stages of ultrasonication: all the filamentous fungi samples were ultimately homogenized (black circled pictures), and the treatment time varies from 150 s to 435 s; (b) Var_{RGB} and Std_{local} to ultrasonication time curves of the six wells in (a).

Due to different angles, the camera detected the various light intensities and shadows that were present in the wells. The standard deviation of these points was 1.9, but the average percentage deviation was 26.3%. Furthermore, evaluation of the accuracy occurred by randomly placing the six physically heterogeneous samples into different wells. Although not significant, various fluctuations were evident in Var_{RGB} of the different wells, with a standard deviation of 10.2 and an average percentage deviation of 11.4%, as shown in **Supplemental Figure S10c**. The relative low accuracy indicated that it was advisable to control the wells independently when using Var_{RGB} .

System Control Result

To validate the control method, an experiment was performed with six *M. circinelloides* sample wells using the same setting as during the modeling process (2 days' cultivation, 26 °C, and 75 W). The vision system successfully screened out the six wells. During the feedback control step, the wells underwent ultrasonic treatment until the system

detected the termination time. **Figure 7a** shows images of the entire procedure, where the pictures circled in black indicate the final states. **Figure 7b** shows the corresponding Var_{RGB} and Std_{local} changes of all wells, clearly indicating that the ultrasonication duration of the six wells varied between 150 s and 435 s. Compared to the open-loop control approach that treated all wells with the same ultrasonication time⁹ the screening-based control reduced the ultrasonication time by 870 s (33.3%) for the six wells if the open-loop control treatment time was set to 435 s.

Consequently, sufficient homogenization of all the fungi samples transpired and reached similar states comparable to the modeling process (refer to the circled wells in **Suppl. Fig. S6**). However, as shown in **Figure 7a**, wells C5, C6, C7, and D7 were entirely homogeneous in the final states, while D5 and D6 still exhibited a small black dot of mycelium that did not appear to display significant changes in size before termination. This result was especially evident in D5, where the size of the mycelium remained the same from the 225-s mark onward, which was also verified by the variance curve in **Figure 7b**. Unless higher sonicator power

was used during the manual tests, the black mycelium dots were extremely difficult to disrupt in some wells. The application of this control method can prevent wasting time to homogenize these challenging mycelium dots if no change is evident in the homogeneity levels after three repetitions.

Limitations and Suggestions

Since the homogeneity measurement method depended on an upward-facing camera, the bottom mycelia primarily determined the color variance calculation. Therefore, the system was not sensitive to the mycelia that remained suspended in the well. On some occasions, the mycelia did not fall to the bottom before the images were captured, which resulted in the acquisition of a smaller Var_{RGB} . For example, in **Figure 7a**, well C5 seems homogeneous at 120 s and 135 s and the Var_{RGB} values are small in **Figure 7b**. Owing to the termination method by which Std_{local} was checked three times before terminating, the robot continued treating the sample and the mycelium returned at 150 s.

However, based on our tests, for some filamentous fungi, such as *Penicillium expansum*, it seems that the density of the mycelia was lower and close to water, so the mycelia were always suspended in the water. This made homogeneity levels challenging for the imaging system to measure due to the upward-facing camera. A possible improvement might be to use a camera that faces the sides of the wells. However, this requires placing the sample in a separate well for ultrasonication rather than a well plate. Another solution might be to aspirate the sample after each treatment and measure it from the side in a separate well. However, this process would unnecessarily complicate the system since the separate well requires thorough cleaning between samples.

In addition, the *P. expansum* samples were easily homogenized. The tests in this study indicated that the *P. expansum* samples could be fully homogenized within 15 s using the same setting as for *M. circinelloides* (2 days' cultivation, 26 °C, and 75 W). However, the control system only terminated after obtaining three small, continuous Std_{local} values, suggesting that the treatment for each well was only terminated after 105 s. This feature wasted the valuable processing time due to overtreatment but did not affect the final results. To minimize the time required, sample wells that are easily homogenized could be preloaded into the system.

We tested the system with filamentous fungi and found that filamentous fungi homogenization by ultrasonication might be an exponential decay process. However, this theory has not been verified by testing various fungi. Further work should include testing of other types of fungi or even other microorganisms.

In conclusion, this study developed a novel inexpensive platform to automate filamentous fungi homogenization using ultrasonication and constructed the platform hardware by modifying an inexpensive 3D printer with various

custom-designed parts and additional electronics. While machine vision distinguished between sample wells and blank wells based on image subtraction and color thresholding, it also measured the level of fungi homogeneity using color variance. The utilization of model fitting indicated that all the tested fungal homogenization using ultrasonication caused significant exponential decay. This process allowed for the rapid homogenization of fungal samples during the initial stages of ultrasonication treatment followed by gradual homogenization. In addition, one-way ANOVA analysis denoted that higher sonicator power and temperature accelerated the homogenization process, while the cultivation time exhibited no effect on homogenization. Moreover, the model parameters varied between the wells, even when subjected to the same settings, meaning that the system cannot use the same asymptote of the homogeneity level to establish the termination time for different wells. Therefore, we used the standard deviation of the four closest homogeneity level values to determine the termination time. This method allowed for feedback control, forming a fully automated robot that did not require manual intervention during the experiment. A validation test on filamentous fungi demonstrated that the system was efficient and able to provide target quality of samples.

Acknowledgments

We thank Julie Eymard for helping to prepare filamentous fungi samples.

Declaration of Conflicting Interests

The authors declared no potential conflicts of interest with respect to the research, authorship, and/or publication of this article.

Funding

The authors disclosed receipt of the following financial support for the research, authorship, and/or publication of this article: This research was funded by Norwegian University of Life Sciences.

ORCID iD

Ya Xiong  <https://orcid.org/0000-0001-5593-8440>

References

- Shapaval, V.; Møretro, T.; Wold Åsli, A.; et al. A Novel Library-Independent Approach Based on High-Throughput Cultivation in Bioscreen and Fingerprinting by FTIR Spectroscopy for Microbial Source Tracking in Food Industry. *Let. Appl. Microbiol.* **2017**, *64*, 335–342.
- Shapaval, V.; Schmitt, J.; Møretro, T.; et al. Characterization of Food Spoilage Fungi by FTIR Spectroscopy. *J. Appl. Microbiol.* **2013**, *114*, 778–796.
- Shapaval, V.; Møretro, T.; Suso, H. P.; et al. A High-Throughput Microcultivation Protocol for FTIR Spectroscopic Characterization and Identification of Filamentous Fungi. *J. Biophotonics* **2010**, *3*, 512–521.

4. Burden, D. Guide to the Disruption of Biological Samples. *Random Prim.* **2012**, *25*, 1–25.
5. Klimek-Ochab, M.; Brzezińska-Rodak, M.; Zymańczyk-Duda, E.; et al. Comparative Study of Fungal Cell Disruption-Scope and Limitations of the Methods. *Folia Microbiol. (Praha)*. **2011**, *56*, 469–475.
6. Borthwick, K. A. J.; Coakley, W. T.; McDonnell, M. B.; et al. Development of a Novel Compact Sonicator for Cell Disruption. *J. Microbiol. Methods* **2005**, *60*, 207–216.
7. Gogate, P. R.; Kabadi, A. M. A Review of Applications of Cavitation in Biochemical Engineering/Biotechnology. *Biochem. Eng. J.* **2009**, *44*, 60–72.
8. Tiwari, B. K.; O'Donnell, C. P.; Cullen, P. J. Effect of Sonication on Retention of Anthocyanins in Blackberry Juice. *J. Food Eng.* **2009**, *93*, 166–171.
9. Li, J.; Shapaval, V.; Kohler, A.; et al. A modular liquid sample handling robot for high-throughput Fourier transform infrared spectroscopy. In *Advances in Reconfigurable Mechanisms and Robots II*, **2016**, *36*, 769–778.
10. Smagowska, B.; Pawlaczyk-Luszczynska, M. Effects of Ultrasonic Noise on the Human Body: A Bibliographic Review. *Int. J. Occup. Saf. Ergon.* **2013**, *19*, 195–202.
11. Mancía, F.; Love, J. High-Throughput Expression and Purification of Membrane Proteins. *J. Struct. Biol.* **2010**, *172*, 85–93.
12. Almo, S. C.; Garforth, S. J.; Hillerich, B. S.; et al. Protein Production from the Structural Genomics Perspective: Achievements and Future Needs. *Curr. Opin. Struct. Biol.* **2013**, *23*, 335–344.
13. Wei, B.; Feng, J.; Rehmani, I. J.; et al. A High-Throughput Robotic Sample Preparation System and HPLC-MS/MS for Measuring Urinary Anatabine, Anabasine, Nicotine and Major Nicotine Metabolites. *Clin. Chim. Acta* **2014**, *436*, 290–297.
14. Breitwieser, H.; Dickmeis, T.; Vogt, M.; et al. Fully Automated Pipetting Sorting System for Different Morphological Phenotypes of Zebrafish Embryos. *SLAS Technol.* **2018**, *23*, 128–133.
15. Saretta, E.; de Camargo, A. P.; Botrel, T. A.; et al. Test Methods for Characterising the Water Distribution from Irrigation Sprinklers: Design, Evaluation and Uncertainty Analysis of an Automated System. *Biosyst. Eng.* **2018**, *169*, 42–56.
16. Nejatimoharrami, F.; Faina, A.; Stoy, K. New Capabilities of EvoBot: A Modular, Open-Source Liquid-Handling Robot. *SLAS Technol.* **2017**, *22*, 500–506.
17. Schneidereit, D.; Kraus, L.; Meier, J. C.; et al. Step-by-Step Guide to Building an Inexpensive 3D Printed Motorized Positioning Stage for Automated High-Content Screening Microscopy. *Biosens. Bioelectron.* **2017**, *92*, 472–481.
18. Zhang, Z. A Flexible New Technique for Camera Calibration (Technical Report). *IEEE Trans. Pattern Anal. Mach. Intell.* **2002**, *22*, 1330–1334.
19. Xiong, Y.; Ge, Y.; Liang, Y.; et al. Development of a Prototype Robot and Fast Path-Planning Algorithm for Static Laser Weeding. *Comput. Electron. Agric.* **2017**, *142*, 494–503.

Supplemental Material

A laboratory-built fully automated ultrasonication robot for filamentous fungi homogenization

By Ya Xiong, Volha Shapaval, Achim Kohler, Pål Johan From

Faculty of Science and Technology, Norwegian University of Life Sciences, Ås 1432, Norway

Correspondence: Ya Xiong, Faculty of Science and Technology, Norwegian University of Life Sciences, Drøbakveien 31, Ås 1432, Norway. Tel: +4745126458. E-mail: yaxio@nmbu.no.

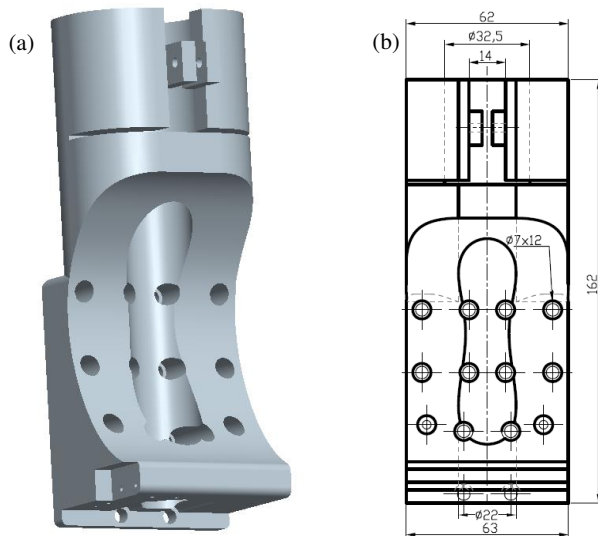


Fig. S1. 3D model of the 3D-printed sonicator holder: (a) 3D model, this holder was printed using low-cost polylactic acid (PLA) filaments; (b) front view 2D drawing with key dimensions. The 3D model is available at this [link](#).

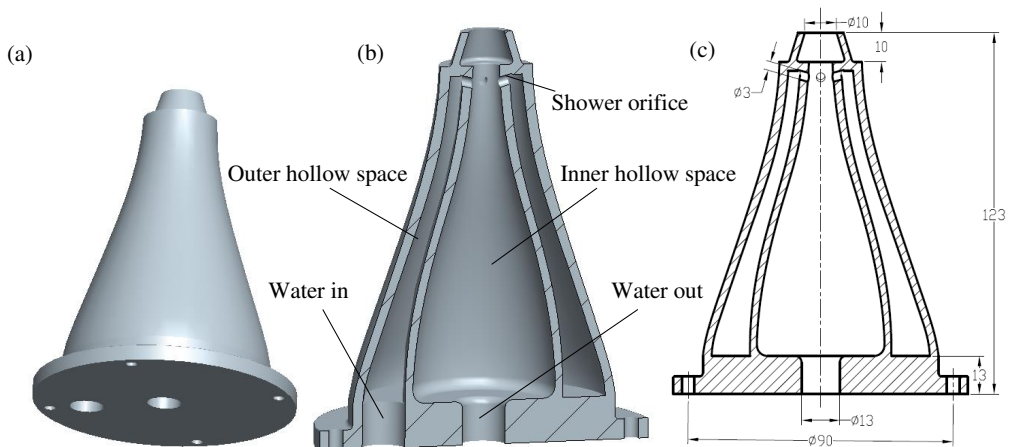


Fig. S2. 3D model of the wash station: (a) the wash station; (b) half-section view of the wash station: the fresh water passes through the outer hollow space of the wash station to clean the sonicator tip, and then flows through the hollow inner space into the waste bottle; to avoid contamination during washing, the wash station was designed to rinse the tip of the sonicator probe through the shower orifice; (c) half-section view 2D drawing of the wash station with key dimensions. The 3D model is available at this [link](#).

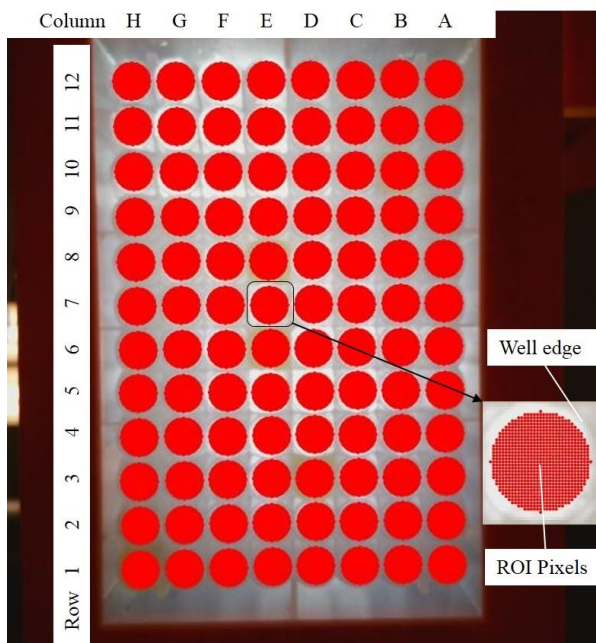


Fig. S3. ROI pixels for image processing: camera view of a microtiter plate; the red circles show the ROI pixels for single-well based measurement; the enlarged figure in the lower right illustrates that the ROI

pixels are located in the center of the well and are smaller than the well edge to avoid edge effects.

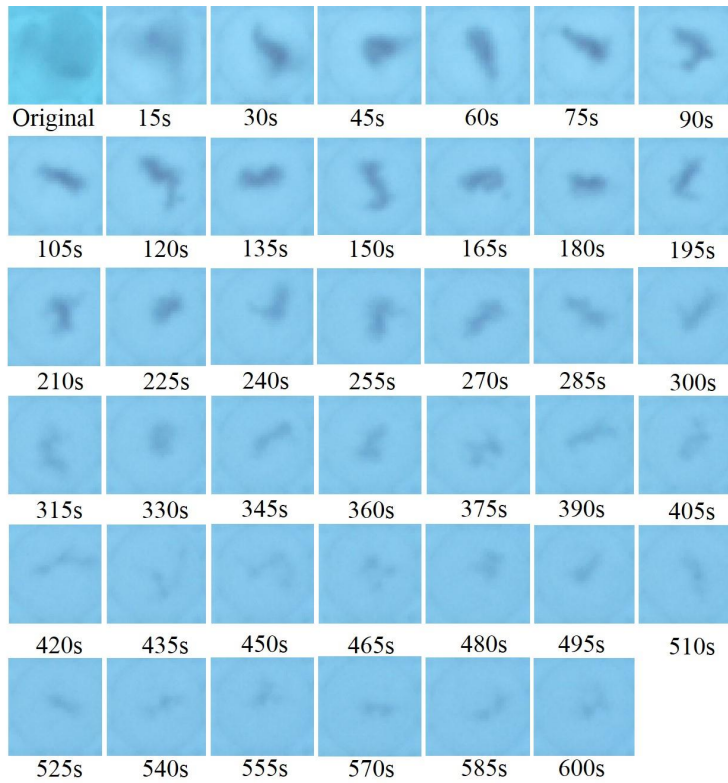


Fig. S4. Corresponding pictures of the well at various time points in **Fig. 3**, captured by the robot camera: the size of the black mycelium in the well becomes increasingly smaller, while the decreasing speed seems faster at the beginning yet slower at the end.

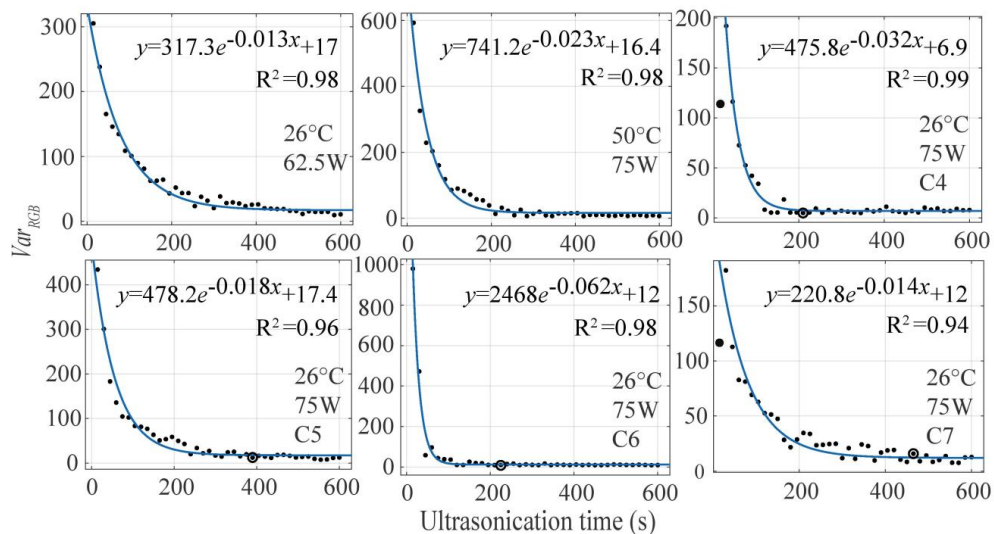


Fig. S5. Var_{RGB} - ultrasonication time curves for wells with different temperatures and sonicator power: all the wells can be well modelled, however the parameters are different from well to well even when the temperature and sonicator power were the same.

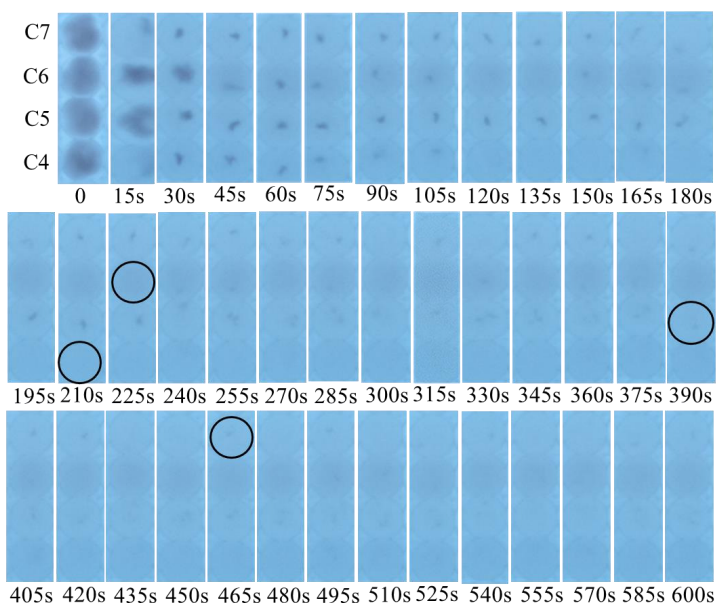


Fig. S6. Corresponding images of the four wells (26°C and 75W) at time points in **Fig. S5**; the four circled wells indicate the required homogeneity levels based manual estimation.

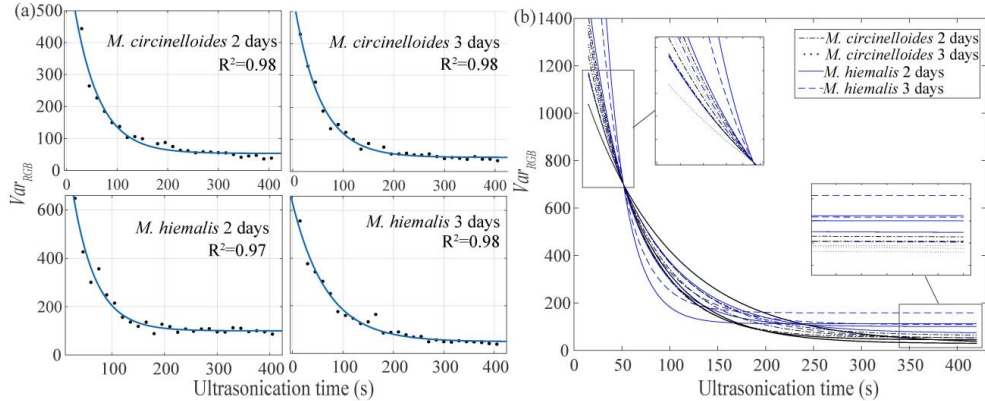


Fig. S7. Modeling and comparison of homogenization *M. hiemalis* and *M. circinelloides* samples: (a) Var_{RGB} – ultrasonication curves for each setting (variety and cultivation time); (b) all fitted models were plotted in one figure and consolidated using x-axis translation for comparison.

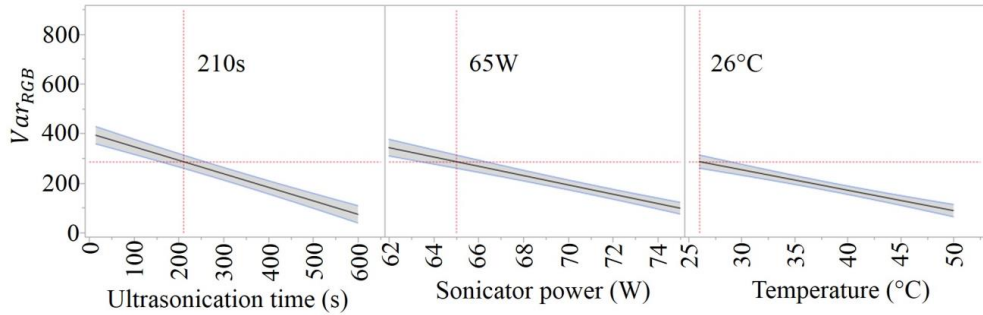


Fig. S8. Prediction trends of Var_{RGB} against ultrasonication time, sonicator power and temperature using one-way ANOVA: the shadow along the lines shows the confidence intervals; in addition to ultrasonication time, both sonicator power and temperature were predicted to have negative influences on Var_{RGB} , which means that a higher sonicator power and temperature would speed up the homogenization process.

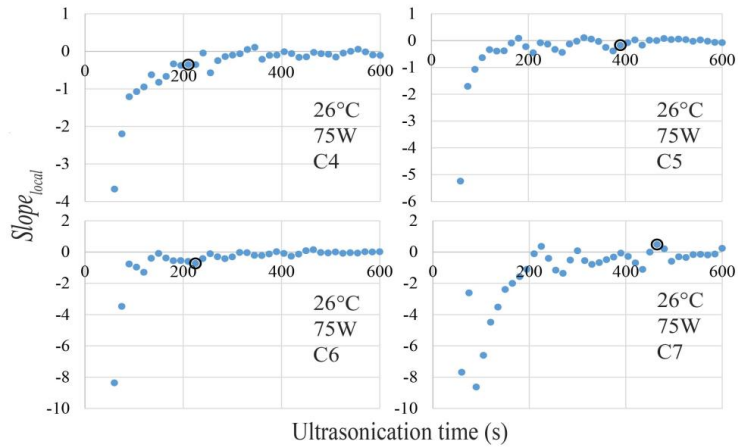


Fig. S9. $Slope_{local}$ – ultrasonication time curves for the four wells in **Fig. S5** (26°C and 75 W).

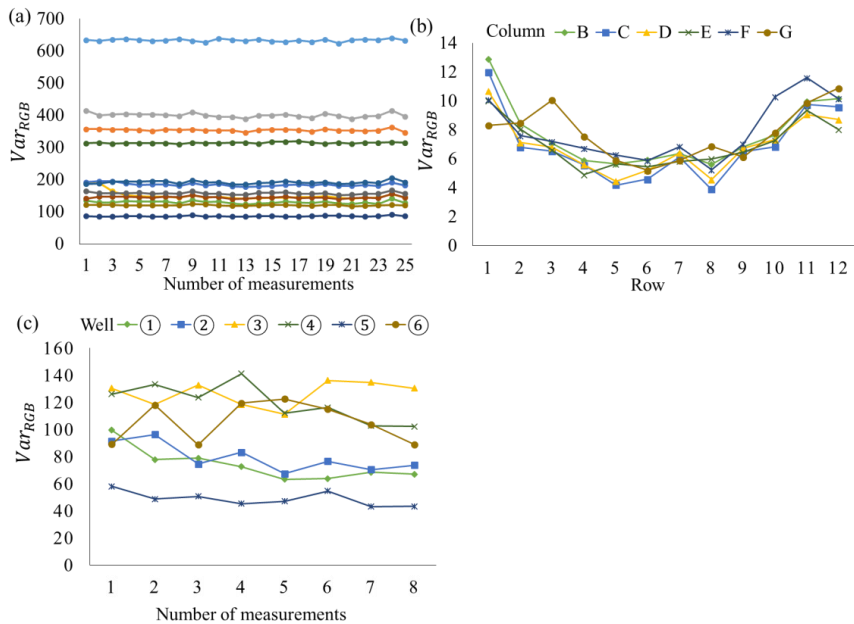


Fig. S10. Measurement precision and accuracy of fungi homogenization levels: (a) repeatability test of the measurement method on 11 wells with different homogeneity levels; (b) with same filamentous fungi samples, wells located at the edges of the microtiter plate (low or high row number) row number) present

higher Var_{RGB} , while the wells in the middle row exhibit relatively low Var_{RGB} ; (c) the accuracy test performed by putting six heterogeneous samples randomly into different wells.

Table S1. Factor effect test using one-way ANOVA

Effect indicators	Ultrasonication time	Sonicator power	Temperature	Cultivation time	Varieties	Wells
F ratio	172.0	142.1	100.6	0.035	25.4	24.1
<i>p</i> -value	<0.0001	<0.0001	<0.0001	0.85	<0.0001	<0.0001

p-value shows that all the factors, except for cultivation time, have significant influences on Var_{RGB} (using $\alpha=0.05$)

Part I – Sample preparation robots for FTIR spectroscopy

Paper II

Xiong, Y., Shapaval, V., Kohler, A., Li J. and From, P.J., 2019. A Fully Automated Robot for the Preparation of Fungal Samples for FTIR Spectroscopy Using Deep Learning. *IEEE ACCESS*, 7, pp.1-12. DOI: <https://10.1109/ACCESS.2019.2941704>

Received July 29, 2019, accepted September 12, 2019, date of publication September 16, 2019,
date of current version September 26, 2019.

Digital Object Identifier 10.1109/ACCESS.2019.2941704

A Fully Automated Robot for the Preparation of Fungal Samples for FTIR Spectroscopy Using Deep Learning

YA XIONG¹, VOLHA SHAPAVAL¹, ACHIM KOHLER¹, JICHUN LI², AND PÅL JOHAN FROM¹

¹Faculty of Science and Technology, Norwegian University of Life Sciences, 1432 Ås, Norway

²Department of Engineering, Teesside University, Tees Valley TS1 3BX, U.K.

Corresponding author: Ya Xiong (ya.xiong@nmbu.no)

This work was supported by the Norwegian University of Life Sciences.

ABSTRACT Manual preparation of fungal samples for Fourier Transform Infrared (FTIR) spectroscopy involves sample washing, homogenization, concentration and spotting, which requires time-consuming and repetitive operations, making it unsuitable for screening studies. This paper presents the design and development of a fully automated robot for the preparation of fungal samples for FTIR spectroscopy. The whole system was constructed based on a previously-developed ultrasonication robot module, by adding a newly-designed centrifuge module and a newly-developed liquid handling module. The liquid handling module consists of a high accuracy electric pipette for spotting and a low accuracy syringe pump for sample washing and concentration. A dual robotic arm system with a gripper connects all of the hardware components. Furthermore, a camera on the liquid handling module uses deep learning to identify the labware settings, which includes the number and positions of well plates and pipette tips. Machine vision on the ultrasonication robot module can detect the sample wells and return the locations to the liquid handling module, which makes the system hand-free for users. Tight integration of all the modules enables the robot to process up to two 96-well microtiter (MTP) plates of samples simultaneously. Performance evaluation shows the deep learning based approach can detect four classes of labware with high average precision, from 0.93 to 1.0. In addition, tests of all procedures show that the robot is able to provide homogeneous sample spots for FTIR spectroscopy with high positional accuracy and spot coverage rate.

INDEX TERMS Laboratory automation, robotics, deep learning, ultrasonication, spotting, FTIR spectroscopy.

I. INTRODUCTION

Characterization, identification and classification of microorganisms (bacteria, yeast, filamentous fungi and algae) has a high importance in the field of environmental, industrial, medical and agriculture microbiology, and microbial ecology [1]. There are two principle ways to characterize, identify and classify microorganisms - by using Genotyping and/or Phenotyping technologies. Genotyping technologies are based on PCR/sequence typing and genome typing approaches, have gone through tremendous developments in the last decade. This has resulted in Next Generation Sequencing (NGS) and CRISPR/Cas9 technologies allowing highly precise and robust analysis of DNA and its

products [2]. As the application of genotyping technologies reached into new levels of development, academic, biotechnological and clinical diagnostics laboratories had to address the logistics of consistently running the high-throughput operations - DNA extraction, shearing, cleanup, amplification, and sequencing. Considerable progress has been made on automating these individual elements. Automated, high-throughput DNA extraction and sequencing was implemented in multiple core sequencing laboratories soon after NGS was established [3]. As an example, bacterial genotyping was automated in some laboratories soon thereafter [4]–[6].

While genotyping technologies have been advancing rapidly and through the integration of robotics, phenotyping technologies have been for a long time represented by the conventional microbiological techniques providing

The associate editor coordinating the review of this manuscript and approving it for publication was Omid Kavehei.

morphological, physiological and cultural characteristics. Commonly employed phenotypic methods are protein-based methods including biotyping, serotyping, bacteriocin typing, phage typing, antimicrobial susceptibility patterns etc. These phenotypic methods are associated with several problems related to reproducibility, discriminatory power, high variability etc. Such shortcomings of phenotypically based methods have therefore led to the development of novel so called Next Generation Phenotyping (NGP) technologies, represented by two biophysical non-invasive techniques - Fourier Transform Infrared (FTIR) spectroscopy [7] and Matrix-Assisted Laser Desorption/Ionization Time-of-Flight (MALDI-TOF) spectrometry (MS) [8]. Both techniques provide, with a high level of precision, a cellular biochemical phenotype of microbial cells - MALDI-TOF MS provides protein profile while FTIR provides total biochemical profile (proteins, lipids, polysaccharides). In addition, it has to be noted that FTIR provides not only cellular phenotype in the form of intracellular metabolites, but also extracellular phenotype in the form of extracellular metabolites. Both techniques are based on the high-throughput platform with the potential for analyzing up to 159 - 384 samples in a single analytical run.

Manual preparation of multi-well fungal samples for FTIR involves sample washing to remove culture medium, homogenization by ultrasound, up concentration for FTIR and spotting on the multi-well infrared (IR) plates. In case of high-throughput set-up fungi are cultivated in 96-well MTP plates and the whole process for manual preparation of a 96 microbial samples may take more than 10 hours depending on the type of fungi and technician experiences. The whole process also requires highly skilled technicians to oversee the process [9], especially for sample homogenization and spotting. In addition, manual operation may introduce variation to the samples due to the subjective nature of visual inspection [10]. In order to explore the high-throughput potential of the FTIR techniques, there is a strong need for the implementation of liquid-handling robotics for the sample preparation procedures.

In the laboratory automation field, a number of platforms have been developed to automate the sample preparation procedures. Meier *et al.* [11] presented an automatic sampling spotting method using a commercially available synthetic robot to prepare samples for MALDI-TOF MS. Nejatimoharrami *et al.* [12] developed a liquid-handling robot based on a 3D printer for placing droplets (spotting). The system used a camera to monitor the droplet size and position. Kwee *et al.* [10] described a robotic platform that used a vision system to identify cells and control a robotic arm to pick and place the selected cells for cell-based assays. Cherezov *et al.* [13] showed a dual-arm system that used one arm for pick-up and placement of precipitant solutions and the other arm equipped with a microsyringe for sample dispensing.

Our previous work [14] attempted to build a robotic platform for all the procedures of sample preparation for

FTIR spectroscopy. The system simply used a robotic arm consisting of two linear motion units for manipulation of sampling washing, homogenization and spotting without closed-loop control strategies for monitoring or automated control. The open-loop feature, however, resulted in insufficient or excessive ultrasonication and, more important, might not always provide well-homogenized samples [9]. Also, due to the low accuracy of the dispensing unit, the spotting process did not provide reliable sample spots. Moreover, the washing and spotting used the sample dispensing unit that may introduce contamination. As a result of these limitations, we developed a closed-loop control system based on a low-cost 3D printer for sample homogenization using ultrasonication [9]. The robot used machine vision to distinguish between sample wells and blank wells and measure the homogeneity level of cell suspension. The control system enabled the robot to provide the desired homogeneity level of cell suspension efficiently. In this paper, we present the design, development and integration of a complete system to prepare fungal samples for FTIR spectroscopy. The whole system is an extension to the ultrasonication robot [9], by adding a newly-designed centrifuge module and a newly-developed liquid handling module.

While deep learning as an emerging technology has been widely used for many applications ranging from vehicle classification [15] to fruit detection [16] or drug design [17], few studies have reported the applications in laboratory automation, especially for the labware identification. In this paper, we show the method and results of using deep learning based vision system to identify the labware settings, including the number and location of MTP plates, IR plates and pipette tips. This technique has been successfully integrated into the robotic system forming a fully automated robot.

The proposed system was validated by the preparation of filamentous fungi but might also be applicable to other types of microorganisms, such as yeasts, bacteria, and algae. Also, the developed system was used for the preparation of samples for FTIR spectroscopy, but might also be useful for MALDI-TOF spectrometry with a different working sequence.

II. SYSTEM DEVELOPMENT

A. SYSTEM OVERVIEW

To enable the robot to perform different tasks independently, such as sample homogenization, sample spotting, washing and concentration, we used the concept of modular design for the system development. As shown in Fig. 1, the developed platform is an integration of three modules, namely ultrasonication robot module, centrifuge module and liquid handling module. Each module is able to be operated independently and they can also form a complete system for the full process preparation of fungal samples for FTIR spectroscopy. The machine vision system enables the full automation of the robot without any manually pre-input information. Specifically, the camera on the liquid handling module uses deep learning to identify the labware information, for

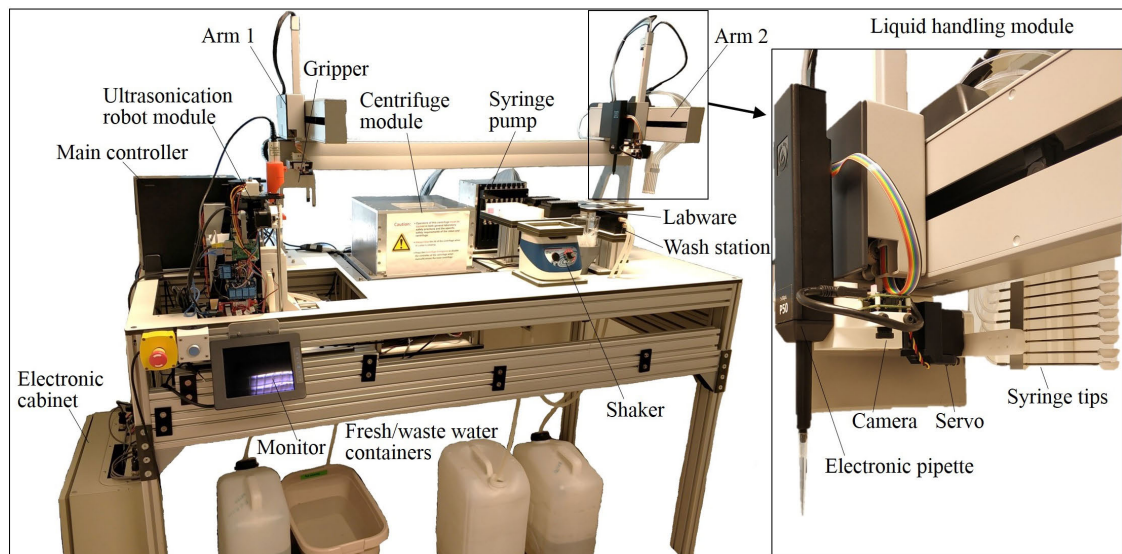


FIGURE 1. Hardware assembly of the FTIR sample preparation robot.

example detecting the number and positions of well plates and pipette tips. The machine vision system on the ultrasonication robot module can distinguish between the sample wells and black wells and also monitor the homogenization process of each well, thus ensuring that the robot can provide the desired homogeneous samples [9]. The left arm (Arm 1) of the Cartesian-type dual robotic arm system (Cavro Omni Robot; TECAN, Switzerland) connects all of the hardware modules. The gripper attached to the Arm 1 picks and places the 96-well MTP plates (CR1496; EnzyScreen, Netherlands) between the three modules.

B. ULTRASONICATION ROBOT MODULE

Ultrasonication robot module is used to homogenize filamentous fungal mycelia to get homogeneous cell suspension for sample spotting on 384-well IR plates (Bruker Optik GmbH, Germany). In the previous work, we introduced an ultrasonication robot that can provide desired homogeneity of filamentous fungal cell suspension [9]. The robot uses machine vision to screen sample wells and measure the level of fungi homogeneity. In this work, as shown in Fig. 1 and Fig. 7, the ultrasonication robot module was integrated into the sample preparation system for FTIR spectroscopy without hardware modifications. In order to integrate with the other modules, the controller of the ultrasonication robot module (Raspberry Pi 3) was installed with an open-source system Ubuntu MATE to run the software under the Robot Operating System (ROS) architecture. A new ROS node in the Pi controller communicates with the main controller via Ethernet network to call the previously developed functions. In the meanwhile, this node also listens to the buttons on the user interface of the ultrasonication robot so that the robot module

can still work independently. The ultrasonication robot module is able to detect the sample well locations [9], so after each homogenization, the robot sends the sample well locations to the main controller for sample spotting.

C. CENTRIFUGE MODULE

Fig. 2 shows the design of the centrifuge module. The module is 400 mm long, 400 mm wide and 390 mm high. The centrifuge was constructed from 6 aluminum panels to which other components were mounted. The centrifuge mainly consists of 6 panels, a servo motor to drive a rotor that was mounted with 2 MTP plate holders and a sliding door mechanism. The centrifuge rotor is driven by an 800 W servo motor (PR-802.8; Servotronics, Israel) with a maximum speed of 5000 rpm. The servo motor is controlled by a servo drive (CDHD; Servotronics, Israel), which communicates to the main controller based on CANopen motion control protocol via a CANbus to USB converter (PCAN-USB; Peak-system, Germany). The sliding door mechanism comprises a sliding door that was attached to a linear motion rail and driven by a DC motor, a sliding door locker and 2 limit switches. The sliding door was designed to open or close when the robot manipulator picks and places the MTP plates. The sliding door stops at fixed positions in “open” or “closed” configurations using the two limit switches. For safety and health reasons, the sliding locker will automatically lock the sliding door in the closed configuration when centrifugation is in operation. The DC motor is controlled by an additional microcontroller, which will be described in Section III. The designed centrifuge module has a capacity for centrifugation for two MTP plates. It is specifically designed to be integrated

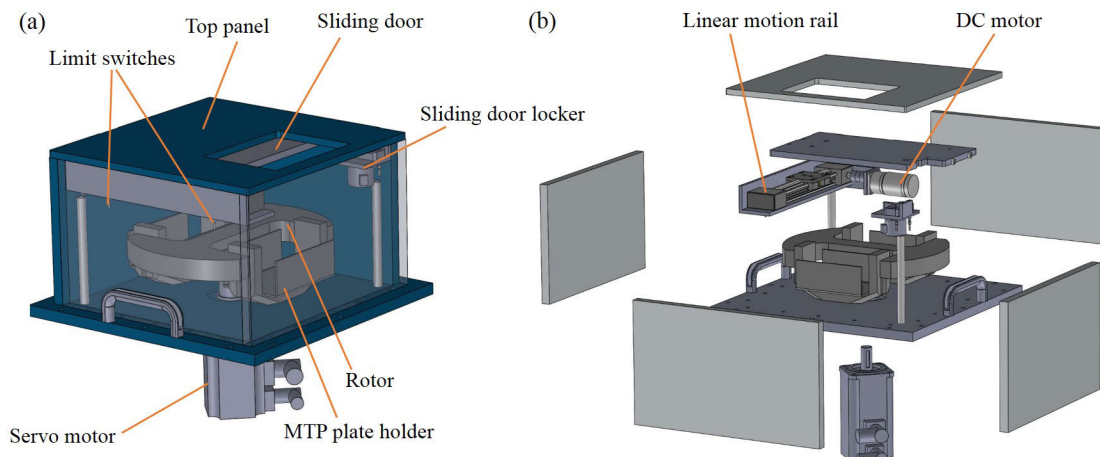


FIGURE 2. The 3D model of the centrifuge module (a) and its exploded view which shows the internal components and structure (b).

into the robotic platform and uses a CANbus communication interface to allow the robot control the rotor.

D. LIQUID HANDLING MODULE

As shown in Fig. 1, the liquid handling module comprises the right arm (Arm 2) of the dual-arm system, an 8-channel syringe pump (Cavro XMP 6000; TECAN, Switzerland), an electronic pipette (P50; Opentrons, USA), an RGB camera (See3CAM_CU135; e-co systems, USA), a custom-made wash station and a well plate shaker (MicroPlate Genie; Scientific Industries, USA). The main function of the liquid handling module is to provide sample washing, concentration and spotting, in which the sample washing and concentration procedures involve centrifuge module.

Sample washing and concentration require aspiration and dispensing of high volume liquid (we use $800\ \mu\text{L}$) with relative low accuracy, whereas sample spotting on IR plates needs to take a small volume ($10\ \mu\text{L}$) on each spot with high accuracy. Based on our test, the syringe pump did not meet the requirements of sample spotting in terms of accuracy. Therefore, we used the syringe pump (maximum volume $800\ \mu\text{L}$ for each channel) for sample washing and concentration, and the electronic pipette (maximum volume $50\ \mu\text{L}$) for sample spotting. Both the syringe tips and the pipette were mounted on Arm 2. To enable them to work without collisions, a servo (HS-5645MG; Hitec, South Korea) was used to rotate the syringe tips to either vertical or horizontal to the ground. When used for sample washing and concentration, the syringe tips are vertical to the ground, while for spotting, the syringe tips move to the horizontal position to give the space for the pipette.

1) SAMPLE WASHING AND CONCENTRATION

Sample washing includes centrifugation, liquid aspiration and dispensing. After centrifugation, the fungal mycelia

formed one or more pellets at the bottom of the wells of the MTP plate, and the syringe tips aspirated the supernatant above the mycelia ($800\ \mu\text{L}$). Thereafter, the wells were filled with the same amount of deionized water as the aspirated supernatant. The wash station consists of two sinks, one for wastewater and the other one for fresh water, connecting to a peristaltic pump (WPL 810; Williamson, UK) and a wastewater container, respectively. Sample concentration was performed after ultrasonication to increase the concentration of homogenized samples for spotting, which contains centrifugation and liquid aspiration. In our case, ultrasonication requires at least $800\ \mu\text{L}$ of liquid for the selected well plate, whereas the FTIR spectroscopy needs enough density of samples for measurement. Therefore, we used the centrifuge to separate fungal mycelia (pellets) and supernatant at first and then removed some above supernatant ($600\ \mu\text{L}$) to increase the sample concentration.

During the aspiration in the sample washing stage, the syringe tips were easily blocked by the fungal mycelia in the previous system [14]. To solve this problem, we designed a filter attached to the end of the syringe tip, which can prevent the fungal mycelia from entering the syringe tips. As shown in Fig. 3, the filter has a 90-degree surface that can be inserted into the square well. The smooth, spherical outer surface pushes the fungal mycelia to the outer space. During aspiration, the sample liquid passes through the grooves on the edge of the filter to the sonicator probe. To avoid blockage on the filter, the filtering grooves were placed on the edge instead of having holes inside of the filter. The filter was 3D printed using polylactic acid (PLA) filaments (MP05780; MakerBot, USA) and glued to the sonicator probe.

2) SAMPLE SPOTTING

Sample spotting was conducted after the sample concentration, which is the final step for FTIR sample preparation.

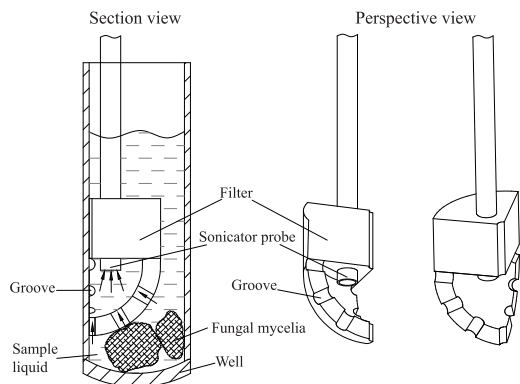


FIGURE 3. Schematic of the new-designed filter.

As shown in Fig. 5e,f, we define the droplet on the IR plate as spot. The main task of spotting is to dispense homogenized cell suspension on the black wells of IR plates, in which the system should guarantee that the sizes and locations of the dispensed spots are close to the well limit circle on the IR plates. Fig. 5a shows the labware and the liquid handling module. As shown in Fig. 4, after concentration, the robot first picks up the MTP plate to the shaker to decrease sediments (Fig. 5b). Thereafter, the system received the tip locations and sample well locations from the vision system droplet and the ultrasonication robot module, respectively. This procedure is an integration of the vision system, ultrasonication robot module and the liquid handling module, which can ensure that the system only picks up or processes the locations with tips or wells with samples and skips blank tip location or wells. After that, Arm 2 changed to spotting mode, which means the servo rotated the syringe tips to horizontal place and gave the space for pipette to pick up the tips (Fig. 5c).

Before spotting on the IR plate, the system first aspirated $10\ \mu\text{L}$ sample liquid at the bottom of the well and dispensed it to the wastewater sink of the wash station (Fig. 5d). This is because that the bottom of the well may contain some undisturbed pieces of fungal mycelia that may result in blockage and failure spotting. Next, the pipette aspirated $30\ \mu\text{L}$ cell suspension and dispensed $10\ \mu\text{L}$ on each IR plate well in the form of three spots - three technical replicates (Fig. 5e). To avoid the droplets mixing together, the robot skipped a well between every two droplets. To protect the IR plate, non-contact dispensing method was utilized, so the pipette dispensed liquid with a short distance above the IR plate. Once the size of the droplet was big enough, the droplet dropped on the IR plate. During spotting, the pipette had a circular motion inside of the well limit circle (Fig. 5f). The circular motion can provide homogeneous distribution of the sample on the spot of the IR plate. In addition, the circular motion increases the spot coverage rate on the target well. Due to the positional error, the pipette tip is unable to position

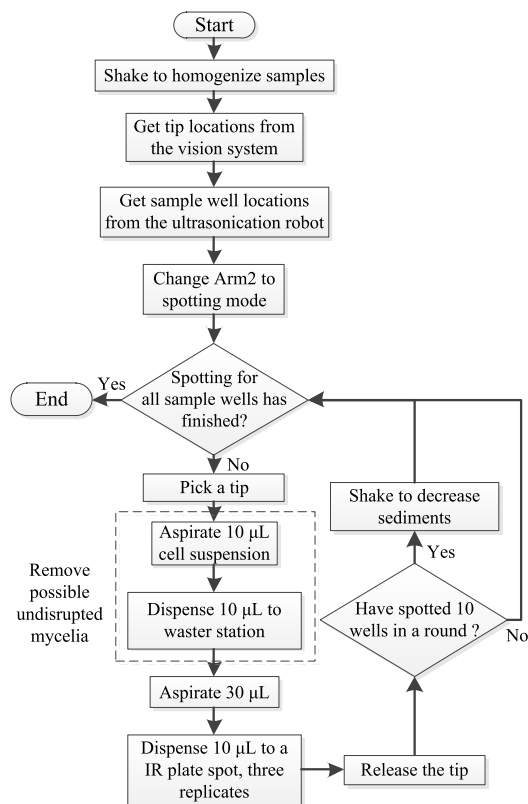


FIGURE 4. Workflow of sample spotting.

at the center of the target well every time. There may be some blank regions between the initial spot and the well limit circle. While the well limit circle can prevent the droplet from spreading outside of the well area to some extent, the circular motion of the tip can increase the coverage area of the droplet on the blank regions obtaining the final spot. For spotting of every 10 wells, the robot picks up the MTP plate to the shaker to decrease the sediments.

E. VISION SYSTEM - AUTOMATIC DETECTION OF LABWARE USING DEEP LEARNING

Traditional laboratory robots highly rely on manual input for labware information, for example, inputting the well plate number and locations, tip number and locations. This limits the full automation of laboratory robots. The main challenge is that when using traditional image processing techniques, it is hard to segment and identify the labware, especially for the transparent and small objects, such as the pipette tips. We introduce to use a convolutional neural network (CNN) model namely YOLOv3 [18] for the identification of labware based on the online images captured by the camera on Arm 2. The labware in the robot system includes the

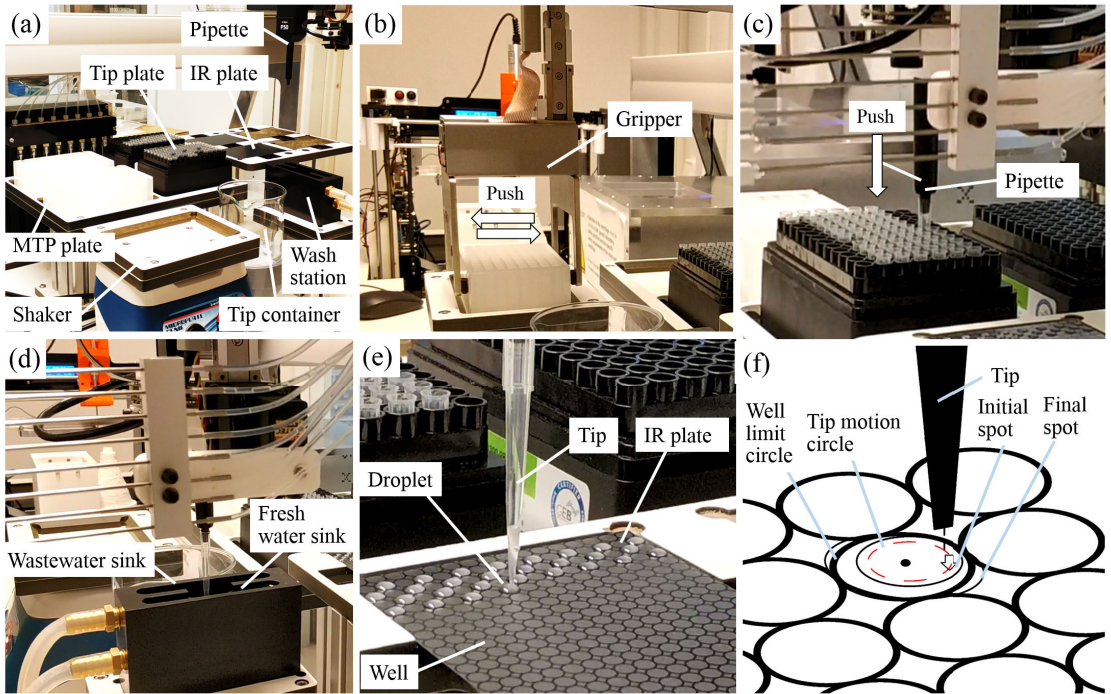


FIGURE 5. The process of sample spotting on IR plates: (a) labware and the liquid handling module; (b) the gripper is picking up a MTP plate to the shaker; (c) the pipette is picking up a new tip from the tip plate; (d) the pipette is removing the possible fungal mycelium chunk from the sample well to the wash station; (e) the spotting action; (f) schematic of the spotting motion.

96-well MTP plates, 384-well IR plates and pipette tips. Therefore, the first training attempt was to use these labware as three object classes. We collected a 261 image dataset using the camera on the robot with different angles of views. The dataset contains 287 MTP plates, 255 IR plates and 672 tips. The images were annotated using Lableme software [19]. The training took 43 hours using GTX 1070 GPU and i7-8750 CPU.

The first model showed good performance on the detection of MTP plates and IR plates. However, as shown in Fig. 6a, many blank tip positions were recognized as tips. One possible reason is that the blanks have white circles under the light that looks similar to the tips. Therefore, we trained a second model that included the blank as the fourth class. The new training dataset contains 177 blanks and 783 tips whereas the dataset of MTP plates and IR plates remains the same.

Fig. 6b,c and d show the detection results of the final model. It can be seen that the blanks were successfully classified. The other three classes have very high confidence rate, over 90% for most of the cases.

To apply the deep learning technique into the robotic system, we used the Darknet ROS package [20] to run the model in real time using the camera on the liquid handling

module. In the network, the confidence threshold was set to 0.5 and the resolution of network's input image was 416 times 416. The output of the package is the detected object bounding boxes with class IDs whose confidences exceed the threshold. During the identification procedure, the Arm 2 moved the camera to four different positions that cover IR plates, tip plates and MTP plates, respectively, as the views are shown in Fig. 6. The object positions in the camera view were fixed each time. To detect whether the object is existing or not, we used Intersection over Union (IoU) to compare the detected bounding boxes (B_{de}) to the ground truth bounding boxes (B_{gt}) under the condition that the class ID is the same. The ground truth bounding boxes were labelled manually. Only the object with an IoU higher than 0.5 was considered to be existing. In summary, three criteria to determine an object existing can be expressed as follow:

$$\begin{cases} \text{Confidence} > 0.5 \\ ID_{de} = ID_{gt} \\ IoU > 0.5, \quad IoU = (B_{de} \cap B_{gt}) / (B_{de} \cup B_{gt}) \end{cases} \quad (1)$$

where, ID_{de} represents the detected class ID of the object whereas ID_{gt} means the ground truth class ID.

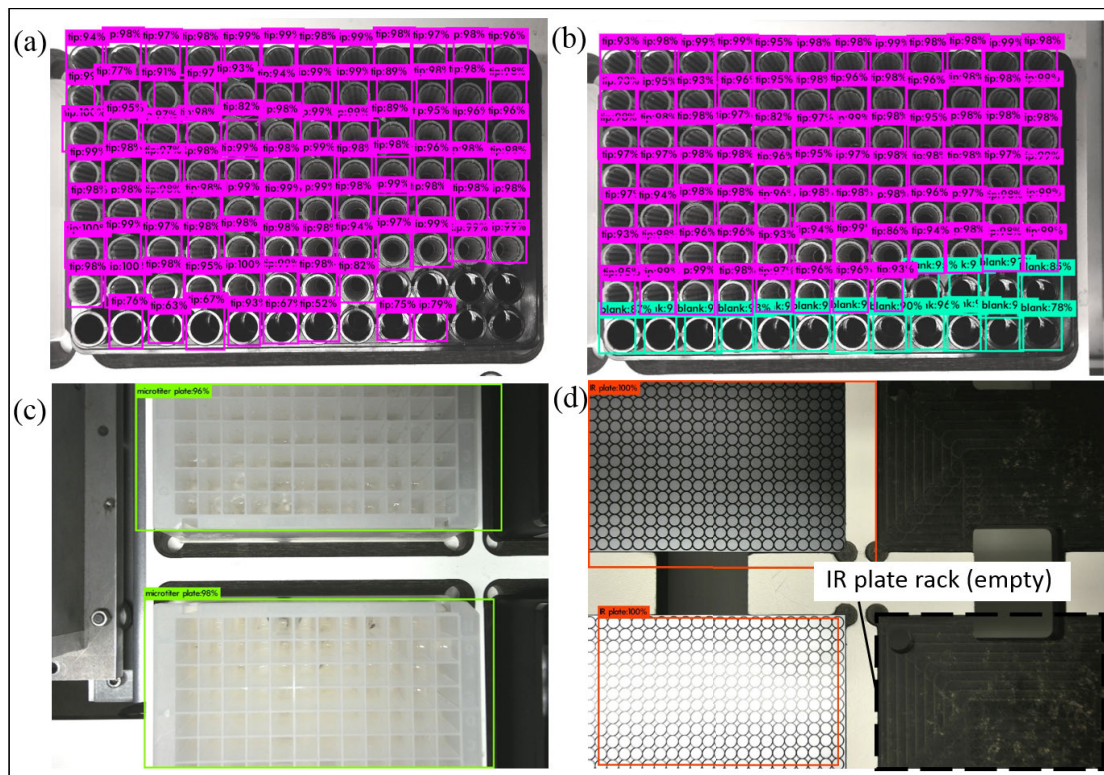


FIGURE 6. Detection results of labware using YOLOv3 CNN model: (a) tip detection results using the first model; (b) tip detection results using the final model, in which the blank position is included as a class; (c) detection results of MTP plates; (d) detection results of IR plates.

III. SYSTEM INTEGRATION AND CONTROL

A. HARDWARE AND SOFTWARE INTEGRATION

Fig. 7 shows the hardware and software architecture of the whole system, in which the outside hexagons represent the hardware components while the inside rectangles are the software functions. All of the hardware modules and components are connected via ROS. The master node is used to coordinate and control all the other sub-functions with a correct sequence. Except for the communication node of the ultrasonication robot module, all other hardware control or servo nodes run in the main controller (blue dashed box). The communication node of the ultrasonication robot receives commands from the master node to start ultrasonication and returns the sample well locations once the homogenization is finished.

The labware identification node listens to the master node to capture images when Arm 2 arrives at the target position and outputs the bounding boxes together with class IDs of the detected objects. The master node determines the existing labware using IoU calculation. The dual-arm system has a controller to control the arm motion and gripper status, which can be accessed via TCP/IP based on its built-in protocol.

We developed a dual-arm server node running in the main controller that is able to decode and encode the position, speed and gripper operation commands and communicate to the dual-arm system. Furthermore, the server node also can output the arm and gripper status as ROS topics in 30 Hz. This includes the arm speed, position, gripper status and the completion of commands. Once a failure happens, for example, an object dropping from the gripper, the master node stops any further operations immediately. Similar to the dual-arm system, a syringe server node was developed to decode and encode the commands of syringe zeroing, aspiration and dispensing. The syringe pump controller communicates to the main controller via RS-232 serial bus.

Most of the actuators in the liquid handling module are controlled by an Arduino microcontroller (Mega 2560; Arduino.cc, Italy) running with ROS. The Arduino uses the serial bus to connect to a *rosserial* node for communication with other ROS nodes. A motor shield (v2.3; Adafruit, USA), mounted to the Arduino, is used to control the stepper motor of the pipette and also the servo motor. Also, a 4-way relay module (SainSmart, USA) connects to the Arduino controller to control the on/off or open/close operations of the

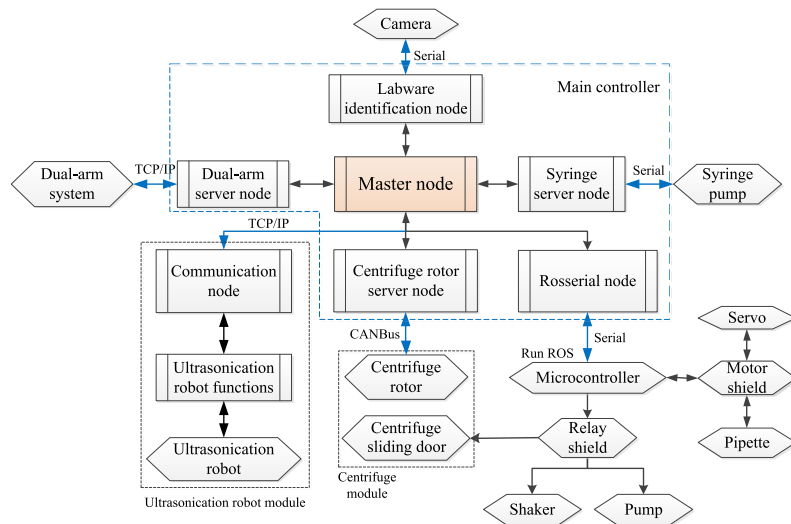


FIGURE 7. Hardware and software architecture of the FTIR sample preparation robot: The hexagons represent the hardware components, while the rectangles are the software functions.

shaker, pump and centrifuge sliding door, respectively. The servo motor drive of the centrifuge rotor controls the motor and communicates to the main controller according to the CANopen protocol. To control it in the high level, we developed a centrifuge rotor server node to encode and decode the commands and motor status, which is similar to dual-arm system. The input commands to the server node are the target position, speed, stop/run, block/unblock and zeroing whereas the output feedback includes the motor position, speed and completion of commands.

B. WORKING SEQUENCE

The working sequence was planned according to the manual operation protocol of preparing fungal samples for FTIR spectroscopy [7]. As the system has a modular design, users can choose to run either the specific functions or the whole process. As shown in Fig. 8, the whole process ④ implements all the procedures starting from system initialization and calibration. The labware identification loads labware settings and determines to use one-MTP mode or two-MTP mode. Two-MTP mode means the system processes two MTP plates of samples simultaneously, which can reduce the operation time. If no pipette tips or MTP plates or IR plates are detected, the system would not run any further procedures and display a warning. Once the labware is sufficient for experiments, the system washes the samples three times using the centrifuge and the syringe pump. After washing, the MTP plate is moved to the ultrasonication robot module for sample homogenization. In this stage, if two-MTP mode is selected, the system would use the liquid handling module to wash one MTP plate of samples and the ultrasonication robot module to homogenize the samples in the other MTP plate simultaneously. The ultrasonication takes more time compared

to other stages. Thereafter, we used a concentration step to increase the density of the homogenized cell suspension for the better quality of FTIR spectra. The concentration stage includes centrifugation, aspiration of upper supernatant, re-ultrasonication and shaking to reduce sediments appearance. The whole process is ended with sample spotting, where the system would implement spotting for one MTP plate and ultrasonication for the other MTP plate if it is in a two-MTP mode.

When running specific functions, the system selects to implement some procedures accordingly. For instance, when spotting ② is commanded, the system would skip MTP plate selection, sample washing, ultrasonication and concentration. While for sample washing and ultrasonication function ③, the system executes all the procedures excluding concentration and spotting.

C. A FEW PUSHING ACTIONS

In the development of the system, we used a few pushing actions to make the system more robust. For example, in Fig. 5b, the gripper is taking a MTP plate to the plate holder of the shaker. The plate might not fit to the plate due to the positional error of the arm. This may result in a serious failure especially for spotting where a fixed position of well is used for aspiration. To solve this, we used the gripper inner fingers to push the MTP plate from side to side during placing. Based on our observations, this small technique can significantly improve the placing performance. We also used the gripper to push the MTP plate to the plate holder of the ultrasonication robot module to make it fit well (Fig. 9a). In this case, the gripper fingers are in closed status and push the MTP plate down to the plate holder using the finger tips. In addition, the pipette uses pushing actions to pick up a tip

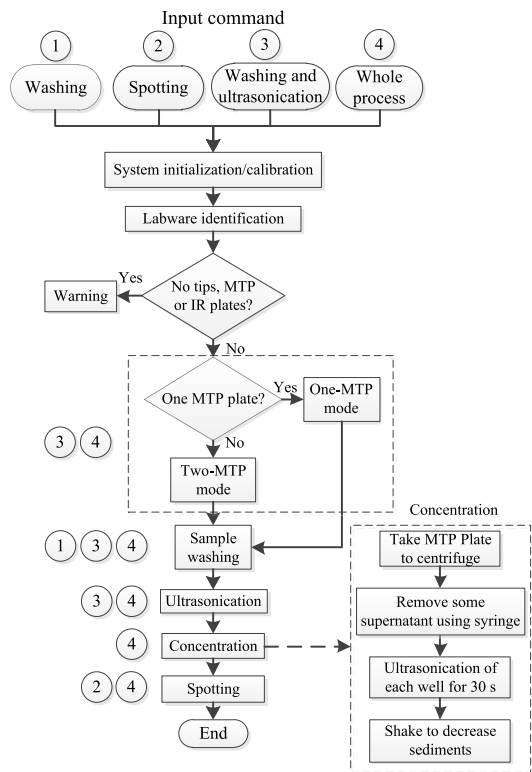


FIGURE 8. Whole system working sequence: The function is implemented according to the input command.

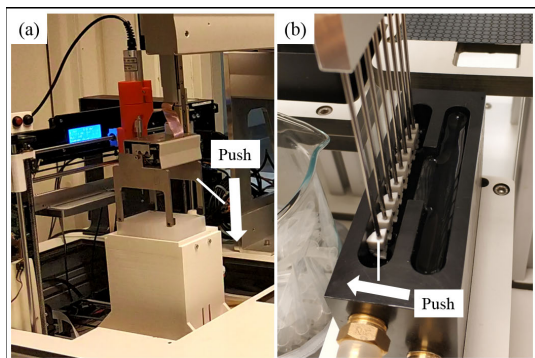


FIGURE 9. A few pushing actions to make the system robust.

(Fig. 5c) and the syringe tips push to the wall of the wash station to remove droplets when moving up (Fig. 9b).

IV. EXPERIMENTAL RESULTS AND DISCUSSIONS
A. PERFORMANCE OF LABWARE IDENTIFICATION

We used a test image dataset that contains 70 MTP plates, 60 IR plates, 270 tips and 82 blanks to evaluate the performance of the labware identification method. The objects

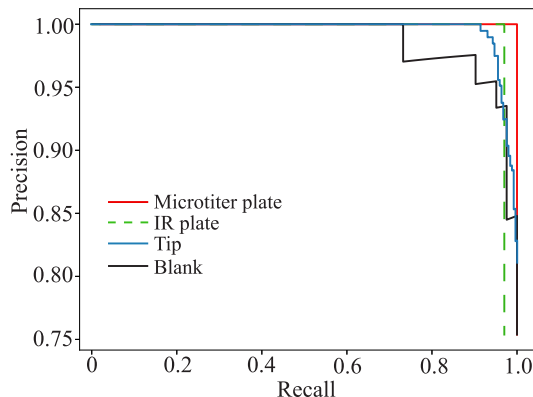


FIGURE 10. Precision-recall curves for the performance evaluation of the labware identification.

TABLE 1. Average precision of the labware identification method.

Class name	MTP plate	IR plate	Tip	Blank
Average Precision	1.0	0.97	0.98	0.93

in the images were manually labelled with bounding boxes and class IDs. Similar to Xiong *et al.* [21], the correct and incorrect detection were defined as True Positive (*TP*) and False Positive (*FP*), respectively. Undetected objects were marked as False Negative (*FN*). Then, precision is defined as *TP* over the sum of *TP* and *FP*, while recall is *TP* over the sum of *TP* and *FN*.

By varying confidence threshold, the precision-recall curves of the four classes are obtained and shown in Fig. 10. The IoU threshold for the evaluation is the same to the real application (Eq. 1, 0.5). All the four classes show both high precision and recall. High precision and recall represent that most of the objects have been detected and most of the detection results are correct. Further, the average precision of the detection is shown in Table 1, where the average precision is the area under the precision-recall curve. The detection of MTP plates, IR plates and tips show close-to-perfect results, while the average precision of blank is slightly lower, which may be relevant to the relative smaller training dataset. Overall, the labware identification system using deep learning shows significant high performance and has been successfully integrated into the robotic system. The reason of the high performance might be due to the fact that the identification environment is relatively simple and unchanged.

B. SAMPLE SPOTTING ACCURACY

To evaluate the performance of the whole system, we conducted a test of the entire process for both one MTP plate and two MTP plates of fungal samples. The fungal samples are filamentous fungi - namely, *Mucor circinelloides* VI 04473 (Norwegian School of Veterinary Science, Norway) using the same cultivation method as it was described in the

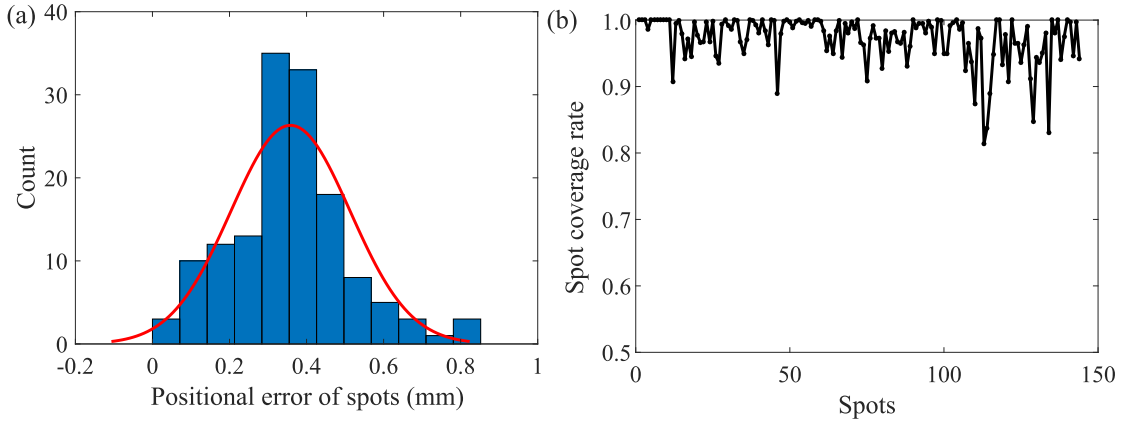


FIGURE 11. Spotting accuracy: (a) positional error distribution of spots; (b) spot coverage rates.

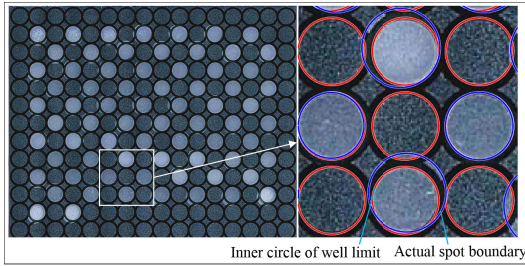


FIGURE 12. Final IR plates with sample spots and spotting accuracy measurement method.

previous work [9]. There were 24 wells of samples for each MTP plate, so it created 72 spots on the IR plates. After spotting, the IR plates were dried and scanned to measure the spotting accuracy. Fig. 12 shows the scanned picture of the IR plates and the accuracy measurement method. Generally, the dried samples of fungi on the spots are homogeneous and the spots are located in the center of the well limit circles on the IR plates. As it can be seen in the right enlarged picture, we manually labelled the inner circle of the well limits as red circles (ground truth) and the actual spot boundaries as blue circles. The distance between the centroid of the blue circle and the centroid of the nearest red circle relates to the positional error of the pipette tip. To find the nearest red circle, each blue circle was compared to all the red circles and the minimum distance value returns the nearest circle. The measurement results of two IR plates are shown in Fig. 11a. It can be seen that the positional error test revealed a near normal distribution, indicating that the results seem reliable. Most of the positional errors are located between 0.3 to 0.5 mm, with a mean of 0.36 mm and a 0.15 mm standard deviation. The positional error is mainly caused by the picking up of the pipette tips, because the orientation of the tips remains uncertainty when pushed into the pipette.

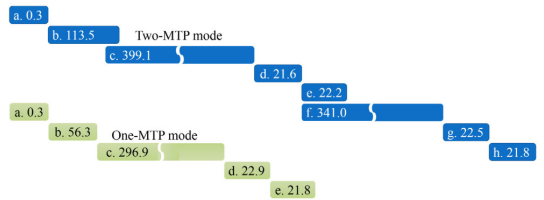


FIGURE 13. Processing time for both one-MTP and two-MTP modes (unit: minute): The first letter in the blocks represents procedures: a - labware identification, b - sample washing of two MTP plates for two MTP mode, one MTP plate for one-MTP mode, c - ultrasonication of MTP 1, d - concentration of MTP 1, e - spotting of MTP 1, f - ultrasonication of MTP 2, g - concentration of MTP 2, h - spotting of MTP 2; the number is the processing time.

Another important factor is the coverage rate of the spot. The FTIR analysis requires that the sample spot covers the well limit circle as much as possible. As mentioned above, to avoid spots mixing together, the size of the droplets should not be too large. The coverage rate can be defined as:

$$Coverage = S_{red} \cap S_{blue} / S_{red} \quad (2)$$

where, the equation means that the coverage is the overlap area between the blue circle (S_{blue}) the nearest red circle (S_{red}) over the red circle (S_{red}). The coverage rates of two IR plates are shown in Fig. 11b, which indicates that most of the coverage rates are around 0.97 (mean) with minimum value at 0.81. Our practical experience on the coverage rate suggests a minimum value of 0.8, which means that the system can provide desired samples spots for FTIR analysis.

C. SYSTEM OPERATION TIME

We also recorded the execution time of each procedure for the two tests (one MTP plate and two MTP plates). The working sequence together with the processing time is displayed in Fig. 13. For two MTP plates (blue blocks), the whole

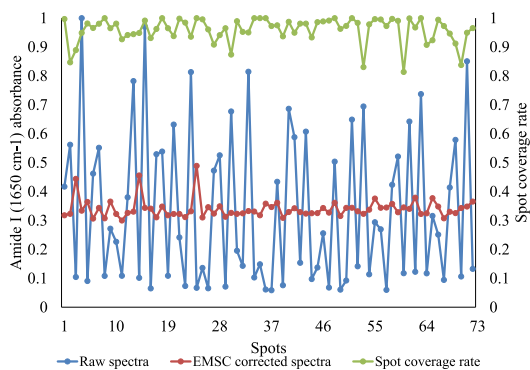


FIGURE 14. Amide I (using wavenumber of 1650 cm^{-1}) absorbance in FTIR spectra with comparison of spot coverage rate.

processing time was 942 minutes, during which ultrasonication (c and f) took up most of the time (78.6%) followed by washing of the two MTP plates (12%). In two-MTP mode, the final stage of sample washing (b) and ultrasonication of MTP plate 1 (c) have been processed simultaneously. The overlap happened at aspiration and dispensing of MTP plate 2 of the sample washing. Due to the vibration of the centrifuge module, the robot cannot perform other operations during centrifugation in the washing procedure. The other overlap is spotting of MTP plate 1 (e) and ultrasonication of MTP plate 2 (f), wherein the entire process of e can be operated simultaneously with f. The robot saved a total of 32.5 minutes in two-MTP mode. For one-MTP mode (green blocks), all the five procedures were processed one after another without overlapping. It must be mentioned that the ultrasonication time for each MTP plate is different. This is due to the variation of fungal biomass in each well that results in the difference of homogenization time. The ultrasonication robot homogenizes the entire MTP plate of samples until the desired homogeneity of samples are obtained [9].

D. ANALYSIS OF FTIR

We finally performed a FTIR measurement on one of the IR plates of samples using a high-throughput screening spectrometer (HTS-XT; Bruker Optik GmbH, Germany). We extracted the Amide I (using wavenumber of 1650 cm^{-1}) absorbance data from the spectra. According to the OPUS Quality Test (OPUS QT) - a standard quality test for FTIR spectra, the absorbance at Amide I band should be in a range 0.3 - 1.2. As shown in Fig. 14, 46% of the absorbance in the raw spectra (blue line) is below 0.3. By using the Extended Multiplicative Signal Correction (EMSC) method [22], we can correct the differences in absorbance and obtained the red line. With comparison to the spot coverage rate (green line), we did not find the spot coverage rate has significant influence on the absorbance. The main reason for the differences is that the absorbance at Amide I is highly related to the concentration of the sample spotted on the IR plate.

The results indicate that all the obtained spots on the IR plate could be used for FTIR analysis, but for the future work the droplet concentration should be controlled more precisely to provide higher quality of spectra.

V. CONCLUSION

In this paper, we show the design and development of a laboratory robot that fully automates the preparation of fungal samples for FTIR spectroscopy. We extended the previously-developed ultrasonication robot module to the new system by adding a newly-designed centrifuge module, a newly-developed liquid handling module and additional electronics. The liquid handling module uses a high accuracy electric pipette for spotting and a low accuracy syringe pump for sample washing and concentration. A camera on the liquid handling module uses deep learning to identify the labware settings, which includes the number and positions of the well plates and pipette tips. We also present the development of the software under ROS architecture in low level for controlling each components and in high level for integration of all modules. The software was modular designed, so the robot is capable of performing each procedure of the operation independently, such as sample washing and spotting. The robot is able to process up to two 96-well MTP plates of samples simultaneously. Vision system evaluation indicates that labware identification using deep learning can achieve high average precision due to the simple environment. Tests of all procedures show that the obtained sample spots have high positional accuracy (mean 0.36 mm) and can cover most of the desired region (mean 97%). In addition, the FTIR measurement indicates all the obtained spots of one IR plate could be used for FTIR analysis, but future work is required to control the concentration of the droplets to provide higher quality of spectra.

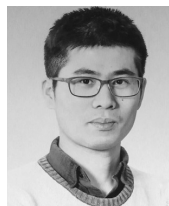
ACKNOWLEDGMENT

The authors thank Mr. Mikkel Danielsen for his help in the development of mechatronics.

REFERENCES

- [1] M. Fakrudin, S. B. Mannan, R. M. Mazumdar, A. Chowdhury, and N. M. Hossain, "Identification and characterization of microorganisms: DNA-fingerprinting methods," *Songklanakarinn J. Sci. Technol.*, vol. 35, no. 4, pp. 397-404, 2013.
- [2] A. Pickar-Oliver and C. A. Gersbach, "The next generation of CRISPR-Cas technologies and applications," *Nature Rev. Mol. Cell Biol.*, vol. 20, pp. 490-507, May 2019.
- [3] D. Meldrum, "Automation for genomics, part one: Preparation for sequencing," *Genome Res.*, vol. 10, no. 8, pp. 1081-1092, 2000.
- [4] S. C. Clarke, "Nucleotide sequence-based typing of bacteria and the impact of automation," *Bioessays*, vol. 24, no. 9, pp. 858-862, 2002.
- [5] S. C. Clarke and M. A. Diggle, "Automated PCR/sequence template purification," *Mol. Biotechnol.*, vol. 21, no. 3, pp. 221-224, 2002.
- [6] C. B. Sullivan, J. M. C. Jefferies, M. A. Diggle, and S. C. Clarke, "Automation of MLST using third-generation liquid-handling technology," *Mol. Biotechnol.*, vol. 32, no. 3, pp. 219-225, Mar. 2006.
- [7] V. Shapaval, J. Schmitt, T. Møretør, H. P. Suso, I. Skaar, A. W. Åsli, D. Lillehaug, and A. Kohler, "Characterization of food spoilage fungi by FTIR spectroscopy," *J. Appl. Microbiol.*, vol. 114, no. 3, pp. 788-796, 2013.

- [8] A. L. Bryson, E. M. Hill, and C. D. Doern, "Matrix-assisted laser desorption/ionization time-of-flight: The revolution in progress," *Clinics Lab. Med.*, vol. 39, no. 3, pp. 391–404, 2019.
- [9] Y. Xiong, V. Shapaval, A. Kohler, and P. J. From, "A laboratory-built fully automated ultrasonication robot for filamentous fungi homogenization," *SLAS Technol., Translating Life Sci. Innov.*, vol. 30, pp. 1–13, Jul. 2019.
- [10] E. Kwee, E. E. Herderick, T. Adams, J. Dunn, R. Germanowski, F. Krakosh, C. Boehm, J. Monnich, K. Powell, and G. Muschler, "Integrated colony imaging, analysis, and selection device for regenerative medicine," *SLAS Technol., Translating Life Sci. Innov.*, vol. 22, no. 2, pp. 217–223, 2017.
- [11] M. A. R. Meier, R. Hoogenboom, M. W. M. Fijten, M. Schneider, and U. S. Schubert, "Automated MALDI-TOF-MS sample preparation in combinatorial polymer research," *J. Combinat. Chem.*, vol. 5, no. 4, pp. 369–374, 2003.
- [12] F. Nejatimohammadi, A. Faina, and K. Stoy, "New capabilities of EvoBot: A modular, open-source liquid-handling robot," *SLAS Technol., Translating Life Sci. Innov.*, vol. 22, no. 5, pp. 500–506, 2017.
- [13] V. Cherezov, A. Peddi, L. Muthusubramanian, Y. F. Zheng, and M. Caffrey, "A robotic system for crystallizing membrane and soluble proteins in lipidic mesophases," *Acta Crystallographica D, Biol. Crystallogr.*, vol. D60, no. 10, pp. 1795–1807, 2004.
- [14] J. Li, V. Shapaval, A. Kohler, R. Talintyre, J. Schmitt, R. Stone, A. J. Gallant, and D. A. Zeze, "A modular liquid sample handling robot for high-throughput Fourier transform infrared spectroscopy," in *Advances in Reconfigurable Mechanisms and Robots II*. Cham, Switzerland: Springer, 2016, pp. 769–778.
- [15] W. Liu, M. Zhang, Z. Luo, and Y. Cai, "An ensemble deep learning method for vehicle type classification on visual traffic surveillance sensors," *IEEE Access*, vol. 5, pp. 24417–24425, 2017.
- [16] S. Bargoti and J. P. Underwood, "Image segmentation for fruit detection and yield estimation in apple orchards," *J. Field Robot.*, vol. 34, no. 6, pp. 1039–1060, 2017.
- [17] A. D. da Silva, G. Bitencourt-Ferreira, and W. F. de Azevedo, "Taba: A tool to analyze the binding affinity," *J. Comput. Chem.*, to be published.
- [18] J. Redmon, S. Divvala, R. Girshick, and A. Farhadi, "You only look once: Unified, real-time object detection," in *Proc. IEEE Conf. Comput. Vis. Pattern Recognit.*, Jun. 2016, pp. 779–788.
- [19] K. Wada. (2016). *Labelme: Image Polygonal Annotation with Python*. [Online]. Available: <https://github.com/wkentaro/labelme>.
- [20] J. Redmon. (2016). *Darknet: Open Source Neural Networks in C*. [Online]. Available: <http://pjreddie.com/darknet/>
- [21] Y. Xiong, C. Peng, L. Grimstad, P. J. From, and V. Isler, "Development and field evaluation of a strawberry harvesting robot with a cable-driven gripper," *Comput. Electron. Agricult.*, vol. 157, pp. 392–402, Feb. 2019.
- [22] A. Kohler, C. Kirschner, A. Oust, and H. Martens, "Extended multiplicative signal correction as a tool for separation and characterization of physical and chemical information in Fourier transform infrared microscopy images of cryo-sections of beef loin," *Appl. Spectrosc.*, vol. 59, no. 6, pp. 707–716, 2005.



YA XIONG received the B.Sc. and M.Sc. degrees in vehicle/mechanical engineering from China Agricultural University, Beijing, in 2016, and the M.Sc. degree in mechatronic engineering from Harper Adams University, U.K., in 2016. He is currently pursuing the Ph.D. degree with the Agricultural Robotics and Laboratory Automation, Norwegian University of Life Sciences. He was a Visiting Ph.D. Student with the University of Minnesota from 2017.5–2017.8. His research interests include agricultural robotics and laboratory automation, especially on manipulator design and its control.



VOLHA SHAPAVAL received the two M.S. degrees in microbiology from BSU, Minsk, Belarus, the M.S. degree in biotechnology from Lund University, Lund, Sweden, and the Ph.D. degree in biospectroscopy from the Norwegian University of Life Sciences (NMBU), where she is currently an Associate Professor in bioprocess technology with the Faculty of Science and Technology. She has a multidisciplinary background in microbial biotechnology, biospectroscopy, and bioprocess development. Her current research interests include bioprocess development by applying vibrational spectroscopy techniques and characterization, screening, and the differentiation of microorganisms by vibrational spectroscopy.



ACHIM KOHLER is currently a Professor in physics with the Faculty of Science and Technology, Norwegian University of Life Sciences (NMBU). He has a background in data analysis and physics. He has 20 years of experience in data modeling and measurement technology within vibrational spectroscopy. He is also leading the BioSpec Group, RealTek. The BioSpec group is a multidisciplinary group doing research in the field of vibrational spectroscopy of biological materials. The group has been doing work in the understanding and modeling of scattering and absorption of infrared spectroscopy of biological materials. The group is further one of the world-leading groups in the multivariate analysis of vibrational spectroscopic data.



JICHUN LI received the B.S. and M.S. degrees in mechatronic engineering from the China University of Geosciences, Wuhan, in 2000 and 2003, respectively, and the Ph.D. degree in mechanical engineering from Kings College London, University of London, U.K., in 2013. He is currently a Lecturer/Senior Lecturer with the Department of Engineering, School of Science, Engineering and Design, Teesside University. His current research interests include medical devices, electric car battery, non-destructive testing, operational management and Intelligent transportation, the IoT and AI solutions for bespoke robotics in chemical, environmental, life science, energy, and agri-food industries. He is a member IET and IMeChE.



PÅL JOHAN FROM received the Ph.D. degree in modeling and control of complex robotic systems from the Norwegian University of Science and Technology.

Since 2010, he has been the Head of the Robotics Group, Norwegian University of Life Sciences, which has designed and built the Thorvald agricultural robot. He is currently a Professor of agri-robotics with the Norwegian University of Life Sciences and also with the University of Lincoln, U.K. He is also the CEO of saga robotics, which develops and commercializes the agricultural platform Thorvald. He has more than 50 international publications in robotics and has written one book. He has also held a large number of peer-reviewed grants from various sources. These include both research grants and grants for commercialization.

• • •

Part II – Strawberry-harvesting robots

Paper III

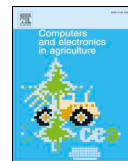
Xiong, Y., Peng, C., Grimstad, L., From, P.J. and Isler, V., 2019. Development and Field Evaluation of a Strawberry Harvesting Robot with a Cable-driven Gripper. *Computers and Electronics in Agriculture*, 157, pp.392-402. DOI:

<https://doi.org/10.1016/j.compag.2019.01.009>



Contents lists available at ScienceDirect

Computers and Electronics in Agriculture

journal homepage: www.elsevier.com/locate/compag

Original papers

Development and field evaluation of a strawberry harvesting robot with a cable-driven gripper[☆]Ya Xiong^{a,*}, Cheng Peng^b, Lars Grimstad^a, Pål Johan From^a, Volkan Isler^b^a Faculty of Science and Technology, Norwegian University of Life Sciences, Ås, Norway^b Department of Computer Science, University of Minnesota, Minneapolis, USA

ARTICLE INFO

Keywords:

Agricultural robotics
 Strawberry harvesting robot
 Cable-driven gripper
 Field evaluation
 System integration

ABSTRACT

This paper presents the development and evaluation of a robot for harvesting strawberries (*Fragaria × ananassa*) grown on table-tops in polytunnels. The robot is comprised of a newly-designed gripper mounted on an industrial arm which in turn is mounted on a mobile base along with an RGB-D camera. The novel cable-driven gripper can open fingers to “swallow” a target. Since it is designed to target the fruit not the stem, it just requires the fruit location for picking. Moreover, equipped with internal sensors, the gripper can sense and correct for positional errors, and is robust to the localisation errors introduced by the vision module. Another important feature of the gripper is the internal container that is used to collect berries during picking. Since the manipulator does not need to go back and forth between each berry and a separate punnet, picking time is reduced significantly. The vision system uses colour thresholding combined with screening of the object area and the depth range to select ripe and reachable strawberries, which is fast for processing. These components are integrated into a complete system whose performance is analysed starting with the four main failure cases of the vision system: undetected, duplicate detections, inaccurate localisation and segmentation failure. The integration enables the robot to harvest continuously by moving the platform with a joystick. Field experiments show the average cycle time of continuous single strawberry picking is 7.5 s and 10.6 s when including all procedures. Furthermore, the robot is able to pick isolated strawberries with a close-to-perfect success rate (96.8%). However, in farm settings, the average picking success rate is 53.6%, and 59.0% when including “success with damage”, testing on the strawberry cultivar of “FAVORI”. The failure cases are analysed and most failures are found when picking strawberries in clusters, in which both the detection algorithm and the gripper struggles to separate the berries.

1. Introduction

Strawberry (*Fragaria × ananassa*) is a high-value crop with a significant production cost, especially in labour. Labour represents the largest cost and also a large operational uncertainty for strawberry growers (Yamamoto et al., 2014). It was reported that the harvesting operation takes up one quarter of all working hours in Japan (Yamamoto et al., 2014). Harvest labour cost depends on the production method, type of strawberries and yield. In Norway, the harvesting portion of the cost could be as high as 60% of the entire labour cost. Therefore, automated fruit picking is desirable. However robotic picking at a commercial level is very challenging: First of all, strawberries are easily damaged and bruised (Dimeas et al., 2015). Second, strawberry harvesting requires highly selective procedures (Hayashi

et al., 2010), since the strawberries tend to ripen unevenly. As a result, at a given time, berries exhibit large variations in colour and size. Finally, strawberries tend to grow in clusters, which makes it hard to identify and pick individual strawberries (Yamamoto et al., 2014).

Several systems for autonomous harvesting have been developed over the last decades. Chiu et al. (2013) presented a picking robot to harvest tomatoes, which took 74.6 s to pick a target. Another tomato harvesting robot equipped with a rotational gripper can pick a tomato in 23.0 s at a success rate of about 62.2% (Yaguchi et al., 2016). The main challenge is picking in clusters where the gripper might grasp multiple tomatoes (Yaguchi et al., 2016). Similarly, a harvesting robot was developed to harvest sweet peppers, which could harvest a target in 94 s with success rates of 6% when using a Fin Ray end effector and 2% when using a Lip-type end effector in natural environment (Bac et al.,

[☆] An earlier version of the cable-driven gripper section in this paper was presented at the IEEE International Conference on Robotics and Automation (ICRA) 2018 (Xiong et al., 2018).

* Corresponding author.

E-mail address: yaxio@nmbu.no (Y. Xiong).

<https://doi.org/10.1016/j.compag.2019.01.009>

Received 22 August 2018; Received in revised form 31 December 2018; Accepted 11 January 2019
 0168-1699/ © 2019 Elsevier B.V. All rights reserved.

2017). The success rate increased to 26% and 33%, respectively when testing in simplified environment (Bac et al., 2017). Also for pepper, a robot named “Harvey” equipped with a suction-blade end-effector can achieve a 42% success rate for unmodified crop with multi attempts, and 58% for modified crop (Lehnert et al., 2017). The picking time is about 35–40 s for each fruit and the most common detachment failure was the cutting tool missing either side of the peduncle (Lehnert et al., 2017). In addition to fruits, robots are also used for harvesting flowers. Rath and Kawollek (2009) presented a system for the automated harvest of *Gerbera jamesonii* pedicels with a success rate of about 80%. For strawberry, a harvesting robot was developed targeting at peduncle detection, with 41.3% success rate when using a suction gripper and 34.9% when using a scissor-like cutter (Hayashi et al., 2010). The execution time for the successful harvest of a single fruit was 11.5 s (Hayashi et al., 2010). Except for academia, start-up companies have also developed some strawberry harvesting robots but none of these are commercialized. This includes AGROBOT (Huelva, Spain) who uses 24 independent picking systems mounted on a mobile base to increase efficiency, OCTINION (Leuven, Belgium) who designed a force-limit soft gripper to avoid damage while grasping, and Harvest CROO (Florida, USA) who designed a rotation apparatus that includes several grippers for picking strawberries on the ground.

Strawberry harvesters generally consist of four subsystems: (i) vision for detection of strawberries, (ii) a gripper for picking the strawberries, (iii) an arm for moving the gripper to the berries, and finally (iv) a platform to increase the work space of the robot and provide mobility. In our previous work, a mobile robot platform was developed that is capable of navigating autonomously in strawberry polytunnels (Grimstad and From, 2017). We also presented an earlier version of a novel cable-driven gripper with perception capabilities for strawberry picking robots (Xiong et al., 2018). This paper presents the gripper and vision system, as well as the integrated system for harvesting strawberries grown on table-tops in polytunnels. Table-top systems in polytunnels will generally reduce disease pressure and increase yield. In the same way as these systems facilitate the work for human pickers, robotic strawberry harvesters can also benefit from this type of production. The end effector is a critical component in robotic systems as it could simplify requirements from other subsystems (Eizicovits et al., 2016) as well as enhance operation stability and efficiency substantially (Chiu et al., 2013). There are a few different designs of end effectors for strawberry picking, such as scissor-like cutters (Hayashi et al., 2010), cutters with suction device (Hayashi et al., 2010), as well as force-limit grasping grippers (Dimeas et al., 2015). As the individual strawberry peduncle (picking point) is difficult to detect (Huang et al., 2017), especially in a cluster where locating the correct stem is much harder than find a strawberry body, the scissor-like end effectors thus require a relatively advanced vision system to be developed. It is also easy to cut more than one stem at the time and unintentionally pick green strawberries. Force controlled grippers are also hard to use as one would very easily bruise fragile strawberries (Hayashi et al., 2010).

The main contributions of this paper are as follows: (a) the design and development of a novel cable driven non-touch picking gripper that has a high tolerance for positional errors and can reduce picking time with a storage container (Xiong et al., 2018); (b) the tight integration of all these subsystems into a complete and working system for strawberry picking, which enables the robot to harvest continuously by moving the mobile platform manually; (c) the evaluation of the vision and gripper performance and the whole system in the farm, for example whether failure occurs as a result of a single subsystem or due to the integration, which is useful for further improvement of the system. The system is not at a commercial level in terms of reliability yet, but it is believed that the speed of the system is reaching a level where it is becoming suitable for a commercial product.

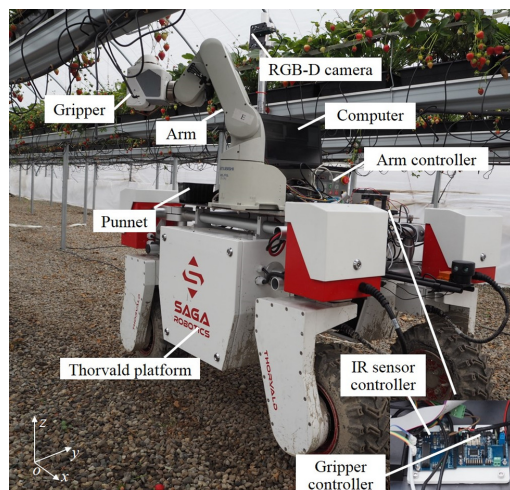


Fig. 1. Hardware assembly in a strawberry farm: the robot mainly consists of a RGB-D camera, a 5-DOF arm, a gripper and a mobile platform.

2. Materials and methods

2.1. System overview and experimental setting

The strawberry harvesting robot system is comprised of four subsystems: vision, arm, gripper and the mobile platform, as shown in Fig. 1. An RGB-D camera (R200, Intel, USA) is mounted on the top frame for front view strawberry detection. A serial arm with 5 degrees of freedom (RV-2AJ, Mitsubishi, Japan) is mounted on our previously developed Thorvald II platform (Grimstad and From, 2017). Finally, a newly-designed cable-driven gripper with perception ability is used for picking. The whole assembly of the robot is 145 cm long, 110 cm wide and 170 cm high. Generally, if the horizontal distance (in y axis) from the gripper to the centre of the platform ranges from 50 cm to 70 cm, the height of the fruits (in z axis) that can be reached is around 120–150 cm with a width of about 35 cm (in x axis). All the field tests reported in this paper were conducted at the Myhrene strawberry farm (Drammen, Norway) on “FAVORI” cultivar at the end of the picking season (early September). The farm is equipped with table-top strawberry growing system, with a table bed height of around 140 cm.

2.2. Robotic platform

Thorvald II is a modular robotic system designed to allow quick assembly of custom robots for a wide range of agricultural environments (Grimstad and From, 2017). A small set of specialized modules connect to simple frame members through standardized mechanical and electrical interfaces, and robots can be assembled or re-configured by into robots of different sizes and shapes. Different modules serve different and specific purposes such as propulsion, steering, battery placement, sensor placement, suspension, etc.

The mobile base used in the present work is a variation of the Thorvald II agricultural robot. It is created almost solely of standard Thorvald II modules and frame members, with the only exception being one custom piece of sheet metal on which the robotic arm is mounted. As polytunnels come in different designs and with ground surfaces ranging from grass to rocks, the mobile robot is fitted with four-wheel

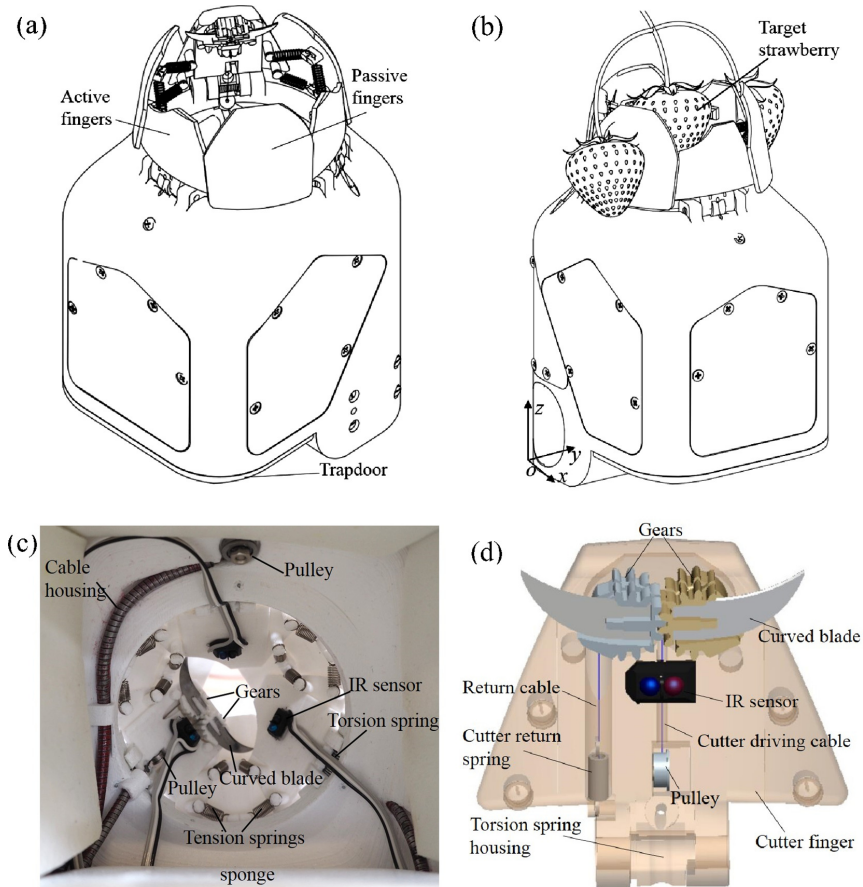


Fig. 2. The cable-driven gripper: (a) perspective view of the gripper; (b) schematic of picking in simple cluster where a target has been swallowed and two surrounded objects have been separated; (c) inside bottom view of the prototype; (d) 3D model of the cutter mechanism.

drive and four-wheel steering to ensure agility and traction in tough conditions.

The mobile base is capable of navigating autonomously in strawberry polytunnels (Grimstad and From, 2017). However, in this work, the platform has not been fully integrated as the scope here is more on the picking system. It is controlled manually by a joystick along the table-tops.

2.3. Cable-driven gripper

2.3.1. Design

The main objectives and challenges of the gripper design are (i) to not damage the target and surrounding berries, (ii) to separate strawberries that are in clusters, (iii) to achieve a high tolerance for positional error, and (iv) to achieve high picking speeds.

The proposed gripper is shown in Fig. 2. The overall size of the gripper is $110 \times 130 \times 178$ mm. It has four parts each with a unique function: picking, transmission, sensing, and storing. The gripper is designed so that its workspace is strictly Cartesian with no rotations needed, so a 3-DOF Cartesian arm is sufficient to generate this motion. In this project, the orientation of the 5-DOF arm is locked to keep the gripper horizontal.

Fruit localisation is much easier than stem recognition (Yaguchi et al., 2016), because ripe fruits have large size and red colour (strawberry) that is clearly different from leaves. Therefore, the gripper is designed to target the fruit and not the stem, which means it just needs the fruit location for picking rather than stem location. Compared to other strawberry picking robots that use stem as picking point (Hayashi et al., 2010; Huang et al., 2017), this system becomes more robust to positional errors of localisation and requires less vision localisation capacities. Also, strawberries are positioned in the 3D space. When targeting a strawberry in the back, it is unclear how existing scissor-like grippers avoid cutting the front branches and possibly green strawberries. Therefore, the gripper is designed to pick from below and thus only “swallow” the targeted strawberry, as shown in Fig. 2(b).

The picking mechanism, as shown in Fig. 2(a), consists of three active fingers, three passive cover fingers and a cutter mechanism. The six fingers can open simultaneously to form a closed ring to swallow a strawberry from below. The designed maximum diameter of the gripper open size is 60 mm. To protect the parts and motors, the open diameter is set to 45 mm, which is enough to “swallow” normal strawberries (average size is 30–40 mm). The initial design idea is that the gripper open size is controlled based on the strawberry size to avoid swallowing surrounding obstacles. However, estimation of fruit size is still a

challenging vision problem especially for partially occluded strawberries. After swallowing the berry, the gripper uses fingers to push the stem to the cutting area. The fingers also enable the gripper to separate surrounding strawberries away from the target, as indicated in Fig. 2(b). To move the fingers simultaneously, this gripper has three active fingers and three passive fingers (cover fingers). Four small tension springs are used to keep the cover fingers adhering to the active fingers regardless of their rotation. After closing the fingers, the cutter that comprises of two curved blades (Ideal Tek, Switzerland) rotates quickly to cut the stem. The cutter is hidden inside of the fingers to avoid damage to the target strawberry as well as the surrounding ones.

Simultaneous motion of the fingers can be achieved by gear transmission. However, this kind of transmission needs significant space below the fingers which is undesirable. Furthermore, it would be too complex to control the three fingers using only one motor. Therefore, a cable-driven method is adopted for remote transmission which provides more space under the fingers for picking and storing strawberries since the motor can now be placed away from the joints. Extra flexible steel cables (Ormiston, England) are selected so the direction can be changed easily using normal bicycle cable housings and pulleys (Fig. 2(c)). To reduce cost and complexity, only one servomechanism (MX-28T, DYNAMIXEL, South Korea) with multiple rotation directions to control both the fingers and cutter is used. The fingers open by driven cables and close by torsion springs. As shown in Fig. 2(d), the cutter is mounted on a pair of small gears. One active driving gear is pulled by a cable so the cutter can close and the other passive driving gear, connects to a return tension spring, is used to open the cutter. As a consequence, at the central position, the servo turns clockwise to rotate the cutter and counter-clockwise to open fingers.

Furthermore, the gripper employs three internal infrared (IR) sensors (TCRT5000, Vishay, USA) to identify the target location with respect to the gripper and then control the arm to move the gripper to the optimal cutting position. This control is named gripper-level close-loop control, since the gripper senses positional errors by itself without passing through the vision system. Hence, different from high-level closed-loop control system such as visual servoing, this control method can increase processing speed. These distance sensors are also utilized to avoid physical interaction with the berries during picking and verify success or failure after picking.

Additionally, the gripper has an internal container, which enables it to pick several strawberries continuously. Therefore, unlike most of the previous fruit picking systems (Hayashi et al., 2010; Chiu et al., 2013; Bac et al., 2017) that require a back-and-forth arm motion for every single picking, the proposed gripper can potentially decrease execution time significantly. The gripper approaches the plant and picks several strawberries until the container is filled. Then, a trapdoor on the bottom of the gripper is opened to dispense all the strawberries into a commercial punnet or another storing unit. For the current version of the gripper, the container can store 7–12 strawberries, depending on the size of the berries. After the stem has been cut, the berries fall on an inclined dropping board to reduce the fall and the impact on the strawberries due to the dropping distance. To further reduce the impact on the berries, pieces of soft sponge are mounted inside the gripper to prevent damage on impact. Except for the servos, sensors and transmission system, all the other parts of the gripper prototype were 3D printed using polylactic acid (PLA) filaments (MP05780, MakerBot, USA).

2.3.2. Optimal cutting position control

To achieve optimal cutting position control, it is essential to know the position of strawberry with respect to the gripper. Fig. 3 shows strawberry position inside the gripper for both front view and section view. The IR sensors can measure the distances (defined as mdp) from the strawberry to the sensor itself. With a given finger rotation angle (θ), the projection distance md can be described as:

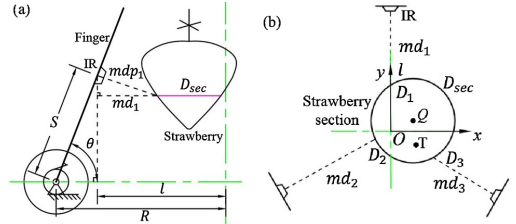


Fig. 3. Schematic of strawberry optimal cutting position control (see description of symbols in the text): a. front view sketch; b. section view sketch.

$$\begin{aligned} md_1 &= mdp_1 \sin(\theta) \\ md_2 &= mdp_2 \sin(\theta) \\ md_3 &= mdp_3 \sin(\theta) \end{aligned} \tag{1}$$

Also, the distance (l) between IR centre and gripper centre is:

$$l = R - S \cos(\theta) \tag{2}$$

where S is the mounting position of IR centre to finger joint. Then, as shown in Fig. 3(b), coordinates of detected points D_1, D_2, D_3 in Oxy can be expressed as:

$$\begin{aligned} D_1 &(0, l - md_1) \\ D_2 &(-\cos(\pi/6)(l - md_2), -\sin(\pi/6)(l - md_2)) \\ D_3 &(\cos(\pi/6)(l - md_3), -\sin(\pi/6)(l - md_3)) \end{aligned} \tag{3}$$

Based on the above three points, assuming strawberry section is a strict circle, the centroid (Q) and diameter (D_{sec}) are obtained as:

$$\begin{aligned} a &= 2(D_2(x) - D_1(x)) \\ b &= 2(D_2(y) - D_1(y)) \\ c &= D_2^2(x) + D_2^2(y) - D_1^2(x) - D_1^2(y) \\ d &= 2(D_3(x) - D_2(x)) \\ e &= 2(D_3(y) - D_2(y)) \\ f &= D_3^2(x) + D_3^2(y) - D_2^2(x) - D_2^2(y) \end{aligned} \tag{4}$$

$$\Rightarrow \begin{cases} offset_x = Q_x = \frac{bf - ec}{bd - ea} \\ offset_y = Q_y = \frac{dc - af}{bd - ea} \\ D_{sec} = \sqrt[3]{(Q_x - D_1(x))^2 + (Q_y - D_1(y))^2} \end{cases} \tag{5}$$

The distance data are collected every 50 ms, which is quick enough for continuous measuring and closed-loop control. To set a desirable constant position T (target_x, target_y) not only the origin O as the cutting position, the errors ($error_x, error_y$) can be defined as the distance from the actual position Q to the target position T :

$$\begin{cases} error_x = offset_x - target_x \\ error_y = offset_y - target_y \end{cases} \tag{6}$$

Then two parallel PID control loops are used for minimising $error_x$ and $error_y$, respectively. An example of the output of the control can be seen in Fig. 4(a). With initial error of 6.3 mm and threshold error of 0.1 mm, the relative stable settling time of PID control is around 3 s. In a real scenario, this level of accuracy is not necessary as the gripper itself has a high mechanical tolerance. Hence, 1.5 mm is used as an error threshold, which reduces the average settling time to around 1 s. In the farm environment, we have shown that arm moves the gripper gently to place the strawberry sufficiently close to the target cutting position (gripper central position), as shown in Fig. 4(b).

2.4. Machine vision

The RGB-D camera is composed of an RGB colour sensor and two infrared sensors for stereo sensing with the guidance of laser grid,

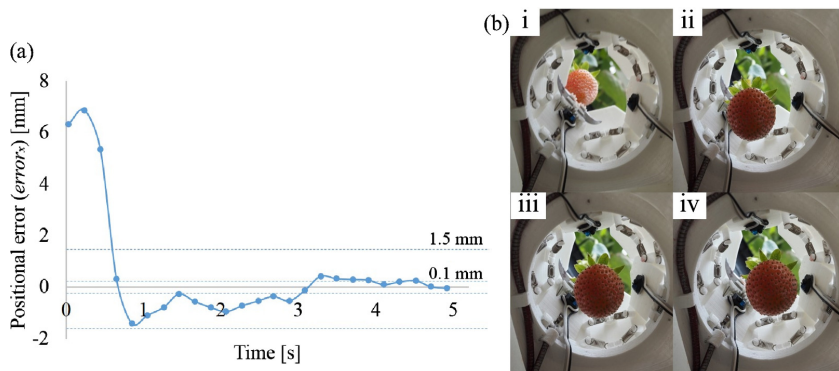


Fig. 4. Optimal cutting position control results: (a). PID control test of strawberry position with respect to the gripper (using $error_x$ as an example, $error_x$ and $error_y$ are controlled in parallel loops); (b). real environment test of optimal cutting position control: from i to iv, the arm moves gripper gently to place strawberry at a target cutting position with respect to the gripper.

which is capable of detecting depth in an outdoor environment. The vision component of the proposed system has two primary capabilities:

Detection: where the goal is to identify individual strawberries in each image.

Localisation: where the goal is to localize the detected strawberries in the robot frame.

The camera module allows us to locate three-dimensional coordinates of the fruit in the camera frame. A calibration procedure has been performed to obtain the extrinsic camera parameters enabling 3D transformation between the camera and the arm frame.

Similar to other fruit picking research (Hayashi et al., 2010; Bac et al., 2017), a simple colour thresholding algorithm based on the Red, Green and Blue (RGB) channels is utilized in this system for detecting strawberries. The method is fast for processing, which is necessary for a real-time system. To remove noise pixels and fill holes, a morphological opening-closing operation is implemented on Fig. 5(a) getting Fig. 5(b), which is based on erosion and dilation of binary images, similar to Xiong et al. (2017). Next, the areas and centroids of all objects are calculated and small objects are removed based on an empirical value. Then a depth filtering based on the depth image (Fig. 5(c)) removes the

objects that are too far or too close to the robot. Finally, as shown in Fig. 5(a), the ripe strawberries are detected with blue-white circles. Some vision failure cases are:

- 1) *Undetected:* This is mainly caused by occlusions. For example, in Fig. 5(a), three yellow-circled ripe strawberries are partially occluded by several green stems and green berries, so their areas in Fig. 5(b) are small and not detected. Particularly, the yellow-circled strawberry on the top of Fig. 5(a) has been segmented into three parts after thresholding due to the two crossing green stems. Then the first eroding operation makes the two smaller segmented parts disappear resulting a small area in Fig. 5(b).
- 2) *Duplicate Detections:* Again, because of occlusions, as shown in Fig. 5(d), a ripe strawberry is split into two objects by the front green stem (yellow circled).
- 3) *Inaccurate Localisation:* Occlusions might also bring localisation error, as can be seen in Fig. 5(f), in which a front green berry results in the detected centroid of the red berry on the left side (bottom yellow circled). Also, occlusions might disturb depth sensing.
- 4) *Segmentation Failure:* Another frequently occurring failure is touching objects that cannot be segmented. As shown in Fig. 5(e), the yellow circles show two connected strawberries that could not

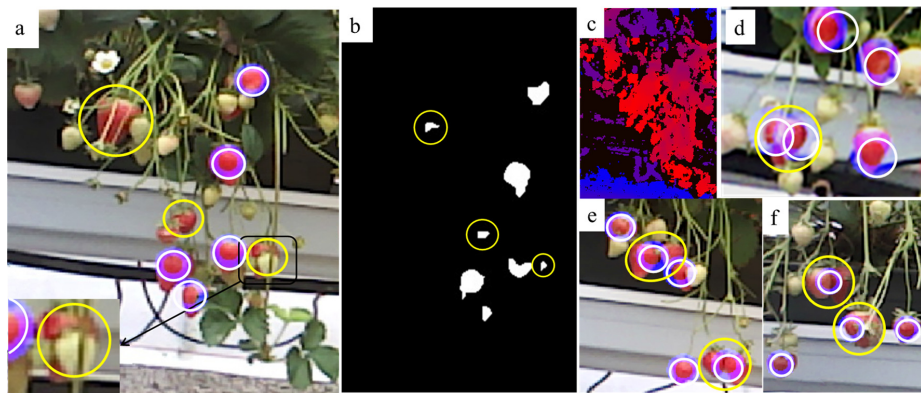


Fig. 5. Strawberry detection, blue-white circles are detected objects, yellow circles show failure cases: (a). detected strawberries (blue-white circles) and undetected (yellow circles), (b). binary image after processing of (a), undetected targets in (a) are also circled in yellow, (c). depth image of (a), (d). duplicate detections (yellow circle), (e). two segmentation failure cases (circled in yellow), (f). inaccurate localisation (bottom yellow circle) and segmentation failure (top-left yellow circle). (For interpretation of the references to colour in this figure legend, the reader is referred to the web version of this article.)

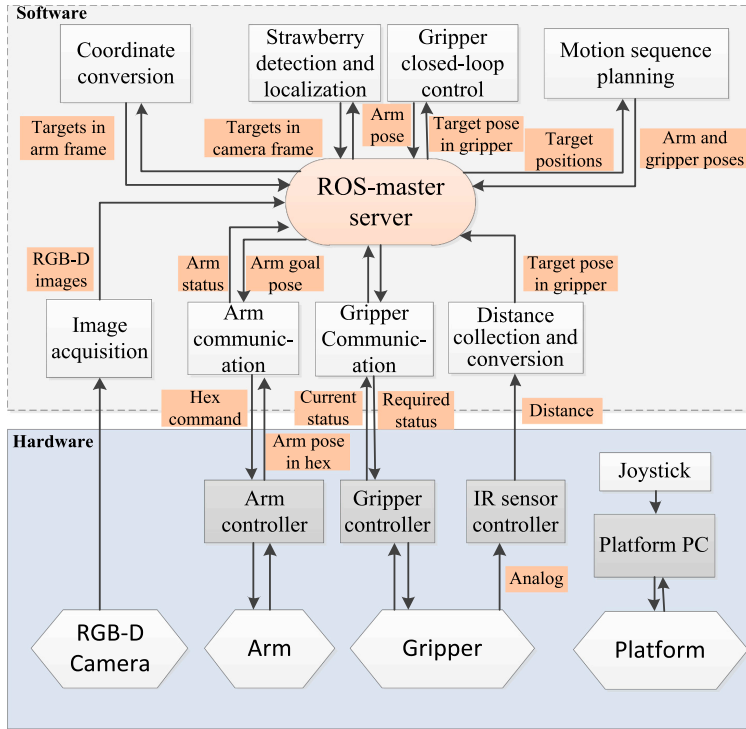


Fig. 6. System architecture: it shows system hardware modules, software nodes and their communication with true information.

be separated and thus are regarded as a single target.

As for localisation, given the intrinsic matrix K of the camera and the depth d_{P_i} for the available pixels $P_i = [u, v]^T$, the pixel 3D location ${}^C P_i = [x, y, z]^T$ with respect to the camera coordinate frame C is calculated by

$${}^C P_i = d_{P_i} K^{-1} P_i \quad (7)$$

For each detected strawberry, 10 pixels ($N = 10$) around the centroid are used to estimate the location of the strawberry ${}^C S$ in the arm frame, so ${}^C S$ is the mean over all ${}^C P_i$.

3. System integration and control

3.1. System architecture

The system architecture is illustrated in Fig. 6. The robot is fully automated except for moving the mobile platform along the table-tops. The platform was developed independently and moved by a joystick according to the picking sequence. Hardware modules, camera, arm and gripper controllers all communicate to the host PC via serial ports. All of the software modules were written in either C++ or Python and implemented in the Kinect distribution of the Robot Operating System (ROS) installed on Ubuntu 16.04. Both gripper controller and IR sensor controller were flashed with *rosserial_arduino* ROS package for robust and convenient communication. In the software block, the five ROS nodes below the ROS master are utilized for communication to the hardware controllers, including data conversion, encoding and decoding. The upper four nodes are used for image processing, coordinate conversion, task sequence planning and picking position closed-loop controlling, respectively.

3.2. Control strategy of the complete system

Fig. 7 depicts the control algorithm of the entire system. The task sequence starts with the vision system. First, the image acquisition node grabs the RGB and depth images then passes them through the ROS master to the strawberry detection and localisation node.

- 1) *Strawberry Detection and Localisation*: The strawberry centroids and areas are calculated and only the targets that are located in the arm reach region (workspace) and whose ripeness areas (obtained by red colour thresholding) are large enough for picking are passed to the next step. The locations of target strawberries are converted into the arm frame afterwards by a coordinate conversion node.
- 2) *Picking Sequence Planning*: Once the motion sequence planning node receives multi-berry locations, it sorts all of the strawberries from low position to high. The reason why simple ascending order rather than minimal-time order was used for picking multiple berries is because the gripper is picking from below. If the robot picks a higher-hanging strawberry first, then the lower strawberry location might be affected by the arm during the first picking action.
- 3) *Individual Picking*: Next, the motion sequence planning node determines the trajectories for the manipulator arm for individual picking.
- 4) *Strawberry Dispensing*: After all the target berries are picked, the gripper dispenses collected strawberries into a punnet.
- 5) *Moving Platform*: Meanwhile, the platform is moving to a new image area for continuous picking.

3.3. Individual picking control

In Fig. 7, the right hand side blue-dash block shows the flowchart of

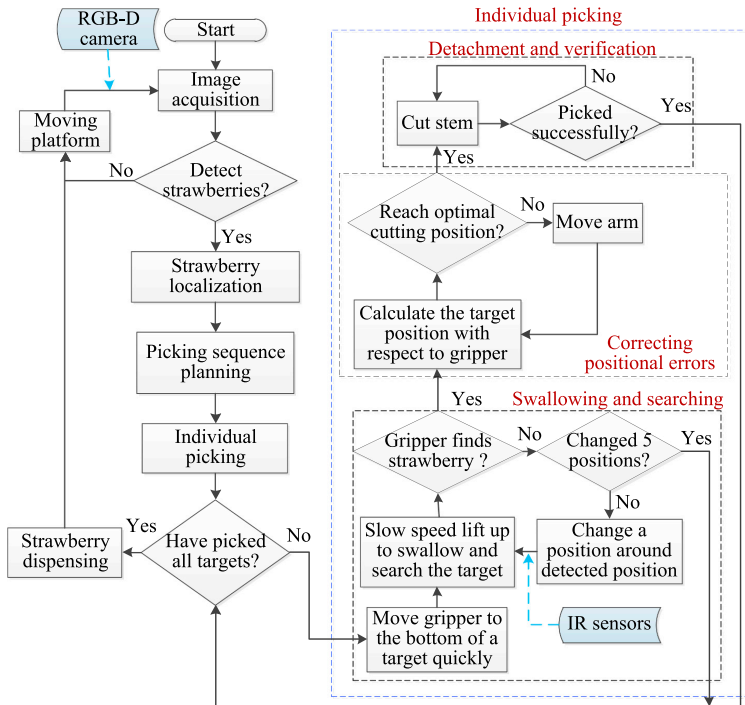


Fig. 7. System control: system control algorithm, left side is the whole system task sequence while the right side shows the individual picking steps.

controlling individual strawberry picking. It can be divided into three key steps:

- 1) *Swallowing and Searching*: The gripper is moved quickly to just underneath the target and then the arm raises the gripper vertically at low speed to swallow the strawberry. The internal IR sensors then verify the presence and position of the strawberry.
- 2) *Correcting Positional Errors*: Once the gripper detects the strawberry, it calculates the target location with respect to the gripper. During this procedure, if no strawberry is detected, the arm changes its position around the target (15 mm offset to the vision localized position) for a wider range search for up to 5 times. After that, the gripper returns the target location to the system and it uses PID control to move the arm until the target is at the optimal cutting position. The closed-loop control at the gripper-level avoids processing in the vision system, which is meaningful for high speed control.
- 3) *Detachment and Verification*: Finally, the cutter is actuated to detach the strawberry. The cutting result is verified by the IR sensors. If the attempt is unsuccessful, the cutter will continue cutting for up to 5 times.

3.4. Harvesting sequence in action

Fig. 8 demonstrates the task sequence and control strategy in the field test. First, two strawberries that are located in the arm reach region are detected and selected. Then, swallowing and searching: as shown in Fig. 8(a), the arm moves quickly to the bottom of the first strawberry and lifts the gripper up slowly to search the target and swallows it when found. Correcting positional errors: next, as shown in

Fig. 8(b), the gripper uses internal sensors to detect positional errors and correct for them by controlling the arm using a simple PID controller. Detachment and verification: the strawberry is detached by the cutter and the result is verified by gripper IR sensors (Fig. 8(c)). Then it executes the same operations to pick the second target (Fig. 8(d)). Moving platform: once the first image area finishes, the platform is moved manually to the next image area for continuous picking (Fig. 8(f)). Strawberry dispensing: finally, the picked strawberries that have been collected in the container are released gently into a punnet (Fig. 8(h)).

4. Results and discussions

To assess the performance of the robot, several sets of experiments were designed to evaluate both the individual subsystems and the entire system, including detection performance, gripper performance, system localisation accuracy and repeatability, picking execution time, picking success rate, and failure modes.

4.1. Detection performance

First, the detection performance of the vision system was evaluated based on a 100 image dataset by using precision-recall curves. The ripe strawberries were manually labelled with bounding boxes, which are used as ground truth, as the blue box shown in Fig. 9(a). Similar to Habaragamuwa et al. (2018), the correct and incorrect detection of ripe strawberries are defined as True Positive (TP) and False Positive (FP), respectively. Since the gripper manipulation is based on the object centroids, the correct detection here means the detected centroid of a target is within a pre-defined region. As shown in Fig. 9(a), the pre-

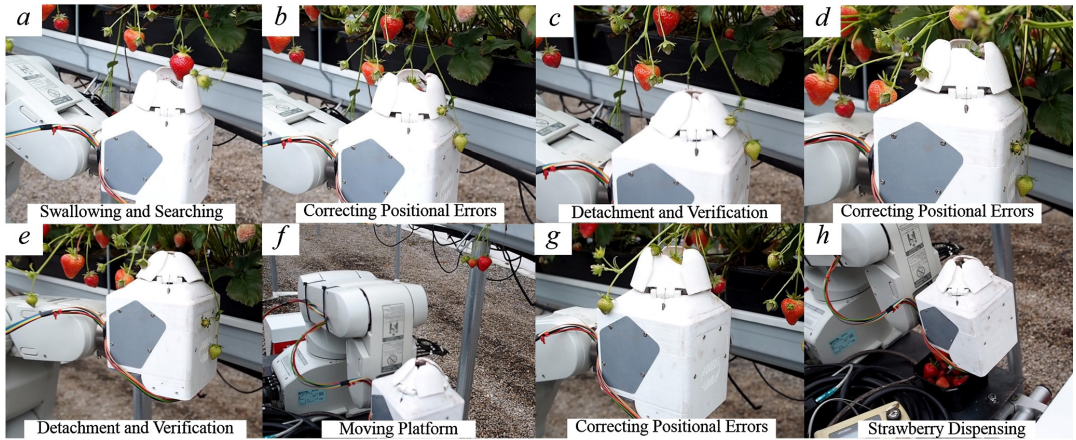


Fig. 8. Harvesting procedures of continuous strawberry picking with manually controlled mobile platform in field test: (a) swallowing and searching; (b) correcting positional errors; (c) detachment and verification; (d) picking the second one; (e) detachment and verification; (f) moving platform to the next image area; (g) picking a target in the new image area; (h) strawberry dispensing.

defined regions (blue, green and orange boxes) are located in the central of the manually labelled bounding box. The area of the pre-defined region over the ground truth area (blue box) is expressed as the precision level of *TP*. In this test, three precision levels of *TP* are used, 1.0 (blue box), 0.5 (green box) and 0.25 (orange box), respectively. If duplicate detections occur on one ripe strawberry, only one of them is marked as *TP* and the others are regarded as *FPs*. For segmentation failure case, at most one is recorded as *TP* if one of the detected centroids is inside of the above mentioned pre-defined region, and the others are regarded as normal undetected cases that are classified as False Negative (*FN*). Then, precision is obtained by using *TP* dividing the sum of *TP* and *FP*, while recall is defined as *TP* over the sum of *TP* and *FN*. By varying RGB threshold range, the precision-recall curves of the detection system are obtained and shown in Fig. 9(b). As can be seen, if the precision level of *TP* is 0.25 (orange curve), the precision and recall can reach about 0.72 at the same time with appropriate thresholds. The performance of different varieties and environments may vary, since detection of clusters are more difficult than isolated strawberries.

4.2. Gripper performance

The second test was conducted in simplified environment in order to identify the optimal blade cutting position. Also, the picking success rate for isolated strawberries was obtained. During the test, the target cutting position *T* was changed along the perpendicular bisector of the cutter finger (the dashed line *md₃* in Fig. 3(b)). The stem diameters of the strawberries in the test varied from 1.7 mm to 2.5 mm. The result is illustrated in Table 1. The optimal cutting position is the central of the gripper, which is the middle position of the cutter. In this case, the success rate for picking isolated strawberries with a single attempt is 96.8% at the optimal position (previous strawberry picking research is around 70% (Hayashi et al., 2010)).

4.3. Absolute accuracy and repeatability of system localisation

The third test is to determine the localisation accuracy of the whole system, which indicates the positional error of the end effector central point where the arm reaches with respect to the target's actual location.

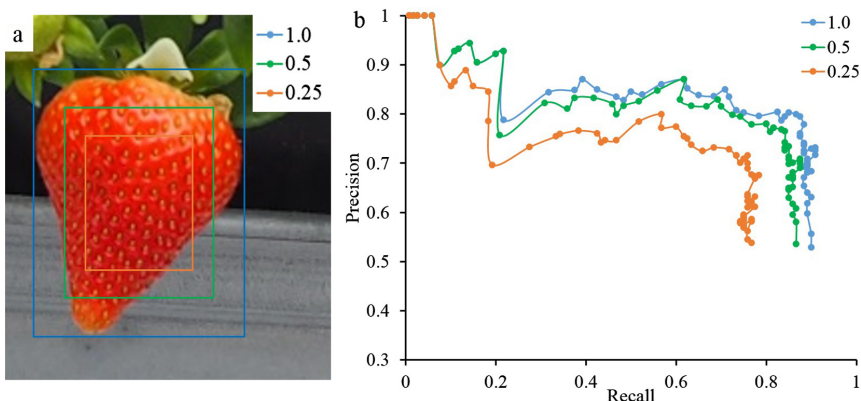


Fig. 9. Detection performance evaluation: (a) diagram of precision level of *TP*, where the blue box (ground truth), green box and orange box represent precision of 1.0, 0.5 and 0.25 with respect to the ground truth; (b) the precision-recall curves of detection system with different precision levels of *TP*. (For interpretation of the references to colour in this figure legend, the reader is referred to the web version of this article.)

Table 1
Picking isolated strawberries success rate with single attempt at different cutting position.

Cutting position T to gripper origin O [mm]	Success	Failure	Success rate [%]
-2	17	2	89.5
0	30	1	96.8
2	28	2	93.3
5	13	1	92.9
8	15	1	93.8
10	9	2	81.8

As a whole system, the localisation accuracy mainly consists of vision detection and localisation accuracy, calibration accuracy and arm accuracy. However, accurate measuring the positional error is difficult and may need expensive equipment. In this system, the industrial arm has high repetition precision of ± 0.02 mm, so the arm was used to measure the target actual location in the arm frame. As shown in Fig. 10(a), a pointer with a sharp tip was mounted on the arm and it was moved manually to the target centre point. Then the tip position of the pointer in the arm frame (P_{ref}) was obtained from the arm controller after geometry conversion. After finding the actual locations, these targets were detected and localized by the vision system and converted from their central locations into the arm frame obtaining (P_{est}). This estimation procedure was repeated 18 times. Using this method, the arm does not need to reach the targets after vision detection, and at the same time the arm accuracy is excluded in the measurement.

In industry, evaluation of robot arm accuracy comprises two criteria: absolute positioning accuracy (A_s) and positioning repeatability (defined as precision P_s , which describes the deviation of all P_{est} points) according to the ISO 9283 standard (Stephan et al., 2009). Similarly, these two indicators are used for assessing the whole system accuracy but excluding the arm in this paper. A_s is the Euclidean distance between the point \bar{P}_{est} and P_{ref} , where \bar{P}_{est} is the centre point of all measured points P_{est} . P_s can be expressed as

$$P_s = \bar{l} + 3\sigma_{l_i} \tag{8}$$

where \bar{l} denotes the mean of distance l_i from measured points P_{est} to \bar{P}_{est} , while σ_{l_i} is the standard deviation of l_i . The 3D plot of all measured and reference points is shown in Fig. 10(c). Fig. 10(b) illustrates the calculation results for the 9 reference points. The mean of absolute accuracy \bar{A}_s is 9.8 mm and the mean of repetition precision \bar{P}_s is 4.6 mm. Since the frame transformation matrix is constant, the repetition error is mainly caused by the vision system. Furthermore, the measured points in Fig. 10(c) are almost in a line around the reference point. Based on observation, the line direction is close to the camera projection direction, which means the uncertainty is mainly from the IR depth sensor of the camera.

The absolute accuracy might be lower in the farm due to the complex environment. In the farm, the actual positions of target strawberries are hard to measure. Similar to sweet pepper harvesting robot research (Bac et al., 2017), the distance between the fruit surface centre and the pointer tip that attached to the gripper was measured as absolute error, as shown in Fig. 11(a). The test result is presented in Fig. 11(b). The big errors mainly occur on partially hidden strawberries, since the front plants disturb the depth sensing. The average error is 13.3 mm, with a standard deviation of 7.0 mm, which is higher than in indoor the environment.

4.4. Execution time

The execution time is illustrated in Table 2, which was found based on the successful tests in the farm. The average cycle time of continuous single strawberry picking is 7.5 s (excluding initial vision detection, first and final arm travelling and placing strawberries), while including all procedures, the average time is 10.6 s for picking one strawberry. As a consequence, the perception and storage ability of the gripper enables the robot to avoid slow control in the whole system level such as visual servoing and also reduced travel time for each strawberry. As a result, the picking execution is faster than the previous results reported on strawberry picking of 11.5 s (Hayashi et al., 2010), cucumber harvesting of 37.8 s (Van Henten et al., 2003), sweet pepper picking of 94 s (Bac et al., 2017) and 35.0–40.0 s (Lehnert et al., 2017), as well as tomato picking of 23.0 s (Yaguchi et al., 2016) and 74.6 s (Chiu et al., 2013). The average picking time for each strawberry will decrease substantially if the number of strawberries collected in the container increases. It is still much slower than a human picker (about 3.5–5.0 s (Hayashi et al., 2010)), but multiple manipulators can be employed to increase efficiency.

4.5. Success rate, failure cases and lessons learned

The success rate is an essential indicator for evaluating a harvesting machine and the failure reasons are useful for further improvements. Generally, isolated strawberries are much easier for both localisation and picking. Table 1 shows the success rate for picking isolated strawberries with a single attempt is 96.8%. However, in a natural environment, especially for dense clusters, the system still has substantial challenges. Table 3 shows picking test results. All results were recorded with only a single attempt. “Success” means the picking was successful without damage to the strawberry based on observation, while “success with damage” indicates the detachment of the target was successful but it also picked or damaged surrounding objects or slightly bruised the target strawberry. “Failure attempts” describes all attempts that are not included in the above two classes and also undetected ripe berries. One “failure attempt” may have two or more failure reasons. Overall, with 112 picking trials, the success rate with single attempt is

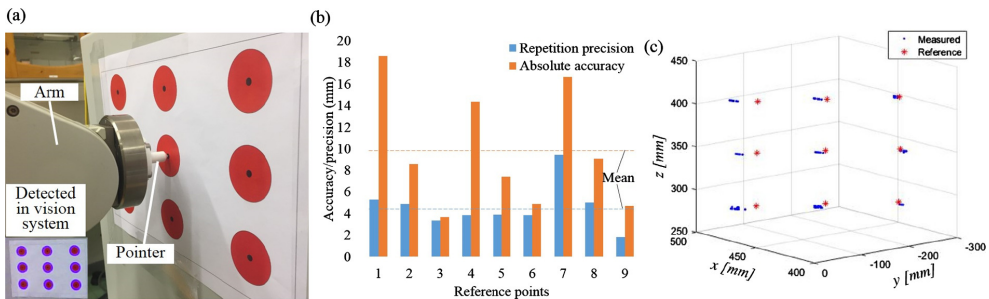


Fig. 10. System localisation accuracy and precision test in the indoor environment: (a) a pointer was mounted on the arm to get the circles’ positions in the arm frame; (b) test results of absolute accuracy and repetition precision; (c) 3D plot of all measured and reference points.

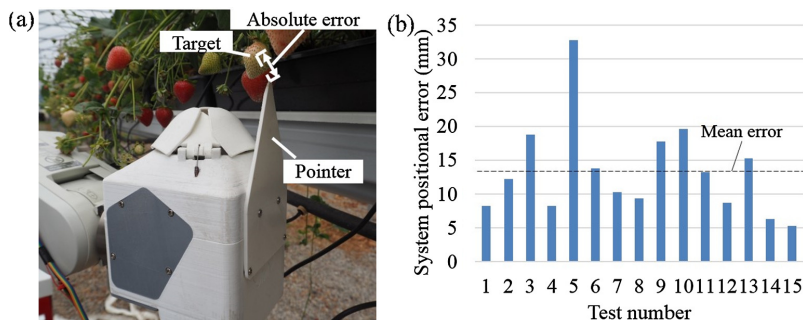


Fig. 11. System absolute localisation accuracy test in the farm: (a) the fruit surface centre to the pointer tip was regarded as absolute error; (b) test result of absolute accuracy.

Table 2
Execution time test result.

Test No.	Number of picked strawberries	Single picking execution time [s]	Single picking execution time including all procedures [s]
1	4	8.0	10.5
2	2	5.6	7.7
3	2	7.9	11.1
4	3	7.7	9.9
5	2	7.7	12.6
6	1	7.5	14.5
Average	2.3	7.5	10.6

Table 3
Performance test result of picking robot in unchanged natural environment.

	Success	Success with damage	Failure attempts	Failure reasons					
				a	b	c	d	e	f
No.	60	6	46	15	9	9	9	3	4
Rate [%]	53.6	5.4	41.1	30.6	18.4	18.4	18.4	6.1	8.2

Failure reasons list:

- a. Gripper separation failure + duplicate detections + segmentation failure (vision): in clusters, gripper “mouth” was covered or blocked by other branches, leaves and strawberries, and/or duplicate detections and segmentation failure in vision subsystem.
- b. Inaccurate localisation + segmentation failure: localisation error is too big, so the gripper could not “swallow” the target, mainly happened on partially hidden targets and one of the unsegmented targets.
- c. Arm reach region: arm working space is limited, so the gripper could not reach targets.
- d. Gripper was disturbed: gripper swallowed below or surrounded green strawberries and regarded them as targets when lifting.
- e. Undetected: did not detect ripe strawberries because of front occlusions.
- f. Communication failure: arm or gripper communication failed.

53.6%, and 59.0% when including “success with damage”. The success rate is higher than the previous strawberry picking research of 41.3% with suction picking gripper and 34.9% with no-suction picking (Hayashi et al., 2010), and also sweet pepper picking of 6.0% with a Fin Ray end-effector in natural environment (Bac et al., 2017), another sweet pepper research of 42.0% with multi-attempt for unmodified crops (Lehnert et al., 2017), but lower than tomato picking 62.2% (Yaguchi et al., 2016) and apple picking 84.0% (Silwal et al., 2017). Generally, harvest rate is incomparable for different crops or even for the same crops but different varieties or environment, since picking large-size, top and separated fruits are easier than small, soft and clustered fruits.

The failure mainly happens in clusters where both detection and picking struggles to separate strawberries, which is labelled case (a) in Table 3. In clusters, segmentation of touching strawberries is extremely hard for the vision system and could also result in duplicate detections and undetected cases (e). Multi-view in the vision system might solve this case (e). Most importantly, the gripper opening mouth is easily covered or blocked by surrounding branches, leaves and strawberries in clusters.

Another problem (case (b)) caused by the vision system occurs when the localisation error is too big for the gripper to swallow the strawberry. This includes inaccurate localisation and segmentation failure cases as described in the machine vision section. In the segmentation failure case, the detected target might be in the centre of two or more targets, so it might result in an unsuccessful swallowing attempt. Problems (c) and (d) are also noticeable. The employed industrial arm has a small workspace. For future work, it is possible to use a low-cost 3-axis Cartesian arm for this application. Case (d) happens when there are some strawberries below the target or within the gripper searching area, so the gripper detects the disturbing strawberries and regards them as the targets, or when the arm touches the lower-hanging plants and affects the target locations. Therefore, the vision system also needs to detect green strawberries or even the whole plants to avoid occlusions or confusions.

To address these problems, on the one hand, more advanced perception system, manipulation algorithm and gripper hardware need to be developed or improved. For example, 3D point-cloud image processing and deep learning might get significant results for object segmentation, localisation and fruit size estimation. Advanced path planning of gripper picking could control the gripper to avoid or even push the surrounding obstacles for cluster picking. On the other hand, horticulture of strawberry growing method may also be adjusted to leave the berries more isolated in the first place.

5. Conclusions

An autonomous strawberry-harvesting robot has been developed. The robot hardware comprises an RGB-D camera, an industrial arm, a gripper and a mobile platform. The gripper is robust to positional errors due to its fruit-oriented design and internal sensing capacities and abilities of picking several strawberries continuously using an internal container. The vision subsystem employs a simple colour thresholding method for fast-speed strawberry detection. System integration enables the robot to harvest continuously by moving the mobile platform manually. Performance test shows that the average cycle time of continuous single strawberry picking is 7.5 s for the picking operation only, and 10.6 s when including all procedures, which is faster than other reported picking research. Gripper-level control to correct positional errors and collecting strawberries while picking are the main reasons

for achieving high speed. In addition, experiments demonstrate that the robot is able to pick isolated strawberries with a close-to-perfect success rate (96.8%). However, in the field, the success rate drops considerably due to the occlusion or other failure cases. In the natural situation, the average picking success rate for a single attempt is 53.6% without causing damage to the berries, and 59.0% when including “success with damage”. The main challenge is picking clusters of strawberries, where both the detection and the gripper struggles to separate the strawberries.

For future work, the plan is to address clusters of strawberries, and in particular look into how more advanced visual algorithms can be implemented to merge the detection from multiple frames so that occluded strawberries can be visible from a different view. The work in Roy et al. (2018) reports a viable approach for apples which may be used as a starting point.

Conflicts of interest

The authors declare that there are no conflicts of interest regarding the publication of this paper.

Acknowledgements

This work was supported by the Norwegian Centennial Chair. We thank Mr. Simen Myhre from the Myhre farm for providing the strawberry tunnels and accommodation to conduct field experiments.

Appendix A. Supplementary material

Supplementary data to this article can be found online at <https://doi.org/10.1016/j.compag.2019.01.009>.

References

- Bac, C.W., Hemming, J., Barth, R., Wais, E., Henten, E.J., Van, 2017. Performance Evaluation of a Harvesting Robot for Sweet Pepper. *J. F. Robot.* 34, 1123–1139. <https://doi.org/10.1002/rob.21709>.
- Chiu, Y.C., Yang, P.Y., Chen, S., 2013. Development of the end-effector of a picking robot for greenhouse-grown tomatoes. *Appl. Eng. Agric.* 29, 1001–1009. <https://doi.org/10.13031/aea.29.9913>.
- Dimeas, F., Sako, D.V., Moulaniitis, V.C., Aspragathos, N.A., 2015. Design and fuzzy control of a robotic gripper for efficient strawberry harvesting. *Robotica* 33, 1085–1098. <https://doi.org/10.1017/S0263574714001155>.
- Eizicovits, D., van Tuijl, B., Berman, S., Eidan, Y., 2016. Integration of perception capabilities in gripper design using graspability maps. *Biosyst. Eng.* 146, 98–113. <https://doi.org/10.1016/j.biosystemseng.2015.12.016>.
- Grimstad, L., From, P., 2017. The thorvald II agricultural robotic system. *Robotics* 6, 24. <https://doi.org/10.3390/robotics6040024>.
- Habaraamuwa, H., Ogawa, Y., Suzuki, T., Shiigi, T., Ono, M., Kondo, N., 2018. Detecting greenhouse strawberries (mature and immature), using deep convolutional neural network. *Eng. Agric. Environ. Food.* <https://doi.org/10.1016/j.eaef.2018.03.001>.
- Hayashi, S., Shigematsu, K., Yamamoto, S., Kobayashi, K., Kohno, Y., Kamata, J., Kurita, M., 2010. Evaluation of a strawberry-harvesting robot in a field test. *Biosyst. Eng.* 105, 160–171. <https://doi.org/10.1016/j.biosystemseng.2009.09.011>.
- Huang, Z., Wane, S., Parsons, S., 2017. Towards automated strawberry harvesting: Identifying the picking point. *Lect. Notes Comput. Sci. (including Subser. Lect. Notes Artif. Intell. Lect. Notes Bioinformatics)* 10454 LNAI, 222–236. https://doi.org/10.1007/978-3-319-64107-2_18.
- Lehnert, C., English, A., McCool, C., Tow, A.W., Perez, T., 2017. Autonomous sweet pepper harvesting for protected cropping systems. *IEEE Robot. Autom. Lett.* 2, 872–879. <https://doi.org/10.1109/LRA.2017.2655622>.
- Roy, P., Kislav, A., Plonski, P.A., Luby, J. and Isler, V., 2018. Vision-based preharvest yield mapping for apple orchards. arXiv preprint arXiv:1808.04336. < <https://arxiv.org/abs/1808.04336> > .
- Rath, T., Kawollek, M., 2009. Robotic harvesting of Gerbera Jamesonii based on detection and three-dimensional modeling of cut flower pedicels. *Comput. Electron. Agric.* 66, 85–92. <https://doi.org/10.1016/j.compag.2008.12.006>.
- Silwal, A., Davidson, J.R., Karkee, M., Mo, C., Zhang, Q., Lewis, K., 2017. Design, integration, and field evaluation of a robotic apple harvester. *J. F. Robot.* 34, 1140–1159. <https://doi.org/10.1002/rob.21715>.
- Stephan, P., Heck, I., Kraus, P., Frey, G., 2009. Evaluation of indoor positioning technologies under industrial application conditions in the Smart Factory KL based on EN ISO 9283. *IFAC Proc.* 13, 870–875. <https://doi.org/10.3182/20090603-3-RU-2001-0294>.
- Van Henten, E.J., Van Tuijl, B.A.J., Hemming, J., Kornet, J.G., Bontsema, J., Van Os, E.A., 2003. Field test of an autonomous cucumber picking robot. *Biosyst. Eng.* 86, 305–313. <https://doi.org/10.1016/j.biosystemseng.2003.08.002>.
- Xiong, Y., Ge, Y., Liang, Y., Blackmore, S., 2017. Development of a prototype robot and fast path-planning algorithm for static laser weeding. *Comput. Electron. Agric.* 142, 494–503. <https://doi.org/10.1016/j.compag.2017.11.023>.
- Xiong, Y., From, P.J., Isler, V., 2018. Design and evaluation of a novel cable-driven gripper with perception capabilities for strawberry picking robots. 2018 IEEE International Conference on Robotics and Automation (ICRA). IEEE.
- Yaguchi, H., Nagahama, K., Hasegawa, T., Inaba, M., 2016. Development of an autonomous tomato harvesting robot with rotational plucking gripper. *IEEE Int. Conf. Intell. Robot. Syst.* 2016–November, 652–657. <https://doi.org/10.1109/IROS.2016.7759122>.
- Yamamoto, S., Hayashi, S., Yoshida, H., Kobayashi, K., 2014. Development of a stationary robotic strawberry harvester with picking mechanism that approaches target fruit from below. *Japan Agric. Res. Q. JARQ* 48, 261–269. <https://doi.org/10.6090/jarq.48.26>.

Part II – Strawberry-harvesting robots

Paper IV

Xiong, Y., Ge, Y., Grimstad, L. and From, P.J., 2019. An Autonomous Strawberry-Harvesting Robot: Design, Development, Integration, and Field evaluation. *Journal of Field Robotics*, 36, pp.1-23. DOI: <https://doi.org/10.1002/rob.21889>

REGULAR ARTICLE

An autonomous strawberry-harvesting robot: Design, development, integration, and field evaluation

Ya Xiong  | Yuanyue Ge | Lars Grimstad | Pål J. From

Faculty of Science and Technology, Norwegian University of Life Sciences, Ås, Norway

Correspondence

Ya Xiong, Faculty of Science and Technology, Norwegian University of Life Sciences, Ås 1433, Norway.
Email: yaxio@nmbu.no

Funding information

Norges Miljø- og Biovitenskapelige Universitet; Norwegian University of Life Sciences, Norway

Abstract

This paper presents an autonomous robot capable of picking strawberries continuously in polytunnels. Robotic harvesting in cluttered and unstructured environment remains a challenge. A novel obstacle-separation algorithm was proposed to enable the harvesting system to pick strawberries that are located in clusters. The algorithm uses the gripper to push aside surrounding leaves, strawberries, and other obstacles. We present the theoretical method to generate pushing paths based on the surrounding obstacles. In addition to manipulation, an improved vision system is more resilient to lighting variations, which was developed based on the modeling of color against light intensity. Further, a low-cost dual-arm system was developed with an optimized harvesting sequence that increases its efficiency and minimizes the risk of collision. Improvements were also made to the existing gripper to enable the robot to pick directly into a market punnet, thereby eliminating the need for repacking. During tests on a strawberry farm, the robots first-attempt success rate for picking partially surrounded or isolated strawberries ranged from 50% to 97.1%, depending on the growth situations. Upon an additional attempt, the pick success rate increased to a range of 75–100%. In the field tests, the system was not able to pick a target that was entirely surrounded by obstacles. This failure was attributed to limitations in the vision system as well as insufficient dexterity in the grippers. However, the picking speed improved upon previous systems, taking just 6.1 s for manipulation operation in the one-arm mode and 4.6 s in the two-arm mode.

KEYWORDS

active obstacle separation, agricultural robotics, cable-driven gripper, field evaluation, strawberry-harvesting robot

1 | INTRODUCTION

Strawberries (*Fragaria × ananassa* Duch.) are farmed extensively in most parts of the world, growing either outdoors in open fields or in controlled environments, like greenhouses or polytunnels. In 2016,

according to market research company IndexBox, the global strawberry market amounted to 9.2 million tons, increasing by 5% against the previous year. Strawberry production is heavily reliant on human labor, especially for harvesting (Xiong, Peng, Grimstad, From, & Isler, 2019). It was reported that 25% of all working hours in Japan

This is an open access article under the terms of the Creative Commons Attribution-NonCommercial-NoDerivatives License, which permits use and distribution in any medium, provided the original work is properly cited, the use is non-commercial and no modifications or adaptations are made.

© 2019 The Authors. *Journal of Field Robotics* Published by Wiley Periodicals, Inc.

are consumed by harvesting operations (Yamamoto, Hayashi, Yoshida, & Kobayashi, 2014). Strawberry producers in the Western world, particularly the United Kingdom and United States, are similarly concerned about the future availability of labor for picking, as well as about inflation in the cost of labor. In the United Kingdom, for example, the need is especially significant in the soft fruit sector, which uses 29,000 seasonal pickers to generate over 160,000 tons of fruit every year (British summer fruits seasonal labor report, 2017). In California, the cost of manual harvesting cost could be as much as 60% of production costs for fresh market strawberries (Anjom, Vougioukas, & Slaughter, 2018), which concurs with research conducted in Norway (Xiong et al., 2019). These dual labor challenges of shortages and high costs are, therefore, advancing developments in the automation of fruit harvesting operations.

Despite several attempts to develop a robotic solution for harvesting strawberries and many other crops, a fully viable commercial system has yet to be established (Silwal et al., 2017). One of the major challenges is that the robots need to be able to operate equally efficiently within diverse, unconstrained environments and crop variations with a variety of features (Bac, Hemming, & Van Henten, 2013; Silwal et al., 2017). A harvesting robot is generally a tightly integrated system, incorporating advanced features and functionalities from numerous fields, including navigation, perception, motion planning, and manipulation (Lehnert, McCool, Sa, & Perez, 2018). These robots are also required to operate at high speed, with high accuracy and robustness and at a low cost, all features that are especially challenging in unstructured environments, such as the strawberry farm utilized for testing in this paper.

Fruit harvesting offers significant opportunities for the field of agricultural robotics and has, thus, gained much attention in recent decades. Several robots have been developed for harvesting fruits and vegetables, including those for apples, sweet peppers, cucumbers, tomatoes, litchis, and strawberries. An apple robotic harvester was designed and evaluated with an overall success rate of 84% and an average picking time of 6.0 s per fruit; however, they encountered challenges, such as obstacle detection and avoidance (Silwal et al., 2017). A sweet pepper-harvesting robot achieved success rates of between 26% and 33% in a modified environment and a cycle time of 94 s for a full harvesting operation (Bac et al., 2017). Similarly, another sweet pepper-harvesting robot, named Harvey, achieved a 46% success rate for unmodified crops and 58% for modified crops, with average picking times of 35–40 s (Silwal et al., 2017). They reported that the most common detachment failure was that of the cutter missing either side of the peduncle. This team subsequently presented an improved version of Harvey, with a higher success rate of 76.5% in a modified scenario (Lehnert, McCool, et al., 2018). A harvesting robot was developed for greenhouse tomatoes, with a success rate of 86% and a picking speed of approximately 15 s per tomato (Lili et al., 2017); however, the literature provides no in-depth analysis of their failure cases. A study of cherry tomato harvesting robot reported a success rate of 83%, with an average 1.4 attempts for each successful picking and a time cost of 8 s for a single

successful harvesting excluding the time cost of moving between targets (Feng, Zou, Fan, Zhang, & Wang, 2018). The main failure found in the tests was collisions between the end-effector and the plant stems (Feng et al., 2018).

An increasing number of robots for autonomous strawberry picking have also been developed in recent few years. Japanese researchers developed and evaluated a strawberry-harvesting robot with a scissor-like cutter, which had a success rate of 34.9% and 41.3% when picking with suction and without suction, respectively (Hayashi et al., 2010). Their harvesting time for single fruit was 11.5 s. They concluded that a suction end-effector did not greatly contribute to picking performance and further reported that their failures were incorrect peduncle detection (Hayashi et al., 2010). The groups subsequent version of this strawberry-harvesting robot achieved a success rate of 54.9%. Another strawberry-harvesting robot using a 3D Cartesian-type arm was tested by its detection of the peduncle before picking target strawberries laid out on a laboratory surface (Cui, Gejima, Kobayashi, Hiyoshi, & Nagata, 2013). The system achieved a successful detection rate of 70.8% with a successful picking cycle time of 16.6 s per fruit, and the authors reported the main challenge for their work as peduncle detection (Cui et al., 2013). Unlike the abovementioned selective harvesting robots, researchers also proposed a strawberry harvester that shook the plants to detach fruits (Vakilian, Jafari, & Zarafshan, 2015). The focus of this study was mainly on the dynamics modeling and control. Aside from research in academia, a number of start-up companies have also recently developed several strawberry-harvesting robots, none of which have successfully commercialized. These include AGROBOT (Huelva, Spain), who used 24 independent picking systems mounted on a mobile base to increase efficiency, OCTINION (Leuven, Belgium), who designed a force-limit soft gripper in an attempt to avoid damage while grasping, and Harvest CROO (Florida) who designed a rotation apparatus that includes several grippers for picking strawberries on the ground. Generally, strawberry harvesting in cropping environment is very challenging. First, ripe strawberries are easily damaged and bruised (Dimeas, Sako, Moulianitis, & Aspragathos, 2015; Hayashi et al., 2014; Xiong et al., 2019). This feature requires gentle handling during manipulation procedures. Noncontact picking might be an acceptable solution to avoid damage. Second, strawberries are small in size and tend to grow in clusters, which makes it difficult to identify and pick individual strawberries (Xiong et al., 2019; Yamamoto et al., 2014). Picking in clusters with dense obstacles is one of the main challenges for strawberry harvesting (Xiong et al., 2019; Yamamoto et al., 2014) as well as for many other crop harvesting systems, such as tomato harvesting (Yaguchi, Nagahama, Hasegawa, & Inaba, 2016) and sweet pepper robot (Bac et al., 2016).

In this paper, we address some of the challenges of working in unstructured farming environment. The main contributions of this paper are as follows:

- (1) A novel active obstacle-separation path-planning algorithm for cluster picking: The gripper can actively push aside the bottom

- obstacles before swallowing and separate the top obstacles during swallowing. The pushing vectors are derived based on the surrounding obstacles that are calculated using downsampled blocks of 3D point cloud.
- (2) Improvements to the vision system, the gripper, the arm, and the control: An adaptive color thresholding for adaption of ambient changing light, a new feature of the gripper that can pick a market punnet and harvest berries straight into the container and a low-cost dual-arm system with optimized harvesting order.
 - (3) A fully integrated harvesting system: The robot is able to pick strawberries continuously in polytunnels. Field evaluation shows the robot's first-attempt success rate for picking partially surrounded or isolated strawberries ranged from 50% to 97.1%, depending on the growth situations.

2 | RELATED WORK

2.1 | Fruit identification

Machine vision is an essential component for agricultural robots, enabling them to detect and localize the target crop. When the 3D position of a target is obtained, its coordinates can be further utilized to instruct the movements of the manipulation. For strawberry detection, image processing based on color thresholding is a frequently applied method in research papers (Hayashi et al., 2014; Yamamoto et al., 2014), primarily due to the significant differences of color among ripe strawberries, green strawberries, and green plants. Peduncle detection is another widely researched harvesting step (Cui et al., 2013; Hayashi et al., 2010; Huang, Wane, & Parsons, 2017; Shiigi et al., 2008). Color-based image processing methods were used to detect the strawberry first and then set a certain region above the strawberry for peduncle detection, with the accuracy influenced by the results of preprocessing and complexity of the environment. Other researchers have explored feature learning methods to analyze strawberry fruit shapes (Ishikawa et al., 2018). Recently, extensive work used deep learning as an approach for fruit detection. Deep learning, which can autonomously extract fruit features, has shown results in strawberry detection (Habaragamuwa et al., 2018). In addition to strawberries, deep learning, especially the Faster RCNN network, has been widely used for detection of many other fruits, including sweet pepper, mango, apple, almond, and kiwifruit (Fu et al., 2018; Mai, Zhang, & Meng, 2018; Sa et al., 2016; Zhang et al., 2019). All these systems used detection networks to generate bounding boxes around the target fruits.

Unstructured growing conditions, including variable clustering, occlusions, and varying lighting conditions, have been considered as the common challenges for fruit detection in farm environments (Silwal et al., 2017). Consequently, the focus of much ongoing research is novel ways to resolve these situations. One study proposed a color-based adaptive thresholding method for sweet pepper detection that can deal with changing illumination conditions (Vitzrabin & Edan, 2016), for example, while another proposed a

visual servoing-based method accurately localizes sweet peppers in occlusion situations (Lehnert, Tsai, Eriksson, & McCool, 2018). Deep learning is a promising method to deal with the lighting variations and the general idea is to capture and train images under different lighting conditions (Bargoti & Underwood, 2017; Fu et al., 2018). However, this method may require additional hardware (GPU) and a large data set as well as intensive work on image annotations, thus increasing the cost and power consumption.

2.2 | Mobile platform and navigation

Over the years, mobile platforms have been developed for a range of agricultural applications, from weeding (McCool et al., 2018), to high throughput phenotyping (Vijayarangan et al., 2017), to transportation (Ye et al., 2017). Some mobile robots are task-specific, meaning that they are specially designed for one particular application. Several task-specific mobile bases can be found in literature including the sweet pepper-harvesting robot (Lehnert, English, McCool, Tow, & Perez, 2017) and robots for phenotyping (Mueller-Sim, Jenkins, Abel, & Kantor, 2017). Task-specific mobile bases can also be found in various commercial projects, for example, the weeding robots created by companies like ecoRobotix and Franklin Robotics, and harvesting robots being developed by companies like AGROBOT or Harvest CROO Robotics. Other mobile robots are generic, designed to work with multiple, interchangeable implements, and can thus be used in several different applications. Examples include Bonirob by Bangert et al. (2013), and Robotti by commercial company Agriointelli.

Most agricultural robots rely on a mobile base, that is, specifically designed for one type of environment. A mobile base designed for driving in tractor-sized tracks in open fields, for example, will normally not fit in a greenhouse. There is a lot of variation found in agriculture, and there may be large differences between farms, even if they grow the same crop. The mobile platform used in the current work is the Thorvald robot (Grimstad, Skattum, Solberg, Loureiro, & From, 2017). It is created from modules that may easily be reconfigured into robots of different sizes and shapes for different environments. A slim robot configured for greenhouses and polytunnels, such as the one used in this study, may quickly and easily be resized wide enough to fit within tractor tracks. The robots navigation system is different depending on project and application. In previous work we used techniques based on light detection and ranging (LIDAR) and cameras (Grimstad, Zakaria, Le, & From, 2018) as well as RTK-GPS (Grimstad et al., 2017). The navigation system used in polytunnels in current work is based on well-established techniques of probabilistic localization (Thrun, Burgard, & Fox, 2005) as well as the use of topological maps (Fentanes, Lacerda, Krajnik, Hawes, & Hanheide, 2015). The navigation setup is briefly described in Section 4.

2.3 | End-effector and manipulation

Various end-effectors have been developed for strawberry-harvesting robots. The most widely used is the scissor-like end-effector for

fruit detachment purpose only (Cui et al., 2013; Hayashi et al., 2014; Yamamoto et al., 2010; AGROBOT Ltd.; Dogtooth Technologies Ltd.). With an additional suction device, the scissor-like end-effector might be able to hold fruit (Feng, Wang, Zheng, Qiu, & Jiang, 2012; Hayashi et al., 2010). Contact grasping grippers are also common to see, such as the three-finger clamps with force-limit function (Dimeas et al., 2015) and two or more fingers with rotational motion to break peduncles (Yamamoto et al., 2014; OCTINION Ltd.). The scissor-like gripper requires more advanced vision system to detect the peduncle position and might unintentionally cut surrounding plants in clusters (Hayashi et al., 2010; Xiong et al., 2019). The grasping contact type grippers might easily bruise fragile strawberries (Hayashi et al., 2010).

Due to the uncertain environment, such as the presence of obstacles and clusters of fruits, manipulation is considered one of the main challenges in getting harvesting robots to become a reality (Lehnert, McCool, et al., 2018; Silwal et al., 2017). Cluster picking is difficult since the surrounding fruits, leaves, stems and other obstacles are difficult to separate from the target, both in detection and in manipulation. Similar to many other picking systems (Cui et al., 2013; Hayashi et al., 2014), our previous system used a point-to-point path-planning method to move the arm from a start point to a point underneath the target. However, with this method, it was difficult for the gripper to avoid swallowing below-hanging or surrounding berries, leaves, or stems along with its target berry. To avoid occlusions, a "3D-move-to-see" method was proposed to find the best view with less occlusions (Lehnert, Tsai, et al., 2018). To avoid obstacles, a method for cucumber picking was developed that uses a search algorithm to explore the search space for a feasible trajectory, in which each step of the trajectory is checked by a collision detector (Van Henten et al., 2002). Another work used a randomized path planner to generate a random path tree and then tested each path with a local path planner to determine the collision-free one for pruning grape vines (Botterill et al., 2017). Furthermore,

to avoid the arms self-collision or collision with obstacles, they incorporated a collision detector based on geometric primitives. Most of the methods found in the literature are passive obstacle avoidance methods, in which the aim is to avoid existing obstacles without changing the environment. However, obstacles are not always avoidable, especially when picking small-size fruits in clusters, where the obstacles may be extremely close to the targets.

2.4 | Previous work and challenges

In 2017, we developed the first version of a strawberry-harvesting robot and implemented a set of field experiments for performance evaluation (Xiong et al., 2019). As shown in Figure 1a, the robot hardware comprised four modules: (a) a cable-driven gripper attached to (b) a Mitsubishi five-degrees-of-freedom (5-DOF) serial arm, mounted on (c) the Thorvald platform (Grimstad et al., 2017) and (d) a stationary RGB-D camera facing one side of table-top grown strawberries. The fingers of the novel cable-driven gripper (Figure 1b) were able to separate surrounding berries out of the way and could open to form a closed space in which to swallow a target strawberry (Xiong, From, & Isler, 2018). Equipped with three internal infrared (IR) sensors, the gripper could sense and correct for positional errors. An integrated container was used for collecting picked strawberries, which reduced picking time significantly; however, this system necessitated repacking the strawberries into punnets for market. The vision system of this version used a color thresholding-based algorithm for object detection and localization; however, the thresholds needed to be changed manually according to the changing sunlight intensity. Furthermore, while the industrial arm was robust and convenient, it was not suitable for use in small working spaces, which limited its picking operation, and the systems significantly low baud rate made it unsuitable for closed-loop control. The robot could pick strawberries continuously without being integrated into the platform, which was moved with a joystick.

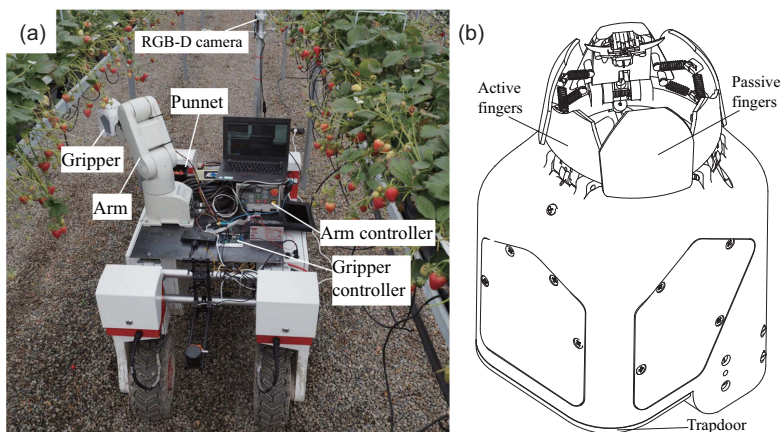


FIGURE 1 The previous version of our strawberry picking robot: (a) The first version robot in a strawberry tunnel and (b) the cable-driven gripper with perception capabilities. Source: Xiong et al., 2018 [Color figure can be viewed at wileyonlinelibrary.com]

The evaluation results showed that the robot was capable of a 96.8% success rate when picking isolated strawberries, but it struggled when picking in clusters, resulting in a low success rate (53.6% without damage) in farm setting.

48 hr of continuous picking. All of the components are connected to a laptop (Intel i5-6700 CPU and 16 GB RAM), including the robotic platform, thus simplifying communication. The entire system is fully integrated into the robot operating system (ROS).

3 | OVERVIEW OF THE NEW SYSTEM

The autonomous strawberry-harvesting system described in this paper incorporates the lessons and addresses the challenges of the original robot, described above. The images and captions in Figure 2 provide an overview of the new robot, photographed during field testing on an English strawberry farm. As with the previous system, the hardware consists primarily of four modules, namely, an Intel R200 RGB-D depth camera, a newly developed single-rail dual-arm manipulator, two improved patented grippers, and a previously developed Thorvald platform. A Hokuyo LIDAR is mounted on the front of the robot for navigation sensing. The arm module is mounted horizontally on the platform for picking strawberries along one side of the table-top trays. The stationary RGB-D camera faces the same side for strawberry detection and localization. An additional one-axis punnet station, attached to the left side of the platform, lifts up to enable the grippers to pick or release the punnets and returns to its lower position once the operation is complete. The punnet station uses the same motor and control system as the arm system. Electronics are placed on the rear of the robot. These include a gripper controller, a CAN to USB convertor for the arm, a DC 48 to 12V power convertor, and a power switch. All power is provided by the Thorvald battery, which supports approximately

4 | NAVIGATION IN TABLE-TOP FARMS

Table-top systems are commonly used in polytunnels and greenhouses. Several different systems exist, and there is therefore a great deal of variation between farms in terms of infrastructure. Some farms have tables mounted on poles in the ground, while others suspend their tables from the ceiling. The spacing between rows, as well as the overall layout of the tunnels or greenhouses, also varies between farms. As the navigation system for the mobile base used in this study was tested in a polytunnel with table-tops mounted on poles in the ground, it is this type of environment that is discussed here.

The mobile robot was assembled using modules from the previously developed Thorvald II modular system, described above. The robot has four-wheel drive and four-wheel steering, which enables it to move in any direction, and also turn in place, thus substantially increasing its ability to navigate tight spaces. The system is fitted with a Hokuyo UTM-30LX-EW 2D LIDAR and an Xsens MTi-30 IMU; however, the latter was not used for the purposes of this paper.

In addition to tens, or even hundreds of polytunnels on a strawberry farm, there are several other points of interest for a robot, including charging stations and cold storage units for harvested fruit. Therefore, to simplify the task of navigating this

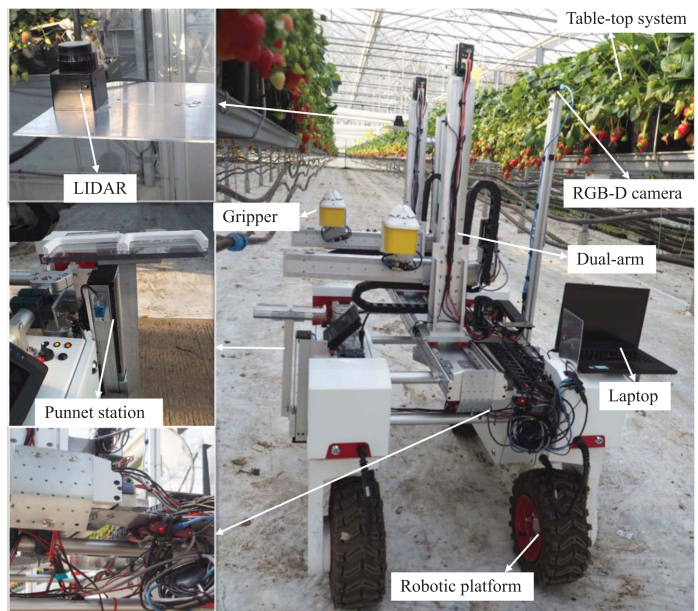


FIGURE 2 Hardware assembly of the new strawberry-harvesting robot in a strawberry greenhouse: The robot consists mainly of a RGB-D camera, a single-rail dual-arm manipulator, two grippers, and a mobile platform [Color figure can be viewed at wileyonlinelibrary.com]

type of complex environment, a topological navigation system is employed (Fentanes et al., 2015). Here, a metric map is used together with a graph. Nodes in the graph represent goals or gateways found in the polytunnel, while edges represent navigable paths between two nodes. The robot can only move between connected nodes. When provided with a goal, the robot will find a connected set of nodes to the goal node, and move through these nodes to reach its target. Different actions for moving the mobile robot can be defined for the different edges. For example, if the robot needs to dock at a charging station, a special action for accurate docking may be required. Moreover, different behavior may be required when the robot is moving in an open space, compared to when it is driving inside a tunnel row where movement is far more constrained. Edges between two nodes can be defined as either unidirectional or bidirectional, enabling operators to enforce one-way traffic where necessary, specifying that a robot may, for example, move from Node A to Node B, but not from Node B to Node A.

Encoder-based velocity estimates are used together with data from the 2D LIDAR to create a map using the GMapping simultaneous localization and mapping (SLAM) technique (Grisetti, Stachniss, & Burgard, 2007). During this process the robot is teleoperated. The resulting map is stored and used by the robot during autonomous operation. The robot uses the map, LIDAR data, and encoder-based odometry to localize in the tunnel. A copy of the map is altered to mark out areas where the robot is not allowed to drive and the robots global costmap is generated from this no-go map. This prevents the robot from planning paths through certain areas, such as underneath the table trays between rows.

The robots navigation system was tested in a polytunnel at a research farm. As such, the size of the topological map presented here (Figure 3) is somewhat limited; however, the principles are equally applicable to larger polytunnel environments. First, we defined the topological nodes on either sides of four rows in the tunnel, as well as intermediate nodes inside these rows. A node representing the robots charging station and a few gateway nodes between the charging station and the tunnel rows were further defined. Unidirectional edges (for one-way driving) was defined for inside two of the rows, and the remaining two rows were defined as bidirectional edges. Possible actions for moving the robot along the edges were specified as simple waypoint navigation, with either forward drive, sideways drive, or reverse drive, as well as a dynamic window approach for navigation around unforeseen

obstacles. For edges inside the rows, only simple waypoint navigation was used, with no planning around unforeseen obstacles (if an obstacle appears, the robot will simply stop and wait until the obstacle is moved). A reverse action was specified for the edge going to the charging station, while the robot would use forward drive along the edge moving away from the charging station. Edges between rows were specified as either forward drive or sideways drive.

Using this system, the mobile robot was able to successfully navigate the somewhat cramped environment inside the polytunnel. In the supplementary materials, the robot can be seen navigating the tunnel, starting at the node representing the charging station and then driving once through all four rows before returning to park at the charging station.

5 | ENVIRONMENT ADAPTIVE MACHINE VISION

5.1 | Motivation

As with many other field machines (Bac et al., 2017; Hayashi et al., 2014), a color-based algorithm was utilized in this system to take advantage of color differences and retain a fast processing speed. Hue saturation value (HSV) images are transformed from the RGB images and used for image processing. The aim with this machine vision subsystem is to detect and localize ripe strawberries and to pass the detected strawberry bounding boxes to the other subsystems.

Changing ambient illumination in the field is a challenge for image processing. During the experiments, it was found that changes in the available sunlight significantly influenced the detection results. As shown in Figure 4, Figure 4a displays situations with weak light intensity, while Figure 4b shows much stronger light intensity in the same place. As a result, four strawberries were detected in Figure 4a (blue circles) but only one in Figure 4b, with the same thresholds. This problem was also pointed out by Hayashi et al. (2014), who subsequently adjusted the thresholds on their system manually on the farm, as with our previous system. Raja et al. (1998) proposed a statistical approach, in which light intensity was estimated over time, while other researchers have investigated how robots can learn to adapt to various lighting conditions (Sridharan & Stone, 2007). In this paper, we propose a modeling-based technique for automatic updating thresholds by using the grippers IR sensor.

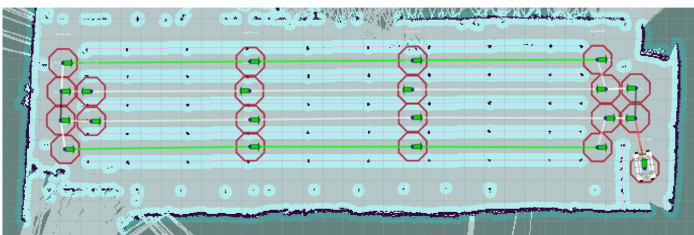
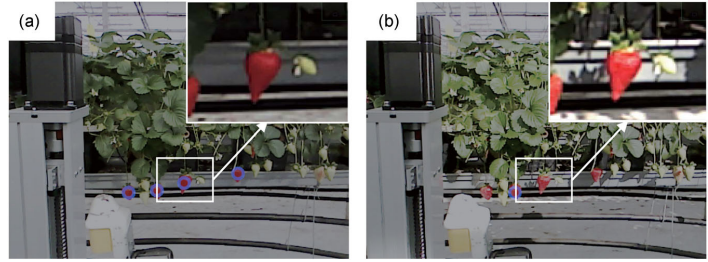


FIGURE 3 Topological map for driving in a polytunnel. Here, the robot can be seen parked in the lower right corner [Color figure can be viewed at wileyonlinelibrary.com]

FIGURE 4 Two set of images capturing the same area with different light intensities: (a) shows low sunlight intensity, in which four strawberries were detected (in blue circles) and (b) shows high sunlight intensity, in which only one berry was identified, despite having the same threshold as (a) [Color figure can be viewed at wileyonlinelibrary.com]



5.2 | Light intensity modeling and adaptive color thresholding

The robots gripper has internal IR sensors that can sense pure sunlight IR light intensity when the emitter light-emitting diodes are turned off in a mouth-open configuration (Figure 1b). Therefore, the HSV in the region of a ripe strawberry and the gripper IR value were recorded for almost an entire day. A sufficient amount of data about the range of sunlight intensities and corresponding HSV values is essential to ascertain the relationship between them. In total, 243 sets of data were recorded with various sunlight intensities and the corresponding HSV values of the ripe strawberry. To determine the connection between the values, the HSV data were analyzed independently, as can be seen in Figure 5. Here, hue range is from 0 to 179 (circular) in OpenCV and the value for pure red is 0. To clearly see the dependent relationship in the coordinate system, data around 0 were added by 179 to obtain Figure 5a. As the variations in the range of hue are relatively small, at around 5, the interaction is not significant and, therefore, it can be concluded that light density has a low influence on the hue for strawberry detection. However, based on the data in Figure 5b,c, it is clear that saturation and value change regularly with the variances in sunlight intensity. The correlation equations of saturation-sunlight intensity and value-sunlight intensity can thus be concluded as follows:

$$y_s = -0.00069x^2 + 0.13x + 157.03 (R^2 = 0.86), \quad (1)$$

$$y_{value} = -0.049x + 137.07 (R^2 = 0.86). \quad (2)$$

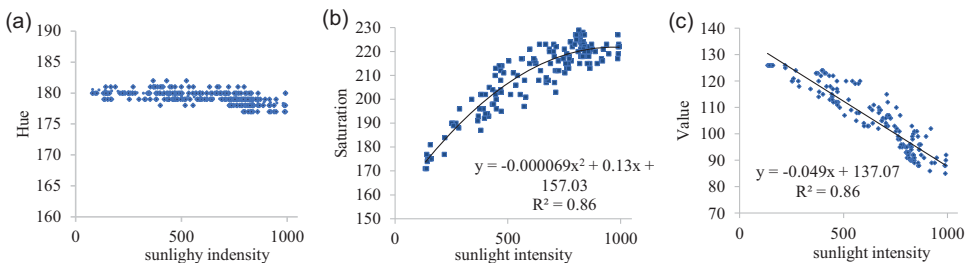


FIGURE 5 Modeling of HSV and sunlight intensity: (a) Hue to sunlight intensity, no significant interactions; (b) saturation to sunlight intensity, significant quadratic relationship; and (c) value to sunlight intensity, significant linear relationship. HSV, hue saturation value [Color figure can be viewed at wileyonlinelibrary.com]

In application, the above models would be recorded in the codes. The gripper would detect the real-time sunlight intensity at the beginning of each image frame for every picking circle. The image processing algorithm would then set the saturation and value thresholds within ranges based on the detected sunlight intensity according to the correlation equations, thus forming an adaptive color threshold. After the basic color-thresholding process, the strawberry image would go through a series of postprocessing based on erosion and dilation, as previously described by the authors (Xiong, Ge, Liang, & Blackmore, 2017). During this processing, two commonly connected strawberries can be segmented. Once all the strawberries have been detected, their coordinates would be transferred to the gripper frame according to the calibrated extrinsic parameters.

6 | SINGLE-RAIL MULTIPLE CARTESIAN ARMS

In the authors' previous strawberry-harvesting system, a Mitsubishi serial arm (RV-2AJ) with 5-DOF was employed, which was robust in terms of control and communication (Xiong et al., 2018). However, the high cost of the industrial arm is not appropriate for application in commercial farming robots, especially when multiple manipulators are required to optimize the harvesting efficiency. Moreover, in the previous system, the orientation of the 5-DOF arm was locked to keep the gripper horizontal, which also made its working space small,

however, in the system, the gripper is designed so that its workspace is strictly Cartesian, with no rotations needed, and, therefore, a 3-DOF Cartesian arm is sufficient to generate this motion. The Cartesian arm is widely used due to its simplicity and low cost. Moreover, unlike the serial arm, it has no singularity problem and it has a wider working area if no rotations are required. In their development of harvesting robotics, researchers have developed a 3-DOF Cartesian-type arm for strawberry picking (Cui et al., 2013) as well as an algorithm to plan the movements of multiple (Zion et al., 2014), independently functioning 3-DOF Cartesian arms for crop harvesting, mounted in backward-forward positions on the platform. In this current system, to mitigate cost and complexity, a low-cost single-rail-based Cartesian-type multiarm system was developed.

6.1 | Arm design and hardware

Figure 6 shows the concept design and the prototype of the proposed arm. In Figure 6a, the three arms have independent y-axis and z-axis rails, mounted on a common x-axis rail. The vertical z-axis rail uses ball-screw transmission for lifting heavy loads, while the y-axis uses a belt transmission for fast movement. The pinion-rack helical gear transmission between the x-axis rail and the y/z-axis rails enables the arms to have independent movement on the x-axis. Compared to a system with several independent arms, the single-rail multiarm system has three key advantages for harvesting robots: (a) two or more arms can be mounted on the same rail so that the transformation between the arm frame and the camera frame need only be calibrated once; (b) there is no unreachable space between the arms; (c) the cost is reduced as fewer parts are required and the time required for platform mounting is also reduced.

Figure 6b shows the assembly prototype of the proposed arm, which has two arms mounted on the x-axis rail. The arm rails

TABLE 1 Key specifications of the single-rail dual Cartesian arms

Parameters	Value
Dimensions (mm)	1,400 × 900 × (930–1,080)
x-axis stroke (mm)	1,200
y-axis stroke (mm)	500
z-axis stroke (mm)	500
Max velocity (mm/s)	600
Approximate payload (kg)	10
Communication type	CANbus
Operating system	Linux
Control method	ROS topics
Input voltage (V)	48
Rated power (W)	900
Approximate weight (kg)	120

Abbreviation: ROS: robot operating system.

structure was manufactured by the GaoGong Intelligence Mechanical Drive Co., Ltd., China. PL-05N/2 inductive proximity sensors were used as end stops for homing the arms and limiting their movement range. A collision avoidance frame was mounted on Arm 2 that will trigger the end-stop sensor on Arm 1 when the arms are close, so as to avoid any mechanical collision. Stepper servo motors (Shenzhen Just Motion Co., Ltd., China) were selected as they are low in cost and deliver precise position control. These motors have integrated encoders and controllers and can be easily communicated via a CANbus network. A CAN to USB converter was used to enable the computer to access the CANbus network.

Table 1 describes the key specifications of the developed arms. The axis strokes and dimensions were determined by estimating the required picking space in the strawberry tunnels.

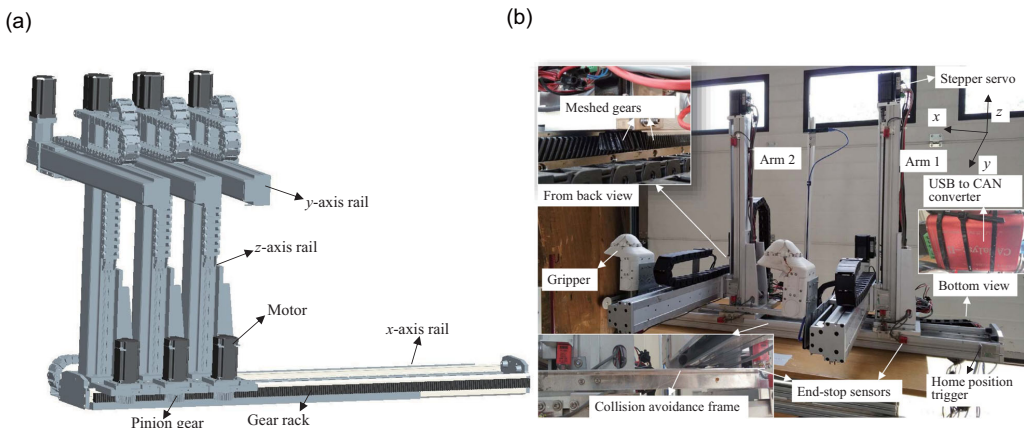


FIGURE 6 Single-rail Cartesian-type multiarm: (a) 3D model shows that the three Cartesian arms move on a single rail (x-axis) using pinion-rack gear transmission; the single-rail (x-axis) could be mounted with two or more arms; (b) the prototype of a dual-arm system; the single-rail multiarm only needs to be calibrated once to identify the transformation between the arm frame and the camera frame [Color figure can be viewed at wileyonlinelibrary.com]

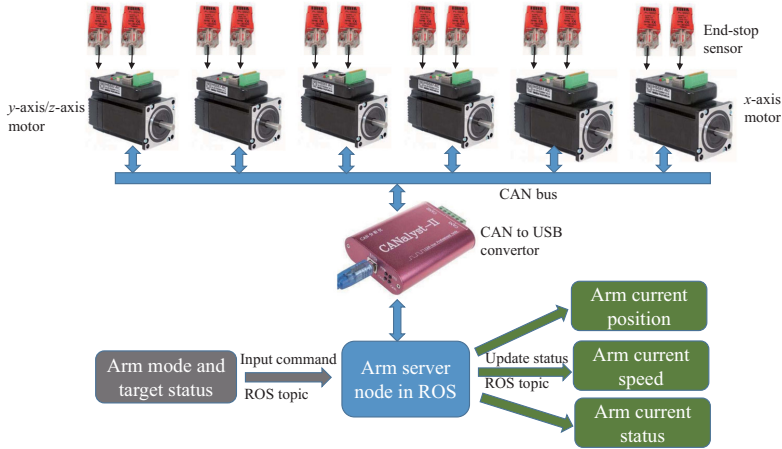


FIGURE 7 Control architecture of the single-rail dual Cartesian arms: All the stepper servos are connected to the CANbus network; a ROS servo node is built to receive target mode and status commands from the user nodes and then control the motors by using CiA 402 protocol; the servo node can also get motor information and update the arm position, speed and status in 40 Hz, which can be used for feedback control. ROS, robot operating system [Color figure can be viewed at wileyonlinelibrary.com]

6.2 | Arm control

Figure 7 indicates the control architecture of the single-rail dual Cartesian arms. The stepper servo is written with CiA (CAN in Automation) 402 motion control protocol. All motors are connected to the host computer through a CAN to USB converter via the CANbus network. To modularize the arm system, an arm server node in ROS was built as a coordinator between user nodes and arms. For input, user nodes can simply send an arm target mode together with the status command to the server node via the ROS topics.

The server node will then decode and encode these commands to control the individual motors. Six modes were established on the basis of the harvesting robots requirements: home, pause, continue, position control, unblock, and reset. The status command includes the arm target positions and the moving speed. Acceleration and deceleration can be automatically adjusted according to the required speed in the server node. Furthermore, the server node can also output the arms status as ROS topics in 40 Hz by reading the motor status. The output data topics include the arms current position, speed, and status, which can be used as feedback control information.

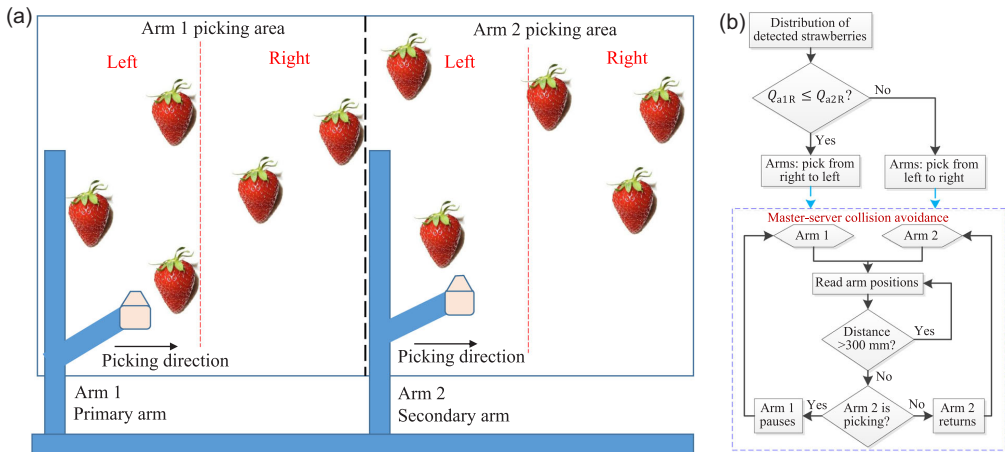


FIGURE 8 Harvesting order planning: (a) Schematic of harvesting order planning, with the picking area divided into two sections, namely, for Arm 1 and Arm 2; the picking area of each has been further separated into two subsections (left and right); if strawberries are uniformly distributed, the two arms systematically pick strawberries from left to right; if they are not uniformly distributed, strategies must be specified to increase picking efficiency and avoid collision; (b) the control algorithm for planning the harvesting order as well as for collision avoidance [Color figure can be viewed at wileyonlinelibrary.com]

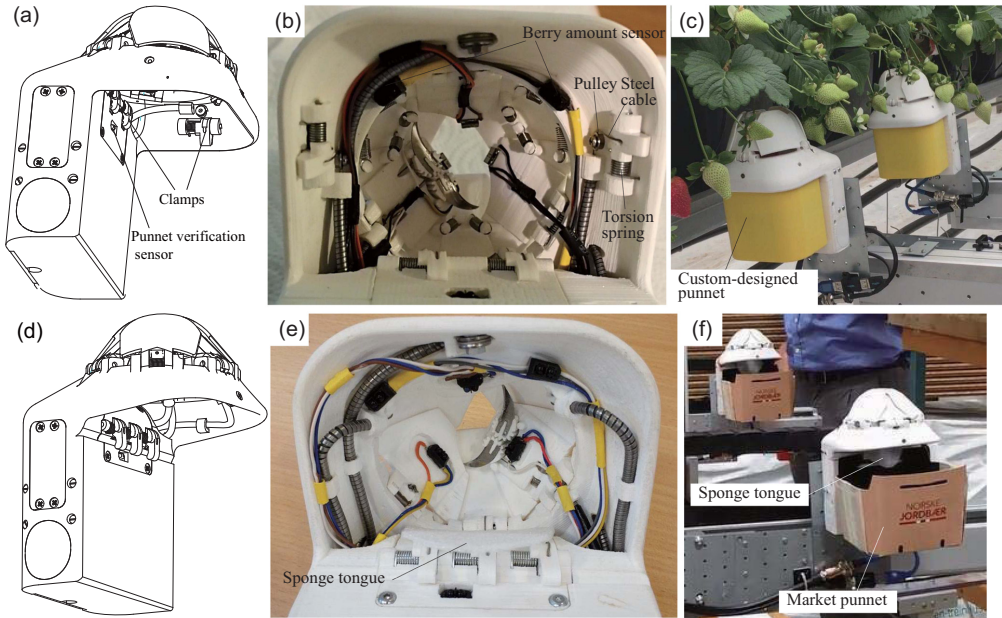


FIGURE 9 Improved gripper design: (a) Sketch of the version 2.1 gripper; (b) bottom view of version 2.1 prototype; three additional IR sensors are used to detect the punnet and estimate the amount of strawberries in it; (c) attaching 3D-printed punnets during picking; (d) sketch of version 2.2 gripper; (e) bottom view of version 2.2 prototype; a sponge tongue is used to reduce impact; (f) market punnets are attached for picking. IR, infrared [Color figure can be viewed at wileyonlinelibrary.com]

The arm current status topic publishes information such as whether the arm has reached the target position or not and its current running status (normal or faulty).

6.3 | Collision avoidance and harvesting order planning

One challenge that the single-rail dual-arm system presents is the effective cooperation between the two arms to increase picking efficiency and avoid collision with each other. In this harvester, as illustrated in Figure 8a, the picking area in the cameras view is divided equally into sections for Arm 1 (the primary arm) and Arm 2 (the secondary arm). Each section is then further separated into two subsections: left and right. Within these, one requirement is that the robot should pick berries from the bottom of the tray working upwards to the top. This is because the gripper is designed to pick from below. If the upper strawberry is picked first, the gripper and arm might touch and move the lower ripe strawberries, which may result in failure when picking the lower targets.

Figure 8b shows the control algorithm for planning the harvesting order as well as for collision avoidance. In the process of inputting the detected strawberries to the algorithm, the first aim is to determine the picking sequence for the arms to maximize the simultaneous picking period of both arms and avoid their possible collisions. The default picking sequence for both arms is from the left

subsection to the right subsection. However, if the quantity of strawberries in the right subsection of Arm 1 (Q_{o1R}) is equal to or less than that in the right subsection of Arm 2 (Q_{o2R}), it is better that both arms pick strawberries from right to left, since Arm 1 will finish picking in its right subsection and move across to the left subsection earlier than Arm 2 will complete its operation. Similarly, when the quantity of strawberries in the Arm 1 left subsection (Q_{o1L}) is equal to or more than that in the Arm 2 left subsection (Q_{o2L}), the distance between the two arms is always larger than the safety distance if they all pick from left to right. Theoretically, then, in this particular case, the distance between the two arms will always be greater than one subsection width (normally around 300 mm, which is equal to the safety distance between the two arms); however this has not been tested in other situations and, therefore, the distance between the two arms on this system cannot be guaranteed to be within the safety range.

In Figure 8b, a primary-secondary method is proposed to control the arms within a closed loop to avoid collisions. Arm 1 is the primary arm, and has picking priority, while Arm 2 acts as the secondary arm. The distance between the two arms is compared in real-time so that, should they come within the safety distance, the secondary arm will return to a safety position provided it is not in picking status and will wait until the primary arm finishes and moves away. However, if the secondary arm is in picking status and close to the primary arms target, the primary arm will not interrupt current picking but will wait

until the secondary arm completes its operation. Thereafter, the picking priority of the primary arm will be restored, so the secondary arm will return to a safety position if the next target is not within safety range.

7 | IMPROVEMENTS ON GRIPPER DESIGN

7.1 | Punnet picking and releasing

The previous version of our gripper included an integrated container for collecting picked strawberries, a feature that could reduce picking time as the arm does not need to move to store each picked strawberry. However, collecting with the container and repacking to the punnets could increase the risk of damage and, therefore, to avoid repacking, the gripper in the new system is designed to pick a punnet and harvest directly into it, as shown in Figure 9. Figure 9a–c shows the design, prototype, and field application of the version 2.1 gripper that was used in the field tests. In this version, instead of a container, the gripper has a hollow space under its fingers to attach a custom-designed punnet, which it picks from the punnet station (Figure 2). Four cable-driven clamps, distributed on three sides of the gripper, are used for picking and holding the punnet. These clamps are opened simultaneously by a servo motor and closed by torsion springs. In addition, an IR sensor placed under the front-side clamps is used to verify the attachment of the punnet. Another two IR sensors, mounted on the bottom of the fingers, are used to estimate the amount of strawberries in the punnet. The IR sensors detect the distance between the obstacle (strawberries in the punnet) and the sensor, which is changed during collection. Once the desired amount of strawberries has filled the punnet, the gripper returns it to the same location on the punnet station. A punnet transportation system is required for stocking empty punnets and collecting full punnets.

A further improved version (2.2) of the gripper was also subsequently developed, as shown in Figure 9d–f. This version of the gripper can pick a market punnet directly, as shown in Figure 9f, in which a new Norwegian standard strawberry punnet is attached. Instead of having four clamps on three sides, this version only has

three clamps on the front side so that the gripper can successfully pick various punnet shapes. Under the clamps, there is a groove for fitting the convex edge of some market punnets. Moreover, a sponge tongue is mounted on the top of the clamps, which can reduce impact significantly. The clamp module is independent of the gripper body, so it can be easily mounted and replaced.

7.2 | Scanning control

In the previous system, the gripper could control the arm using internal IR sensors to correct any positional errors. When targeting a strawberry, the gripper moved to the bottom of the target and used a slow lifting speed in search of the strawberry. Once detected, the arm stopped lifting and moved horizontally to place the gripper at the optimal cutting position based on one located section of the strawberry. This method works well when strawberries are growing vertical to the ground, however, if a strawberry is inclined towards the ground, as per the example shown in Figure 10a (enlarged red berry), one section located on the lower part of the strawberry might be different to another, upper section. This would affect the systems estimation of the location of the peduncle, which it requires for picking. To overcome this challenge, a scanning control method was used in the current system, in which the arm lifts and simultaneously moves the gripper in a horizontal plan to scan the shape of the strawberry. The gripper uses IR sensors to estimate the diameter and centroid of a circular section of an object. Without the gripper moving horizontally, the scanner can even reconstruct the shape and orientation of the strawberry, as is shown in the scan examples in Figure 10a,b.

Figure 10c shows the scanning control path of the gripper for picking the target enlarged in Figure 10a. First, the arm moves quickly to the bottom of the target and lifts the gripper slowly to search for the strawberry. Due to inertia, the arm is not able to come to an abrupt stop once the target has been located, but it will return to the first detection point, so there is an overshoot path. The gripper then uses the scanning control method to control the arm path according to the target strawberry's shape. When the strawberry is

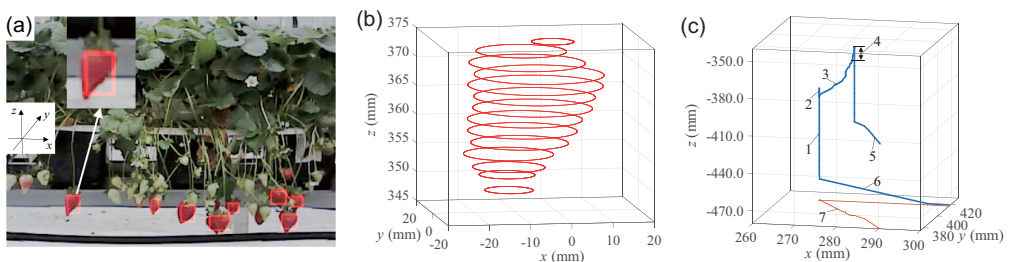


FIGURE 10 Scanning control: (a) An example of detected strawberries, in which the left strawberry (enlarged in image) is inclined to the ground; (b) reconstruction of the shape and orientation information from the grippers scan of the enlarged strawberry in Figure 8a; (c) scanning control path of the gripper for picking the enlarged target in Figure 8a; number represents: 1—searching path, 2—overshoot path, 3—scanning control path, 4—peduncle length adjustment, 5—return path, 6—forward path, and 7—trajectory projection [Color figure can be viewed at wileyonlinelibrary.com]

out of gripper sensing range, the arm moves up quickly with a desired peduncle length compensation value to control the peduncle length that remains on the strawberry after picking. Compared to the previous system, which used properties in the strawberry shape to estimate the peduncle length, this method is robust to the differences in shape and variety, however it does require an increased computation resource.

8 | A NOVEL ACTIVE OBSTACLE-SEPARATION PATH-PLANNING STRATEGY FOR CLUSTER PICKING

The previous system achieved a high success rate for picking isolated strawberries, however, it struggled with cluster picking. In this current work, inspired by human pickers who usually use their hands to push and separate surrounding obstacles during picking, we propose a novel active obstacle-separation path-planning strategy, using the gripper to push obstacles in the clusters.

8.1 | Algorithm

8.1.1 | Scanning control

The first step for obstacle separation or avoidance is to obtain a 3D image of the area. In the current system, a single-view image is used to create the 3D point clouds based on a combination of depth and RGB images. To reduce computation costs, this system extracts and focuses only on the obstacles closest to the target, or region of interest (ROI) obstacles. As illustrated in Figure 11a, the ROI obstacles are those that are located on the bottom or at the same height as the target. The obstacles above the target are irrelevant since the gripper picks from below and, when it is swallowing the target strawberry, they will not affect fruit detachment. Unlike Bac et al. (2013) who classified obstacles into hard and soft types with more efforts from the vision side but did not get significant results, we simply use the quantity of 3D points within the

ROI to determine obstacles without further classification. Our goal is to gently separate all pushable obstacles, similar to human picking. The only nonmovable obstacle is the table-top system, which can be avoided by screening of distance.

ROI obstacles are divided into two main sections: top obstacle blocks and bottom obstacle blocks. Both top and bottom obstacle sections have been further separated into six subsections, based on their directions: left front, left rear, front, rear, right front, and right rear, respectively. The bottom blocks are used to guide the gripper when pushing obstacles aside before reaching its target while the top blocks assist the gripper in avoiding neighboring obstacles. The block size is mainly determined by the bounding box size of the detected target in the vision system. Among the top blocks, the front and rear have the same dimensions as the target block, while the length of the four left and right blocks is 1.5 times that of the target block. The length and width of the bottom blocks are the same as the top left and right blocks, but their height is three times that of the target block.

The two obstacle-separation actions can be described as either pushing aside the bottom obstacles before swallowing or pushing aside the top obstacles during swallowing. The operations are as follows: First, the gripper travels from a start point, S , to an intermediate point, P , that is next to the bottom blocks with the same height, as shown in Figure 11b. The gripper then uses the outside of its fingers to push the bottom obstacles from P to the origin, O , of the Oxy frame in the bottom blocks. This pushing path can be defined as a vector, G_{push} . Block vectors (B_{LF} , ..., B_{LR}) are used to describe the obstacles and calculate the pushing vector, G_{push} . If obstacles are founded within a block, the vector in the block is labeled a unit vector; otherwise the empty block has a zero vector. Currently, the threshold of 3D point quantity for being an obstacle or an empty block is 50. The direction of the vector is determined by the block location. They all face towards the origin of the coordinate system, either vertical or at 45 degree to the x axis. G_{push} can be expressed as

$$A = B_{LF} + B_{LR} + B_F + B_R + B_{RF} + B_{RR}, \quad (3)$$

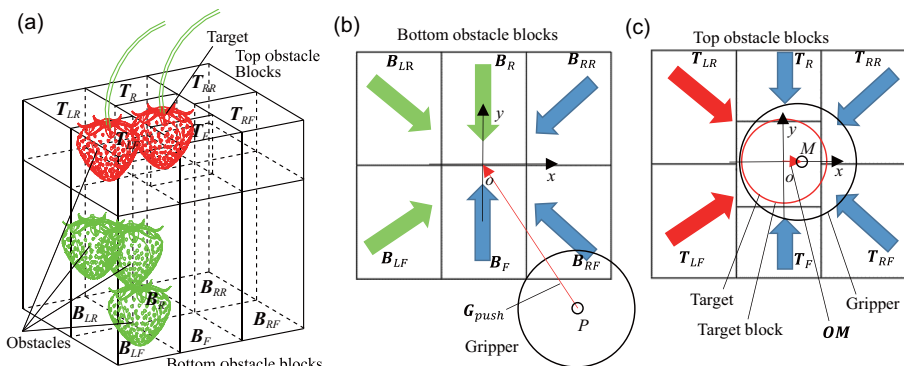


FIGURE 11 Active obstacle-separation algorithm: (a) Schematic of ROI obstacle blocks; (b) top view of bottom obstacle blocks; and (c) top view of top obstacle blocks. ROI, region of interest [Color figure can be viewed at wileyonlinelibrary.com]

$$j = |\mathbf{B}_{LF}| + |\mathbf{B}_{LR}| + |\mathbf{B}_F| + |\mathbf{B}_R| + |\mathbf{B}_{RF}| + |\mathbf{B}_{RR}|, \quad (4)$$

$$\mathbf{C} = (2 - |\mathbf{B}_{LF}| - |\mathbf{B}_{RR}|)(\mathbf{B}_{LF} - \mathbf{B}_{RR}) + (2 - |\mathbf{B}_F| - |\mathbf{B}_R|)(\mathbf{B}_F - \mathbf{B}_R) + (2 - |\mathbf{B}_{RF}| - |\mathbf{B}_{LR}|)(\mathbf{B}_{RF} - \mathbf{B}_{LR}), \quad (5)$$

$$\mathbf{G}_{push} = \begin{cases} -r\mathbf{A}, & \mathbf{A} \neq 0, \\ |\mathbf{A}|, & \mathbf{A} = 0 \text{ and } j \neq 0, \\ \pm r\mathbf{C}, & \mathbf{A} = 0 \text{ and } j \neq 0, \\ 0, & \mathbf{A} = 0 \text{ and } j = 0, \end{cases} \quad (6)$$

where $\mathbf{B}_{LF}, \dots, \mathbf{B}_{LR}$ represents the unit vector that has the same direction as $\mathbf{B}_{LF}, \dots, \mathbf{B}_{LR}$. r is the parameter used to scale the \mathbf{G}_{push} norm, which is 50 mm for the current system. Two opposite vectors, for example \mathbf{B}_{LF} and \mathbf{B}_{RR} , will cancel each other out if they both represent obstacles. If not all vectors are opposite and cancel each other ($\mathbf{A} \neq 0$), the \mathbf{G}_{push} only needs to be obtained using \mathbf{A} and r . j is thus used to determine whether all of the vectors cancel each other out. In the case of $j \neq 0$ and $\mathbf{A} = 0$ (e.g., if only \mathbf{B}_F and \mathbf{B}_R have obstacles), the direction of \mathbf{G}_{push} is then decided by the distance between S and two possible points P (left or right of \mathbf{B}_F and \mathbf{B}_R). The smaller distance point P is selected as it is the shorter traveling time for the gripper. If no obstacles are detected, the gripper has no pushing action at this stage. The intuition of \mathbf{G}_{push} is that the gripper moves from the side of the empty blocks towards the origin O to push the obstacle blocks. The empty blocks can be regarded as the entrance for gripper pushing. Figure 11b demonstrates the obstacle-separation direction for Figure 11a where the left-front, left-rear, and rear blocks (marked as green arrows in Figure 11b) do contain obstacles, so the gripper would come from the bottom right corner to push aside the obstacles.

After clearing aside the bottom obstacles, the gripper will swallow the target and separate it from the top obstacles. As shown in Figure 11a, if an obstacle (left) is next to the target, it is better for the gripper to move an opposite offset (right) at point M before lifting up to swallow the target. In such a way, the gripper can avoid

swallowing the neighboring obstacles. Similarly, the offset vector is calculated \mathbf{OM} by using top block vectors $\mathbf{T}_{LF}, \dots, \mathbf{T}_{LR}$:

$$\mathbf{K} = \mathbf{T}_{LF} + \mathbf{T}_{LR} + \mathbf{T}_F + \mathbf{T}_R + \mathbf{T}_{RF} + \mathbf{T}_{RR}, \quad (7)$$

$$\mathbf{OM} = \frac{R\mathbf{K}}{|\mathbf{K}|}, \quad (8)$$

where R is the norm of \mathbf{OM} , 3 mm in the system. In the situation in 11a, in which a red obstacle is situated to the left of the target, within the left-front and left-rear blocks, the gripper will move 3 mm from the target origin O to the right point M (11b) before moving up to swallow the target. If both bottom and top blocks contain obstacles, the gripper moves directly from P to M without transferring at O .

8.1.2 | Application examples

Figure 12 shows an example of the robot actively separating obstacles by using the proposed algorithm. In Figure 12a, a target ripe strawberry has been detected. The right-top corner figure displays the obstacle blocks around the target. The vision system detected obstacles (marked as green) in three bottom front blocks ($\mathbf{B}_{LF}, \mathbf{B}_F$, and \mathbf{B}_{RF}) and the top front-front block (\mathbf{T}_{RF}). After path-planning, as shown in Figure 13a-1, the gripper moves to the intermediate point P which is behind the obstacles. Then it moves outward to push the front obstacles arriving at point M . After pushing, the gripper is going up to swallow the target. The path of the gripper can be seen in Figure 12b, which is recorded from field test. Without the obstacle-separation algorithm, the below-picking gripper might swallow the surrounding obstacles during lifting.

Figure 13b,c demonstrates two more examples of the active obstacle-separation algorithm in different situations. In Figure 13b-1, a ripe strawberry is detected together with several green strawberries surrounding on the right (\mathbf{T}_F and \mathbf{T}_R) and right-bottom (\mathbf{B}_{RF} and \mathbf{B}_R) sides. Hence, the gripper first move to the left of the obstacles (point P ; Figure 13b-2) and then it pushes the obstacles rightward to point M (Figure 13b-3) for better swallowing. Similarly, as shown in

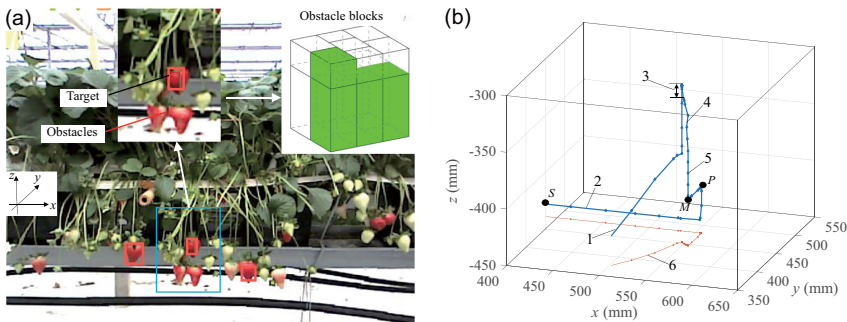


FIGURE 12 An example of active obstacle-separation in the field test: (a) Detection of target strawberries and obstacles; (b) path of the gripper for picking the target using the obstacle-separation algorithm; number represents: 1—return path, 2—forward path, 3—peduncle length adjustment, 4—scanning control path, 5—searching path, and 6—trajectory projection [Color figure can be viewed at wileyonlinelibrary.com]

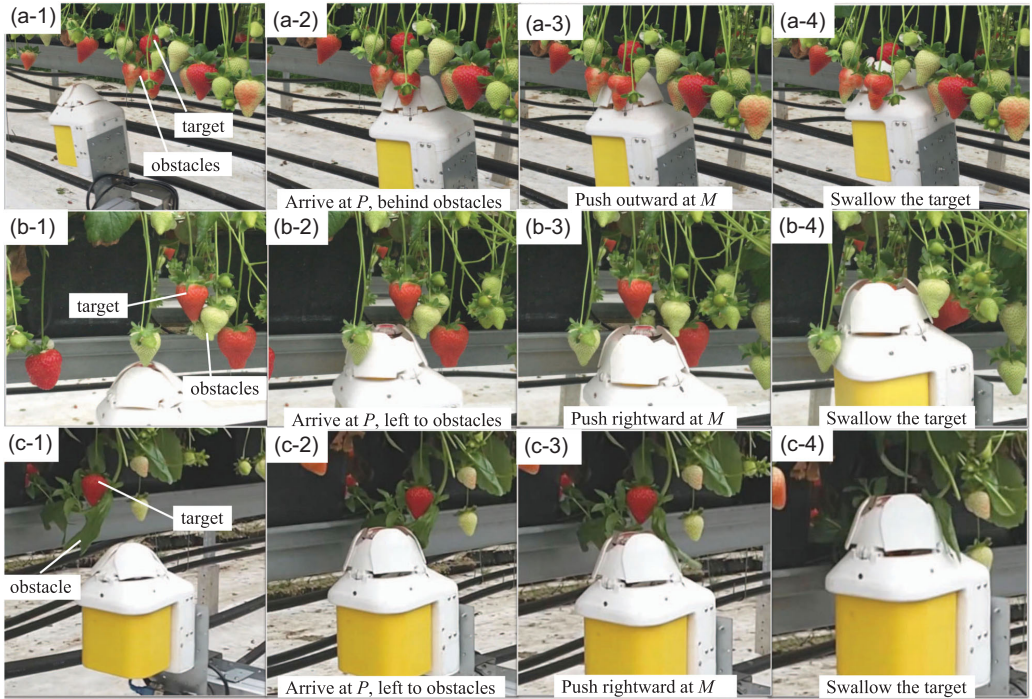


FIGURE 13 Action sequence of active obstacle separation in the field: (a-1 to a-4) picking sequence of the example in Figure 10 to separate the front obstacles; (b-1 to b-4) example of pushing the right-bottom green berries; and (c-1 to c-4) example of removing bottom leaves [Color figure can be viewed at wileyonlinelibrary.com]

Figure 13c-1, a huge leaf is on the bottom of a target. To avoid getting stuck by the leaf (the gripper mouth may be sheltered by the leaf), the gripper moves to the left of the leaf (Figure 12c-2) and pushes the leaf to the right side of the target (Figure 13c-3) before picking.

Figure 12 shows an example of the robot actively separating obstacles by using the proposed algorithm. In Figure 12a, a target ripe strawberry has been detected. The right-top corner figure displays the obstacle blocks around the target: the vision system detected obstacles (marked as green) in three bottom front blocks (B_{LF} , B_F , and B_{RF}) and the top right-front block (T_{RF}). After path-planning, as shown in Figure 13a-1, the gripper moves to the intermediate point P , which is behind the obstacles. Then it moves outward to push aside the front obstacles before arriving at point M . After pushing, the gripper moves up to swallow the target. The path of the gripper can be seen in Figure 12b, recorded from field test. Without this obstacle-separation algorithm, the below-picking gripper is at risk of swallowing the surrounding obstacles during lifting.

Figure 13b,c further demonstrates two more examples of the active obstacle-separation algorithm in different situations. In Figure 13b-1, a ripe strawberry has been detected together with several green strawberries surrounding it on the right (T_F and T_R) and

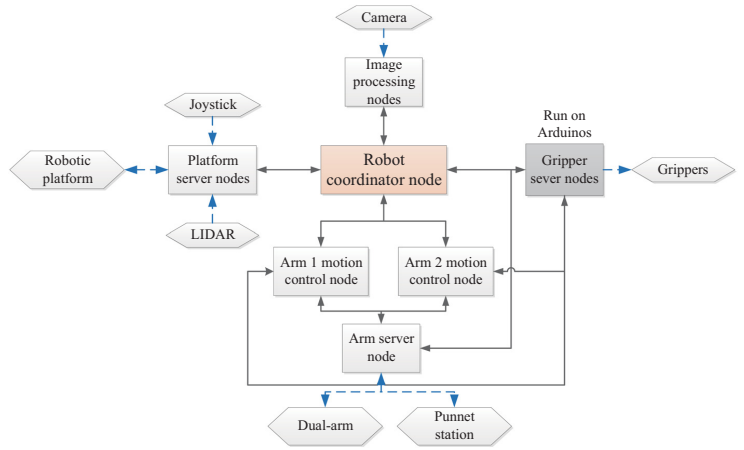
right-bottom (B_{RF} and B_{RR}) sides. Hence, the gripper first moves to the left of the obstacles (point P ; Figure 13b-2) and then it pushes the obstacles rightward to point M (Figure 13b-3) for better swallowing. Similarly, as shown in Figure 13c-1, leaves has been detected on the bottom of a target. To avoid getting stuck (as the grippers mouth may be sheltered by the leaves), the gripper moves to the left of the leaf (Figure 13c-2) and pushes it to the right side of the target (Figure 13c-3) before picking.

9 | SYSTEM INTEGRATION AND CONTROL

9.1 | System architecture

The systems full integration enables the robot to harvest continuously along the strawberry rows. The overall sequence is termed static strawberry harvesting, because the platform will stop, carry out picking operation and then move on when picking is finished, which is similar to the sequences of other agricultural robots (Xiong et al., 2017). The hardware and software architecture of the robot is shown in Figure 14, in which the outside hexagons represent the hardware modules while the inside rectangles are the software functions. Compared to the previous system (Xiong et al., 2019), the main software updates can be summarized as follows: new function

FIGURE 14 Hardware and software architecture of the robot: The hexagons represent the hardware modules, while the inside rectangles are the software functions [Color figure can be viewed at wileyonlinelibrary.com]



of adaptive color thresholding, integration of the platform module, handling with parallel manipulator harvesting, path-planning of the active obstacle separation, punnet picking and releasing, and full autonomous integration.

A robot coordinator node was created to manage and synchronize the information flow for all the modules. The gripper server nodes comprise a servo control node and an IR sensor feedback node, which are running ROS nodes on two Arduino controllers. The arm

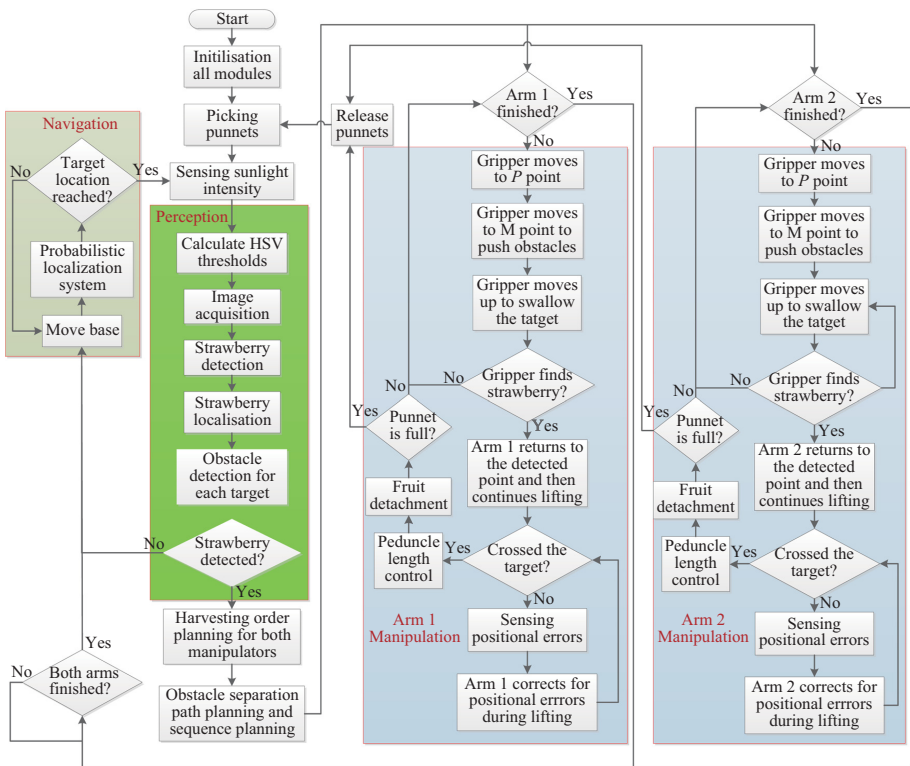


FIGURE 15 Flowchart of the control system: The entire loop shows the top-level sequential control while the four colored modules represent mid-level control loops, in which navigation, Arm 1 manipulation, and Arm 2 manipulation are continuous closed-loop control systems [Color figure can be viewed at wileyonlinelibrary.com]

motion control nodes are used for manipulation. They communicate with the gripper server nodes and the arm server nodes, receive IR sensor feedback, arm positions status and publish the goal mode and status of the arms, as well as the gripper actions. Each arm has an independent motion control node to ensure that the two manipulators pick in parallel. The platform server nodes are used to navigate the mobile base, based on the feedback from the wheel encoders and the LIDAR scanner. The navigation module can also be manually operated with the joystick in case of emergency.

9.2 | Harvesting sequence and system control

The flowchart in Figure 15 illustrates the complete sequence and control strategy for the harvesting robot. The whole system consists of several control loops, which can be classified as three levels: top level, mid-level, and lowest level. The top level is an open-loop sequential control system, which is used to trigger a series of operations in the correct sequence, from perception through manipulation to navigation. In the top-level loop, there is one mid-level open-loop module (perception) and three mid-level continuous closed-loop control systems (Arm 1 manipulation, Arm 2 manipulation, and navigation). The two arm manipulation loops are the same, using a multithread method for computing. The arm manipulation module consists of an open-loop obstacle-separation action, a closed-loop collision avoidance function (see Section 6.3) and a closed-loop scanning control for picking (Section 7.2). The scanning control function closes the loop between the arm and the gripper. The gripper continuously senses each targets location with respect to itself, while the arm uses the feedback from the gripper to control its position and correct positional errors using proportional-integral-derivative (PID) controllers. The detailed control method is introduced in Section 7.2 and our previous work (Xiong et al., 2019). The

navigation module controls the mobile base steering by using a proportional controller based on the feedback from the wheel encoders and the LIDAR scanner. Further, among these mid-level loops, a single actuator makes up a lowest level loop, such as servo stepper motors for the dual-arm and servo motors for the grippers and the mobile base. All of these actuators are continuous closed-loop control systems, using PID controllers.

As shown in Figure 15, with the exception of the four colored rectangle modules, the uncolored processes are all executed by the robot coordinator node. Figure 16 shows an example of the harvesting sequence in the farm. After initialization, the robot first picks punnets from the punnet station with verification from the gripper sensors (Figure 16a). Meanwhile, the perception module draws a light intensity value from the gripper server nodes to update color thresholds. The perception module outputs the detected strawberry bounding boxes to the coordinator, together with obstacle block vectors. If no strawberries are detected at this stage, the platform will move forward to the next image area using the navigation control module. The coordinator node sorts all the input targets and determines the harvesting order for both arms according to the algorithm in Section 6.3. In addition, the coordinator creates a path plan to separate obstacles based on the methods in Section 8 and, finally, sends a full path of arms and gripper actions to the arm manipulation modules.

Once the target coordinates have been obtained, the two arms are actuated to pick strawberries, here shown in the first image area (Figure 16b,c). The arm moves the gripper to separate obstacles before swallowing the target strawberry based on the method describes in Section 8. When the gripper detects the presence of the target during the swallowing searching procedure, the arm will return to the detected point and then use the scanning control method (Section 7.2) to correct for positional errors while passing the target body. If the

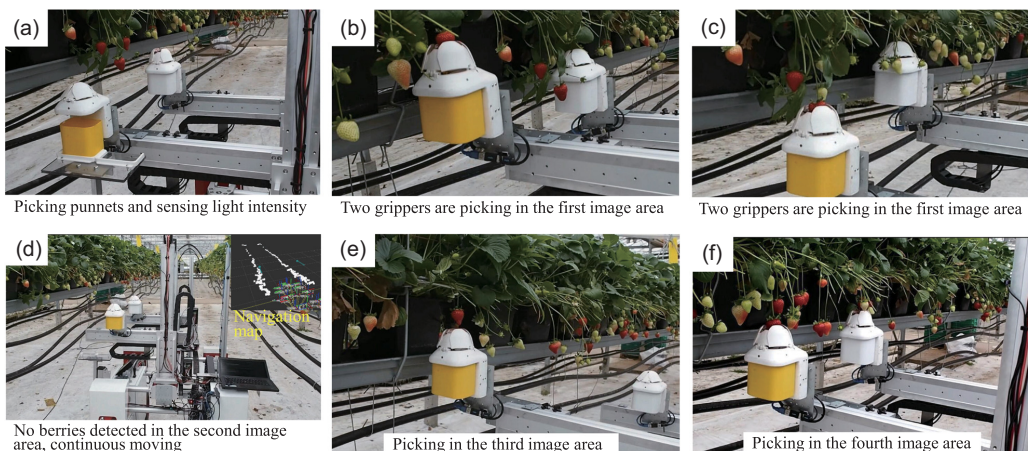


FIGURE 16 Continuous harvesting in the strawberry farm: (a) Picking punnets and sensing light intensity; (b) two grippers are picking in the first image area; (c) two grippers are picking in the first image area; (d) no berries detected in the second image area, continuous moving; (e) picking in the third image area; and (f) picking in the fourth image area [Color figure can be viewed at wileyonlinelibrary.com]

gripper is not able to detect the target in this procedure, the arm will move to the next target directly. After that, the cutter is actuated to detach the target strawberry with verification from the IR sensors. After each picking, the gripper will estimate the amount of picked strawberries in the punnet using berry amount sensors (Section 7.1). If the punnet is full, the arm will move the gripper to pick a new punnet.

When the picking is finished, the arm returns a signal to the coordinator node. As a manager, the coordinator node collects the signal and commands the platform to move to a new image area when both arms finish. As shown in Figure 16d, after it has finished picking in the first image area, the robot moves to the second image area, in which no ripe berries are detected so it continues to move forward. Then the robot is continuously picking in the third and fourth image areas (Figure 16e,f).

10 | FIELD EXPERIMENT SETUP

The experiments were conducted in the Boxford Suffolk Farms (England), which utilizes a table-top strawberry growing system in the greenhouse. The tests were carried out on a variety of strawberries called "Lusa" (Driscolls Ltd.), which is productive in the greenhouse annually from March to July. This variety of

strawberries has long peduncles, making the fruit easy for both humans and robots to pick. Unlike our previous work, which defined all growth situations of strawberries as the natural environment, in this paper the strawberry growing distributions are classified into five types for better evaluation of the robots performance, as illustrated in Figure 17. Based on our observations at the farm, not all strawberry distributions can be classified as a specific type; however, they can all be said to have derived from these five specific types, each of which was evident on the farm and influenced the test results. The five types are defined as follows:

- (1) Type A: One isolated ripe strawberry with no other strawberries around it. This is the simplest situation but also common in this strawberry variety.
- (2) Type B: Two ripe strawberries growing very close to each other but with no other strawberries around. Their distribution may be left-right, front-rear, or top-bottom and so on.
- (3) Type C: One ripe strawberry partially surrounded by unripe strawberries. There are spaces through which the gripper can access the ripe berry. This situation is also common in this variety.
- (4) Type D: Two ripe strawberries partially surrounded by unripe strawberries. This situation is similar to type B and type C but more complicated.

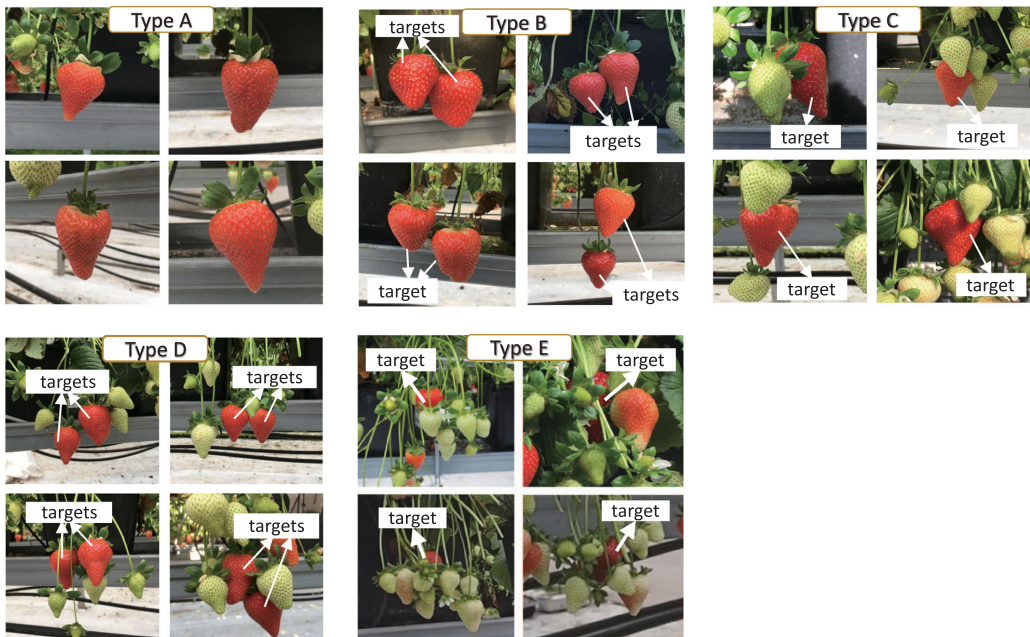


FIGURE 17 Definitions of five strawberry growing types for the picking experiments: Type A: isolated ripe strawberry; Type B: two connected ripe strawberries; Type C: one ripe strawberry with surrounding (not fully) raw strawberries; Type D: two ripe strawberries with surrounding (not fully) raw strawberries; and Type E: one ripe strawberry that is fully surrounded by raw strawberries. Five different types of strawberry growth, as defined for the picking experiments. Type A: isolated ripe strawberry; Type B: two connected ripe strawberries; Type C: one ripe strawberry partially surrounded by unripe strawberries; Type D: two ripe strawberries partially surrounded by unripe strawberries; and Type E: one ripe strawberry fully surrounded by unripe strawberries [Color figure can be viewed at wileyonlinelibrary.com]

(5) Type E: One ripe strawberry that is fully surrounded by unripe strawberries. This is the most challenging growing situation but was not commonly seen in our experiments with the variety "Lusa."

11 | RESULTS

11.1 | Arm repeatability test

To evaluate the arm performance, a repeatability test on the dual-arm system was conducted, which tested each axis independently. As shown in Figure 18a, a dial indicator is attached to the arm z axis, and the y axis will touch the indicator tip when z axis has an up-down movement. Two sets of experiments were performed: with homing and without homing. With homing the arm during each trial, the precision is also influenced by the end-stop sensors. This is meaningful to the nonabsolute motor encoder, as the arms need to be homed every time after restarting and the main positional error is due to robot zeroing (Conrad et al., 2000). With homing option, Figure 18b illustrates the repeatability test results after zero-mean normalization of 50 trials at 200 mm/s traveling speed. Following the ISO 9283 standard on arm repeatability calculation, the repetition precisions of x, y, and z axes are 0.209, 0.032, and 0.006 mm, respectively. Similarly, without homing, as shown in Figure 18c, the repetition precisions of x, y, and z axes are 0.109, 0.011, and 0.007 mm, respectively. The variance of the precision among axes is mainly due to the different transmission type and gear ratio, but all of these precisions are high enough for our harvesting application. To evaluate the performance of the arms in this new strawberry harvester, a repeatability test was conducted on the dual-arm system, with each axis tested independently. As shown in Figure 18a, a dial indicator was attached to the arms z axis, the tip of which

was touched by the y axis during the up-down movement of the z axis. Two sets of experiments were performed, namely one with homing and one without homing. When homing the arm during a trial, the precision is also influenced by the end-stop sensors. This is meaningful to the nonabsolute motor encoder, as the arms require homing after every restart and any positional error is mainly due to robot zeroing (Conrad et al., 2000). Here, Figure 18b illustrates the repeatability test results of the homing experiments after zero-mean normalization of 50 trials at 200 mm/s traveling speed. Following the ISO 9283 standard on arm repeatability calculation, the repetition precisions of the x, y, and z axes were measured at 0.209, 0.032, and 0.006 mm, respectively. Similarly, in the experiments without homing, shown in Figure 18c, the repetition precisions of the x, y, and z axes were 0.109, 0.011, and 0.007 mm, respectively. The variance of the precision among axes is considered to be mainly due to the different transmission types and gear ratios; however, these precisions are all of a sufficiently high standard for this harvesting application.

11.2 | Success rate, failure cases, and cycle times for different types

The performance tests conducted on this new strawberry-harvesting robot provide valuable information on current state and identify the limitations and challenges to the system, which are important for future improvements. The evaluation tests were implemented from April 8, 2018 to April 10, 2018, following the completion of the system integration. Two main indicators were used to evaluate the robots performance, namely success rate, and picking cycle time, representing harvesting accuracy and speed, respectively. The failure cases were recorded and analyzed to identify the challenges, which may be attributed to a variety of

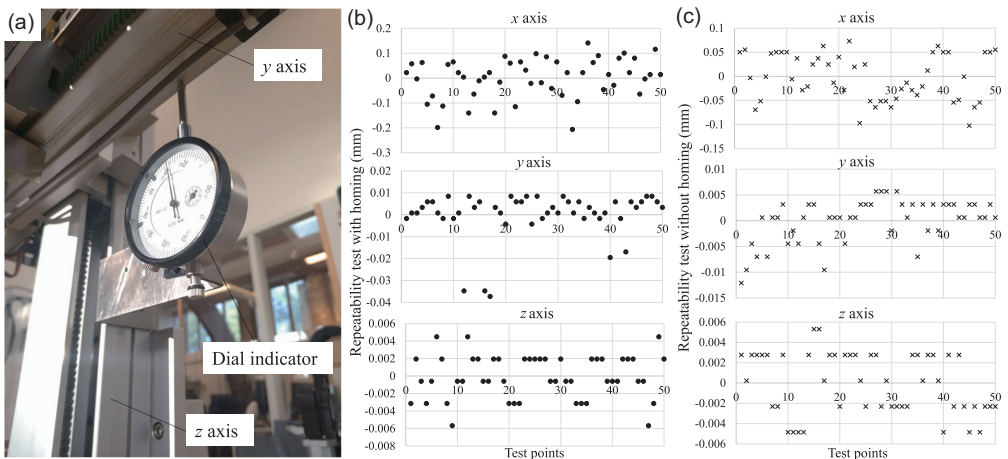


FIGURE 18 Arm repeatability test results: (a) Testing setup for z axis where a dial indicator was mounted on the z axis and the y axis was used to touch the dial indicator tip during the up-down movement of the z axis; (b) repeatability test results for each axis with homing; and (c) repeatability test results for each axis without homing [Color figure can be viewed at wileyonlinelibrary.com]

TABLE 2 Harvesting success rate of the robot in different growing types on the “Lusa” variety of strawberries

Strawberry distribution type	Quantity of target fruit	Success on the first attempt	Success with two attempts	Unpicked two attempts	Success rate on the first attempt (%)	Success rate with two attempts (%)
Type A	34	33	34	0	97.1	100.0
Type B	44	32	40	4	72.7	90.9
Type C	37	28	31	6	75.7	83.8
Type D	40	20	30	10	50.0	75.0
Type E	20	1	4	16	5.0	20.0

factors ranging from the subsystems of the robot to environmental factors or even the strawberry itself. Table 2 shows the rates of harvesting success for the five growing types, while the failure rates are listed in Table 3. In each trial, the robot attempted to pick a second time if the first attempt was a failure. More than two attempts are considered unsuitable since multifailure attempts might damage the fruit, especially fragile strawberries. Some of the reasons for picking failure were found to be common for all growing types; however, there were others in which the robot encountered new problems when the growing environment changed. The total number of failures listed in Table 3 includes both attempts. Therefore, if a strawberry was unreachable, the number of failures listed under common reasons (5) is 2. Additionally, several failure cases can appear in one attempt. For

example, if two ripe strawberries were not segmented (Type B (2)), their localization is listed as incorrect (common reasons (1)).

In general, picking success was seen to decrease gradually from Type A to Type E, as the growing situations became increasingly complex. For Type A, the robot was tested on 34 targets with only one failure at the first attempt, which was because the size of the target strawberry was almost at the maximum limit (diameter 45 mm) that the gripper can swallow. After changing the swallowing position, the second attempt was successful. For Type B, 22 pairs of targets were tested for a total of 44 fruits. On the first attempt, 12 of the 44 picks failed while another 8 were successful in the second attempt, representing a first attempt success rate of 72.7% and 90.9% for the two attempts. For Type B, the most frequent failure was caused by swinging (Type B (3) in Table 3). If two strawberries

TABLE 3 Harvesting failures of the robot in different growing types on the “Lusa” variety of strawberries

Type	Failure reasons	Failure times	Happening rates among all failures (%)
Common reasons	1. Localization error		
	2. Target strawberry not detected		
	3. Target strawberry diameter too big (diameter over 45 mm) for gripper swallowing		
	4. Failure to cut the peduncle of strawberry		
	5. Target locations unreachable, either too high, too low or too far		
Type A	Common reasons (3)	1	100.0
Type B	1. Common reasons (1), (2), (3), and (4)	4, 4, 2, 1	21.1, 21.1, 10.5, 5.3
	2. Two connected ripe strawberries were not segmented during image processing	3	15.7
	3. The second strawberry was swinging after picking the first one, resulting in large positional error	5	26.3
Type C	1. Common reasons (1), (2), (3), and (5)	2, 4, 2, 2	13.3, 26.7, 13.3, 13.3
	2. One or more surrounding immature strawberries were picked together with the ripe strawberry	3	20.0
	3. Peduncle was connected to nearby immature strawberries, stems, or leaves, thus pushing the ripe strawberry together with these obstacles	2	13.3
Type D	1. Common reasons (1), (2), (3), and (4)	7, 10, 2, 1	19.4, 27.8, 5.6, 2.8
	2. Reasons as per Type B (2) and (3)	4, 3	11.1, 8.3
	3. Reasons as per Type C (2) and (3)	5, 4	13.9, 11.1
Type E	1. Common reasons (1) and (2)	16, 22	28.1, 38.6
	2. Reasons as per Type C (2) and (3)	10, 9	17.5, 15.8

are connected with static force between them, picking of the first strawberry could change the position of the second strawberry or even make it swing dynamically. Thus, when the robot is picking the second strawberry, the previously obtained position might be incorrect. This problem can be overcome by incorporating visual servoing or other real-time detection techniques for closed-loop control. In the tests, most of the swinging strawberries were successfully picked on the second attempt, after the image processing results were updated. Moreover, the vision algorithm was sometimes not able to segment the connected strawberries, which meant that the robot would go to the center of the two targets, regarding them as one strawberry. If one of these strawberries was picked in the first attempt, the second attempt was regarded as a Type A situation.

In Type C, new problems appeared because of surrounding immature strawberries. Without segmentation and swinging issues, the first-attempt success rate for Type C was slightly higher than that of Type B (75.7%), but the success rate of the two attempts (83.8%) was lower than in Type B. This is because the second attempt in Type C was on the same target with fewer environment changes, which is markedly different from the circumstances of Type B. If surrounding small immature strawberries are growing too close to the target, they are at risk of being swallowed together it, which would not only decrease future yields but would also mix immature strawberries into the punnets with the ripe fruit. Another issue (Type C (3)) is that the peduncle of the target might be connected to nearby immature berries, stems or leaves, so that the ripe strawberry is pushed up together with these obstacles that should not be swallowed. Type D can be regarded as a combination of Types B and C, so their failure cases may also happen for Type D, making it a more challenging growing situation than the others. In the tests, only half of the targets were picked successfully on the first attempt and, with two attempts, the rate increased to 75.0%. Many of the complex surrounding berries, leaves or stems were not detected by the vision system. Finally, Type E presented an almost impossibly complicated situation for our system, resulting in a mere 5% first-attempt success rate, in which one pick was attributed to luck, and increasing to 20% on the second attempt. Detecting a strawberry with many others in front of it was a challenge and, in fact, 11 berries could not be detected at all. Three of the successful picks during the second attempt were achieved only because the first attempt had cut some of the surrounding obstacles, making the second attempt easier.

To assess the picking speed of the robot, the picking times for both the one-arm and dual-arm modes were calculated from video recordings of the movement. Researchers proposed a definition for cycle harvesting time, which includes perception operation, manipulation of a fruit, placement of the detached fruit, and also the arm traveling time to the next fruit (Bac et al., 2013, 2017). Due to the variation in robots and crops, similar metrics have been used by other works but with some differences, for example, without counting the time for the arm traveling to the next fruit (Lehnert et al., 2017) or without adding the perception time (Silwal et al., 2017). Nevertheless, platform moving time has not been taken into account by

most of the reports (Bac et al., 2017; Lehnert et al., 2017; Silwal et al., 2017). In our system, most of the time taken is in the manipulation process, since the top-level control is open loop so the robot only need to sense an image area once and then the two arms are actuated to pick all the targets in this image without further perception needed. Laboratory tests with fake strawberry plants (6–12 ripe strawberries) indicated that the average time for our perception system is 0.11 s (i5-6200 CPU, 16 GB RAM), including image acquisition, detection, obstacle calculation, and path-planning. The cycle time including perception is varied if the number of strawberries in each image area is different. Also, the gripper can collect strawberries during picking, so the time taken for the manipulator to drop individual fruit does not exit. Therefore, similar to apple harvesting (Silwal et al., 2017), we report the harvesting time on manipulation time only, including the picking time and arm traveling time, excluding the time taken to move platforms and pick punnets. On average, the time in which one arm successfully picked one target and traveled on to the next was 6.1 s, as shown in Table 4. This picking speed is faster than that of our previous versions average of 7.49 s, and is attributed to the increased speed of the arms in both movement and communication, as well as the new scanning control method. When using two arms, one berry was picked in 4.6 s, which is more than half the time taken by the single arm. This is because of delays while one arm waited for the other during picking to avoid collision or while the platform was moved.

12 | DISCUSSION AND LESSONS LEARNED

Results show the new autonomous strawberry-harvesting robot is more accurate and faster than the previous version. These improvements are the combined result of tight system integration, adaptive machine vision, cooperative dual arms, an improved gripper, and intelligent obstacle separation. However, along with these improvements, the new system still faces numerous challenges.

First, the adaptive color-thresholding method in the machine vision subsystem shows the ability to adapt to the changing sunlight. Color thresholding on 2D images is a simple and fast algorithm. It is

TABLE 4 Manipulation time on successful picking with one arm or two arms configurations

Number of arms	Test no.	Number of picked strawberries	Manipulation execution time per strawberry	Average(s)
One arm	1	2	6.8	6.1
	2	3	6.1	
	3	3	6.0	
	4	5	5.4	
Two arms	1	5	4.4	4.6
	2	5	5.2	
	3	7	4.6	
	4	8	4.2	

effective and efficient when the environment is simple. However, during the experiments on the farm, most of the localization errors came from the image processing. For example, two connected strawberries could not be segmented or one strawberry was segmented into two parts because there was a stem in front of it. This problem may be considered commonplace for traditional image processing. The current alternative which is to use more advanced technologies like 3D image processing and deep learning, is likely to solve many of these problems, especially as processing speed is unlikely to remain a problem as new hardware is developed. The whole system was evaluated in the field as listed in Table 3, including all aspects of failures, but lacked specific evaluation of individual system. Our future work will consider to standardize the metrics and data set to compare the adaptive color thresholding with other detection methods. In addition, the current gripper is unable to distinguish between correct (true positive) and incorrect detection (false positive) of mature strawberries, thus once receiving a target location, the gripper will pick it anyway regardless of the actual targets. However if nothing is detected by the gripper, the arm will skip it immediately and move to the next target (Section 9.2). Therefore, future improvements will be to use an additional hand-eye camera for final verification. Additional hand-eye cameras can also be used for closed-loop vision-based manipulation, because the current stationary camera is easily occluded by the arms or grippers during picking operations.

Second, the proposed active obstacle-separation algorithm proved to be effective in field applications, thus improving the harvesting ability of the robot. As long as there was an entrance (empty blocks) within the bottom blocks, the gripper was able to find a way to push aside the surrounding obstacles. However, it was still unable to pick targets that were fully surrounding by obstacles (leaving no entrance). It was also still not robust and revealed some limitations, especially from the vision side. The first limitation is the insufficient view and point cloud. In the current system, only a single view was used to get the 3D scenario. However, because of occlusions and the straight projection of the camera, the rear obstacles were not easily detected, such as the case in Figure 12a when the bottom left-rear obstacle was not detected. Therefore, future work should make use of multi-view images and reconstruct more accurate scenes. The second vision problem is that of inaccurate localization. As the obstacle block size is dependent on the target bounding box, inaccurate localization of ripe strawberries might result in the gripper pushing the target when separating surrounding obstacles. In addition to the vision system limitations, closed-loop control between perception and manipulation may be able to improve the performance of obstacle separation. From a mechanical perspective, an additional manipulator may also help to separate the obstacles, like human manipulation in cluttered environment. Also, in some cases, the gripper size was found to be too large to separate the obstacles delicately, however, a small-sized gripper may not be able to swallow large fruits, so this gap remains to be solved.

Finally, strawberry variety is an important factor that can influence how the robot, especially the gripper, is designed, as well as the picking success rate. Based on field observation, varieties like "Lusa" are easier

for picking than others, such as "Rumba," which has lots of clusters with short peduncles growing on one stem. This feature makes it difficult for robots to separate obstacles. This suggests that the automation of the agriculture industry requires more efforts from horticulture technology in breeding new varieties and developing new growing systems to simplify the environment for robots.

13 | CONCLUSIONS

This paper presents a fully integrated strawberry-harvesting system capable of picking strawberries in clusters. While several harvesters that can cope with isolated strawberries have been developed, those growing in complex clusters remain a challenge. The main scientific contribution of this paper is the novel obstacle-separation path-planning algorithm, which allows the successful harvest of strawberries that are surrounded by other strawberries, as well as by leaves and other obstacles. The algorithm uses the gripper to push surrounding obstacles from an entrance, thus clearing the way for it to swallow the target strawberry. The separation actions consist of pushing aside the bottom obstacles before swallowing and pushing aside the top obstacles during swallowing. The pushing vectors are derived based on the surrounding obstacles that are calculated using downsampled blocks of 3D point cloud. This technique might be applicable to other fruit harvesting systems.

In addition to obstacle separation, improvements were made to the gripper, the vision system, and the control. For adaptation to the field environment, a vision system that could automatically change color thresholds was developed based modeling of color against sunlight intensity, making it robust to variations in lighting. Furthermore, a low-cost single-rail two Cartesian arm system was developed, which makes it suitable for agricultural robot application. The harvesting sequence for the dual-arm was studied to optimize harvesting efficiency and avoid collision. This study also presents an improved gripper design that enables the robot to pick a market punnet and harvest berries directly into the punnet, thus eliminating the cost and time for repacking.

Finally, we show the full integration and control algorithm of the whole system, which enables the robot to harvest continuously along the polytunnels. The system was tested in the field on a strawberry farm. Results revealed that the robot was capable of picking partially surrounded strawberries, with success rates ranging from 50.0% to 97.1% on the first attempt, depending on the different type settings. This rate rose to between 75.0% and 100.0% on the second attempt. However, the system was not able to pick a target that was fully surrounded by obstacles, recording a first-attempt success rate of just 5.0%. The picking speed in the one-arm mode increased to 6.1 s, including both picking and the arm's travel time to the next target, while, for the dual-arm mode, the average picking time was recorded as 4.6 s per strawberry. Failures in this new system were caused mainly by the vision system and insufficient dexterity in the grippers, which will be addressed in future developments of the harvester.

ACKNOWLEDGMENTS

This study was supported by the Norwegian University of Life Sciences, Norway. We thank Mr. Robert England and Mr. Mihail Marita from the Boxford Suffolk Farms (Colchester, UK) for providing the strawberry greenhouse and accommodation to conduct field experiments.

ORCID

Ya Xiong  <http://orcid.org/0000-0001-5593-8440>

REFERENCES

- Anjom, F. K., Vougioukas, S. G., & Slaughter, D. C. (2018). Development of a linear mixed model to predict the picking time in strawberry harvesting processes. *Biosystems Engineering*, *166*, 76–89.
- Bac, C., Hemming, J., & VanHenten, E. (2013). Robust pixel-based classification of obstacles for robotic harvesting of sweet-pepper. *Computers and Electronics in Agriculture*, *96*, 148–162.
- Bac, C. W., Hemming, J., vanTuijl, B., Barth, R., Wais, E., & vanHenten, E. J. (2017). Performance evaluation of a harvesting robot for sweet pepper. *Journal of Field Robotics*, *34*(6), 1123–1139.
- Bac, C. W., Roorda, T., Reshef, R., Berman, S., Hemming, J., & vanHenten, E. J. (2016). Analysis of a motion planning problem for sweet-pepper harvesting in a dense obstacle environment. *Biosystems Engineering*, *146*, 85–97.
- Bangert, W., Kielhorn, A., Rahe, F., Albert, A., Biber, P., Grzonka, S., & Haug, S. (2013). Field-robot-based agriculture: "RemoteFarming. 1" and "BoniRob-Apps". 71th conference LAND. TECHNIK-AgEng 2013, Hannover, Germany, 2193, 439–446.
- Bargoti, S., & Underwood, J. P. (2017). Image segmentation for fruit detection and yield estimation in apple orchards. *Journal of Field Robotics*, *34*(6), 1039–1060.
- Botterill, T., Paulin, S., Green, R., Williams, S., Lin, J., Saxton, V., & Corbett-Davies, S. (2017). A robot system for pruning grape vines. *Journal of Field Robotics*, *34*(6), 1100–1122.
- Conrad, K. L., Shiakolas, P. S., & Yih, T. C. (2000). Robotic calibration issues: Accuracy, repeatability and calibration. In Proceedings of the 8th Mediterranean Conference on Control and Automation (MED2000), Rio, Greece, 1719, 1–6.
- Cui, Y., Gejima, Y., Kobayashi, T., Hiyoshi, K., & Nagata, M. (2013). Study on cartesian-type strawberry-harvesting robot. *Sensor Letters*, *11*(6-7), 1223–1228.
- Dimeas, F., Sako, D. V., Moulitanis, V. C., & Aspragathos, N. A. (2015). Design and fuzzy control of a robotic gripper for efficient strawberry harvesting. *Robotica*, *33*(5), 1085–1098.
- Feng, Q., Wang, X., Zheng, W., Qiu, Q., & Jiang, K. (2012). New strawberry harvesting robot for elevated-trough culture. *International Journal of Agricultural and Biological Engineering*, *5*(2), 1–8.
- Feng, Q., Zou, W., Fan, P., Zhang, C., & Wang, X. (2018). Design and test of robotic harvesting system for cherry tomato. *International Journal of Agricultural and Biological Engineering*, *11*(1), 96–100.
- Fentanes, J. P., Lacerda, B., Krajnik, T., Hawes, N., & Hanheide, M. (2015). Now or later? predicting and maximising success of navigation actions from long-term experience. 2015 IEEE International Conference on Robotics and Automation (ICRA), IEEE, Seattle, USA, 1112–1117.
- Fu, L., Feng, Y., Majeed, Y., Zhang, X., Zhang, J., Karkee, M., & Zhang, Q. (2018). Kiwifruit detection in field images using faster r-cnn with zfnets. *IFAC-PapersOnLine*, *51*(17), 45–50.
- Grimstad, L., Skattum, K., Solberg, E., Loureiro, G. D. S. M., & From, P. J. (2017). Thorvald II configuration for wheat phenotyping. IROS Workshop on Agri-Food Robotics: Learning from Industry, Vancouver, Canada, vol. 4.
- Grimstad, L., Zakaria, R., Le, T. D., & From, P. J. (2018). A novel autonomous robot for greenhouse applications. IEEE/RJS International Conference on Intelligent Robots and Systems (IROS), Madrid, Spain, 1–9.
- Grisetti, G., Stachniss, C., & Burgard, W. (2007). Improved techniques for grid mapping. *IEEE Transactions on Robotics*, *23*(1), 34–46.
- Habaragamuwa, H., Ogawa, Y., Suzuki, T., Shiigi, T., Ono, M., & Kondo, N. (2018). Detecting greenhouse strawberries (mature and immature), using deep convolutional neural network. *Engineering in Agriculture, Environment and Food*, *11*(3), 127–138.
- Hayashi, S., Shigematsu, K., Yamamoto, S., Kobayashi, K., Kohno, Y., Kamata, J., & Kurita, M. (2010). Evaluation of a strawberry-harvesting robot in a field test. *Biosystems Engineering*, *105*(2), 160–171.
- Hayashi, S., Yamamoto, S., Saito, S., Ochiai, Y., Kamata, J., Kurita, M., & Yamamoto, K. (2014). Field operation of a movable strawberry-harvesting robot using a travel platform. *Japan Agricultural Research Quarterly*, *48*(3), 307–316.
- Huang, Z., Wane, S., & Parsons, S. (2017). Towards automated strawberry harvesting: Identifying the picking point. In Gao, Y., Fallah, S., Jin, Y., & Lekakou, C. (Eds.), *Conference Towards Autonomous Robotic Systems* (pp. 222–236). Guildford, UK: Springer.
- Ishikawa, T., Hayashi, A., Nagamatsu, S., Kyutoku, Y., Dan, I., Wada, T. ... Oku, K. (2018). Classification of strawberry fruit shape by machine learning. *International Archives of the Photogrammetry, Remote Sensing and Spatial Information Sciences*, *42*, 2.
- Lehnert, C., McCool, C., Sa, I., & Perez, T. (2018). A sweet pepper harvesting robot for protected cropping environments. Retrieved from <https://arxiv.org/abs/1810.11920>
- Lehnert, C., Tsai, D., Eriksson, A., & McCool, C. (2018). 3d move to see: Multi-perspective visual servoing for improving object views with semantic segmentation. Retrieved from <https://arxiv.org/abs/1809.07896>
- Lehnert, C. F., English, A., McCool, C., Tow, A. W., & Perez, T. (2017). Autonomous sweet pepper harvesting for protected cropping systems. *IEEE Robotics and Automation Letters*, *2*(2), 872–879.
- Lili, W., Bo, Z., Jinwei, F., Xiaohan, H., Shu, W., Yashuo, L., & Chongfeng, W. (2017). Development of a tomato harvesting robot used in greenhouse. *International Journal of Agricultural and Biological Engineering*, *10*(4), 140–149.
- Mai, X., Zhang, H., & Meng, M. Q.-H. (2018). Faster r-cnn with classifier fusion for small fruit detection. 2018 IEEE International Conference on Robotics and Automation (ICRA), IEEE, Brisbane, Australia, 7166–7172.
- McCool, C., Beattie, J., Firn, J., Lehnert, C., Kulk, J., Bawden, O., & Perez, T. (2018). Efficacy of mechanical weeding tools: A study into alternative weed management strategies enabled by robotics. *IEEE Robotics and Automation Letters*, *3*(2), 1184–1190.
- Mueller-Sim, T., Jenkins, M., Abel, J., & Kantor, G. (2017). The robotanist: A ground-based agricultural robot for high-throughput crop phenotyping. IEEE International Conference on Robotics and Automation (ICRA), Singapore, 3634–3639.
- Raja, Y., McKenna, S. J., & Gong, S. (1998). Tracking and segmenting people in varying lighting conditions using colour. Proceedings Third IEEE International Conference on Automatic Face and Gesture Recognition, Nara, Japan, 228–233.
- Sa, I., Ge, Z., Dayoub, F., Uproct, B., Perez, T., & McCool, C. (2016). Deepfruits: A fruit detection system using deep neural networks. *Sensors*, *16*(8), 1222.
- Shiigi, T., Kurita, M., Kondo, N., Ninomiya, K., Rajendra, P., Kamata, J., & Kohno, Y. (2008). Strawberry harvesting robot for fruits grown on table top culture. An ASABE Meeting Presentation, American Society of Agricultural and Biological Engineers, Providence, Rhode Island, 1–9.
- Silwal, A., Davidson, J. R., Karkee, M., Mo, C., Zhang, Q., & Lewis, K. (2017). Design, integration, and field evaluation of a robotic apple harvester. *Journal of Field Robotics*, *34*(6), 1140–1159.

- Sridharan, M., & Stone, P. (2007). Color learning on a mobile robot: Towards full autonomy under changing illumination. *International Joint Conference on Artificial Intelligence, Hyderabad, India*, 2212–2217.
- Thrun, S., Burgard, W., & Fox, D. (2005). *Probabilistic robotics*. Cambridge, USA: MIT Press.
- Vakilian, K. A., Jafari, M., & Zarafshan, P. (2015). Dynamics modelling and control of a strawberry harvesting robot. 2015 3rd RSI International Conference on Robotics and Mechatronics (ICROM), IEEE, Tehran, Iran, 600–605.
- VanHenten, E. J., Hemming, J., VanTuijl, B., Kornet, J., Meuleman, J., Bontsema, J., & VanOs, E. (2002). An autonomous robot for harvesting cucumbers in greenhouses. *Autonomous Robots*, 13(3), 241–258.
- Vijayarangan, S., Sodhi, P., Kini, P., Bourne, J., Du, S., Sun, H., & Wettergreen, D. (2017). High-throughput robotic phenotyping of energy sorghum crops. *Field and Service Robotics* (5, pp. 99–113). Cham, Switzerland: Springer.
- Vitzrabin, E., & Edan, Y. (2016). Changing task objectives for improved sweet pepper detection for robotic harvesting. *IEEE Robotics and Automation Letters*, 1(1), 578–584.
- Xiong, Y., From, P. J., & Isler, V. (2018). Design and evaluation of a novel cable-driven gripper with perception capabilities for strawberry picking robots. 2018 IEEE International Conference on Robotics and Automation (ICRA), IEEE, Brisbane, Australia, 7384–7391.
- Xiong, Y., Ge, Y., Liang, Y., & Blackmore, S. (2017). Development of a prototype robot and fast path-planning algorithm for static laser weeding. *Computers and Electronics in Agriculture*, 142, 494–503.
- Xiong, Y., Peng, C., Grimstad, L., From, P. J., & Isler, V. (2019). Development and field evaluation of a strawberry harvesting robot with a cable-driven gripper. *Computers and Electronics in Agriculture*, 157, 392–402.
- Yaguchi, H., Nagahama, K., Hasegawa, T., & Inaba, M. (2016). Development of an autonomous tomato harvesting robot with rotational plucking gripper. 2016 IEEE/RSJ International Conference on Intelligent Robots and Systems (IROS), IEEE, Daejeon, South Korea, 652–657.
- Yamamoto, S., Hayashi, S., Saito, S., Ochiai, Y., Yamashita, T., & Sugano, S. (2010). Development of robotic strawberry harvester to approach target fruit from hanging bench side. *IFAC Proceedings Volumes*, 43(26), 95–100.
- Yamamoto, S., Hayashi, S., Yoshida, H., & Kobayashi, K. (2014). Development of a stationary robotic strawberry harvester with a picking mechanism that approaches the target fruit from below. *Japan Agricultural Research Quarterly*, 48(3), 261–269.
- Ye, Y., Wang, Z., Jones, D., He, L., Taylor, M. E., Hollinger, G. A., & Zhang, Q. (2017). Bin-dog: A robotic platform for bin management in orchards. *Robotics*, 6(2), 12.
- Zhang, L., Gui, G., Khattak, A. M., Wang, M., Gao, W., & Jia, J. (2019). Multi-task cascaded convolutional networks based intelligent fruit detection for designing automated robot. *IEEE Access*, 7, 56028–56038.
- Zion, B., Mann, M., Levin, D., Shilo, A., Rubinstein, D., & Shmulevich, I. (2014). Harvest-order planning for a multiarm robotic harvester. *Computers and Electronics in Agriculture*, 103, 75–81.

SUPPORTING INFORMATION

Additional supporting information may be found online in the Supporting Information section.

How to cite this article: Xiong Y, Ge Y, Grimstad L, From PJ. An autonomous strawberry-harvesting robot: Design, development, integration, and field evaluation. *J Field Robotics*. 2019;1–23. <https://doi.org/10.1002/rob.21889>

APPENDIX: INDEX TO MULTIMEDIA EXTENSIONS

The table shows some videos of the field experiments presented in this paper.

Extension	Media type	Description
1	Video	Gripper actions and field test of the robot
2	Video	Obstacle separation actions in the field
3	Video	Failure cases in the field
4	Video	Lab demo of the robot (including the newest version of the gripper)
5	Video	Navigation in the farm

Part II – Strawberry-harvesting robots

Paper V

Xiong, Y., Ge, Y. and From, P.J.. An Obstacle-separation Method for Robotic Picking of Fruits in Clusters. (Submitted to *IEEE Robotics and Automation Letters (RA-L)*).

An obstacle-separation method for robotic picking of fruits in clusters

Ya Xiong, Yuanyue Ge and Pål Johan From

Abstract—Selectively picking a target fruit surrounded by obstacles is one of the major challenges for fruit harvesting robots. This paper presents a method for actively separating obstacles from the target by using a combination of push and drag motions. A linear push is used to clear the obstacles from the area below the target, while a zig-zag push is used to push aside more dense obstacles. The zig-zag push can help the gripper capture a target since the generated shaking motion can break the static contact force between the target and obstacles. Furthermore, we propose a novel dragging operation to address the issue of mis-capturing obstacles located above the target, in which the gripper drags the target to a place with fewer obstacles and then push back to move the obstacles aside for further detachment. Furthermore, an image processing protocol is developed for the application in a harvesting robot. Field tests show that the proposed method can improve the picking performance substantially. This method helps to enable complex clusters of fruits to be harvested with a higher success rate than conventional methods.

I. INTRODUCTION

Fruit production that requires selective harvesting is heavily reliant on human labour [1]. This is applicable to crops such as strawberries, sweet peppers, tomatoes, cucumbers, etc.. Labour represents the largest cost and also a large operational uncertainty for fruit growers [2]. Therefore, several attempts have been made to develop a robotic solution for selective harvesting of fruits. Some fruits, such as strawberries and tomatoes, tend to grow in clusters. This makes it difficult to identify and pick individual ripe fruit without damaging or accidentally picking unripe fruit [1], [2]. Harvesting fruits that grow in clusters or are surrounded by obstacles, such as branches and/or leaves, while leaving the other fruits to remain undamaged on the plant, is one of the primary challenges for fruit harvesting systems [1], [3]. The surrounding fruits, leaves, stems and other obstacles are often difficult to separate from the target, both in terms of detection and in manipulation.

In agricultural robotics field, many researchers try to avoid obstacles in both vision and manipulation. To avoid occlusions in sweet pepper picking, a 3Dmoversee method was proposed to find the best view with less occlusions [4]. To avoid obstacles, a method for cucumber picking was developed that uses a search algorithm to explore the search space for a feasible trajectory, in which each step of the trajectory is checked by a collision detector [5]. Most of the methods found in the literature are passive obstacle avoidance methods, in which the aim is to avoid existing obstacles

without changing the environment. However, obstacles are not always avoidable, especially when picking smallsize fruits in clusters, where the obstacles may be extremely close to the targets.

Our previous work presented a gripper for strawberry harvesting that can open fingers to enclose a target from below [6]. Without moving the obstacles out of the way, obstacles may prevent the gripper from capturing the target and may also be swallowed with the target if they are located close to the target. Similar problems occur when approaching the fruit from other angles. To solve this issue, in a later work [1], we proposed to use a single linear push operation to push aside the obstacles below the target based on the obstacle sensing from a 3D camera. We found that pushing obstacles aside, rather than simply avoiding them makes it possible to pick fruit that would otherwise be inaccessible to the robot. However, a single linear push may be insufficient for dense obstacles from multi-direction with respect to the target, since the linear push moves towards only one direction. Moreover, the obstacles may be adjacent together that can not be separated during the push. Furthermore, when the obstacles connect to the target at the same height, the gripper may not be able to swallow the whole target but push it up due to the static contact force between the target and obstacles. In addition to that, one frequent failure is the gripper may capture obstacles above the target when it moves up to detach the fruit, which has not been addressed in the previous work.

In the field of robotic manipulation, most studies focus on obstacle avoidance. Nevertheless, we found some research working on obstacle separation for simple situations. For a warehouse picking application on desk environment, two linear pushing policies were proposed to separate rigid obstacles during the way of the gripper to reach a target bin [7]. Another work used Learning from Demonstration (LfD) algorithm for the same application that involves a pushing action [8]. For a similar situation, researchers proposed to use physical engine to calculate the dynamics to predict the object locations for motion planning, which also involves pushing motions [9], [10], [11]. Reinforcement learning was also used to train a robot to rearrange objects on a desk using pushing method to make them sparse for individual grasping [12]. However, all these methods were tested at simple environment where some rigid objects were placed on a 2D desk surface. In the agricultural environment, for example strawberry plants, fruits are located in 3D within diverse and unconstrained environments. The flexible peduncles, deformable fruits and many other crop variations make the dynamics difficult to calculate and predict. Moreover, the

*This work was supported by Research council of Norway, FORNY2020, project number 2962020.

Authors are with Noronn AS and Faculty of Science and Technology, Norwegian University of Life Sciences, Ås, Norway {ya.xiong, yuanyue.ge, pal.johan.from}@nmbu.no

operation speed of these methods seem very slow, which may not be suitable for fruit harvesting.

This paper provides the improvements to our previously proposed obstacle separation method [1]. We extend the pushing policy by adding a zig-zag push for both horizontal and upward directions. Most importantly, a novel dragging operation is proposed to avoid upper obstacles. The proposed method might be also applicable to harvest other fruits, such as tomatoes and cucumbers.

II. METHODS

A. Region of Interest

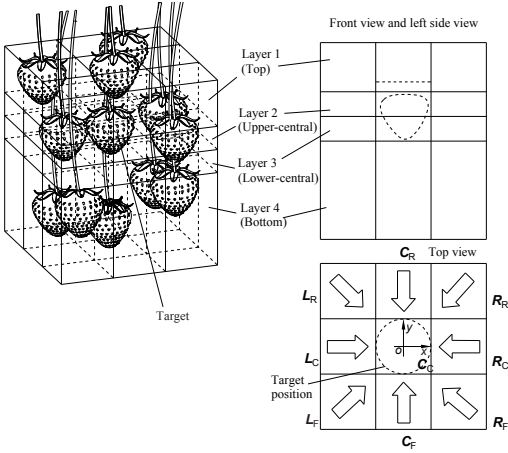


Fig. 1. Region of interest area around the target to determine the presence of obstacles.

We select a region of interest (RoI) area around the target to determine the presence of the obstacles. The RoI comprises a volume of 3D point cloud that contains the target fruit and potentially one or more obstacles. As shown in Fig. 1, in this study we extend the height of the RoI to include the area above the target, such that the target lies (e.g. wholly) within the RoI. The RoI area can be divided into four horizontal layers: a top layer 1, an upper-central layer 2, a lower-central layer 3 and a bottom layer 4.

As the top view is shown in Fig. 1, each layer of the RoI is further segmented into nine cuboid blocks. On each layer, the blocks are arranged in a 3x3 grid that has its centre at the horizontal midpoint of the target strawberry such that the central block C_C encompasses the position of the target strawberry in the xy plane. In the horizontal view, the length and width of the outside eight blocks are equal to the central block. In the front view and left side view, the heights of layer 1 and layer 4 are equal to one and two of the height of the target block, respectively. The height of layer 2 and layer 3 are the half of the height of the target block. Particularly, the central block of layer 1 is shorter than other blocks in the same layer, 80% of other blocks. This is because the object segmentation method does not include the green calyx. To

avoid the calyx being detected as an obstacle, we leave the bottom of the central block in layer 1 blank. Each block is assigned a horizontal vector representative of the direction from the block to the central block C_C . The direction of the vector is determined by the position of the block so that all vectors are directed from the centre of the corresponding block towards the centre of the central block C_C . We use the number of points N in the block of point cloud to determine whether there are obstacles present in the block or not. In this paper, the threshold of N for layer 1, layer 2/3 and layer 4 are 200, 100 and 300, respectively, using the resolution of 1280 x 720 of the RGB-D camera.

The gripper is instructed to operate in three distinct stages. As the gripper is picking from below, during the first stage, the gripper moves obstacles horizontally within layer 4. During the second stage, the device moves up to swallow the target and separates the obstacles within layer 2 and layer 3. During the third stage, the gripper drags the target into a picking position with less obstacles if the central block C_C in layer 1 is occupied. The detailed separation policies will be elaborated in the below sections.

B. Horizontal Push

The first stage is to separate the obstacles horizontally under the target in layer 4. Compared to our previous method [1], we add a zig-zag pushing policy in addition to the single push. A single push means that the gripper linearly pushes the obstacles aside once, starting from the region with less obstacles. A zig-zag push is a motion where the gripper uses a zig-zag movement that contains several linear motions to push the obstacles side to side. The pushing policy is selected based on the number and distribution of the obstacles in layer 4. Also, to generate more accurate pushing directions or a higher resolution, the grid in layer 4 is modified from 2x3 to 3x3.

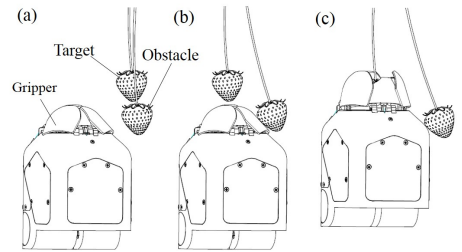


Fig. 2. Single push to move the obstacles under the target in layer 4

1) *Single Push*: As shown in Fig. 2(a), if an obstacle is located below the target (layer 4), the gripper may capture the obstacles if it were to move up to enclose the target. In this case, the gripper can use a single-push operation to push aside the obstacle (to the right in the figure) before swallowing the target (Fig. 2(b) and (c)).

Since the gripper size is limited, a single-push operation makes it easier to move a few number of adjacent obstacles

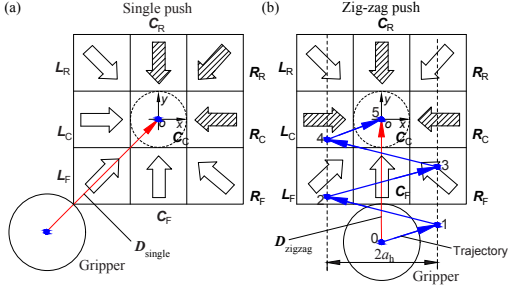


Fig. 3. Diagram of the calculation of horizontal push: (a) single push, where the red arrow is the pushing direction; (b) zig-zag push, where the red arrow shows the overall direction and the blue arrows are the zig-zag paths.

out of the way, but hard to separate sparsely distributed obstacles. Therefore, ignoring the central block, we use the number of blocks n_h within the largest group of adjacent unoccupied blocks (without obstacles) to determine whether to use a single-push or zig-zag operation. As shown in Fig. 3(a), ignoring the central block, filled arrows in the blocks mean the blocks are occupied with obstacles, while the blank arrows represent unoccupied blocks. In this case, the n_h is 5 and greater than a predetermined threshold t_h (using 4 in this paper), so a single-push operation is appropriate to push the obstacles aside. As the pushing operation is moving towards the obstacles, the direction of the single-push operation for the gripper is calculated based on the positions of the occupied blocks according to the following equation:

$$D_{single} = -r \sum_1^n O_i / |\sum_1^n O_i|, \quad n_h \geq t_h \quad (1)$$

where, O is the vector of the i^{th} occupied block within the largest group of adjacent occupied blocks and n is the total number of blocks within the largest group of adjacent occupied blocks. The parameter r is used to scale the D_{single} norm, which should guarantee that the gripper pushes from the outside of the blocks (50 mm is used for the current system). The red arrow in Fig. 3(a) shows the calculated pushing direction for the single-push operation. It can be seen that the gripper moves from the center of the unoccupied blocks to the center of the occupied blocks, such that the gripper has the highest possibility to move all the obstacles out of the way. If only the central block C_C is occupied, then $D_{single}=0$. In this situation, the direction in which the gripper must move in order to push the obstacles is instead determined by calculating the shortest path from the current location of the gripper to the center of the central block C_C . If no obstacles are detected in the blocks, the gripper has no pushing action at this stage and moves up straightly from the below.

2) *Zig-zag Push*: Ignoring the central block, if the number n_h of the largest group of adjacent unoccupied blocks comprises fewer than the threshold number t_h of blocks, the

method determines that a horizontal zig-zag push operation is appropriate. Fig. 3(b) shows a case where a zig-zag operation is selected to push the obstacles side to side. The red arrow is the overall direction of the operation, while the blue arrows are the zig-zag paths. Since the zig-zag operation involves three directions of movement (forward, left and right), the gripper can push the three directions of obstacles out of the way. Therefore, it makes sense that the gripper moves from the entrance which contains less obstacles. Hence, different from the single push, the overall direction of the zig-zag push operation is calculated based on the positions of the unoccupied blocks according to the following equation:

$$D_{zigzag} = -r \sum_1^m U_j / |\sum_1^m U_j|, \quad n_h < t_h \quad (2)$$

where, U is the vector of the j^{th} unoccupied block within the largest group of adjacent unoccupied blocks and m is the total number of blocks within the largest group of adjacent unoccupied blocks. The norm of D_{zigzag} is scaled using the same parameter r as Eq. 1. During a horizontal zig-zag push operation, the device moves in the xy plane, wherein the resultant vector of the zig-zag motion is equal to D_{zigzag} and the amplitude a_h and number of pushes n_{hp} of the zig-zag motion are determined according to the specific picking scenario. For example, the effectiveness of the values may be affected by the peduncle length, fruit weight or the damping ratio of the fruit, which are difficult to calculate. Based on some tests in the farm, in the current system, we tune the a_h and n_{hp} to fix values of 20 mm and 5, respectively.

C. Upward Zig-zag Push

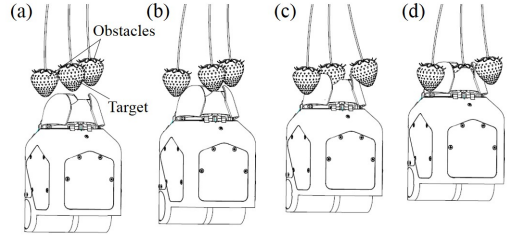


Fig. 4. Upward zig-zag operation: when moving upward, the gripper moves to the left and right to push aside the two sides of obstacles.

After finishing the separation in layer 4, the gripper moves up to enclose the target in layer 3 and 2. In the previous work, we introduced a method that moves the gripper with an offset to the central position of the target for swallowing a target with a connected berry [1]. This method can help to avoid swallowing the other connected obstacle. However, we observed that the target or the obstacles might not fall down, but are moved up by the gripper when the gripper moves up due to the static contact force. Inspired from our daily experience that a shaking operation can help insert an object into a target place surrounding with obstacles, we add an upward zig-zag operation to help the gripper swallow the target and also make it easier for the obstacles to fall on the

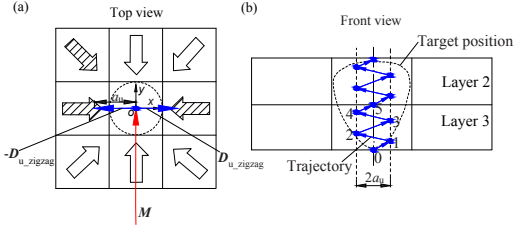


Fig. 5. Diagram of the calculation of the upward zig-zag push: (a) top view shows the calculation of the principle push direction; (b) front view shows the vertical paths (blue arrows).

outside of the fingers. Also, similar to the horizontal zig-zag motion, the upward zig-zag operation can help separate obstacles in more than one directions. As an example is shown in Fig. 4, when moving upward, the gripper moves to the left and right to push aside the two sides of obstacles.

The upward zig-zag push operation comprises the movement of the gripper in a principally vertical direction towards the target fruit and a side-to-side movement to clear obstacles. The vertical direction passes through the center of the target. Similar to the horizontal push, we calculate the direction \mathbf{D}_{u_zigzag} of the upward push in xy plane based on the number of blocks n_u within the largest group of adjacent unoccupied blocks. If n_u is greater than the threshold t_h , the situation is same to the single push in layer 4, so the direction \mathbf{D}_{u_zigzag} can be calculated according to the occupied blocks.

$$\mathbf{D}_{u_zigzag} = a_u \frac{\sum_1^n \mathbf{O}_i}{|\sum_1^n \mathbf{O}_i|}, \quad n_u \geq t_h \quad (3)$$

where, a_u is the parameter used to scale the \mathbf{D}_{u_zigzag} norm (5 mm is used for the current system). If the n_u is fewer than the threshold t_h , as shown in Fig. 5(a), the calculation then uses the unoccupied blocks, which is similar to the calculation of the zig-zag push in layer 4. The calculation can be concluded as following equation:

$$\begin{cases} \mathbf{M} \cdot \mathbf{D}_{u_zigzag} = 0, & n_u < t_h \\ \mathbf{M} = -\sum_1^n \mathbf{U}_j \\ |\mathbf{D}_{u_zigzag}| = a_u \end{cases} \quad (4)$$

where, \mathbf{M} is the intermediate vector to calculate \mathbf{D}_{u_zigzag} . Therefore, for the case in Fig. 5(a), the gripper moves along with \mathbf{D}_{u_zigzag} and $-\mathbf{D}_{u_zigzag}$ to push aside the two sides of obstacles. The front view in Fig. 5(b) shows the gripper moves gradually at left or right intermediate points to pass over layer 3 and 2. We set the number of pushes n_{up} in each layer to 5 in the current system.

D. In-hand Drag Above The Target

If an obstacle is located above the target (layer 1), such as the case shown in Fig. 6(a), the gripper may swallow or damage the obstacles when moving upward to capture the target strawberry. Furthermore, the obstacles may stop the fingers closing thus result in cutting failure of the target peduncle. To solve this problem, we propose an in-hand dragging

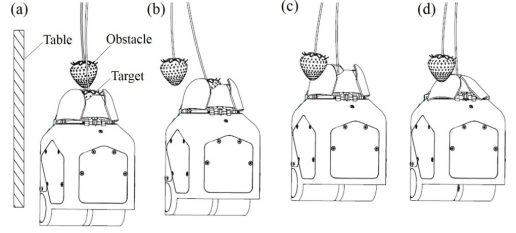


Fig. 6. Dragging operation to avoid capture the obstacles: an upward dragging step moves the target to an area that contains fewer obstacles ((a) and (b)); an upward push-back step pushes the upper obstacles aside (c) before closing the fingers (d).

operation, which is opposite to the push operation as used in other layers. The dragging operation allows the gripper to pick the target fruit without capturing unwanted obstacles. The operation comprises an upward dragging step to move the target to an area that contains fewer obstacles (Fig. 6(b)) and an upward push-back step that pushes the upper obstacles aside (Fig. 6(c)) before closing the fingers. The push-back step is necessary because when at the dragging position (Fig. 6(b)), the peduncle is inclined such that the fruit is difficult to fall due to the static force and easily damaged when the gripper moves up further towards a cutting position.

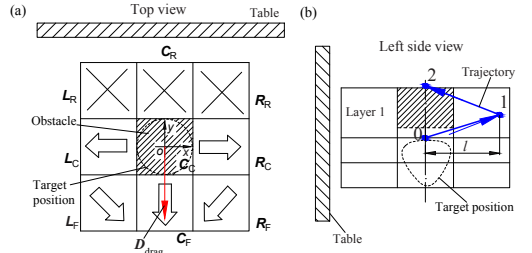


Fig. 7. Diagram of the calculation of the dragging operation: (a) a top view shows the calculation of the dragging direction \mathbf{D}_{drag} in xy plane; (b) a left side view shows the dragging and push-back paths (blue arrows).

The dragging operation is performed only when there are obstacles in the central block C_C of the top layer. If the C_C is unoccupied, the gripper moves directly upwards to pick the target strawberry. Fig. 7 shows the diagram of the calculation method of the dragging operation with corresponding to the example in Fig. 6. As shown in Fig. 7(a), to avoid the collision between the gripper and the table, the three blocks L_R , C_R , R_R that are close to the table are skipped for the calculation of the dragging direction. Then the dragging direction \mathbf{D}_{drag} in the xy plane can be determined according to the following equation:

$$\mathbf{D}_{drag} = \frac{|\sum_1^m \mathbf{U}_j|}{|\sum_1^m \mathbf{U}_j|} \quad (5)$$

where, \mathbf{U} is the vector of the j^{th} unoccupied block within the largest group of adjacent unoccupied blocks. The blocks

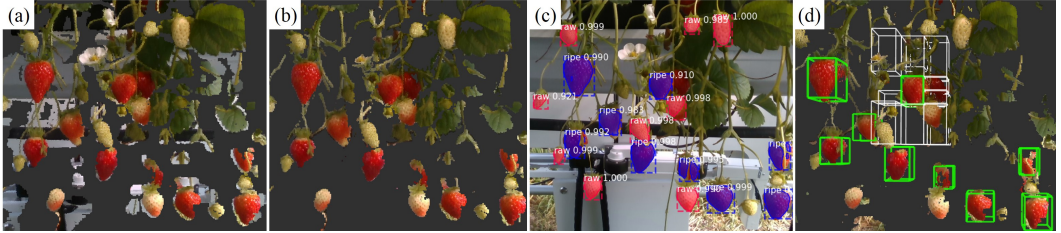


Fig. 8. The workflow of the fruit detection and obstacle determination: (a) original point cloud captured by an RGB-D camera; (b) 3D HSI color thresholding to remove the adjacent noise points from the background; (c) using deep learning to detect the ripe strawberries in an RGB image; (d) fruit localization and obstacle determination in 3D point cloud.

used for calculation are L_C , L_F , C_F , R_F , R_C . The parameter m is the total number of blocks within the largest group of adjacent unoccupied blocks. The norm of D_{drag} is scaled to l (50 mm is used in the current system). If all blocks are occupied by obstacles, the dragging direction is aligned to C_F , where there are fewer obstacles in general. Fig. 7(b) shows the dragging and push-back steps, wherein the dragging and push-back operations moves up the same height in the vertical direction.

III. EXPERIMENTS

A. Image Processing

The image processing includes the detection and localization of ripe strawberries and also the determination of obstacles within the RoI for each target. An RGB-D camera (D435; Intel, USA) was used for image acquisition. The image processing contains three steps: 1) 3D color thresholding to remove noise points from the background, 2) object detection and localization using deep learning based on our previous work [13] and 3) obstacle calculation.

Fig. 8(a) shows the original point cloud, where we can see some pieces of points from the table (silver) and irrigation tubes (black) around the strawberries. The table and irrigation tubes are behind the berries at a distance of about 150 mm. The inaccurate depth sensing result in some of the points connecting to the front berries, which may be regarded as obstacles. To avoid this influence, the first step is to remove the adjacent noise points (silver and black) by using hue, saturation and intensity (HSI) color thresholding, as the result is shown in Fig. 8(b). This step is performed in point cloud using the *jsk_pclros* ROS package. The second step is the detection and localization of the ripe strawberries. As shown in Fig. 8(c), we use an instance segmentation convolutional neural network Mask R-CNN to segment the objects in pixel level such that the 3D location of the ripe strawberries can be obtained combining with depth images [13]. The detection system outputs the 3D bounding boxes of the target strawberries and the thresholded point cloud for further obstacle calculation, as shown in Fig. 8(d). The obstacles around the target is determined based on the method described in Section II-A. To calculate the number of points in each block, we crop the bounding box of each

RoI block in point cloud using the *CropBox* function in the Point Cloud Library (PCL). Fig. 8(d) shows the obstacle bounding boxes around a target, where only blocks occupied with obstacles are displayed.

B. Field Test Setup

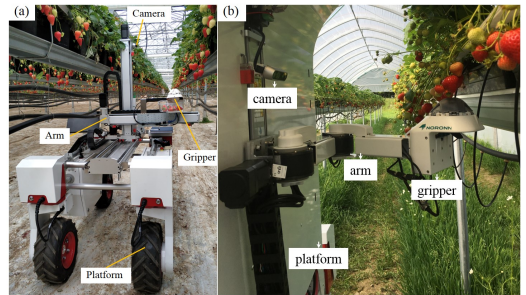


Fig. 9. The strawberry-harvesting robots in the farm: (a) robot version 2.0 using a previous developed Cartesian arm; (b) robot version 3.0 using a newly-developed SCARA arm.

We conducted two sets of experiments in two places: a greenhouse at the Boxford Suffolk Farms (England) and a university experimental tunnel at Norwegian University of Life Sciences (Norway). The tests were carried out on strawberry cultivars of “Malling Centenary” in England and “Murano” in Norway. Generally, “Malling Centenary” is easier for obstacle separation because most of the berries have long and independent peduncles, while “Murano” berries has more clusters with short peduncles growing on one stem. The different biological characteristics may result in different performance of the robot. The England experiments were performed based on our previously developed strawberry-harvesting robot (version 2.0) [1], as shown in Fig. 9(a). The tests in Norway used our newly-developed robot with a SCARA arm (version 3.0), as shown in Fig. 9(b).

C. Results

1) *Application examples*: Fig. 10 demonstrates three examples of the robot separating obstacles in different situations using the proposed algorithm. Each row of the images

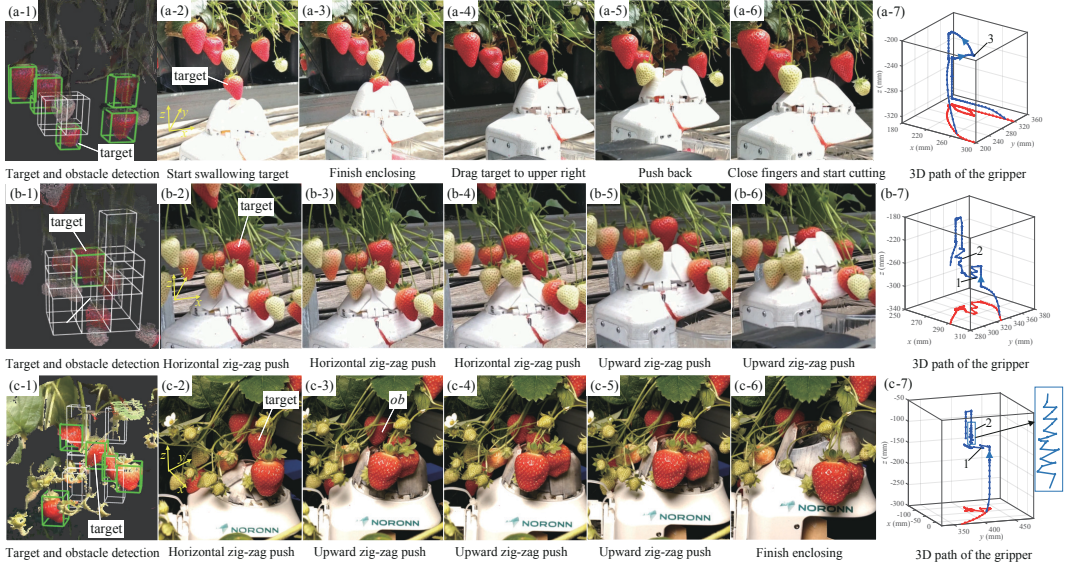


Fig. 10. Examples of the obstacle separation in the field test: each row of images represents a picking case, where the first (left) image shows the detection and localization of target and obstacles and the last image (right) displays the 3D path of the gripper.

in Fig. 10 shows a picking case, in which the first image is the detected target and obstacles in the point cloud and the last image displays the 3D path of the gripper. Fig. 10(a) and (b) show the cases using robot version 2.0 on “Malling Centenary” and Fig. 10(c) illustrates an example using robot version 3.0 on “Murano”.

In Fig. 10(a), a green obstacle is located above the target, which may be swallowed when the gripper is open to capture the target. Fig. 10(a-1) shows that there are no obstacles in layer 2,3 and 4, but in layer 1, the central block C_C and three other blocks L_C , L_F and C_F are occupied with obstacles, so based on Eq. 5, a dragging operation is required and the dragging direction D_{drag} is front right side in the image. As there are no obstacles in layer 2,3 and 4, the gripper moves up directly to enclose the target, as shown in Fig. 10(a-2) and (a-3). After holding the target, the gripper drags the target to the front-right region while moving upward where it contains less obstacles (Fig. 10(a-4)). At this position, if the gripper continues to move up, it might be difficult for the target to fall down towards a cutting position because the peduncle is inclined and the target has a contact force with the fingers. It may also damage the target with such a force. Therefore, in Fig. 10(a-5), the gripper pushes back to the central position while moving up for further fruit detachment (Fig. 10(a-6)), in which the upper obstacles are pushed aside. The blue line in Fig. 10(a-7) shows the recorded 3D path of the gripper during the operation, while the red line is the trajectory projection on the xy plane, from which we can see that the gripper drags the target to $-y$ and $+x$ direction and then moves back. In the last image of each case, path

1, 2 and 3 represents the three stages of operations in the bottom layer, central layers and top layer, respectively.

Fig. 10(b) and (c) demonstrate two more examples of the obstacle separation algorithm with more obstacles in the central layers and bottom layer. Only two blocks (L_R and C_R) in layer 4 are unoccupied with obstacles for the target in Fig. 10(b-1). Therefore, the gripper uses the horizontal zig-zag push from the left rear to right front (the red line in Fig. 10(b-1) shows the direction) to push the obstacles side to side, as can be seen in Fig. 10(b-2) to (b-4). Then, the gripper continues to use the upward zig-zag push to separate the obstacles in the central layers (Fig. 10(b-5) and (b-6)). Without this operation, the target and the obstacles may not be separated but pushed up together due to the contact force between each other. The situation in Fig. 10(c) is similar to Fig. 10(b). The system also determines to use the horizontal zig-zag push to clear the obstacles in the bottom layer and the upward zig-zag push to separate the obstacles from the target in the central layers. Particularly, as shown in Fig. 10(c-3), a red obstacle namely *ob* that is located in the upper left corner of the target may be captured by the gripper if it moves up directly. This may result in failure cutting of the target and also damage to the obstacle *ob*. With the upward zig-zag push, the gripper moves to the right side where the obstacle is out of the fingers, as shown in Fig. 10(c-4). Then it moves back to the left and successfully pushes the obstacle *ob* aside (Fig. 10(c-5)).

2) *Performance test and failure cases:* We recorded the tests data in England and Norway with different settings to analyze the feasibility and performance of the obstacle-

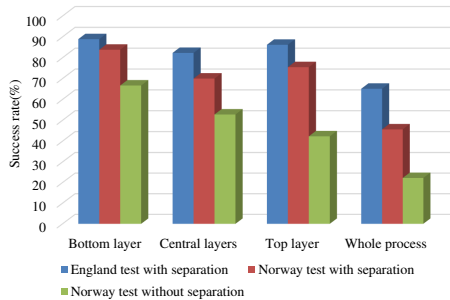


Fig. 11. Comparison of success rate in different layers with different settings.

separation method. The tests in England only show the results using the obstacle-separation method, while in Norway, we conducted a comparison test, using and without using the obstacle-separation method. For the tests in England, we did not include the closed-loop positional error control during picking (see details in [6]), so it may increase the damage. While for the tests in Norway, the closed-loop control has been added before starting the operation in central layers, which may reduce the picking speed compared to the England tests. For each setting, we implemented 100 attempts for the detected targets. Also, as the focus in this study is the obstacle-separation method, only the targets with obstacles were used for the tests. This may result in a lower success rate compared to our previous reports, because the robot has a good performance for isolated strawberries [6].

Fig. 11 reports the success rates in each stage and also the whole process under different settings. The whole process means the manipulation in the whole three stages in the bottom layer, central layers and top layer. In each independent stage, we only considered the results with obstacles in the corresponding layers, while a whole process may contain zero obstacle in one or two stages but at least one obstacle in all the layers. The success in the whole process means that in all the stages the separation is successful. Generally, the comparison tests in Norway show that the obstacle-separation method is effective compared to the attempts without using the obstacle-separation method. Also, the variety of “Malling Centenary” tends to be easier for picking compared to “Murano”. To be more precise, the comparison tests show that the dragging operation in the top layer is most effective, increasing the success rate from 42.3% to 75.5% in the Norway tests. The bottom layer is the easiest layer in terms of obstacle separation. This might be attributed to the gripper design, since the opening action of the fingers under the target can help to push the obstacles aside. The manipulation in the central layers is difficult, showing a success rate of 70% and 52.8% with and without using the upward zig-zag push method, respectively. The success rate of the whole process is relatively low compared to the operation in the individual layer. We included the failures caused by the

inaccurate localization of the targets before manipulation to the success rate calculation of the whole process, which takes up about 18% of all failures. It is also worth noting that in the whole process test, one or two layers may have no obstacles. Therefore, the success rate of the whole process is not simply obtained by the product of the success rates of the three stages. For the test on “Murano”, the success rate of the whole process increases from 22.2% to 45.6% by using the separation method. The same separation method shows a better performance (65.1%) on the variety of “Malling Centenary”.

TABLE I

THE AVERAGE NUMBER OF OBSTACLES AND MANIPULATION TIME.

Test settings	Average number of obstacles								Average manipulation time (s)	
	Bottom layer		Central layers		Top layer		Whole process		Successful cases	Failure cases
	Successful cases	Failure cases	Successful cases	Failure cases	Successful cases	Failure cases	Successful cases	Failure cases		
England test with separation	2.4	3.0	2.0	2.7	1.8	2.0	5.4	8.0	5.0	4.7
Norway test with separation	4.2	4.4	3.1	4.0	2.7	2.6	7.6	8.8	7.6	6.9
Norway test without separation	2.8	3.3	2.4	2.5	2.4	2.4	4.8	5.9	5.3	4.8

We also recorded the average number of obstacles and manipulation time for both successful and failure cases, as shown in Table I. The manipulation time only includes the picking time and arm traveling time [1]. Generally, the average number of obstacles in the successful cases is fewer than that in the failure cases. This means that more obstacles will reduce the success rate. For the comparison tests in Norway, it is clear that without using the separation method, the average number of obstacles is fewer than using the separation method, which means that the separation method is able to work in the cases with more obstacles. In addition, the England tests have fewer obstacles in all cases, which indicates that “Malling Centenary” contains less clusters. As for the manipulation time, it can be seen that the successful cases took more time than failure cases. This is because that in the failures cases, the gripper may return once no targets are captured by the gripper. It is also evident that the tests using the separation method take about 2.2 s more than those without separation in the Norway tests.

As shown in Table II, the most common failure reason before manipulation is the inaccurate depth sensing due to the front obstacles. Also, since our vision system is open loop, the pre-calculated target position might be changed after picking other berries. This is more considerable for “Malling Centenary” as the peduncles are longer and easier to swing after shaking. For the bottom layer, the most frequent failure is caused by the horizontal push because the target position might be changed after pushing other obstacles. This is easier to see when the target and obstacles grow on the same stem. Moreover, if the tip of the target berry is not detected, the top of the bottom layer is higher than the target. Then, the gripper might pushed the target away while moving other obstacles. On the other side, if the top of the bottom layer is lower than the target, the gripper might not be able to push

TABLE II
FAILURE REASONS FOR THE TESTS USING THE SEPARATION METHOD.

Stages	Failure reasons	Murano	Malling Centenary
Before manipulation	1. Target position was changed after picking others	18.7%	33.7%
	2. Inaccurate localization due to front obstacles	81.3%	66.3%
Bottom layer	1. Changed the target position when pushing obstacles	50%	56.3%
	2. Inaccurate estimation of the target bottom position, resulting in pushing the target away or swallowing obstacles	25%	31.2%
	3. Pushed new obstacles to the below of the target, resulting in swallowing small obstacles or pushing the target up	16.7%	12.5%
	4. Did not detect the small obstacles, so did not remove it before the operation in central layers	8.3%	0
Central layers	1. Swallowed small obstacles, due to failure detection or too small to separate	52.6%	38.9%
	2. Swallowed the target, but the connecting obstacles stopped the separation due to the static contact force or short peduncles	26.4%	16.7%
	3. One or more obstacles were captured together with the target, so the gripper is getting stuck	21%	44.4%
Top layer	1. Did not detect small obstacles, or swallowed obstacles in other blocks; did not drag when it is necessary	60.9%	21%
	2. Obstacles moving with the target while dragging or dragging distance is too short	26.1%	63.2%
	3. Dragged to a place that contains obstacles	13%	15.8%

the obstacles aside, resulting in swallowing obstacles. For the central layers, the biggest issue for “Murano” is the mis-capturing of small obstacles due to the unsuccessful detection or too small size to separate. This issue is not very frequent to “Malling Centenary”, since it does not have too many small flowers or berries growing on the same stem of the target. A noticeable failure issue for both varieties is gripper getting stuck due to swallowing of other obstacles together with the target. Then, both the target and obstacles may be pushed up and could not be captured. One reason for this issue is the upward zig-zag push capturing obstacles occasionally. Also, the gripper may swallow obstacles and the target from the beginning due to the inaccurate localization. Another issue is that the gripper may not be able to separate connected berries due to the static contact force between them or short peduncles of the berries. In the top layer, the most frequent failure for “Murano” is the case where a dragging operation is not performed but required. This may be due to the unsuccessful detection of small objects or mis-capturing obstacles in other blocks when the central block in the top layer has no obstacles. However, for “Malling Centenary”, the common failure case is the obstacles moving with the target during the dragging operation due to the long peduncles or the insufficient separation due to short dragging distance. Learned from the failure cases, we think that a closed-loop vision guided manipulation system may improve the performance of the obstacle-separation method considerably, in which the positions of the obstacles and the target are updated continuously.

IV. CONCLUSIONS

We present an obstacle-separation method for selectively picking a target fruit surrounded by obstacles. In addition to the old single push, a zig-zag push operation was used for both bottom layer and central layers of the target, which is able to separate more dense obstacles because of the multi-direction pushes. Also, it helps the gripper capture

a target since the generated shaking motion can break the static contact force between the target and obstacles. Furthermore, we proposed a novel dragging operation to address the issue of mis-capturing obstacles located above the target, in which the gripper drags the target to a place with fewer obstacles and then push back to move the obstacles aside for further detachment. The separation paths are calculated based on the number and distribution of the obstacles. Also, an image processing protocol was developed for the application of the method in a harvesting robot. Field tests showed that the proposed method can improve the picking performance substantially. The performance may be further improved by incorporating a closed-loop vision guided manipulation system. A video of the field experiments can be found at https://drive.google.com/file/d/15B02_4aaR5KHXbgOJq9fV76zf0_i4GJs/view?usp=sharing.

REFERENCES

- [1] Y. Xiong, G. Yuanyue, L. Grimstad, and P. J. From, “An autonomous strawberryharvesting robot: Design, development, integration, and field evaluation,” *Journal of Field Robotics*, pp. 1–23, 2019.
- [2] S. Yamamoto, S. Hayashi, H. Yoshida, and K. Kobayashi, “Development of a stationary robotic strawberry harvester with a picking mechanism that approaches the target fruit from below,” *Japan Agricultural Research Quarterly: JARQ*, vol. 48, no. 3, pp. 261–269, 2014.
- [3] H. Yaguchi, K. Nagahama, T. Hasegawa, and M. Inaba, “Development of an autonomous tomato harvesting robot with rotational plucking gripper,” in *Intelligent Robots and Systems (IROS), 2016 IEEE/RSJ International Conference on*. IEEE, 2016, pp. 652–657.
- [4] C. Lehnert, D. Tsai, A. Eriksson, and C. McCool, “3d move to see: Multi-perspective visual servoing for improving object views with semantic segmentation,” *arXiv preprint arXiv:1809.07896*, 2018.
- [5] E. J. Van Henten, J. Hemming, B. Van Tuijl, J. Kornet, J. Meuleman, J. Bontsema, and E. Van Os, “An autonomous robot for harvesting cucumbers in greenhouses,” *Autonomous Robots*, vol. 13, no. 3, pp. 241–258, 2002.
- [6] Y. Xiong, P. J. From, and V. Isler, “Design and evaluation of a novel cable-driven gripper with perception capabilities for strawberry picking robots,” in *2018 IEEE International Conference on Robotics and Automation (ICRA)*. IEEE, 2018, pp. 7384–7391.
- [7] M. Danielczuk, J. Mahler, C. Correa, and K. Goldberg, “Linear push policies to increase grasp access for robot bin picking,” in *2018 IEEE 14th International Conference on Automation Science and Engineering (CASE)*. IEEE, 2018, pp. 1249–1256.
- [8] M. Laskey, J. Lee, C. Chuck, D. Gealy, W. Hsieh, F. T. Pokorny, A. D. Dragan, and K. Goldberg, “Robot grasping in clutter: Using a hierarchy of supervisors for learning from demonstrations,” in *2016 IEEE International Conference on Automation Science and Engineering (CASE)*. IEEE, 2016, pp. 827–834.
- [9] N. Kitaev, I. Mordatch, S. Patil, and P. Abbeel, “Physics-based trajectory optimization for grasping in cluttered environments,” in *2015 IEEE International Conference on Robotics and Automation (ICRA)*. IEEE, 2015, pp. 3102–3109.
- [10] M. Moll, L. Kavraki, J. Rosell, et al., “Randomized physics-based motion planning for grasping in cluttered and uncertain environments,” *IEEE Robotics and Automation Letters*, vol. 3, no. 2, pp. 712–719, 2017.
- [11] M. R. Dogar, K. Hsiao, M. Ciocarlie, and S. S. Srinivasa, “Physics-based grasp planning through clutter,” *Robotics: Science and Systems VIII*, p. 57, 2013.
- [12] A. Zeng, S. Song, S. Welker, J. Lee, A. Rodriguez, and T. Funkhouser, “Learning synergies between pushing and grasping with self-supervised deep reinforcement learning,” in *2018 IEEE/RSJ International Conference on Intelligent Robots and Systems (IROS)*. IEEE, 2018, pp. 4238–4245.
- [13] G. Yuanyue, Y. Xiong, and P. J. From, “Fruit localization and environment perception for strawberry harvesting robots,” (*Under review: https://drive.google.com/file/d/1gS1QncW6YVnTu8WUXSPz-zlOKZul3-YY/view?usp=sharing*), 2019.

ISBN: 978-82-575-1653-6

ISSN: 1894-6402



Norwegian University
of Life Sciences

Postboks 5003
NO-1432 Ås, Norway
+47 67 23 00 00
www.nmbu.no